



# Durham E-Theses

---

## *New techniques in astronomical multi-slit spectroscopy*

Shaw, Graham David

### How to cite:

---

Shaw, Graham David (1993) *New techniques in astronomical multi-slit spectroscopy*, Durham theses, Durham University. Available at Durham E-Theses Online: <http://etheses.dur.ac.uk/5643/>

### Use policy

---

The full-text may be used and/or reproduced, and given to third parties in any format or medium, without prior permission or charge, for personal research or study, educational, or not-for-profit purposes provided that:

- a full bibliographic reference is made to the original source
- a [link](#) is made to the metadata record in Durham E-Theses
- the full-text is not changed in any way

The full-text must not be sold in any format or medium without the formal permission of the copyright holders.

Please consult the [full Durham E-Theses policy](#) for further details.

# **New Techniques in Astronomical Multi-slit Spectroscopy**

**by Graham David Shaw**

**Submitted in September 1993 for the degree of Doctor of Philosophy**

## **Abstract**

LDSS-2 is a low dispersion survey spectrograph for the William Herschel Telescope. It was constructed to meet an increasing demand for large scale statistical surveys of stellar and galactic populations. This thesis describes its design, construction and installation, together with additional research concerning the fabrication of multi-slit aperture masks.

LDSS-2 has a similar optical system to its predecessor LDSS-1, but it can hold greater numbers of aperture masks, filters and gratings, and its control system is fully automated. This is expected to improve its observing efficiency and allow LDSS-2 to be run as a common-user instrument.

A range of instrument characterisation tests were performed, and they confirmed that LDSS-2 is capable of meeting its astronomical objectives. Its peak efficiency with the medium-blue grism was found to be 20.4% at 5915Å with half-power points at 4135Å and 7225Å.

Six different types of aperture mask were investigated, of which two (photochemically etched and mechanically milled) were tested using LDSS-2. Work was begun towards the development of laser-cut masks, including the procurement of a 16W carbon dioxide laser and a motorised X-Y table.

At present, mechanically milled masks offer the best compromise between cost, lead time, flexibility and quality for an instrument such as LDSS-2. Movable-slit masks may be preferred if access to the focal plane is restricted, but at present they are limited to lower multiplex gains. Laser-cut masks appear to offer the most potential for development in the immediate future, but liquid crystal masks may also become competitive in the longer term.

# **New Techniques in Astronomical Multi-slit Spectroscopy**

**by Graham David Shaw**

Submitted in 1993 for the degree of Doctor of Philosophy  
to the Physics Department of the University of Durham.

The copyright of this thesis rests with the author.  
No quotation from it should be published without  
his prior written consent and information derived  
from it should be acknowledged.

© Copyright 1993 Graham David Shaw

The copyright of this thesis rests with the author. No quotation from it  
should be published without his prior written consent and information  
derived from it should be acknowledged.



22 FEB 1994



LOW DISPERSION SURVEY SPECTROGRAPH

DURHAM-RGO

**LDSS-2**

WHT 1992

# Table of Contents

1	Introduction . . . . .	1
2	Multi-slit Spectrograph Design . . . . .	10
2.1	Introduction . . . . .	10
2.2	Optical Components . . . . .	10
2.3	Dispersion Elements . . . . .	14
2.3.1	Prisms . . . . .	14
2.3.2	Transmission Gratings . . . . .	16
2.3.3	Reflection Gratings . . . . .	18
2.3.4	Grisms . . . . .	19
2.4	Field Acquisition Methods. . . . .	19
2.5	Past and Present Multi-slit Spectrographs . . . . .	21
3	Mask Fabrication Methods. . . . .	25
3.1	Introduction . . . . .	25
3.2	Mask Characteristics . . . . .	26
3.2.1	Cost . . . . .	26
3.2.2	Lead Time . . . . .	26
3.2.3	Slit Quality . . . . .	26
3.2.4	Accuracy of Slit Positions . . . . .	28
3.2.5	Thermal Expansion. . . . .	31

3.2.6	Mask Thickness . . . . .	32
3.2.7	Elasticity . . . . .	36
3.2.8	Optical Properties . . . . .	38
3.2.9	Constraints on Mask Layout . . . . .	39
3.3	Types of Mask . . . . .	39
3.3.1	Photochemically Etched Masks . . . . .	39
3.3.2	Mechanically Punched Masks . . . . .	42
3.3.3	Mechanically Milled Masks . . . . .	43
3.3.4	Laser Cut Masks . . . . .	46
3.3.5	Movable-slit Masks . . . . .	57
3.3.6	Liquid Crystal Masks . . . . .	58
4	LDSS-1 Data Reduction . . . . .	60
4.1	Introduction . . . . .	60
4.2	Field Selection . . . . .	60
4.3	Data Reduction . . . . .	61
4.3.1	Introduction . . . . .	61
4.3.2	Flat-fielding . . . . .	61
4.3.3	Correction of Image Distortion . . . . .	62
4.3.4	Spectrum Extraction . . . . .	63
4.3.5	Wavelength Calibration . . . . .	64

4.3.6	Flux Calibration . . . . .	64
4.4	Results . . . . .	65
4.5	Conclusion. . . . .	65
5	The FOS-2/ISIS Multi-slit Unit . . . . .	68
5.1	Introduction. . . . .	68
5.2	Instrument Characteristics. . . . .	68
5.2.1	ISIS. . . . .	68
5.2.2	FOS-2 . . . . .	69
5.2.3	The Multi-Slit Unit . . . . .	70
5.3	Field Selection. . . . .	71
5.4	Results . . . . .	73
5.5	Conclusion. . . . .	75
6	LDSS-2 Optical and Mechanical Design . . . . .	77
6.1	Introduction. . . . .	77
6.2	Optical Design . . . . .	78
6.2.1	Introduction. . . . .	78
6.2.2	Aperture Masks. . . . .	82
6.2.3	The Collimator . . . . .	84
6.2.4	Filters . . . . .	85
6.2.5	Hartmann Shutters. . . . .	86

6.2.6	Polarisers . . . . .	86
6.2.7	Grisms . . . . .	86
6.2.8	The Shutter . . . . .	87
6.2.9	The Camera . . . . .	88
6.3	Mechanical Design . . . . .	89
6.3.1	Introduction. . . . .	89
6.3.2	The Aperture Wheel . . . . .	89
6.3.3	The Collimator Mount . . . . .	92
6.3.4	The Filter Wheel . . . . .	94
6.3.5	The Grism Wheel. . . . .	94
6.3.6	The Camera Mount. . . . .	95
6.3.7	The Access Ports . . . . .	95
6.3.8	The Handling Frame. . . . .	96
7	The LDSS-2 Control System . . . . .	99
7.1	Introduction. . . . .	99
7.2	Objectives . . . . .	99
7.3	System Overview . . . . .	101
7.4	Mechanism Characteristics. . . . .	104
7.4.1	Introduction . . . . .	104
7.4.2	The Aperture, Filter and Grism Wheels . . . . .	104

7.4.3	The Camera Focus . . . . .	110
7.4.4	The Shutter. . . . .	113
7.4.5	The Access Doors . . . . .	115
7.5	Local Controller Hardware. . . . .	116
7.6	Network Protocol . . . . .	118
7.7	Local Controller Software . . . . .	122
7.8	System Computer Software . . . . .	126
7.9	Testing . . . . .	127
7.9.1	Introduction . . . . .	127
7.9.2	Command Functionality Tests. . . . .	128
7.9.3	Error Condition Tests. . . . .	129
7.9.4	Reliability Tests . . . . .	129
7.9.5	Instrument Attitude Tests . . . . .	131
7.9.6	Conclusion. . . . .	131
8	LDSS-2 Instrument Characterisation . . . . .	133
8.1	Introduction . . . . .	133
8.2	Flexure Tests . . . . .	133
8.2.1	Introduction . . . . .	133
8.2.2	Simulator Tests, Experimental Method. . . . .	134
8.2.3	Simulator Tests, Results . . . . .	135

8.2.4	Astronomical Test, Experimental Method . . .	139
8.2.5	Astronomical Test, Results. . . . .	140
8.2.6	Conclusion. . . . .	140
8.3	Image Distortion. . . . .	142
8.3.1	Introduction . . . . .	142
8.3.2	Experimental Method . . . . .	143
8.3.3	Data Reduction . . . . .	143
8.3.4	Results . . . . .	144
8.3.5	Conclusion. . . . .	145
8.4	Wavelength Calibration . . . . .	146
8.4.1	Introduction . . . . .	146
8.4.2	Experimental Method . . . . .	147
8.4.3	Data Reduction . . . . .	148
8.4.4	Results . . . . .	149
8.4.5	Conclusion. . . . .	150
8.5	Variation of Dispersion with Slit Position . . . . .	151
8.5.1	Introduction . . . . .	151
8.5.2	Experimental Method . . . . .	151
8.5.3	Data Reduction . . . . .	151
8.5.4	Results . . . . .	151

8.5.5	Conclusion . . . . .	153
8.6	Filter Throughput . . . . .	153
8.6.1	Introduction . . . . .	153
8.6.2	Experimental Method . . . . .	154
8.6.3	Data Reduction . . . . .	154
8.6.4	Results . . . . .	155
8.6.5	Conclusion . . . . .	155
8.7	Grism Throughput . . . . .	157
8.7.1	Introduction . . . . .	157
8.7.2	Experimental Method . . . . .	157
8.7.3	Data Reduction . . . . .	159
8.7.4	Predictions . . . . .	160
8.7.5	Results . . . . .	160
8.7.6	Conclusion . . . . .	161
8.8	Flat-field Profile . . . . .	161
8.8.1	Introduction . . . . .	161
8.8.2	Experimental Method . . . . .	162
8.8.3	Results . . . . .	162
8.8.4	Conclusion . . . . .	164
8.9	Ghosting . . . . .	165

8.9.1	Introduction . . . . .	165
8.9.2	Experimental Method . . . . .	165
8.9.3	Data Reduction . . . . .	166
8.9.4	Results . . . . .	166
8.9.5	Conclusion . . . . .	168
8.10	System Throughput . . . . .	170
8.10.1	Introduction . . . . .	170
8.10.2	Theory . . . . .	171
8.10.3	Experimental Method . . . . .	173
8.10.4	Data Reduction . . . . .	174
8.10.5	Results . . . . .	175
8.10.6	Conclusion . . . . .	176
9	Conclusion . . . . .	179
Appendices:		
A	LDSS-2 Wavelength Calibration . . . . .	189
A.1	Introduction . . . . .	189
A.2	Polynomial Coefficients . . . . .	190
A.3	Low Dispersion Grism . . . . .	191
A.4	Medium Dispersion Blue Grism . . . . .	192
A.5	Medium Dispersion Red Grism . . . . .	193

A.6	High Dispersion Grism . . . . .	194
B	LDSS-2 Filter Transmission Functions. . . . .	203
B.1	Introduction . . . . .	203
B.2	PB and PV Filters . . . . .	204
B.3	PR and S1 Filters. . . . .	205
B.4	S2 and S3 Filters . . . . .	206
	Glossary. . . . .	211
	References and Bibliography. . . . .	213
	Acknowledgements . . . . .	218

# List of Tables

1.1	Multi-object spectrographs and fibre-positioners constructed at Durham . . . . .	6
2.1	Chronology of multi-slit spectrographs . . . . .	22
3.1	Variation of throughput with slit position . . . . .	31
3.2	Thermal expansivities of selected materials . . . . .	32
3.3	Variation of throughput with mask thickness (constant slit width) . . . . .	35
3.4	Variation of throughput with mask thickness (variable slit width) . . . . .	35
3.5	Elasticities and Poisson's ratios of selected materials . . . . .	37
3.6	Variation of throughput with mask sag . . . . .	37
3.7	Predicted mask sag for selected materials. . . . .	38
3.8	Synrad CO <sub>2</sub> laser specifications . . . . .	54
3.9	Laser focussing lens specifications. . . . .	54
6.1	LDSS-2 filter specifications . . . . .	85
6.2	LDSS-2 grism specifications . . . . .	87
8.1	LDSS-2 flexure measured using astronomical target . .	140
8.2	Interpolation functions for LDSS-2 image distortion . .	145
8.3	LDSS-2 image distortion at selected radii . . . . .	145

8.4	RMS residuals for LDSS-2 distortion functions . . . . .	145
8.5	Variation of wavelength calibration residual with polynomial order . . . . .	149
8.6	LDSS-2 wavelength calibration results. . . . .	150
8.7	Variation of dispersion with x-coordinate of slit . . . . .	152
8.8	Variation of dispersion with y-coordinate of slit . . . . .	152
8.9	LDSS-2 grism throughput measurements . . . . .	161
8.10	LDSS-2 grism throughput predictions . . . . .	161
8.11	LDSS-2 system throughput calibration exposures . . . . .	174
8.12	LDSS-2 CCD gain measurements for system throughput calibration. . . . .	175
8.13	Summary of measured LDSS-2 system throughput . . . . .	176
8.14	Comparison of measured and expected LDSS-2 system throughput . . . . .	176
A.1	Wavelength calibration polynomial coefficients . . . . .	190
A.2	Recommended wavelength calibration lines for low dispersion grism. . . . .	191
A.3	Recommended wavelength calibration lines for medium-blue grism . . . . .	192
A.4	Recommended wavelength calibration lines for medium-red grism . . . . .	193
A.5	Recommended wavelength calibration lines for high dispersion grism . . . . .	194

B.1	PB and PV filter transmission functions . . . . .	204
B.2	PR and S1 filter transmission functions . . . . .	205
B.3	S2 and S3 filter transmission functions. . . . .	206

# List of Illustrations

1.1	A typical multi-slit spectrograph . . . . .	4
1.2	A typical multi-fibre spectrograph . . . . .	4
2.1	A typical multi-slit spectrograph optical system . . . . .	11
2.2	The pupil of a single-lens collimator. . . . .	13
2.3	The light path through a prism. . . . .	15
2.4	The light path through a transmission grating . . . . .	17
2.5	A blazed transmission grating . . . . .	17
3.1	A slit with a rectangular cross-section. . . . .	34
3.2	A slit with an angled cross-section. . . . .	34
3.3	The width variation of a photochemically etched slit (1) . . . . .	41
3.4	The width variation of a photochemically etched slit (2) . . . . .	41
3.5	The CAMM-3 milling machine. . . . .	44
3.6	An enlargement of a typical CAMM-3 slit . . . . .	45
3.7	The width variation of a CAMM-3 slit (1). . . . .	47
3.8	The width variation of a CAMM-3 slit (2). . . . .	47
3.9	The power transfer function of the Synrad CO <sub>2</sub> laser . . . . .	56
4.1	The spectrum of a galaxy identified by the LDSS-1 survey (1) . . . . .	66

4.2	The spectrum of a galaxy identified by the LDSS-1 survey (2) . . . . .	66
5.1	A display generated by the FOS/ISIS MSU field selection software . . . . .	74
6.1	A schematic diagram of LDSS-2 . . . . .	80
6.2	A typical night sky background spectrum . . . . .	81
6.3	The LDSS-2 aperture wheel clamp (radial view) . . . . .	91
6.4	An LDSS-2 aperture mask cell . . . . .	93
6.5	An LDSS-2 door latch mechanism . . . . .	97
7.1	The LDSS-2 control system . . . . .	103
7.2	The output signals from the rotary incremental encoder . . . . .	107
7.3	The SLVC/ADC signal transfer function . . . . .	112
7.4	The WHT Utility Network. . . . .	119
7.5	The LDSS-2 local controller software. . . . .	124
8.1	Variation of LDSS-2 translational flexure with zenith distance . . . . .	136
8.2	Variation of LDSS-2 rotational flexure with zenith distance . . . . .	136
8.3	LDSS-2 translational flexure hysteresis curve. . . . .	137
8.4	Variation of LDSS-2 flexure with rotator angle . . . . .	137

8.5	Variation of LDSS-2 flexure in dispersion direction versus time . . . . .	141
8.6	LDSS-2 grism efficiencies measured by RGO . . . . .	158
8.7	Unfiltered cross-section through LDSS-2 flat field . . . . .	163
8.8	Filtered cross-section through LDSS-2 flat field. . . . .	163
8.9	Ghost spectra observed in an LDSS-2 calibration exposure . . . . .	167
8.10	Main spectrum for comparison with figure 8.9 . . . . .	167
8.11	LDSS-2 system throughput . . . . .	177
9.1	LDSS-2, installed at the Cassegrain focus of the WHT . . . . .	180
9.2	The spectrum of 5C12-group galaxy number 121. . . . .	181
9.3	The spectrum of 5C12-group galaxy number 131. . . . .	181
9.4	The spectrum of 5C12-group galaxy number 180. . . . .	182
9.5	The spectrum of 5C12-group galaxy number 217. . . . .	182
9.6	A typical dispersed LDSS-2 exposure . . . . .	183
A.1	CuAr line identification chart for low dispersion grism (1) . . . . .	195
A.2	CuAr line identification chart for low dispersion grism (2) . . . . .	196
A.3	CuAr line identification chart for medium-blue grism (1) . . . . .	197

A.4	CuAr line identification chart for medium-blue grism (2) . . . . .	198
A.5	CuAr line identification chart for medium-red grism (1) . . . . .	199
A.6	CuAr line identification chart for medium-red grism (2) . . . . .	200
A.7	CuAr line identification chart for high dispersion grism (1) . . . . .	201
A.8	CuAr line identification chart for high dispersion grism (2) . . . . .	202
B.1	PB, PV and PR filter transmission functions. . . . .	207
B.2	S1 filter transmission function . . . . .	208
B.3	S2 filter transmission function . . . . .	209
B.4	S3 filter transmission function . . . . .	210

# Preface

The work presented in this thesis was carried out between 1989 and 1993 while the author was a research student under the joint supervision of Dr J R Allington-Smith, Dr J M Breare and Dr J V Major in the Physics Department at the University of Durham.

Some of this work was done in collaboration with various colleagues, details of which are given in the introduction. None of this work has been submitted for a degree to Durham or any other university.

Certain results have appeared in the following papers:

1. Allington-Smith *et al* (1990a)
2. Allington-Smith *et al* (1990b)
3. Allington-Smith (1992a)
4. Allington-Smith *et al* (1992c)
5. Colless *et al* (1991)

# Chapter 1: Introduction

This thesis describes some of the work done at Durham University between 1989 and 1993 to investigate and develop the technique of astronomical multi-slit spectroscopy.

Multi-slit spectroscopy is a method used to observe the spectra of many astronomical objects in a single exposure. This requirement arises from an increasing demand for large statistical surveys of stellar and galactic populations. Such surveys are used in several fields of study, including:

- **Cosmology.** To investigate the large-scale structure of the universe, it is necessary to plot the distribution of galaxies in three dimensions. This is done with the aid of a red-shift survey and allows the observer to identify clusters and determine their membership.
- **Cluster dynamics.** If a group of galaxies is bound in a cluster then it is subject to the Virial theorem. The mass of the cluster can thus be deduced from its velocity dispersion. Clusters enclose very large volumes of space, so this allows the mass of the universe to be estimated with fewer assumptions about the abundance of 'dark matter'.
- **Galactic evolution.** The age of a galaxy is correlated to its redshift, so by comparing galaxies at different redshifts it is possible to investigate their evolution. Parameters that can be measured include luminosity, colour, and the relative strengths of different emission and absorption lines.
- **Galactic structure.** Information about the distribution and abundance of different types of star population can be used to study the structure of our galaxy. Much of this work is carried out using photometric data, but multi-object spectroscopy allows stars to be classified more



accurately, and in particular, can reliably differentiate between stars, galaxies and QSOs.

- Stellar evolution. The age of a star cannot be measured directly, but stellar evolution can be investigated using statistical methods. Multi-object spectroscopy is particularly well suited to observing star clusters, which allow comparisons to be made between stars of a common age and origin.
- Exotic objects. Objects such as high-redshift galaxies and QSOs are sparsely distributed, so they are best investigated using conventional long-slit techniques. However, in order to find them, it is necessary to survey large numbers of potential targets. Initial screening can be carried out by colour selection but a spectrum is needed for reliable identification.

Prior to the development of multi-slit and multi-fibre spectroscopy the only practical way to conduct this type of survey was to use a Schmidt camera with an objective prism. Schmidt plates give high multiplex gains (typically of the order of 10,000) but their resolution is poor and they are not suitable for observing faint objects.

The magnitude limit of a faint object spectrograph is largely determined by the sky background level. Conventional long-slit spectrographs prevent most of the background from reaching the detector and most of what remains can be subtracted when the data is reduced. Objective prism cameras do not have slits, so none of the background is intercepted. This results in a relatively poor limiting magnitude of about  $b_j=20$ .

It is possible to observe more than one target per exposure with a long-slit spectrograph, but each group of targets must lie in a straight line. Consequently, the multiplex gain is rarely greater than 2, and even that may require the parallactic angle to be compromised. To overcome this

limitation, it is necessary to block the background without constraining the location of the targets. At present there are two techniques that can be used to do this: multi-slit spectroscopy and multi-fibre spectroscopy.

A typical multi-slit spectrograph is illustrated in figure 1.1. Light from the telescope is focussed onto a multi-slit 'aperture mask'. The mask must be aligned with the image of the target field such that each target is positioned over one of the slits. A different mask layout is thus needed for each field. This can be achieved either with a reusable mask that can be reconfigured, or an expendable mask that is manufactured for a specific set of targets.

When the light has passed through the mask it is dispersed and focussed onto the detector. Each slit generates its own dispersed image, which must be isolated from the others before it is reduced. The necessary coordinates can be derived from the data used to produce the mask. In most other respects the data reduction procedure is similar to that for a long-slit spectrograph.

A typical multi-fibre spectrograph is shown in figure 1.2. It consists of two components: the multi-fibre unit (mounted at the telescope focus) and the spectrograph (located nearby). Each fibre is used to sample light from one point in the focal plane. Most are aligned with target objects, but some are used to measure the sky background level. The light is then dispersed and measured by the spectrograph.

Both types of spectrograph have advantages and both have a role to play in multi-object spectroscopy. Their main differences are as follows:

- Multi-fibre spectrographs can achieve higher multiplex gains, because the position of a spectrum on the detector need not be determined by the position of the corresponding target. This simplifies target selection and allows the detector to be utilised more efficiently. The gain can be further improved by using one multi-fibre unit to feed

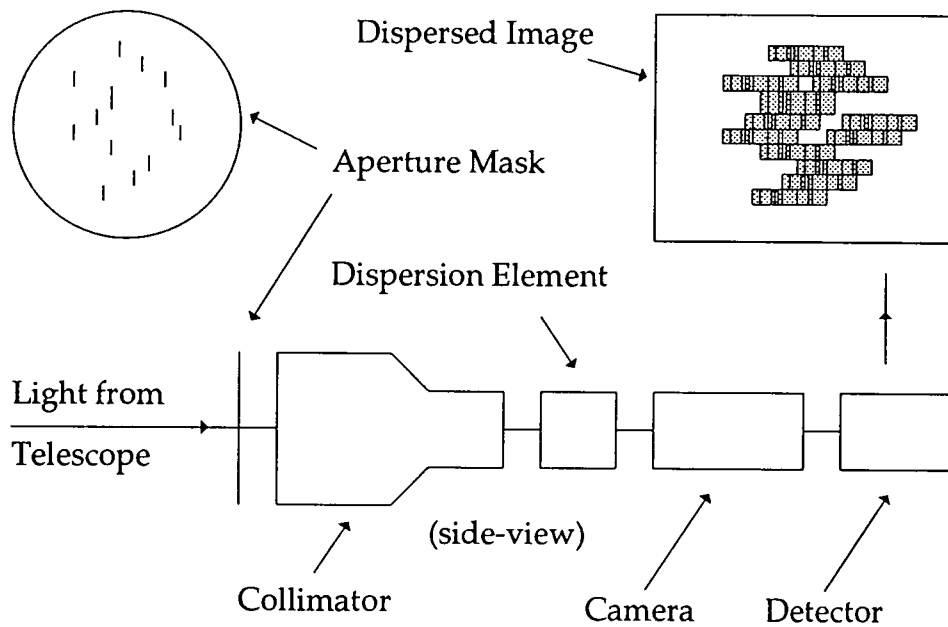


Figure 1.1: A typical multi-slit spectrograph

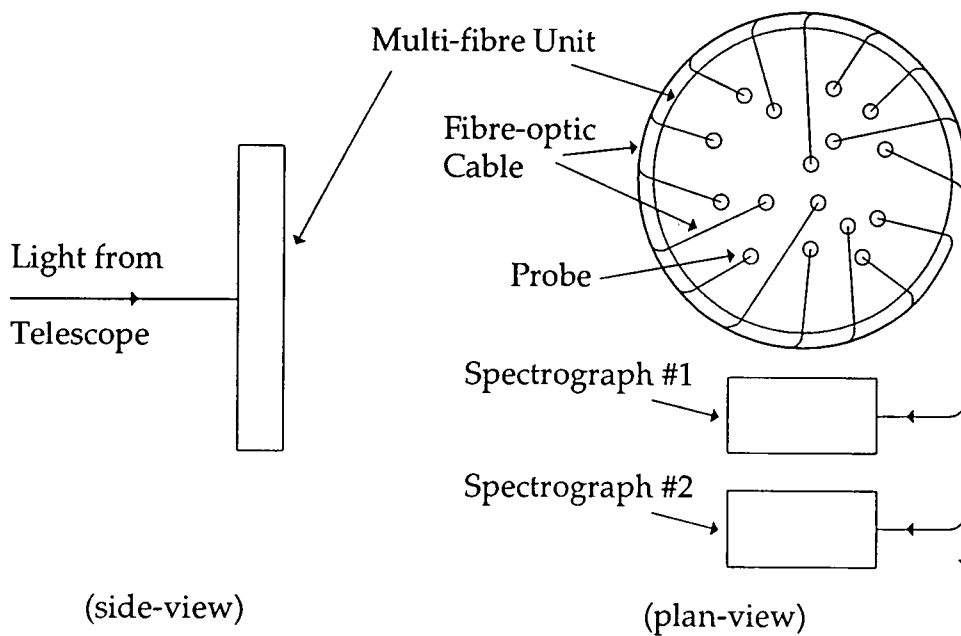


Figure 1.2: A typical multi-fibre spectrograph

several spectrographs; the only limitation is the area available for fibre feeds at the telescope focus. It is currently possible to observe 100–400 simultaneous targets with a multi-fibre spectrograph, compared to 25–100 targets with a multi-slit spectrograph.

- Most multi-fibre spectrographs can be configured remotely, if necessary while the telescope is tracking the target field. This enhances the flexibility of the instrument as targets can be selected immediately before they are observed. Automated multi-slit units have been developed but are currently limited to relatively low multiplex gains (10–20 targets).
- Multi-slit spectrographs can observe to fainter limiting magnitudes than comparable multi-fibre spectrographs (typically by about 1 magnitude). This is partly because their throughput is higher and partly because they allow the sky background level to be estimated more accurately.
- Given a suitable aperture mask, a multi-slit spectrograph can double as a long-slit spectrograph. This can be useful because on a large telescope it is not normally practical to switch between instruments during an observing run.
- Some types of multi-slit aperture mask allow slits to be curved. They can be used to observe gravitationally-lensed arcs, or isophotes along galactic spiral arms. Multi-fibre spectrographs are unsuitable for this type of work because of the clearance required between adjacent fibre probes.
- Some multi-slit spectrographs support direct imaging (by removing the aperture mask and the dispersion element from the light path). This increases the range of field acquisition methods that can be used and allows the instrument to be used for target selection and

astrometry.

The Astronomical Instrumentation Group at Durham University has been responsible for the construction of several multi-slit spectrographs and multi-fibre positioners (in partnership with the relevant observatories). The most recent are listed in table 1.1. My research was concerned with multi-slit spectroscopy, and in particular, with the construction and installation of LDSS-2. Its objectives were twofold: the provision of a facility that could be used by others for astronomical research, and the development of multi-slit techniques so that current and future instruments can achieve their full potential.

Instrument	Telescope	Date	Type
FOS-1 (w/MMU)	INT	Feb'86	Multi-slit
LDSS-1	AAT	Jun'86	Multi-slit
Autofib-1	AAT	Feb'87	Multi-fibre
Autofib-1.5	WHT	Feb'89	Multi-fibre
FOS-2 (w/MSU)	WHT	Feb'90	Multi-slit
Autofib-2	WHT	May'92	Multi-fibre
LDSS-2	WHT	Feb'92	Multi-slit

Table 1.1: Multi-object spectrographs and fibre-positioners constructed at Durham

'LDSS' stands for 'Low Dispersion Survey Spectrograph'. LDSS-1 had been in use at the Anglo-Australian Telescope (AAT) for three years when I began my research. During that period it demonstrated that multi-slit spectroscopy was practical and could yield valuable astronomical results (Colless *et al*, 1990). However, few of the instrument's functions are automated, so an observer must be present inside the Cassegrain focus cage to operate it. For this and other reasons it is not considered to be a 'common-user' instrument, meaning that it can only be used by or in collaboration with its sponsors.

LDSS-2 is intended to address many of the limitations of LDSS-1. It operates at the Cassegrain focus of the William Herschel Telescope (WHT). Unlike its predecessor, LDSS-2 is fully automated and can be operated entirely from

the instrument control room. It is also a common-user instrument which any eligible astronomer can apply to use via PATT.

The optical performance of LDSS-2 is expected to be similar to LDSS-1, the main improvement being a greater maximum dispersion. The WHT is situated at a latitude of 29°N and the AAT at 31°S, so between them LDSS-1 and LDSS-2 can cover the whole sky.

This thesis is divided into nine chapters, including this introduction:

Chapter 2 reviews some of the theory underlying multi-slit spectrograph design. It explains how multi-slit spectrographs differ from long-slit spectrographs, and in particular, how their design is influenced by the need for a wide field of view. A typical design is considered and the function of each component described in detail. The chapter also describes some of the multi-slit spectrographs that have been constructed elsewhere in the world, specifically EFOSC for the ESO 3.6m telescope, EMMI for the NTT, MOS/SIS for the CFHT and LRIS for the Keck.

Chapter 3 investigates the methods that can be used to manufacture aperture masks. It first defines some of the properties that can be used to characterise different types of mask, including cost, lead time, mask quality and accuracy, and restrictions on slit layout. It then describes specific manufacturing techniques in detail and assesses their relative advantages and disadvantages. Experimental results are given for the two types of mask (photochemically etched and mechanically milled) that have been tested with LDSS-2.

Chapter 4 looks at some preliminary work carried out using data from LDSS-1. The main objective of this work was to give me personal experience of multi-slit data reduction, including the problems that are encountered and the techniques that can be applied. The project was carried out in collaboration with Prof R S Ellis (Durham) and Dr M M Colless (Durham).

Chapter 5 details further preliminary work concerning the FOS-2 multi-slit unit. FOS-2 was not designed as a multi-slit spectrograph, but by retrofitting a multi-slit mask holder it was possible to obtain a limited multi-object capability. This was done partly as an interim measure and partly to gain experience. Topics addressed in this chapter include mask manufacture, field acquisition, data reduction, and general problems associated with commissioning a new instrument. The work was carried out in collaboration with Dr J M Breare (Durham), Dr J R Allington-Smith (Durham) and D W Gellatly (RGO).

Chapters 6, 7 and 8 cover the design, construction, installation and testing of LDSS-2. These tasks occupied most of my period of study and were performed in collaboration with Dr J R Allington-Smith (Durham), Dr N R Tanvir (Durham), J Webster (Durham), Dr J M Breare (Durham/LPO), D W Gellatly (RGO), Dr S P Worswick (RGO) and J F Maclean (RGO). My primary responsibilities were the control system and the instrument characterisation, but I assisted at all stages of the assembly, testing and commissioning of the instrument. Most of the design work pre-dated my involvement in the project.

Chapter 6 introduces LDSS-2 by reviewing its optical and mechanical design characteristics. The optics were designed by Dr S P Worswick (RGO) and in most respects are very similar to the optics of LDSS-1 (Wynne and Worswick, 1988). The mechanical structure was designed by D W Gellatly (RGO), with some modifications made in Durham as the instrument was constructed.

Chapter 7 describes the instrument control system, which consists of the 'local controller' (located close to the instrument) and the telescope system computer (located in the control room). I was responsible for the construction of the local controller and for writing part of its control program. The remainder was adapted from the control program for another

instrument, written by A Popplestone (RGO) and J F Maclean (RGO). The system computer software was written by P B Taylor (RGO), adapted from a template written by N Houghton (RGO).

Chapter 8 details the work done to test the optical characteristics of the instrument, including the dispersion curve, the throughput of each filter and grism, and the throughput of the system as a whole. The primary purpose of this was to ensure that the instrument complies with its design specifications and that there are no serious errors in its construction or alignment. In addition, some of the optical parameters that were measured will be useful to astronomers wishing to use the instrument, both for planning observations and for reducing data.

Chapter 9 concludes this thesis, summarising the results of the previous chapters.

# Chapter 2: Multi-slit Spectrograph Design

## 2.1 Introduction

This chapter investigates some of the theoretical issues associated with multi-slit spectrograph design, including:

- the function of each component and the manner in which they interact
- the characteristics of different types of dispersion element and their suitability for multi-slit work
- the optical techniques that can be used to obtain wide fields of view
- the methods that can be used to acquire multi-slit fields using the telescope guidance system

Methods for fabricating multi-slit aperture masks are discussed in the next chapter.

## 2.2 Optical Components

The optical layout of a typical multi-slit spectrograph is illustrated in figure 2.1. It consists of five components: the aperture mask, the collimator, the dispersion element, the camera, and the detector.

The aperture mask is located at the focal plane of the telescope. It is aligned with the target field and contains a slit for each target that is to be observed. The reason for using a slit is to permit the use of a technique known as ‘sky subtraction’. This works by measuring the background spectrum on either side of the target then estimating the background underneath the target by interpolation.

Sky subtraction is most effective when the slit is long and its width is constant. Long slits use more space on the detector, so there is a trade-off between multiplex gain and data quality. Variation in the slit width is largely determined by the mask fabrication method and is considered in the

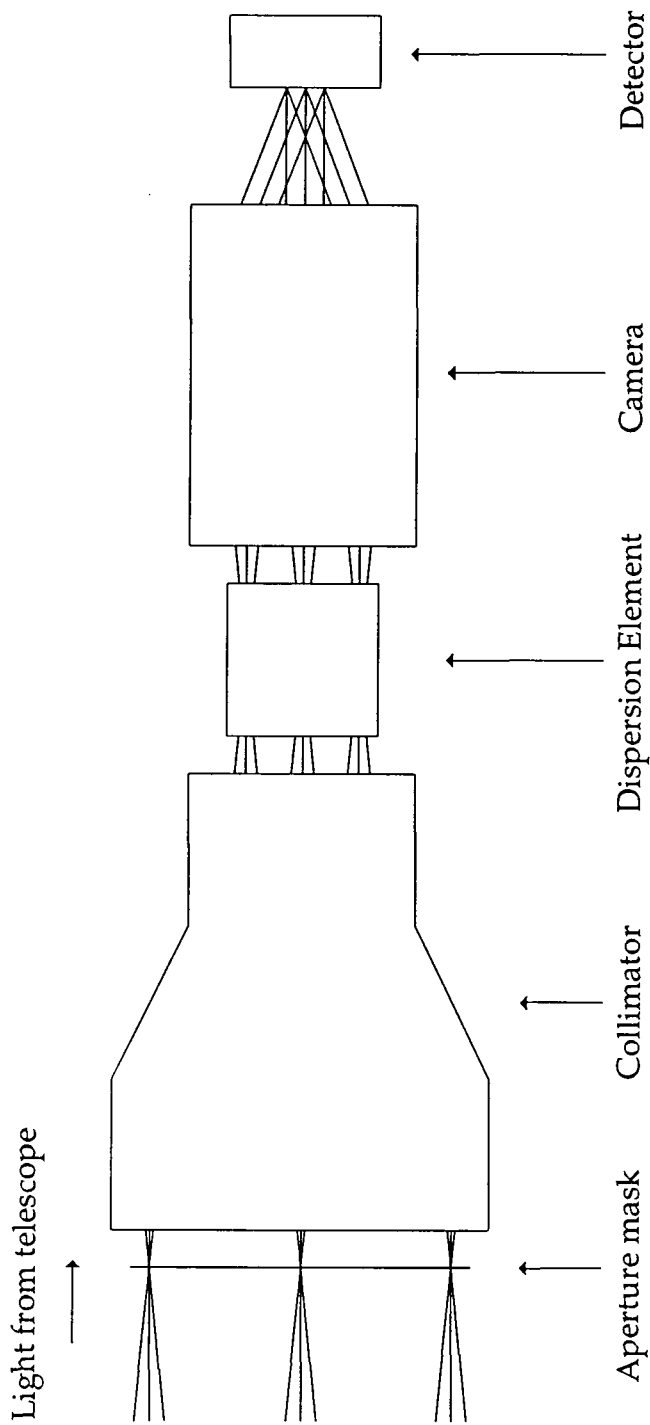


Figure 2.1: A typical multi-slit spectrograph optical system

next chapter.

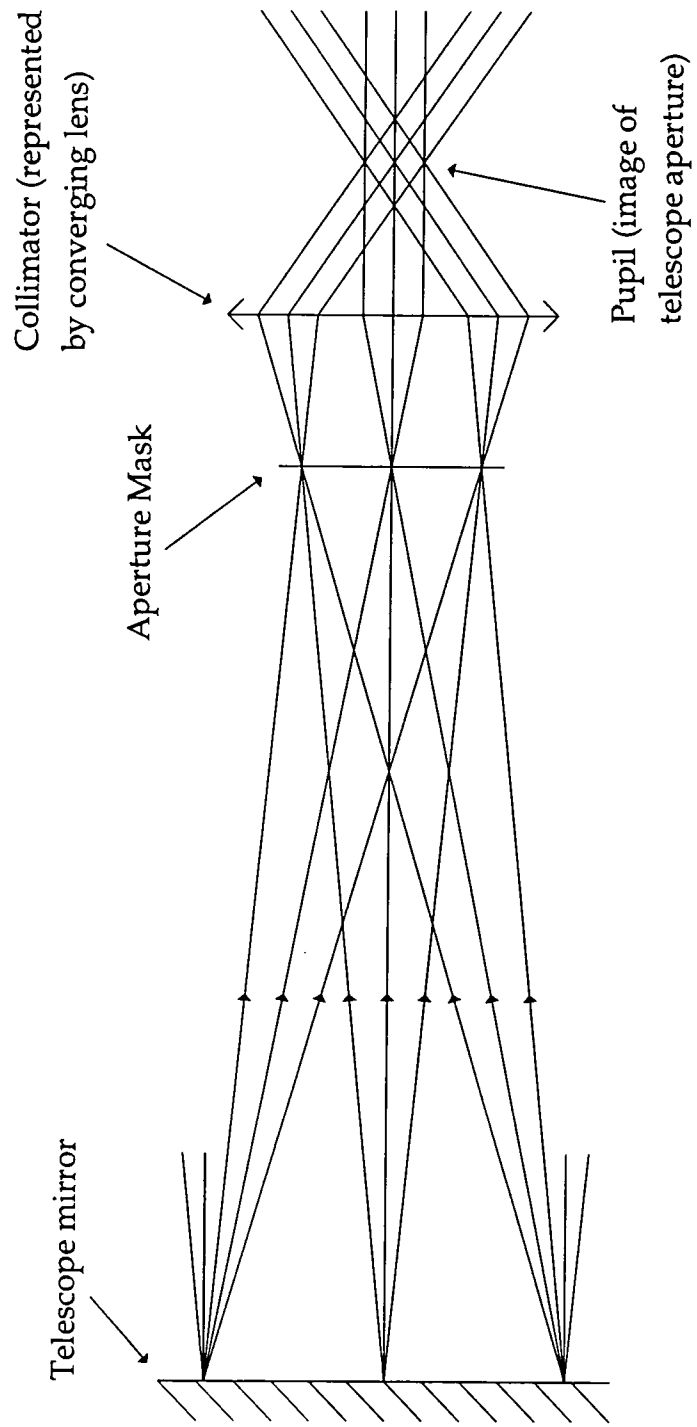
Most types of dispersion element will not function correctly in a strongly diverging beam, so the next spectrograph component is usually a collimator. One of the simplest types of collimator is a single converging lens, but it suffers from a number of limitations including spherical and chromatic aberration. More complex designs are therefore necessary in most cases, especially if the spectrograph must have a wide field of view.

One important consideration is that the collimator must evenly illuminate the dispersion element. This is necessary to avoid off-axis vignetting and to minimise the effect of grating defects. To ensure even illumination, the collimator must form a pupil (an image of the telescope aperture) close to the dispersion element. This is illustrated in figure 2.2.

A simple collimator does form a pupil but its position is effectively dictated by other optical parameters. The pupil is rarely in the location that would be selected given a free choice and this may have serious implications for the design of the rest of the spectrograph. It is therefore desirable that the pupil position be controlled independently. This can be achieved by adding a field lens to the front of the collimator, a technique known as 'pupil imaging'.

There are four common types of dispersion element: the prism, the transmission grating, the reflection grating and the grism. Their characteristics are discussed in section 2.3 below. None is suitable for all applications and the choice of dispersion element for a particular instrument requires detailed analysis of its design objectives.

The camera focuses the light onto the detector. This is effectively the inverse function to the collimator, except that the image scale must be appropriate to the detector resolution. The detector itself may be either internal or external to the instrument. External detectors are preferred, as they are easy to upgrade and can be shared between instruments, but they do require the



(not to scale)

Figure 2.2: The pupil of a single-lens collimator

camera focus to be located outside the instrument. Some optical designs do not permit this, in which case an internal detector must be used.

## 2.3 Dispersion Elements

### 2.3.1 Prisms

When a beam of light passes through a prism it follows the path shown in figure 2.3. The angle of emergence,  $\theta_4$ , can be calculated using Snell's law:

$$n_i \cdot \sin(\theta_i) = n_t \cdot \sin(\theta_t)$$

where  $\theta_i$  is the angle of incidence,  $\theta_t$  is the angle of transmission,  $n_i$  is the refractive index of the first medium, and  $n_t$  is the refractive index of the second medium.

Replacing  $n_2/n_1$  by  $n$ , it follows that for the prism in the diagram:

$$\theta_2 = \sin^{-1}(\sin(\theta_1)/n)$$

$$\theta_4 = \sin^{-1}(n \cdot \sin(\sin^{-1}(\sin(\theta_1)/n) - \alpha))$$

The equation can be simplified by considering the special case in which  $\theta_1=0$ :

$$\theta_4 = -\sin^{-1}(n \cdot \sin(\alpha))$$

If  $n$  varies with wavelength then the light will be dispersed. The dispersion depends on the angle of incidence, the angle between the faces of the prism, and the glass from which the prism is made.

As dispersion elements, prisms have two main disadvantages. A high dispersion can only be achieved if the light enters and leaves the prism at a large angle of incidence. This reduces the throughput, as more of the light is reflected. The dispersion is also highly non-linear. This results in poor utilisation of the detector, as different parts of the spectrum are sampled at different resolutions. For these reasons, prisms are best suited to low

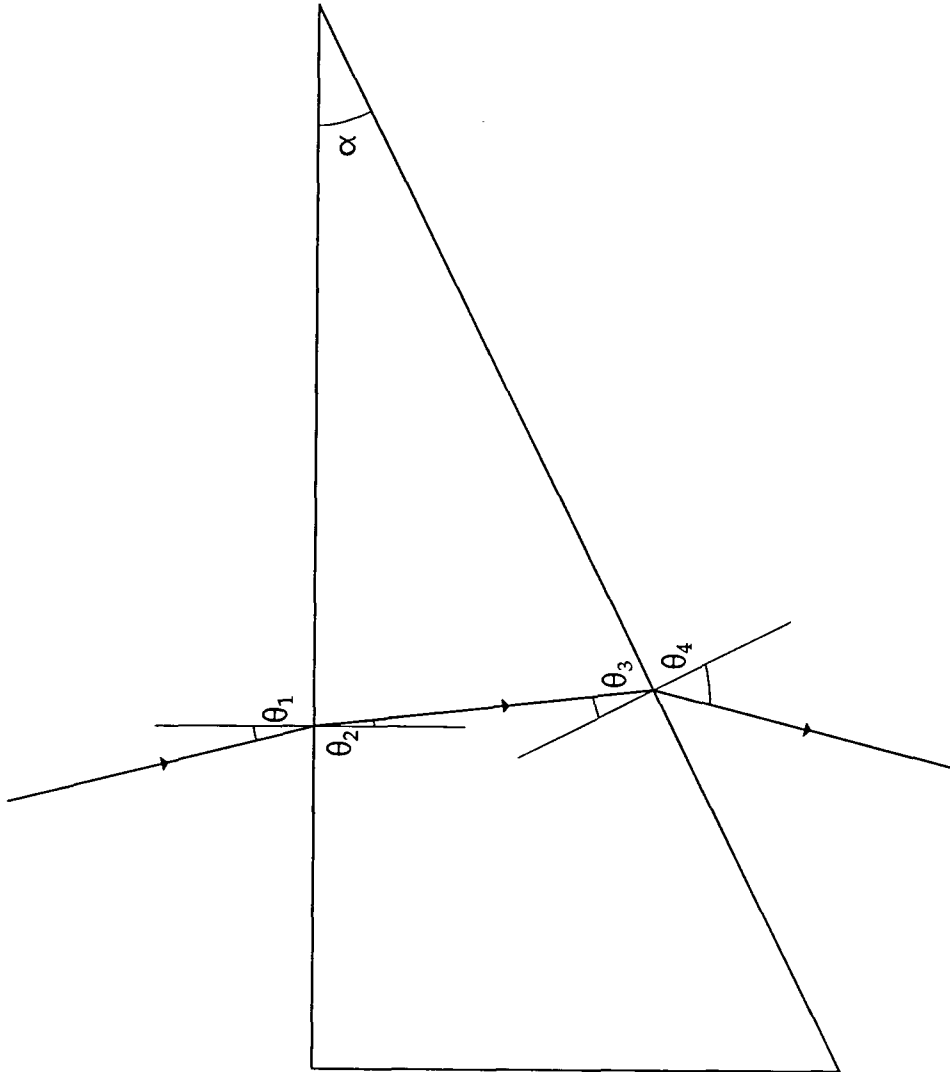


Figure 2.3: The light path through a prism

dispersion applications and are rarely used as primary dispersion elements in astronomical instruments.

### 2.3.2 Transmission Gratings

A transmission grating consists of a transparent substrate on which a large number of parallel lines are ruled. The lines are evenly spaced and split the incident light beam into an array of secondary sources. When the light recombines it is transmitted only in those directions in which there is constructive interference.

This effect is illustrated in figure 2.4. The amplitude  $A$  observed at an angle  $\theta$  is given by the equation:

$$A = A_0 \cdot \sum_{m=0}^M \sin(2\pi \cdot m \cdot d \cdot \sin(\theta) / \lambda)$$

where  $M$  is the number of grating rules illuminated by the incident light beam. Constructive interference occurs when:

$$d \cdot \sin(\theta) = n \cdot \lambda$$

where  $n$  is an integer known as the spectral 'order'.  $n=\pm 1$  defines the 'first-order spectrum',  $n=\pm 2$  the 'second-order spectrum' and so on. The higher order spectra lie at progressively greater angles from the normal, up to a limiting value of  $n$  at which  $\sin(\theta)=\pm 1$ . The dispersion of an order at a given angle is proportional to  $n$ , so the second order spectrum has twice the dispersion of the first order.  $n=0$  corresponds to light that is not deflected or dispersed by the grating and is known as the 'zero-order'.

The presence of many spectral orders in the same exposure presents two problems: first they can overlap, causing inter-order contamination, and second they represent wasted light, reducing the throughput of the instrument.

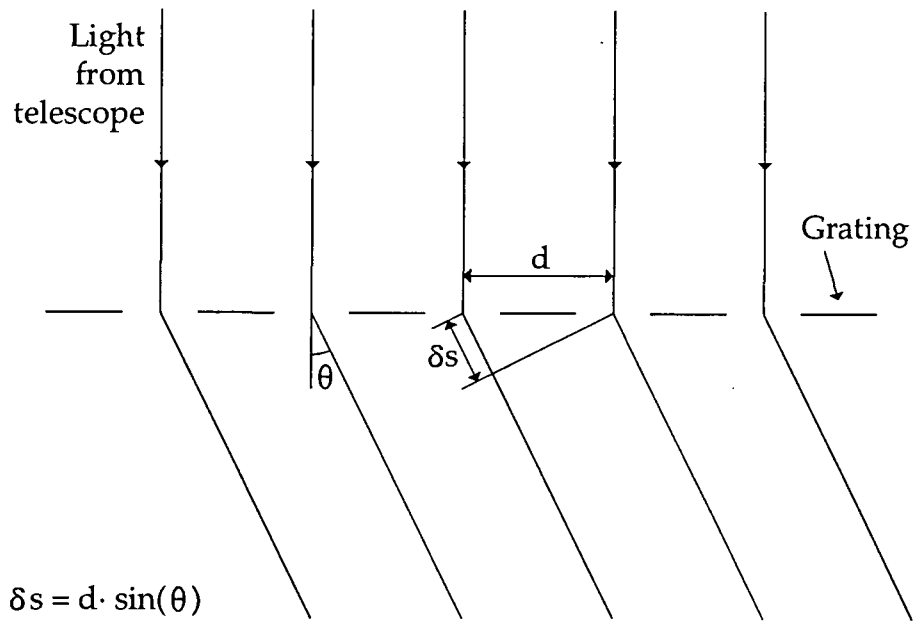


Figure 2.4: The light path through a transmission grating

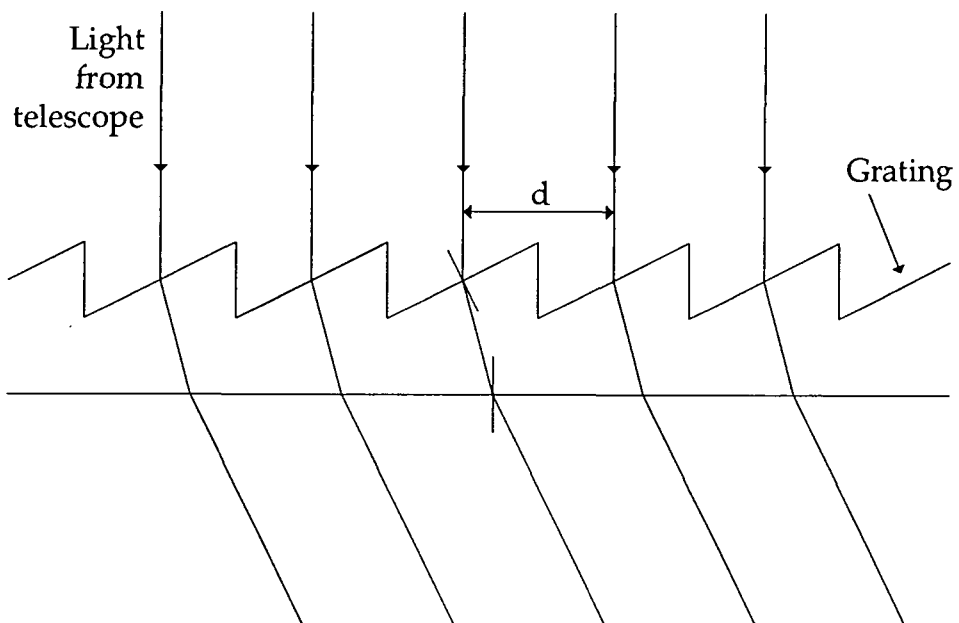


Figure 2.5: A blazed transmission grating

One way in which contamination can be avoided is to separate the spectra using a cross-dispersion prism. This has the additional benefit of extending the spectral range of the instrument, but is unsuitable for multi-slit spectrographs because of the additional space required on the detector. A better solution in such cases is to use an order-blocking filter to prevent the unwanted wavelengths from reaching the detector.

By default, approximately 80% of the incident light is directed into the zero-order, whereas only 10% reaches the first-order spectrum (Brown, 1965, p402). This is clearly very wasteful and would result in an unacceptably low instrument throughput. However, the throughput can be improved greatly by applying a 'blaze' to the grating, as illustrated in figure 2.5. Each grating rule acts as a small prism, which deflects the light towards the first-order spectrum. Dispersion caused by the blaze does not affect the dispersion curve of the grating as a whole. The blaze angle must be optimised for a specified wavelength, but this can be chosen according to astronomical priorities.

### **2.3.3 Reflection Gratings**

A reflection grating operates using the same principle of optical interference as a transmission grating, but is fabricated on the surface of a mirror. This has two significant advantages:

- Reflection gratings are easier to handle, as they can be supported from the back. Transmission gratings can only be supported at their perimeter.
- Blazed reflection gratings are considerably cheaper and easier to manufacture than blazed transmission gratings.

Lower cost allows the size of the grating and thus its spectral resolution to be increased. For this reason, reflection gratings are the preferred dispersion element for most types of general-purpose spectrograph. However, their optical geometry is such that they do require a longer collimated light path

than an equivalent transmission grating and this makes it more difficult to achieve a wide field of view.

#### 2.3.4 Grisms

A grism consists of a transmission grating and a prism that have been cemented together to act as a single optical component. Its dispersion is mostly attributable to the grating; the purpose of the prism is to deflect the first order spectrum so that it is transmitted in approximately the same direction as the incident beam. This has three significant advantages over other types of dispersion element:

- The instrument can have a single optical axis, which simplifies the task of aligning its optics.
- The mechanical structure can maintain an approximate radial symmetry about the optical axis. This simplifies its design and ensures that the centre of gravity of the instrument is close to the axis of the telescope.
- Grisms are interchangeable, as the first-order spectrum always emerges in the same direction. Prisms and reflection gratings can be exchanged, but their angle of tilt must be varied to compensate for the change in deflection.

Grisms are more expensive than equivalent transmission and reflection gratings, but their cost may be justified if they simplify the design of other parts of the instrument.

## 2.4 Field Acquisition Methods

Field acquisition is the process by which the aperture mask and the target field are brought into alignment. The time taken to do this can have a significant effect on the efficiency of the spectrograph, especially where the integration time per field is short. When taking a series of exposures using the same mask it is also useful to be able to check the field acquisition

without moving the mask or the telescope.

The required field acquisition accuracy is calculated in the next chapter. It depends on the image scale, the slit width and the seeing, and normally exceeds the blind pointing accuracy of the telescope by a large factor. The field acquisition procedure must therefore consist of at least two steps: an initial blind offset, followed by one or more corrections.

To calculate the size of each correction, some form of imaging facility is required. If the instrument supports undispersed imaging then the preferred option is to use the main detector. This requires fewer instrument parameters to be calibrated and gives the user more confidence that the acquisition is correct. An autoguider is necessary to ensure that acquisition is not lost as a result of tracking errors.

If the targets are faint, they may be unsuitable for defining the mask position. This is especially true of extended objects, as their centroids may be difficult to measure to the required level of accuracy. It is therefore common practice to acquire the field with a set of relatively bright fiducial stars that are not themselves targets.

Where undispersed imaging is supported there are two main types of acquisition procedure. The first is to use a direct image of the target field to determine the target positions and an image of the mask taken using a comparison lamp to determine the slit positions. Good blind pointing accuracy is desirable, but not necessary. However, the acquisition cannot be checked without moving the mask, which is inconvenient when a long integration time is required.

The second method is to use a single undispersed exposure of the target field, taken through the mask, to determine both the target and slit positions. In this case the fiducial stars must correspond to circular holes in the mask, so cannot also be targets. The data reduction software uses the hole centres

and the star centroids to calculate the telescope offset. The same procedure can be used to check the field acquisition.

For the second method to work, the blind pointing accuracy of the telescope must be good enough to bring the fiducial star images within the corresponding mask holes. If this is not practical then it would be possible to use the first method to acquire the field and the second method to check and if necessary improve the acquisition.

An alternative method that does not require imaging through the mask is to view the slits from above using a secondary camera. Slit-viewing cameras are widely used in long-slit spectrographs, but they normally rely on the slit being angled to maximise the light reflected into the camera. This is not possible with an aperture mask, as the mask must lie flat in the focal plane. A second mask is therefore needed to reflect the light. An implementation of this method is described in chapter 5.

## **2.5 Past and Present Multi-slit Spectrographs**

Chapter 1 introduced the four multi-slit instruments with which Durham has been associated. The FOS-1 and FOS-2 multi-slit units are described in more detail in section 3.3.5 and in chapter 5 respectively; LDSS-1 is described in chapter 4 and LDDS-2 in chapters 6, 7 and 8.

Elsewhere, prominent multi-slit spectrographs include EFOSC for the ESO 3.6m telescope, EMMI for the NTT, MOS/SIS for the CFHT and LRIS for the Keck. Their chronology is given in table 2.1.

EFOSC stands for "ESO Faint Object Spectrograph and Camera". It is a multi-purpose instrument with facilities for direct imaging, grism and echelle slit spectroscopy, multi-slit spectroscopy and slitless spectroscopy. This versatility reduces the need for instrument changeovers and allows more flexible observing programmes.

Instrument	Telescope	Date
EFOSC	ESO 3.6m	Jun'84
FOS-1 (w/MMU)	INT	Feb'86
LDSS-1	AAT	Jun'86
FOS-2 (w/MSU)	WHT	Feb'90
EMMI	NTT	Oct'90
LDSS-2	WHT	Feb'92
MOS/SIS	CFHT	Jun'92
LRIS	Keck	1993

Table 2.1: Chronology of multi-slit spectrographs

The useable wavelength range of EFOSC is 3600Å to 10000Å. Its optical throughput peaks at 65% at 4500Å (low dispersion blue grism). The aperture, filter and grism wheels each have twelve positions, though only four of the aperture wheel positions are available for multi-slit masks. The masks are prepared using a punching machine called PUMA. They have a useable area of 3.7 by 5.7 arc-minutes and can typically accommodate about 10 slits each. Further details can be found in Buzzoni *et al* (1984) and D'Odorico and Dekker (1986).

EMMI stands for "ESO Multi-Mode Instrument". It has two channels (red and blue) and has facilities for direct imaging and for grating, grism and echelle spectroscopy. Multi-slit spectroscopy is performed using the gratings, which are located in the red arm of the instrument. In this mode the useable wavelength range is 4000Å to 10000Å. The field of view is 5 by 7 arc-minutes, typically sufficient for about 20 slits per aperture mask. The aperture wheel can hold four multi-slit masks at any given time.

Like EFOSC, the aperture masks for EMMI are prepared using a mechanical punching machine. However, to enhance observing efficiency the punch mechanism is located inside the spectrograph. The aperture wheel is loaded with up to four blank masks at the start of the night. Slit coordinates are transmitted to the instrument, which then punches the slits under remote control. The punch mechanism has a positional accuracy of  $\pm 8\mu\text{m}$  and can fabricate a 40-slit mask in about 5 minutes. Further details can be found in

D'Odorico (1990), Dekker and D'Odorico (1990) and Dekker *et al* (1991).

A multi-slit instrument is also under construction for the ESO Very Large Telescope (VLT). It is known as FORS, which stands for "FOcal Reducer/low dispersion Spectrograph". Like EFOSC and EMMI it offers a wide range of observing modes. Important differences include the absence of echelle and grating modes and the use of a movable slit mask instead of a mechanical punching system (see section 3.3.5). Further details can be found in Appenzeller and Ruprecht (1992a) and Appenzeller *et al* (1992b).

MOS/SIS stands for "Multi-Object Spectrograph/Sub-arcsecond Imaging Spectrograph". It was jointly designed and built by the Dominion Astrophysical Observatory, the Observatoire de Paris-Meudon and the Observatoire de Marseille. Though constructed as a single unit, the multi-object (MOS) and high resolution (SIS) sections of the instrument are almost entirely independent of each other. The instrument as a whole is mounted at the  $f/8$  focus of the CFHT.

When used in multi-object mode, MOS/SIS has a 10 arc-minute diameter field of view. Its useable wavelength range is  $3650\text{\AA}$  to  $10000\text{\AA}$ , with a throughput of approximately 76% at  $5500\text{\AA}$ . The instrument can accommodate up to 6 grisms and 7 filters at any given time but can only hold 3 aperture masks. The masks have dimensions of 70 by 78mm with a scale of  $139\mu\text{m}$  per arc-second. They are cut using a Nd-YAG laser system known as LAMA (see section 3.3.4). Further details can be found in Crampton *et al* (1992), Le Fèvre *et al* (1993) and Di Biagio *et al* (1990).

LRIS stands for "Low Resolution Imaging Spectrograph" and is a multi-slit spectrograph for the Keck 8m telescope. It is unusual in that its field of view is located away from the optical axis of the telescope. This allows the optical system to cancel out much of the distortion that would otherwise be present. There is provision for two cameras (red and blue), though only the red camera has been implemented at present.

The field of view is irregular in shape, but is equivalent to a rectangle of approximately 6 by 8 arc-minutes. Each mask can typically accommodate 30 to 40 slits. The focal plane of the Keck is significantly curved across the field of view and this must be accommodated if the whole of the mask is to be brought into focus. A first-order correction can be achieved by placing an angle in the mask surface so that the flat sections on either side more closely approximate to the focal plane.

A development of LRIS is the DEEP project for the Keck. The design has four separate off-axis multi-slit fields, located symmetrically about the optical axis. The four fields share a single (1.4m diameter) reflecting collimator but are otherwise independent. The instrument as a whole would be able to observe up to 150 targets simultaneously. The above information about LRIS and DEEP was obtained from an oral presentation by Miller at the ESO Conference on Progress in Telescope and Instrumentation Technologies in 1992.

For comparison, LDSS-2 has a relatively wide field of view (11.5 arc-minutes diameter) so has the potential to achieve large multiplex gains. It has facilities for direct imaging, and for long-slit and multi-slit grism spectroscopy. Up to 7 aperture masks, 7 filters and 3 grisms can be mounted at any given time. The nominal wavelength range is 3700Å to 7500Å. Other optical parameters, including the throughput, are discussed in Chapter 8.

Aperture masks are currently fabricated using a mechanical milling machine, though the instrument has also been used with photochemically etched masks. It is hoped that a laser cutting system will be introduced in the future. The slits can be cut to any required size or shape, with a positional accuracy of 25µm (0.1 arc-seconds). The lead-time for a complete mask is typically about 10 minutes.

# Chapter 3: Mask Fabrication Methods

## 3.1 Introduction

The previous chapter considered many of the design issues involved in building a multi-slit spectrograph, but one issue still to be addressed is that of mask fabrication.

Six different types of aperture mask are considered in this chapter:

- Photochemically etched masks
- Mechanically punched masks
- Mechanically milled masks
- Laser cut masks
- Movable slit masks
- Liquid crystal masks

Each has its own advantages and disadvantages, so the best choice will depend on the prevailing circumstances and priorities. However, it is helpful to characterise each type of mask using the following parameters:

- Cost (both capital and recurrent)
- Lead time to produce a mask
- Quality of slit edge
- Accuracy of slit positions
- Thermal expansivity of mask material
- Mask thickness
- Elasticity of mask material
- Optical properties of mask material
- Constraints on slit size and shape, or mask layout

This chapter begins by defining these properties and considering how they affect the performance of the instrument as a whole. It then looks at each mask type in detail, evaluating its characteristics and assessing both its present and future potential.

## 3.2 Mask Characteristics

### 3.2.1 Cost

Most types of masks are not reusable and have both capital costs (the machinery used during the fabrication process) and recurrent costs (the mask material, maintenance, and in many cases skilled labour). Where the capital cost is excessive it may be possible to contract the work to a private company, though this will increase both the running costs and the lead time.

Reusable masks generally have a higher capital cost than comparable non-reusable masks but minimal running costs. Whether this amounts to a saving will depend on both the rate of mask use and the expected life of the spectrograph.

### 3.2.2 Lead Time

The fabrication lead time can vary greatly between methods, from milliseconds to months. It is important because the lead time determines the flexibility with which the astronomer can operate. Four distinct modes of operation can be identified:

- lead time greater than 48 hours: targets must be selected (and astrometry performed) prior to arrival at the telescope
- lead time between 6 hours and 24 hours: targets may be selected using the telescope, for use on subsequent nights
- lead time between 30 minutes and 2 hours: targets may be selected using the telescope, for use during the same night
- lead time less than 5 minutes: targets may be selected while the telescope is on target and autoguiding

### 3.2.3 Slit Quality

When observing faint objects it is necessary to measure not just the spectrum of the object but that of the surrounding night sky as well. This allows the

level of the sky directly behind the object to be estimated by interpolation and subtracted from the object spectrum.

Sky subtraction is never perfect as it is subject to both noise and systematic errors. One of the main sources of error is variation in the width of the slit along its length. The effect on the final result will depend on the characteristics of this variation:

- Random irregularities at a scale that is small compared with one pixel will be filtered out by the CCD so should have little effect on the result.
- Random irregularities at a scale comparable to one pixel will appear as an error in the level of the sky spectrum. The interpolation function will reduce this by acting as a filter in the spatial direction, but for very short slits even one pixel row can have a substantial effect on the result.
- Irregularities at a scale comparable to the slit length will be compensated for by the interpolation function but at the expense of its ability to filter out noise. As in the case above, the results are less satisfactory for very short slits.
- Point defects can have a very serious effect on the result as they are often much larger than other irregularities. Causes include inhomogeneity of the mask material, faults during manufacture, dust or other contamination, and physical damage to the slit edge. If these faults are noticed at the data reduction stage then they can sometimes be remedied by discarding the pixel rows corresponding to that part of the slit.

It is possible to measure the variation of the width of a slit using a microscope with an x-y micrometer stage. The edge is aligned with the x-axis and the width is measured at a number of regularly spaced x-coordinates. Any small scale variations are smoothed either visually or mathematically, so that the method of sampling is more closely comparable

to that of a CCD.

The result will depend on the x-coordinate increment between measurements, so this should be chosen to be similar to the detector pixel scale. The scale will vary between instruments but is typically between 10 and 50 $\mu\text{m}$ . The measurements in this chapter cover this range by looking at two scales: 10 $\mu\text{m}$  and 100 $\mu\text{m}$ .

It is also possible to measure the variation in slit width using spectroscopic data. A dispersed exposure of the slit, using a source with a smooth spatial intensity distribution, is flat-fielded to remove any systematic variation in the CCD sensitivity. A group of pixel columns are selected and summed to give the intensity profile in the spatial direction. This is filtered to remove any large-scale intensity variation and the RMS variance is calculated. The noise level expected from other sources is subtracted using the formula  $\sigma_{1-2}^2 = \sigma_1^2 + \sigma_2^2$ . The result should be equal to the RMS variance of the slit width, measured at the pixel scale.

The level of variation that is acceptable will depend on the width of the slit and the apparent brightness of the target compared to the surrounding sky. A one hour exposure will result in a sky background of approximately 1200 photons given a 200 $\mu\text{m}$  slit, a 470 $\text{\AA}$   $\text{mm}^{-1}$  grism, a TEK512M CCD and a system efficiency of 0.25. The poisson noise is approximately 34 photons and the readout noise approximately 10 photons, so the fractional noise ( $\sigma/N$ ) is 0.031. This corresponds to 6.1 $\mu\text{m}$  small-scale roughness for a 200 $\mu\text{m}$  slit.

#### 3.2.4 Accuracy of Slit Positions

The purpose of the aperture mask is to transmit light from the target object while blocking light from the surrounding sky. This is only possible if the slit and the target object are accurately aligned with each other. An error will result in more of the target light being blocked and thus reduce the

throughput of the instrument.

There are three factors that determine the level of accuracy that can be achieved:

- the accuracy with which the slits are machined relative to each other
- the thermal expansion of the mask material between it being manufactured and it being used
- the accuracy of the field acquisition procedure

The errors accumulate according to the rule  $\sigma_{1+2}^2 = \sigma_1^2 + \sigma_2^2$ . Some errors are easier to reduce than others, so the optimum distribution is determined by a cost-benefit analysis. The resulting list of tolerances is sometimes known as an 'error budget'.

A limit for the total error was chosen by considering the fraction of incident light that is lost as the slit is displaced. This was done by convolving the image intensity profile with the slit transmission function then integrating the result. For a long exposure, the optical transfer function of the atmosphere,  $OTF_{LE}$ , is:

$$OTF_{LE}(\rho) = \exp(-3.44 (\lambda \cdot \rho / r_0)^{5/3})$$

where  $\lambda$  is the wavelength,  $\rho$  is the angular spatial period (in radians) and  $r_0$  is the coherence length (Fried, 1978). A coherence length of 10cm was used in the calculations below and corresponds to a full width half maximum of approximately 1 arc-second.

The point spread function,  $PSF_{LE}$ , was found by applying an inverse fourier transform to the OTF. The radial symmetry of the OTF allows this to be done using a Hankel transform (Bracewell, 1965, pp241–250):

$$PSF_{LE}(r) = 2\pi \int_0^{\infty} OTF_{LE}(\rho) \cdot J_0(2\pi \cdot \rho \cdot r) \, d\rho$$

The equation given in the reference also allows for the effect of diffraction,

but for a large telescope this is negligible compared to the effect of the atmosphere. The diffraction limit for a circular aperture is  $1.22\lambda/D$ , which for the WHT is approximately 0.03 arc-seconds at  $5000\text{\AA}$ . It is therefore acceptable to omit the diffraction term from the equation.

The equation for the PSF does not have a closed-form analytic solution so it was necessary to evaluate it numerically. This was done using *Mathcad for Windows* version 3.1, running on a Dell 466/M. *Mathcad* integrates using the Romberg method to achieve rapid convergence (Mathsoft, 1991, pp373–375 and Burden and Faires, 1989, pp191–196). The integration limit and the tolerance were set to give a result accurate to six significant figures.

The convolution of the PSF with the slit transmission function and the integration of the result were carried out in a single step. Unfortunately, the Romberg algorithm used by *Mathcad* failed to converge for some of the slit transmission functions investigated later in this chapter, so a short program was written using *Borland C++* version 2.0 to implement rectangle-rule integration instead. The rectangle-rule method is less efficient, but it is more predictable when the transmission function is not smooth. The integration limits and the step size were set to give a result accurate to four significant figures.

For most types of observation the slit width will be between 1 and 2 times the FWHM of the seeing disc. Preliminary tests showed that the slit position is most critical when the slit is narrow so a slit width of 1 arc-second was assumed.

Table 3.1 shows how the throughput varies as the slit position is changed.  $\Delta x$  is the slit displacement,  $w$  is the slit width,  $I$  is the flux that passes through the slit,  $I_0$  is the incident flux, and  $I_1$  is the value of  $I$  when  $\Delta x=0$ . If the maximum allowable drop in throughput is defined to be 5% then  $\Delta x$  must not exceed  $0.18w$ . (5% is an arbitrary figure but is reasonable in this context.) For a  $200\mu\text{m}$  LDSS-2 slit this corresponds to a total error of  $36\mu\text{m}$ .

If the error budget is divided equally then each source of error can contribute up to  $21\mu\text{m}$ .

$\Delta x/w$	$I/I_0$	$1-(I/I_1)$
0.00	0.6786	0.000
0.05	0.6760	0.004
0.10	0.6682	0.015
0.15	0.6554	0.034
0.20	0.6378	0.060
0.25	0.6158	0.093
0.30	0.5899	0.131
0.35	0.5605	0.174

Table 3.1: Variation of throughput with slit position

### 3.2.5 Thermal Expansion

Aperture masks are exposed to a wide range of temperatures during the course of a night and will therefore expand and contract. There is also likely to be a temperature difference between the time and location where a mask is manufactured and the time and location it is used.

The positional error between slits in the same mask,  $\Delta x$ , depends on the thermal expansivity of the mask material,  $\alpha$ , the usable diameter of the mask,  $D$ , and the temperature difference,  $\Delta\theta$ :

$$\Delta x = \alpha \cdot D \cdot \Delta\theta$$

In the case of LDSS-2 the usable mask diameter is 153mm. If a position error of  $21\mu\text{m}$  due to thermal expansion is allowed between a slit and the image then up to  $42\mu\text{m}$  can be allowed between two slits. Assuming a temperature difference of 20K, this sets an upper limit for the thermal expansivity of  $1.4 \times 10^{-5} \text{K}^{-1}$ .

Plastics generally have higher thermal expansivities than metals. Some typical values are given in table 3.2. (The values are taken from Kaye and Laby (1986, pp54–56 and pp287–289), except that marked \* which is taken

from Weast (1977, pC791), and that marked † which is taken from American Society for Metals (1979, p340). The brass listed has a composition of 60Cu-38Zn-2Pb, which is almost identical to the engraving brass used to make CAMM-3 masks.)

Material	$\alpha$
Cellulose Acetate*	10.5-10.8
Nylon 6	28
Polyethylene (HD)	10-20
Polymethylmethacrylate	5-9
Polystyrene	3.4-21
Aluminium	2.31
Brass (C37700)†	2.07
Stainless steel (13-17Cr)	0.95
Tungsten	0.45
Invar	0.013
	/10 <sup>-5</sup> K <sup>-1</sup>

Table 3.2: Thermal expansivities of selected materials

A requirement that  $\alpha$  be less than  $1.4 \times 10^{-5} \text{K}^{-1}$  clearly excludes most plastics and also some metals, so it is useful to consider ways in which the expansion can be reduced.

One option is to pre-compensate for the temperature change by specifying an offset when the masks are made. This is not a perfect solution and its accuracy will depend on the time interval between the masks being made and being used. So long as this is limited to a few hours it should be possible to reduce the effective temperature difference to about  $\pm 2.5 \text{K}$ . In the case of LDSS-2 this would allow a thermal expansivity of up to  $11.5 \times 10^{-5} \text{K}^{-1}$  (sufficient to include most metals and some plastics). For longer periods the dome temperature will be less predictable and  $\pm 5 \text{K}$  ( $5.8 \times 10^{-5} \text{K}^{-1}$ ) would be more realistic.

### 3.2.6 Mask Thickness

The calculations in section 3.2.4 assume that the fraction of light transmitted

through a slit at a given point in the image plane is either zero or one. Whether this is true depends on the mask thickness,  $h$ , the angle between the  $z$ -axis and the sides of the slit,  $\theta$ , and the focal ratio of the telescope,  $F$ .

If the mask is thick and the slits have a rectangular profile (as in figure 3.1) then the slit edges will be blurred. This is because there are two effective edges to the slit, one in the upper face of the mask and one in the lower face, and they cannot both be in focus. The best compromise is to focus half way through the mask.

Light that converges to a point in the focal plane will appear as a disc on the surface of the mask. The appearance of the disc will depend on the telescope optics, but for current purposes it is reasonable to assume that it is uniformly illuminated. If the telescope focal ratio is  $F$  and the distance between the mask surface and the focal plane is  $h/2$  then the radius of the disc will be  $h/4F$ .

If the circle lies entirely within a slit then the mask transmission at the centre of the circle will be equal to 1. If the circle lies across the slit edge then the incident light is partially vignetted and the mask transmission will be equal to the fraction of the circle that is within the slit. If the circle lies entirely outside the slit then the mask transmission will be equal to zero.

To predict how the performance of the instrument would be affected, the integration program described in section 3.2.4 was modified to use this transmission function. The results are given in the following table 3.3, where  $S$  represents the sky background level.

The throughput falls rapidly, but so does the background. For example, a mask thickness of  $h/4F \cdot w = 0.2$  reduces the sky background level by 13% compared to a mask thickness of zero. Conversely, to achieve a given sky background level, the slits in a thick mask may be wider than the slits in a thin mask.

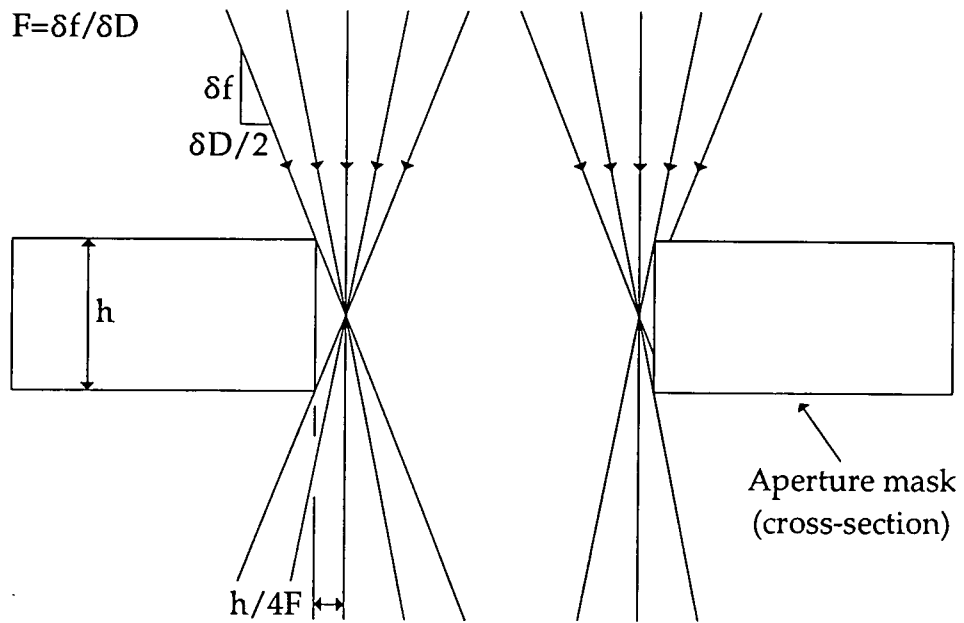


Figure 3.1: A slit with a rectangular cross-section

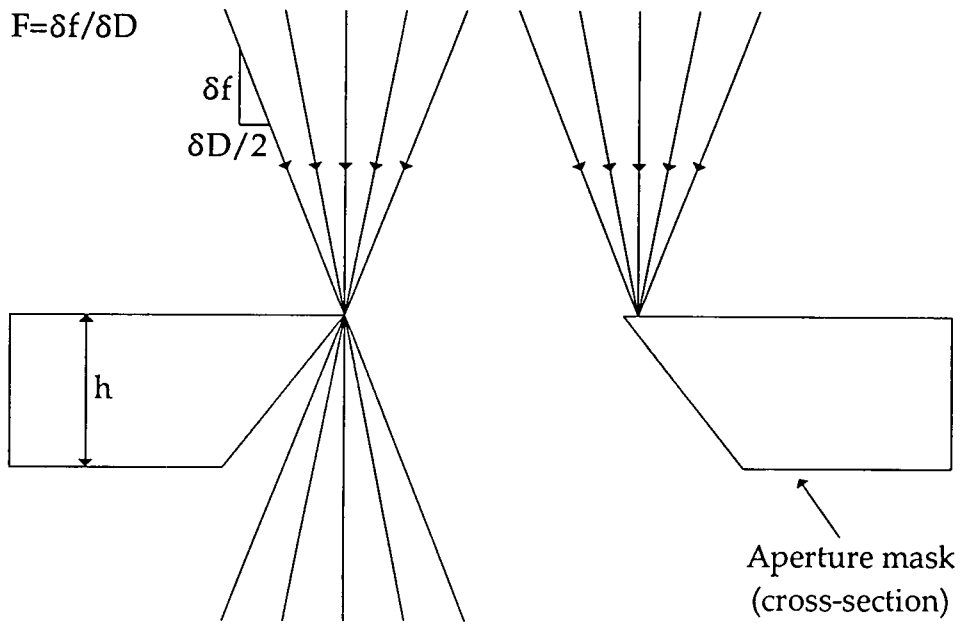


Figure 3.2: A slit with an angled cross-section

$h/4F \cdot w$	$S/S_0$	$1-(S/S_1)$	$I/I_0$	$1-(I/I_1)$
0.00	1.000	0.000	0.6786	0.000
0.05	0.9576	0.042	0.6592	0.029
0.10	0.9151	0.085	0.6385	0.059
0.15	0.8727	0.127	0.6164	0.092
0.20	0.8302	0.170	0.5930	0.126

Table 3.3: Variation of throughput with mask thickness (constant slit width)

There are two ways in which the width can be varied to compensate for this effect: constant sky background level and constant RMS line width. The result of fixing each of these parameters is given in table 3.4, where  $w_b$  is the slit width for constant background and  $w_w$  is the width for constant line width. Constant line width is clearly the more stringent criterion and results in a 5% drop in throughput when  $h/4F=0.41w$ .

$h/4F \cdot w$	Constant sky level		Constant line width	
	$w_b/w$	$1-(I/I_1)$	$w_w/w$	$1-(I/I_1)$
0.00	1.000	0.000	1.000	0.000
0.10	1.085	0.001	1.082	0.003
0.20	1.170	0.004	1.159	0.012
0.30	1.255	0.010	1.230	0.026
0.40	1.340	0.017	1.296	0.047
0.50	1.424	0.027	1.356	0.073
0.60	1.509	0.038	1.412	0.106
0.70	1.594	0.051	1.473	0.144

Table 3.4: Variation of throughput with mask thickness (variable slit width)

The minimum slit width required by the LDSS-2 specification is  $200\mu\text{m}$  and the WHT focal ratio is F/11. This would imply a maximum mask thickness of 3.6mm. In practice, however, it would be very difficult to fabricate a slit with such a large aspect ratio (18:1) even if there were a reason to do so. If such a thick mask were used then it is more likely that the slits would have the cross-section shown in figure 3.2. In that case the mask thickness is immaterial because there is a sharp edge that can be focussed to. The angle required is  $\theta > \tan^{-1}(1/2F)$ , which for an F/11 focal ratio is  $2.6^\circ$ .

### 3.2.7 Elasticity

Aperture masks are not perfectly rigid, so if a mask is supported at its perimeter then it will sag in the middle. The distance that it sags,  $z_0$ , will depend on the radius,  $r_0$ , thickness,  $h$ , density,  $\rho$ , Young's modulus,  $E$ , and Poisson's ratio,  $\sigma$ , of the mask. If  $z_0$  is too large then the image will be blurred.

It is possible to calculate  $z_0$  and a derivation is given in Flügge (1962, pp39.1–39.4 and pp39.24–39.26). A number of assumptions are made to simplify the calculation, including the following:

1. that  $h$  is small compared to  $r_0$
2. that  $z_0$  is small compared to  $r_0$
3. that elastic stresses caused by extension of the mask material are small compared to stresses caused by its flexure
4. that the slits in the mask have no significant effect on its elasticity or its mass distribution

An aperture mask is a clamped plate (in other words, the gradient at its perimeter is constrained to be zero) and is uniformly loaded (by its own weight). The sag at its centre is given by:

$$z_0 = 3 \cdot \rho \cdot g \cdot r_0^4 (1 - \sigma^2) / 16 \cdot E \cdot h^2$$

Metals generally have much higher Young's moduli than plastics, though this is partly offset by their higher densities. Some typical values are given in table 3.5. (The values are taken from Kaye and Laby (1986, pp31–33 and pp287–289), except that marked \* which is taken from Weast (1977, pC791), and that marked † which is taken from American Society for Metals (1979, p340). The brass listed has a composition of 60Cu-38Zn-2Pb, which is almost identical to the engraving brass used to make CAMM-3 masks. No specific values could be found for the Poisson's ratios of any of the plastics, but 0.4–0.45 is typical for plastics in general.)

The optical effect of varying  $z_0$  was simulated using the integration program described in section 3.2.4. The optimum focus is half way between the two extremes of  $z$ , so the maximum distance between the mask and the focal plane is  $z_0/2$ . As when simulating the mask thickness, a point in the focal plane was assumed to become a disc of uniform intensity away from that plane. The results are given in table 3.6.

Material	$\rho$	E	$\sigma$
Cellulose Acetate*	1280-1320	1.3-2.6	N/K
Nylon 6	1120-1170	0.8-3.1	N/K
Polyethylene (HD)	940-965	0.4-1.3	N/K
Polymethylmethacrylate	1170-1200	2.4-3.4	N/K
Polystyrene	1040-1090	2.7-4.2	N/K
Aluminium	2698	70.3	0.345
Brass (C37700)†	8440	105	0.346
Stainless steel (2Ni 18Cr)	7800	215.3	0.283
Tungsten	19254	411.0	0.280
Invar	8000	144.0	0.259
	/ $\text{g m}^{-3}$	/ GPa	

Table 3.5: Elasticities and Poisson's ratios of selected materials

$z_0/4F \cdot w$	$I/I_0$	$1-I/I_1$
0.00	0.6786	0.000
0.10	0.6760	0.004
0.20	0.6683	0.015
0.30	0.6557	0.034
0.40	0.6389	0.059
0.50	0.6184	0.089
0.60	0.5951	0.123
0.70	0.5699	0.160

Table 3.6: Variation of throughput with mask sag

The drop in throughput reaches 5% when  $z_0/4F \cdot w=0.37$ . For a  $200\mu\text{m}$  LDSS-2 slit at an F/11 focus this corresponds to  $z_0=3.2\text{mm}$ . De-focussing can also occur if the mask is tilted, but this is easier to correct so it is not appropriate to divide the error budget equally. A reasonable allowance would be 1.6mm for tilt and 2.8mm for sag.

LDSS-2 masks have a usable diameter of 153mm, so using the formula for  $z_0$  given above the predicted sag would be as shown in table 3.7. Elasticity is not therefore a serious concern for masks of this diameter.  $z_0$  increases rapidly with  $r$ , but it can be partly offset by increasing  $h$ . For a 306mm mask the sag can be limited to 1mm by using 0.2mm stainless steel or 0.6mm polymethylmethacrylate.

Material	$h$	$z_0$
Stainless steel	0.05	0.84
Brass	0.5	0.02
Polymethylmethacrylate	0.1	2.0
Polymethylmethacrylate	0.2	0.53
Polymethylmethacrylate	0.5	0.08
	/mm	/mm

Table 3.7: Predicted mask sag for selected mask materials

### 3.2.8 Optical Properties

An aperture mask must be opaque not just to the wavelengths that the spectrograph is designed for but to all wavelengths to which it is sensitive. Unless a band-pass filter is used this will typically include a small part of the near ultra-violet and a large part of the near infra-red. Care is therefore needed when evaluating plastics for use as masks as their infra-red opacity can differ greatly from their optical opacity.

It is desirable for the mask to be non-reflective. If it is not then light reflected off the upper face of the mask may find another route to the detector, causing an increase in the background light level. It is also possible for reflections from the instrument optics to be directed back into the instrument by the underside of the mask, causing ghost images.

The best colour for a mask is matt black. Plastics are coloured by adding a dye when they are manufactured. This has the advantage that the resulting mask is homogeneous and therefore remains black even if it is cut.

Metals can only be coloured on the surface, either by applying a coating or (for some metals) by chemically treating the surface to produce an oxide layer. Both methods would be time-consuming to perform after the mask had been cut and there is a risk that they would interfere with the quality of the slit edge. A more practical solution would be to coat the masks before cutting and to accept some reflection at the exposed surfaces (this has not yet been tested).

### **3.2.9 Constraints on Mask Layout**

Some mask fabrication methods place restrictions on the size, shape and layout of the slits. This complicates the process of target selection and prevents some techniques from being used. For example, some fabrication methods do not support the manufacture of curved slits, which are useful for observing gravitationally-lensed arcs.

## **3.3 Types of Mask**

### **3.3.1 Photochemically Etched Masks**

Photochemical etching has been used to produce masks for LDSS-1, and to a limited extent for LDSS-2. Manufacture consists of five stages:

1. The mask is coated with a photosensitive chemical that can resist the effects of the etchant.
2. The areas of the mask that are to remain after etching are exposed to light. Many processes use ultra-violet light, in order to avoid the need for a dark-room.
3. The exposed photoresist is developed, hardening it. The unexposed photoresist is washed away.
4. The mask is exposed to the etchant. Areas of the mask that are not covered in photoresist are dissolved.
5. The photoresist is removed and the mask is cleaned.

The method works best with thin masks, because only the surface is protected from the etchant. If the mask is thick then 'undercutting' will occur at the slit edges. The level of undercutting depends on a number of factors, including the way the etchant flows around the tank, but in general it is proportional to the thickness of the mask.

The LDSS-1 masks were made from 0.05mm thick stainless steel, which is mechanically strong and offers good resistance to corrosion. Plastics are generally unsuitable for this process, as they are more difficult to etch and would have poor mechanical characteristics if fabricated as sheets of this thickness.

The main advantage of etching is that the mask material is not thermally or mechanically stressed as it is cut. This reduces distortion and ensures that the slit edge does lie in the plane of the mask. Against this must be set a number of disadvantages, the most important of which are the cost and the lead time. Although etching is straightforward in principle, it does require skills and equipment that could not be provided at the observatory at a reasonable cost. It is therefore necessary to sub-contract the work to a private company. LDSS-1 masks typically cost about £50 each (1992) and have a lead time of about two weeks.

The slit edge quality was measured using data from the LDSS-2 commissioning run. Photo-fabricated masks had been prepared for most of the fields in case the CAMM-3 machine failed and they were used for some of the early exposures. The frame used for this test was a 1s dispersed exposure of the CuAr arc lamp.

The procedure for analysing the data was as described in section 3.2.3. Eight slits were selected, two of which are illustrated in figures 3.3 and 3.4 ( $y$  is the spatial coordinate. The non-zero signal level outside the slit is caused by neighbouring slits with adjacent but non-overlapping  $y$ -coordinates). No noise correction was needed, as other sources of noise are negligible. The

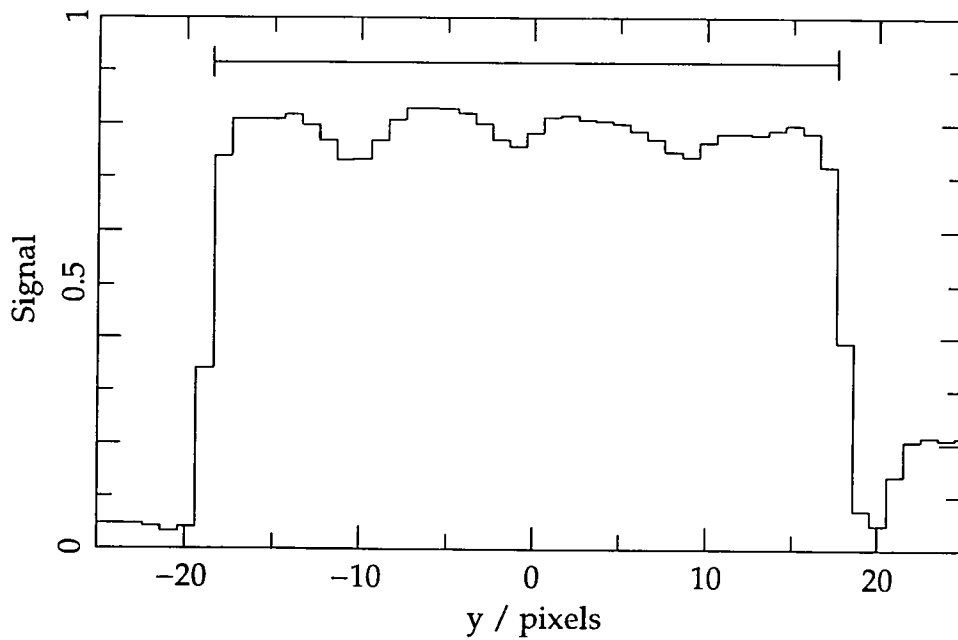


Figure 3.3: The width variation of a photochemically etched slit (1)

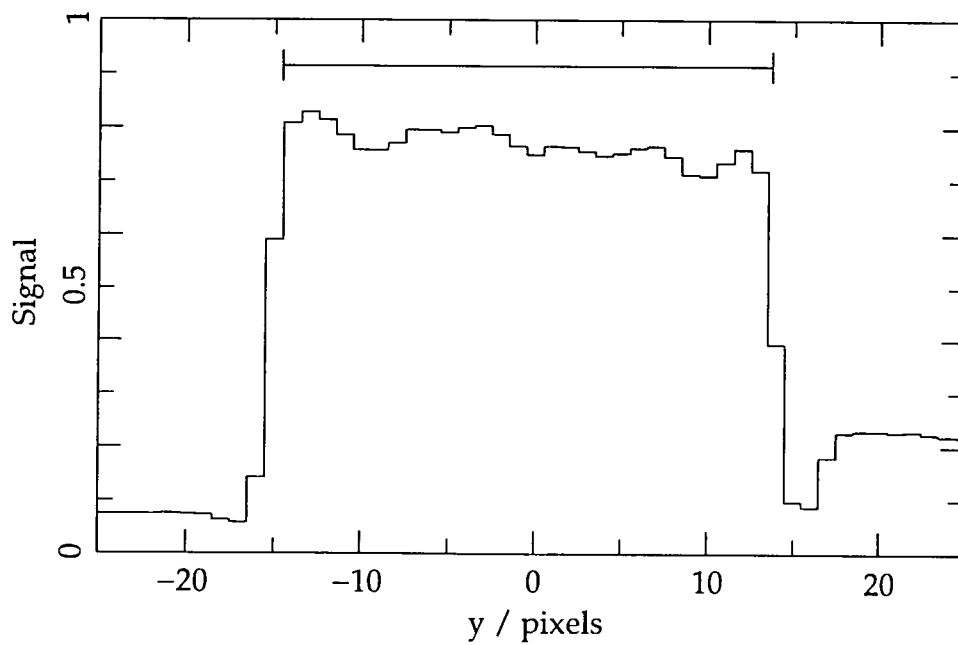


Figure 3.4: The width variation of a photochemically etched slit (2)

average variance was found to be 2.2%, which is an acceptable result but not as good as a CAMM-3 mask.

### 3.3.2 Mechanically Punched Masks

Mechanical punching was briefly investigated for the production of LDSS-2 masks. A prototype punching head was constructed, but it was operated manually and had no facilities to hold or move the mask. The method was later abandoned in favour of mechanical milling.

If mechanical punching were developed then the mask would be mounted on an x-y table and moved underneath a punching head. There would be a die directly underneath the head so that the punch cut through the mask rather than just bending it. A suitable material would be a thin sheet metal such as stainless steel.

The dimensions of the punching head are fixed. Different slit widths can be obtained by using different heads, but it is not practical to change the head part way through punching a mask. To vary the length it is therefore necessary to punch the slit using two or more strokes. Doing so will inevitably result in discontinuities in the slit edge and the width will be greater where the holes overlap. The data reduction software cannot properly compensate for this, so the punch must be extremely accurate. An appropriate tolerance would be the same as that given for pixel-scale roughness in section 3.2.3.

Because of the large amount of material removed in one operation, punching causes more stress in the mask than other methods. The punching head wears quickly and unlike a milling tool it cannot be refurbished.

To measure the slit quality, the prototype punching machine was used to create a 170 $\mu\text{m}$  slit in a thin sheet of stainless steel which was then examined using a microscope. The RMS variation was found to be 10.2 $\mu\text{m}$  at a scale of 10 $\mu\text{m}$  and 5.9 $\mu\text{m}$  at a scale of 100 $\mu\text{m}$ . A slit of this type would be usable, but

it would be poor compared to other types of mask.

### 3.3.3 Mechanically Milled Masks

Mechanical milling has been used to produce masks for both FOS-2 and LDSS-2. It has several advantages over the other current methods:

- CNC milling machines are readily available as self-contained units, so relatively little development work is needed to implement a working system.
- The equipment can be located in the telescope building and operated by observatory staff, so the lead time is relatively short.
- The slit length and width are variable, and if necessary it is possible to cut curved slits.

The machine that was purchased for use on La Palma is called 'CAMM-3' and is shown in figure 3.5. It cost approximately £8000 and is small enough to stand on a bench. It operates from a single phase 240V supply. There are three control axes: the mask moves in the x and y directions and the milling head in the z-direction. The X-Y stage has a nominal resolution of 10 $\mu$ m and an accuracy of about 25 $\mu$ m. The spindle speed is variable up to 10,000 RPM. An LDSS-2 mask can typically be cut in about 10 minutes.

The cutter is triangular, so when it is spinning it traces out a cone. This allows the slit width to be changed by varying the height of the cutter. As a side effect, the slits ends are semicircular and the slit edges have the same angle as the cutter. The latter characteristic is useful as it allows thick masks to be used without defocussing the image. An enlargement of a typical slit is shown in figure 3.6.

The mask material is 0.5mm thick engraving brass (designation CZ120), which has a composition of 59Cu-39Zn-2Pb. A high lead content makes the alloy easy to machine and prevents burrs from forming (Trade & Technical Press, p112). The mask blanks were originally punched from rectangular

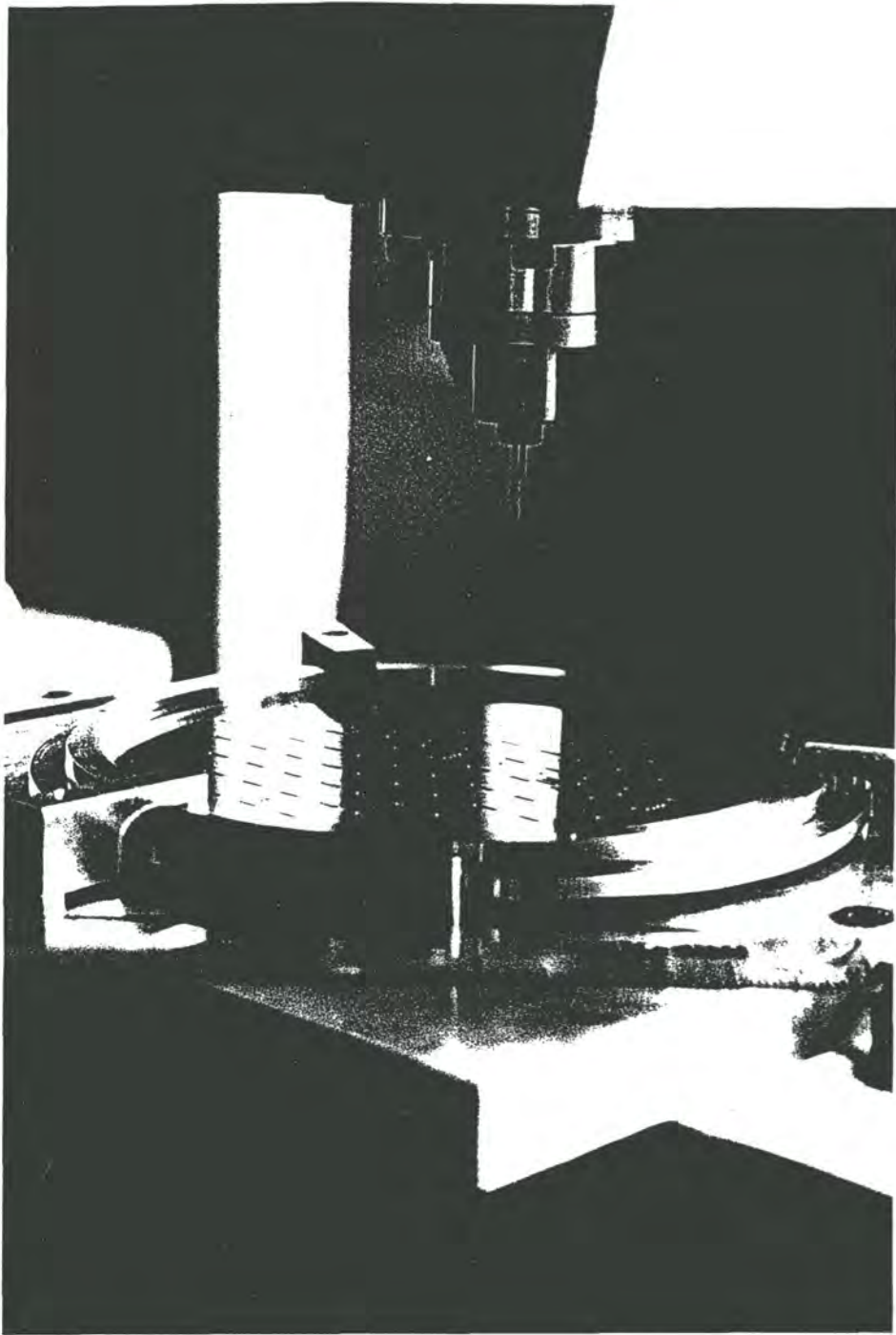


Figure 3.5: The CAMM-3 milling machine



Slit width = 0.35mm (1.6 arc-seconds on the WHT)

Figure 3.6: An enlargement of a typical CAMM-3 slit

sheets, but are now purchased as pre-cut discs at a cost of about £3 each (1993).

One problem with CAMM-3 is cutter wear. A cutting tool will typically last for between 200 and 300 slits, after which it is replaced. The tools cost about £10 each (1993). The machine itself is not especially robust, and while it is easy to use, a considerable amount of experience is needed to produce high quality masks.

The RGO have now purchased a better CNC machine, manufactured by Bridgeport and called 'Interact-4'. It cost about £50,000 and has a nominal accuracy of 5 $\mu$ m. It is expected to be very much more robust than CAMM-3.

The slit edge quality of a CAMM-3 mask was measured using data from the LDSS-2 run in August 1992. The data reduction procedure was as described in section 3.2.3 and was the same as that used to test the photo-fabricated masks. The frame was a 1s exposure of the CuAr arc lamp. Six slits were selected, two of which are illustrated in figures 3.7 and 3.8. (As before, the non-zero signal level outside the slit is caused by neighbouring slits.) The average variance was found to be 0.29%. Other noise sources are significant in this case, but the flat-field noise is not known so this result should be treated as an upper limit. Even so, it is almost an order of magnitude better than a photo-fabricated mask and further improvement would be of marginal benefit.

### 3.3.4 Laser Cut Masks

Laser cut masks are being investigated at Durham as a possible alternative to CAMM-3 masks for LDSS-2. They would have two major advantages:

- A laser cutter has the potential to operate at higher speeds than a milling machine, though this does depend on the laser power and the mask material.
- Many of the problems with CAMM-3 can be attributed to cutter wear.

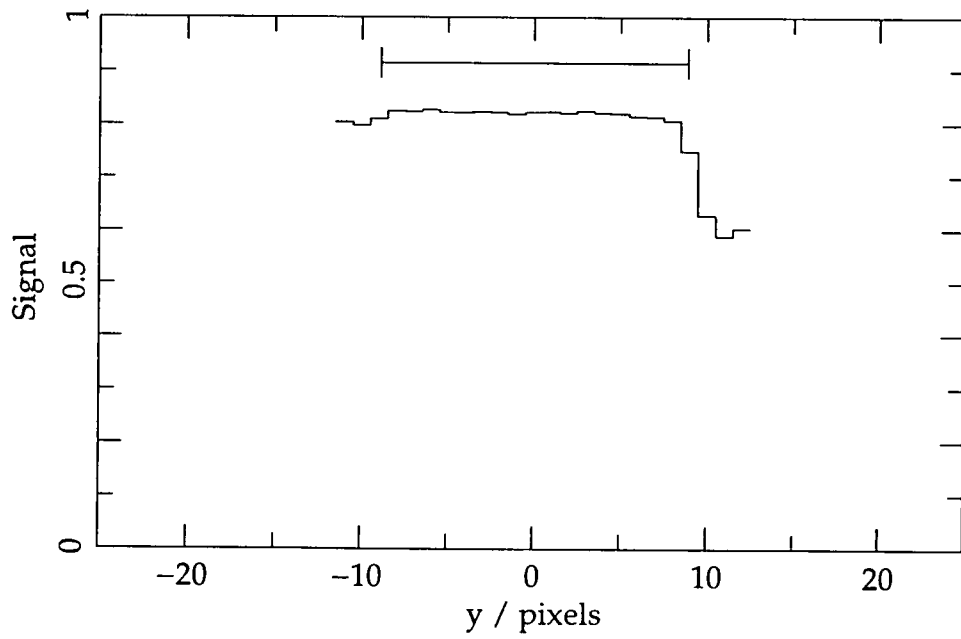


Figure 3.7: The width variation of a CAMM-3 slit (1)

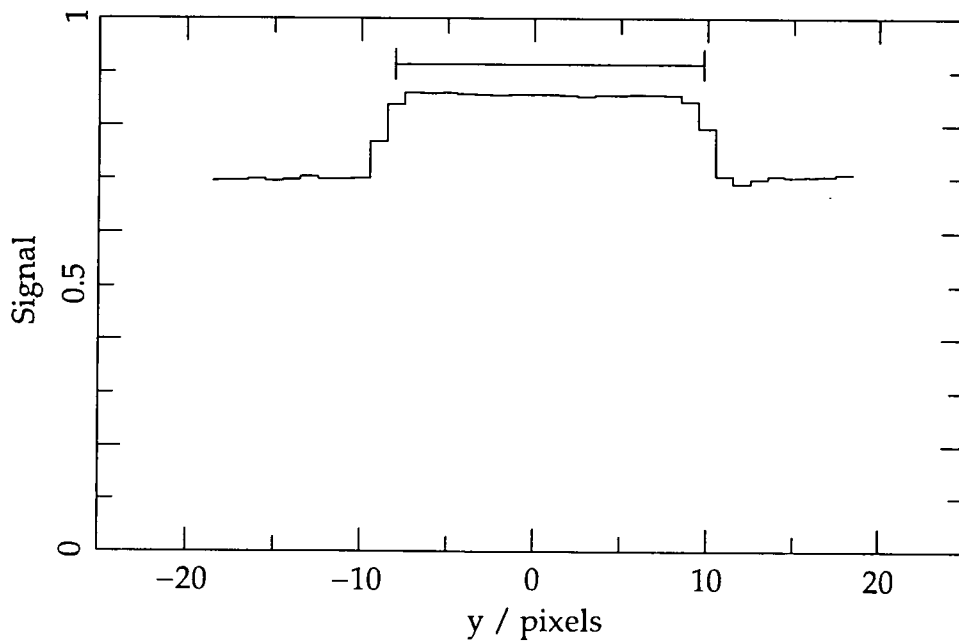


Figure 3.8: The width variation of a CAMM-3 slit (2)

This would not occur with a laser as there is no physical contact with the mask material.

There are many different types of laser, but only a few can generate the power levels needed to cut through an aperture mask. The two most promising options are the CO<sub>2</sub> laser and the Nd-YAG laser (YAG stands for Yttrium-Aluminium-Garnet).

The ability of a laser to cut through a given target material depends on six main factors:

- the output power of the laser
- the spot size to which the beam is focussed
- the speed at which the target is moved
- the thickness of the target
- the fraction of incident radiation that is absorbed by the target material
- the specific energy required to vaporise the target material

CO<sub>2</sub> lasers operate in the infra-red at a wavelength of 10.6µm. They can generate power levels of many kilowatts and compared to other lasers are highly efficient (5 to 20%) (Hecht, 1986, pp139–140). They are widely used in industry for cutting both metals and non-metals.

Nd-YAG lasers operate in the near infra-red at a wavelength of 1.064µm. They can generate power levels of hundreds of watts, but at a relatively low efficiency (0.1 to 1%) (Hecht, 1986, pp291–292). They can cut both metals and non-metals, but they are more expensive than CO<sub>2</sub> lasers so tend to be used in applications where their shorter wavelength is an advantage.

Wavelength has two effects on the performance of a laser cutter. One is to determine the fraction of incident energy that is absorbed by the target (as opposed to being reflected or transmitted). Different materials have different absorption characteristics (Ready, 1978, p401 and p408). In general:

- Metals are more reflective at 10µm than they are at 1µm.

- Plastics absorb well at 10 $\mu$ m, but may not do so at 1 $\mu$ m.

The second effect of the wavelength is to determine the minimum spot size to which the beam can be focussed. The power level needed to cut a given material at a given speed is proportional to the radius of the spot (unless the thermal conduction is very high, in which case the power density will also be relevant). The spot radius,  $r$ , is normally defined to be the radius at which the intensity falls to  $1/e^2$  of its peak value. For a gaussian beam,  $r$  is given by the equation:

$$r = 2\lambda \cdot f / \pi \cdot D$$

where  $\lambda$  is the wavelength,  $f$  is the focal length of the final focussing lens and  $D$  is the diameter of the beam (Koebner, 1984, p210).

In practice, there are several effects that prevent this spot size from being attained, including:

- Vignetting. If this were to be avoided, the beam would have to be small compared to the lens. However, this would not achieve the smallest spot size, because the spot radius is inversely proportional to the beam diameter. It is better to make the beam diameter approximately equal to the lens diameter and accept the vignetting as unavoidable. A beam expander can be used to achieve this.
- Spherical abberation. To minimise the spot size, it is necessary to use a lens with a very fast focal ratio. Singlet lenses of this type are subject to spherical abberation, which can significantly increase the spot size. Doublet lenses are more expensive but give performance that is closer to the diffraction limit.
- Multi-mode resonance. A laser tube is a three dimensional resonant cavity, so in general can have both transverse and longitudinal resonance modes. Transverse electromagnetic (TEM) modes are labelled according to their eigenvalues: TEM<sub>10</sub> and TEM<sub>01</sub> are the fundamental modes in  $x$  and  $y$ , whereas TEM<sub>00</sub> corresponds to a

gaussian beam profile. It is desirable that most of the radiation be concentrated into the TEM<sub>00</sub> mode as this minimises the RMS spot radius. The fraction of energy in this mode is known as the 'mode purity' of the laser.

To allow for vignetting and spherical aberration, it is common practice to quote the minimum practical spot size as 4/3 of the diffraction limit:

$$r_p = 8\lambda \cdot F / 3\pi$$

where F is the focal ratio of the lens (f/D). The result is proportional to wavelength, so in theory a Nd-YAG laser beam can be focussed to a tenth of the diameter of a CO<sub>2</sub> beam.

In order to cut a complex shape such as an aperture mask, it must be possible to switch the beam on and off. Timing is important because an error will result in the mask being cut incorrectly. For example, the LDSS-2 mask specification requires the slit length to be variable in increments of 0.1mm or less, implying an accuracy of about that order. To achieve that at a feed rate of 1 cm s<sup>-1</sup> would require the beam to be switched with an accuracy of 1ms.

There are two ways in which the beam can be controlled. One is to use a mechanical shutter operated by a solenoid. Shutters have the advantage that they can be fitted to any type of laser so long as they are rated for the appropriate power level. However, the time needed to open or close the shutter is limited by its inertia, which will be considerable if the shutter is designed to dissipate large amounts of energy. Shutters are therefore best suited to systems where the feed rate is low or the tolerance wide.

The second method is to modulate the laser with an electrical control signal. Not all lasers have modulation inputs, but those that do normally have response times that are orders of magnitude better than a mechanical shutter. Modulation of the beam at its source is more reliable than using a

shutter as it does not require any additional moving parts.

If the modulation bandwidth is wide enough, it may also be possible to use the modulation input to control the power output of the laser. This would be useful if the laser were required to cut round corners as it may not be possible to maintain a constant feed rate under those circumstances. For a continuous wave (CW) laser, or a pulse laser with a high repetition rate, pulse width modulation would be used. For a pulse laser with a lower repetition rate (comparable to the modulation frequency), it would be better to use pulse period modulation to avoid aliasing.

The lowest modulation frequency that can be used,  $f$ , depends on the feed rate,  $v$ , the cutting radius,  $r_0$ , the width of the slit,  $w$ , and the allowable width variation,  $q$  (equal to  $\delta w/w$ ). If the slit is cut in one stroke ( $r_0=w$ ),  $f$  is given by the equation:

$$f > v / 2w \cdot (2q - q^2)^{1/2}$$

For example, with a feed rate of  $10 \text{ mm s}^{-1}$ , a cutting radius of  $200\mu\text{m}$  and a width variation of 3% (see section 3.2.3), the minimum frequency would be just over 100Hz. This is also the lowest allowable repetition rate for a pulse laser whether it is modulated or not.

High power lasers usually need to be cooled because of the large amounts of waste heat that they generate. Using the efficiency figures given above, a 10W  $\text{CO}_2$  laser will dissipate between 40 and 200W of heat, while a 10W Nd-YAG laser will dissipate between 1kW and 10kW. The most common method of removing this heat is water cooling, which can be either open-loop (the water is used once) or closed-loop (the water is recycled). Closed-loop operation is more expensive, but is the only viable option at a mountain-top observatory where the supply of water is usually very limited.

An additional benefit of closed-loop cooling is that it is possible to regulate

the temperature of the water. Once the laser has reached thermal equilibrium this helps to stabilise the dimensions of the resonant cavity. If the water temperature were allowed to vary then the length of the cavity would change. This would cause the laser to switch between different longitudinal modes and the output power would fluctuate.

Output power variations will affect the slit quality, because a more intense gaussian beam will cut to a greater radius. If the power density at a given point is  $\rho$  and the spot radius is  $r_0$  then:

$$\rho = \rho_0 \cdot \exp(-r^2/r_0^2)$$

and:

$$\delta\rho = (-2r/r_0) \cdot \rho_0 \cdot \exp(-r^2/r_0^2) \cdot \delta r$$

$$\delta\rho/\rho = 2(r/r_0)^2 \cdot (\delta r/r)$$

Lasers typically cut to between 1 and 2 times  $r_0$ . If the whole of the slit is cut in one stroke and the allowable width variation is 3% (see section 3.2.3) then this would limit the power variation to between 6% and 24%. (In practice, there are other factors that influence the slit edge quality, so these are upper limits.)

During its warm-up period it is not uncommon for the output power of a laser to vary by 10% or more. There may also be a loss of mode purity, or even a switch to a completely different transverse mode. For this reason it is highly desirable to allow the laser to reach thermal equilibrium before attempting to cut a mask. The time required to achieve this should therefore be considered as part of the fabrication lead time.

Any laser capable of cutting metal or plastic is potentially dangerous. Safety can be assured in two ways: by training and by design. There are three main hazards:

- If a collimated Nd-YAG laser beam enters the eye then it will be

focussed onto the retina. At power levels greater than a few milliwatts this can cause immediate and permanent damage. Appropriate precautions include shielding the beam until it reaches the focussing lens and using safety goggles that block the wavelength being used. Diverging beams are less dangerous in this respect, but precautions are still necessary. This hazard does not apply to CO<sub>2</sub> lasers because the eye is opaque to 10.6µm radiation.

- If a high-power laser beam hits the skin, or indeed any other part of the body, then it will burn the surface. The level of danger depends on the power density; for very high power lasers even diffuse reflections can be a hazard. Collimated beams remain dangerous over long distances, whereas diverging beams do not. Appropriate precautions include shielding the beam, and also the laser cutter as a whole. The latter enclosure would have to be opened to access the mask, so a safety interlock should cut the beam unless it is closed. This hazard applies to any type of high-power laser beam at any wavelength.
- The most dangerous part of a laser is usually its high voltage power supply. All high voltage connections must therefore be well insulated and preferably located in the same case as the laser tube.

There is also a further hazard that must be considered when cutting plastics:

- Many plastics decompose when they are vaporised and release toxic byproducts such as carbon monoxide, phosgene and hydrogen cyanide (Lefaux, 1968, pp202–207). The volume of material removed from an aperture mask is small, so in most cases it will be adequate to ensure good ventilation, but for some materials active fume extraction may be necessary.

In order to develop a prototype laser mask cutting system at Durham, a laser was purchased together with suitable beam delivery optics and an X-Y table. The main objective was to produce masks of a similar quality to CAMM-3, but with a significantly shorter lead time. It was also hoped that, ultimately,

a laser system would be more reliable and require less skill to operate and maintain than a comparable milling machine.

Several makes of CO<sub>2</sub> and Nd-YAG lasers were investigated, but financial constraints effectively ruled out the purchase of a CO<sub>2</sub> laser suitable for cutting metal or a Nd-YAG laser suitable for cutting anything. The final choice was a 'Synrad 48-1-28' CO<sub>2</sub> laser, which cost £2200 (1990). Its specifications are given in table 3.8.

Output power (typical)	12W
Beam diameter	3mm
Beam divergence	5 milli-radians
Mode purity	95% TEM <sub>00</sub>

Table 3.8: Synrad CO<sub>2</sub> laser specifications

The optical system consisted of a 5× beam expander, a mirror, a focussing lens and fine-focus adjuster, and a gas nozzle. Its total cost was £3200 (1990). A doublet lens was used in order to reduce spherical aberration. Its specifications are given in table 3.9.

Material	ZnSe
Clear diameter	25mm
Focal length	50.8mm

Table 3.9: Laser focussing lens specifications

The beam expander increases the diameter of the beam from 3mm to 15mm, which is significantly less than the diameter of the lens. In theory, the spot size should therefore be close to the diffraction limit of 23µm. (In practice, it is currently believed to be significantly greater than this.)

The laser and its power supply are integrated into a single case so there are no external high voltage connections. The case acts as a heatsink and has channels for water cooling. At present it is cooled using tap water, but if it

were transferred to La Palma then a closed-loop cooling unit would be needed. The lens mount also has the facility to be water cooled but this does not appear to be necessary at current power levels.

The gas nozzle is used to blow away debris produced as the mask is cut and to prevent the remaining material from overheating. It also acts as a shield, enclosing the beam to within about a millimetre of its focus. The nozzle was tested with low pressure compressed air (up to about 5 psi) and was found to result in a significant improvement in the slit quality.

The laser has a control input which was used to modulate its output. A control unit was built to generate a variable duty-cycle rectangle wave at a frequency of 8.6kHz (variable between 5 and 10kHz). A laser power meter was used to measure the transfer function between the duty cycle and the output power. The results are shown in figure 3.9, with a direct proportion line for comparison. The graph is clearly non-linear, but this could be hidden from the user by building a look-up table into the control system.

A second function of the control unit was to generate what Synrad describe as 'tickle' pulses. They are 10 $\mu$ s pulses (variable between 5 and 20 $\mu$ s) applied to the control input at a rate equal to the modulation frequency. This is not sufficient to cause the device to lase, but it does ensure that the gas remains in an excited state. If tickle pulses are not used and the laser is switched off for an extended period then according to the manufacturer there may be a delay before the laser responds when it is switched on. (Tests confirmed that the tickle pulses do not generate any radiation, but their beneficial effects have not been verified.)

The X-Y table cost £7800 (1991) and has an absolute accuracy of 20 $\mu$ m. It consists of two orthogonal crossed-roller slides driven by stepper motors and is monitored by two linear optical encoders. The control system consists of an indexer card which fits into an ISA bus slot and two micro-stepping drive units. The indexer can drive both axes simultaneously and within its

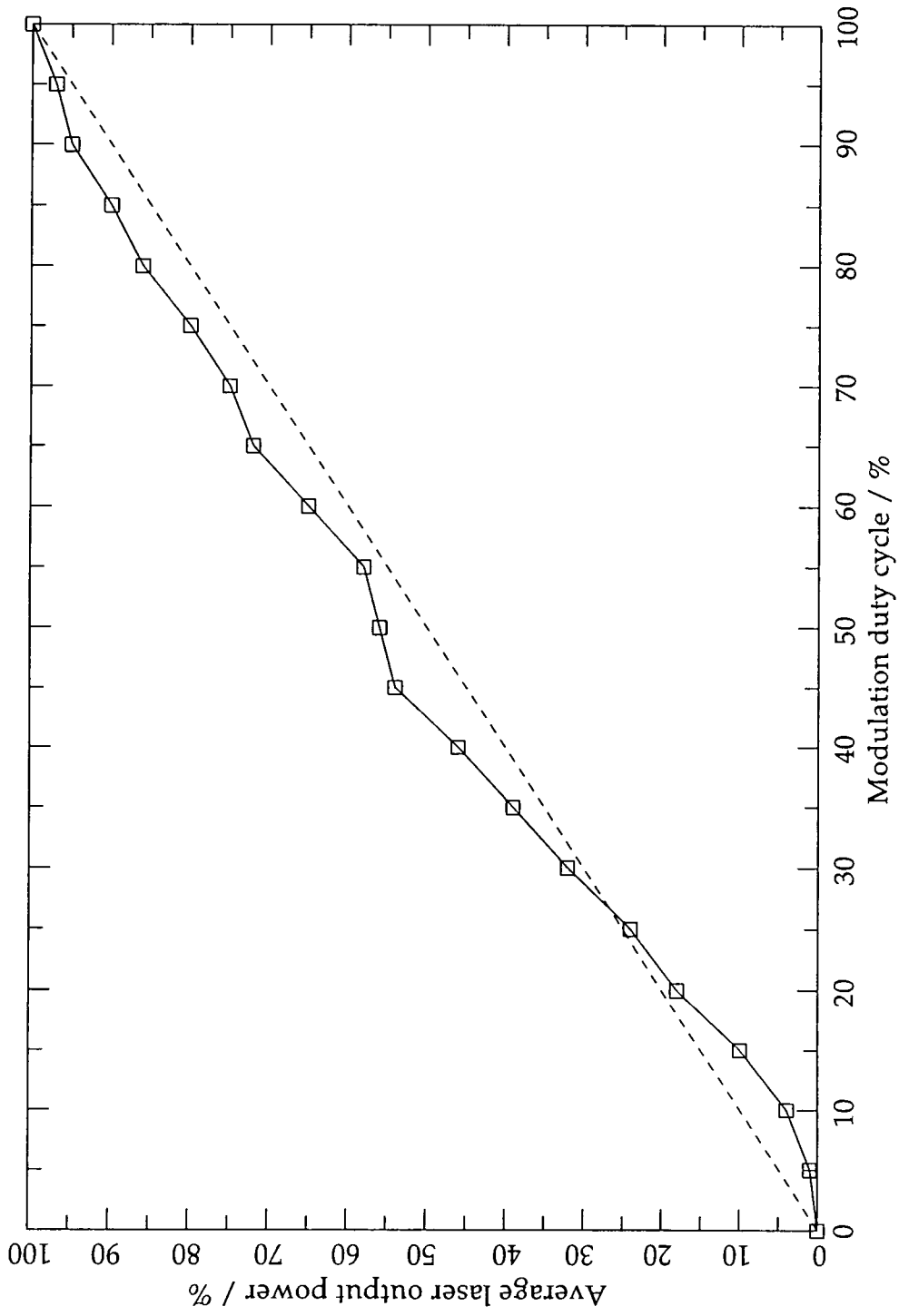


Figure 3.9: The power transfer function of the Synrad CO<sub>2</sub> laser

limits can follow an arbitrary velocity profile. If required this would allow the laser to cut a curved slit at a controlled feed rate.

A suitable mask material has not yet been identified and is one of the main outstanding areas of research. Many types of plastic have the required cutting qualities, but most are ruled out by their thermal expansivity. Availability is also an issue as many plastics manufacturers are understandably reluctant to supply very small quantities of their products.

A different type of laser mask cutting system has been developed by a group at the Observatoire de Marseille for use with the MOS/SIS instrument (Multi-Object Spectrograph/Sub-arcsecond Imaging Spectrograph) on the CFHT (Canada/France/Hawaii Telescope) (Lemaître and Vigroux, 1987 and Di Biagio *et al*, 1990). The mask cutting machine is known as 'LAMA' and is built around a 14kW pulsed (2.1W average) Nd-YAG laser.

Unlike the laser at Durham, LAMA is designed to cut metal masks. It is able to achieve very high slit quality but the feed rate is limited to between 50 and  $150\mu\text{m s}^{-1}$ . This could be improved by increasing the laser power but the cost would be considerable (their current laser system cost approximately £50,000). It is therefore necessary to use very thin mask materials, which are easier to cut but lack the rigidity and robustness of, for example, a CAMM-3 mask.

### 3.3.5 Movable-Slit Masks

A movable slit mask was developed by the Royal Greenwich Observatory for use with FOS-1 (a faint object spectrograph on the Isaac Newton Telescope) and was commissioned by the RGO and Durham University in February 1986. The mask consists of 10 rectangular segments which can be moved relative to each other in the dispersion direction. Each segment includes a slit, so by moving them it is possible to create a wide range of different mask configurations.

Masks of this type are reusable, yet have a relatively low capital cost (the FOS-1 mask cost about £2000). The slit edges can be machined to the same standard as conventional long-slit spectrographs and it is possible to position them to any required standard of accuracy. The FOS-1 unit was configured manually, but a fully developed system would allow the slits to be controlled remotely.

The main disadvantage is the constraint on the slit layout. The slit lengths are fixed, as are their positions in the spatial direction. This can cause serious problems when selecting target fields, especially if the slit position angle is constrained to match the parallactic angle. Movable slit masks are therefore best suited to applications where the number of potential targets in a given field greatly exceeds the number of available slits.

It was for this reason that movable slit masks were not used with subsequent Durham spectrographs. However, a similar system is being developed by ESO for use with the FOcal Reducer/low dispersion Spectrograph (FORS) on the Very Large Telescope (VLT) (Appenzeller and Rupprecht, 1992a). It will allow up to 19 objects to be viewed simultaneously and it can be configured remotely. This is necessary because the focal plane is located in an alcove in the primary mirror cell. Consequently, there is insufficient space for an aperture wheel of the type used in LDSS-2, and even if there was, access to the wheel (for loading masks) would be very difficult.

### **3.3.6 Liquid Crystal Masks**

Liquid crystals are substances that combine the bulk transport properties of a liquid with the local self-organisation of a crystal. They are used in electronic displays because their optical properties can be varied in response to an applied electric field. Liquid crystals can also respond to temperature, pressure and magnetic fields.

To be used as an aperture mask, a liquid crystal display (LCD) would have

to have a high throughput, large contrast ratio, wide spectral bandwidth, large area and small pixel size. The throughput and contrast ratio are of particular concern as conventional masks have 100% transmission and contrast at all wavelengths. Any attenuation or light leakage will increase the exposure time per field and this must be justified by advantages such as reduced field acquisition time.

Several types of LCD were tested by Wurtz and Stocke (1992) with a view to using them as aperture masks. They concluded that with current technology it was possible to achieve a clear-state transmission of 50–70% across the optical band with an off-state opacity approaching 10 magnitudes. The resolution would be relatively poor and the development costs would be considerable. The issue of slit quality was not considered, but it is likely that this too would be poor.

Given these limitations, LCD masks would not achieve the same performance as, for example, CAMM-3 masks, particularly when observing faint objects. While they would undoubtedly be more convenient to operate, there is currently no technical justification for using them with an instrument such as LDSS-2. However, LCD technology has improved greatly in recent years and future developments may improve its performance to a level where this assessment could be reconsidered.

An alternative use of liquid crystal technology would be to configure the mask thermally rather than electrically. This could be achieved using a medium-power laser and would avoid many of the problems inherent in multiplexed dot-matrix addressing schemes. Further research is needed to assess the feasibility of this type of mask.

## Chapter 4: LDSS-1 Data Reduction

### 4.1 Introduction

This chapter describes an astronomical project conducted using LDSS-1, a multi-slit spectrograph at the Anglo-Australian Telescope (AAT). The purpose of the project was to carry out a statistical survey of faint compact objects, as part of an investigation of faint star populations within our galaxy.

My involvement with the project began after the observations had been completed but before the data had been fully analysed. My primary objective was to gain experience of multi-slit data reduction, but in doing so I was able to assist with the wider aims of the project.

LDSS-1 was the predecessor to LDSS-2 and has a very similar optical system. Like LDSS-2 it is capable of direct imaging and uses similar aperture masks. Data is reduced using a specially written data reduction package known as 'LEXT', which also has facilities for mask layout and general image manipulation. The performance of LEXT was of particular interest as it was intended to adapt it for use with LDSS-2.

### 4.2 Field Selection

Full details of the methods used to select targets for the survey can be found in Colless *et al* (1991), but a summary is given here for information.

The survey covered a total of 128 targets in four equatorial fields (two at  $10^{\text{h}}44^{\text{m}}$  and two at  $13^{\text{h}}41^{\text{m}}$ ). Targets were chosen with the aid of the COSMOS measuring machine using two selection criteria: magnitude and compactness. The magnitude range was  $22.5 \leq b_j \leq 23.5$ , though some objects between  $21 \leq b_j \leq 22.5$  were included for cross-calibration with a previous survey. The compactness criterion was defined empirically in terms of the

magnitude and peak intensity of the target. Mask layout was carried out with the aid of LEXT.

LEXT translates each set of target coordinates into an X-Y offset from the field centre and creates a slit at that point. The slits are then expanded using the 'GROW' command, which determines how long the slits can be made before their spectra start to overlap. The growth rate can be weighted if some objects are more important than others.

To check whether any of the spectra do overlap, LEXT predicts the position of each target spectrum, each sky spectrum, and each zero order image. The only overlap that is allowed is between a zero order image and part of a sky spectrum. If it is not possible to accommodate a target with a sensible slit width without causing an overlap then this fact is reported to the user.

When the mask design is complete it is output to an X-Y plotter. The plot is used by the mask fabrication company to create a photo-tool and manufacture the mask. This process typically takes between 2 and 4 weeks.

## **4.3 Data Reduction**

### **4.3.1 Introduction**

The LDSS-1 data reduction procedure consists of five stages:

1. Flat-fielding (CCD exposures only)
2. Correction of image distortion (IPCS exposures only)
3. Spectrum extraction
4. Wavelength calibration
5. Flux calibration

### **4.3.2 Flat-fielding**

Flat-fielding is a standard procedure that can be applied to a CCD exposure to reduce the level of noise. It works by compensating for the local pixel-to-

pixel variation in the sensitivity of the CCD. To do this, a reference frame is needed. This need not be a flat field in an absolute sense, but any variation in intensity must be slow compared to the pixel scale.

The variation in sensitivity may be wavelength dependent, so when flat-fielding a dispersed image the reference frame should also be dispersed. It is therefore taken using the same grism and aperture mask as the data frame. A tungsten lamp is used as the source to ensure that its spectrum is smooth.

To apply the flat-field, it is first necessary to measure the CCD bias level and subtract it from both frames. This is done because the bias does not scale with the pixel sensitivity whereas the signal does. The reference frame is smoothed using a 2D gaussian filter and the unsmoothed version divided by the smoothed version. The result is a frame that is proportional to the sensitivity of the corresponding CCD pixels, normalised to an average value of 1. Dividing it into the (bias-subtracted) data frame thus cancels out any variation in the pixel sensitivity.

#### **4.3.3 Correction of image distortion**

There are two main sources of distortion in LDSS-1: the spectrograph optics and the detector. All spectrograph optical systems cause distortion, and this must be accepted as a trade-off against other optical parameters and against the cost of the instrument. In LDSS-1, the distortion amounts to approximately 2% near the edge of the field.

LDSS-1 can be used with both CCD and IPCS detectors. A CCD causes very little distortion, due to its monolithic solid-state construction. An IPCS, however, can distort the image by 5 to 10% near to the edge of its field of view, which greatly exceeds the distortion caused by the spectrograph optics.

The image must be resampled in order to correct the distortion and this inevitably reduces its resolution. The algorithm used for spectrum

extraction can accommodate the distortion present in a CCD image, but would have difficulty with an image from an IPCS. For this reason dispersed CCD images are not normally resampled whereas IPCS images are.

A special mask is used to map the distortion, consisting of a number of holes in a square matrix. An undispersed exposure of the mask is taken using a tungsten lamp and the centroid of each hole found in terms of detector coordinates. The coordinates are then compared with the known layout of the mask to obtain the displacement of each point.

The displacements are modelled using a two-dimensional interpolation function. LEXT uses splines for this purpose because of their stability. Once the interpolation function is known, it is used to correct the distortion by resampling the image into an undistorted coordinate system.

(Note that this procedure is also applied to undispersed CCD images if they are to be used to measure coordinates for an aperture mask, because 2% distortion would be sufficient to prevent much of the field from being acquired. IPCS images are not normally used for this purpose as they do not have the dimensional stability required for astrometric measurements.)

#### **4.3.4 Spectrum extraction**

A dispersed image from LDSS-1 will typically contain 25–100 separate spectra. To extract them, they must first be isolated from each other. It is possible to specify the position of a spectrum manually, but LEXT normally takes the coordinates directly from the mask layout file.

Conventional sky subtraction algorithms, such as that used by the FIGARO program 'POLYSKY', require the user to identify which pixel rows correspond to the object and which to the sky. They then fit an interpolation function to the sky level in each pixel column and subtract the result from that column.

LEXT can operate in a very similar manner and if requested can derive the object and sky coordinates from the mask layout file. However, the results may be unsatisfactory if the targets are faint or the slits very short, so a more sophisticated procedure is also available. It allows the user to divide the spectrum into several blocks (typically between 2 and 10) and to manually specify which pixels belong to the target and which to the sky for each block. This is time-consuming if too many blocks are used but it does allow moderate slit curvature to be accommodated.

A different polynomial order can be specified for each block. The slit profile is measured by fitting the polynomial to the block as a whole, as this maximises the signal to noise ratio. However, the background is highly wavelength dependent, so the result must be scaled to fit individual pixel columns. The target signal is then summed and the interpolated background level subtracted.

#### **4.3.5 Wavelength calibration**

The wavelength scale for each spectrum is measured using an emission line spectrum from an arc lamp. The dispersion of the instrument varies across its field of view, so it is necessary to measure a separate wavelength scale for each slit. LEXT automates this procedure by using the slit position to predict an approximate calibration, searching for a pre-determined set of emission lines, and using the positions of those lines to calculate a more accurate calibration function.

#### **4.3.6 Flux calibration**

The type of survey astronomy for which LDSS-1 is best suited does not normally require absolute flux calibration of the results. However, calibration is necessary in order to equalise the gain of the instrument at different wavelengths. Failure to do so will change the relative strength of emission lines and distort the shape of the continuum.

The fluxing function is calculated by observing a spectrophotometric calibration star then dividing the observed spectrum by the true spectrum. Subsequent spectra are calibrated by multiplying them by the fluxing function. This corrects the shape of the spectrum, but its absolute level should be considered approximate unless very wide slits are used. (Narrow slits are not suitable for spectrophotometry, as they give results that are highly sensitive to field acquisition errors.)

## 4.4 Results

Of the 128 targets, 2 were identified as QSOs, 7 as galaxies, 47 as M-stars and 11 as earlier types of star. 50 could not be identified and 11 were not detected at all.

8 of the 11 undetected targets were subsequently found to represent erroneous measurements by COSMOS. The remaining 3 could have been caused by incorrect astrometry, mask manufacture or field acquisition.

The unidentified spectra are mostly the result of poor signal-to-noise ratios. As would be expected, the identification rate falls as the magnitude increases: for  $b_j \leq 22.5$  it is 82%, but for  $b_j > 22.5$  it is 48%. There is also a colour dependence, red targets being easier to identify than blue ones.

A full analysis of the results of this project can be found in Colless *et al* (1991). The spectra of two of the galaxies identified by the survey are shown in figures 4.1 and 4.2.

## 4.5 Conclusion

LEXT was found to be well suited to LDSS-1 data reduction and with modifications was adaptable for use with LDSS-2. Necessary enhancements included the ability to import and export data in a wider range of formats, migration from the interim Starlink environment to Adam, support for an improved field acquisition procedure, and improvements to the sky

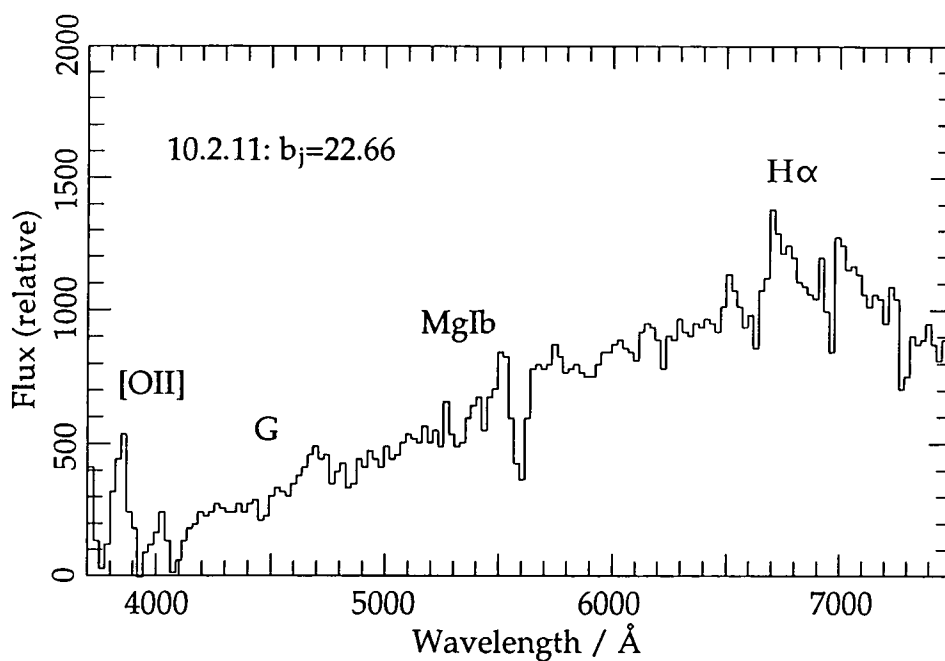


Figure 4.1: The spectrum of a galaxy identified by the LDSS-1 survey (1)

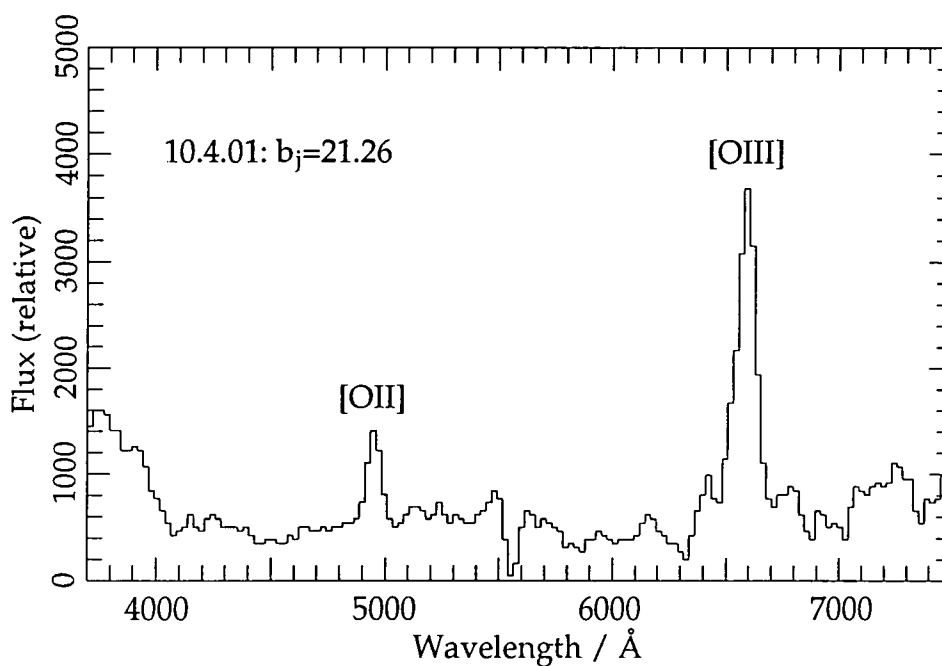


Figure 4.2: The spectrum of a galaxy identified by the LDSS-1 survey (2)

subtraction and wavelength calibration procedures.

The fraction of spurious targets in the survey (6%) was acceptable but undesirable. Visual inspection of sky survey plates prior to an observing run would be time consuming but may be justified if this result is typical. Targets lists derived from CCD images should be more reliable and easier to verify, but imaging the target field beforehand is not always practical. The remaining fraction of undetected targets (2%) is encouraging and indicates that the astrometry and the field acquisition are both accurate and reliable.

The much larger fraction of unidentified targets is to be expected when an instrument is used so close to its limiting magnitude. LDSS-2 should give a better signal-to-noise ratio for a given target, mostly because of improved detector efficiency. This could be used either to improve the identification rate and/or increase the survey depth.

# Chapter 5: The FOS-2/ISIS Multi-slit Unit

## 5.1 Introduction

This chapter describes the commissioning in February 1990 of a multi-slit unit for the FOS-2 and ISIS spectrographs at the William Herschel Telescope (WHT).

FOS-2 is a faint object spectrograph, built at Durham University and commissioned in 1987. It was the first spectrograph to be used on the WHT and was originally an independent instrument. It has since been integrated with ISIS, which is a two-channel intermediate dispersion spectrograph. All three spectrograph channels share the same slit assembly so the multi-slit unit can be used with either instrument.

Neither FOS-2 nor ISIS were designed for multi-slit spectroscopy and as a consequence the multi-slit unit has a number of limitations. It was built for four reasons:

- As an interim measure, to cover the two years prior to the installation of LDSS-2
- To test the ability of the CAMM-3 milling machine to produce multi-slit aperture masks at the telescope
- To gain practical experience of multi-slit spectroscopy, including field acquisition and data reduction techniques
- To learn about more general problems associated with commissioning a new instrument

## 5.2 Instrument Characteristics

### 5.2.1 ISIS

ISIS is attached to the telescope at the F/11 Cassegrain focus, underneath the A&G box. Neither it nor FOS-2 have the ability to make undispersed

exposures so field acquisition is by means of a slit-viewing camera. The slit lies at a shallow angle to the focal plane ( $7.5^\circ$ ) and the slit jaws are reflective. Any light that does not pass through the slit is therefore reflected into the camera. An image intensifier tube is used, enabling the camera to detect objects down to about 19th magnitude. In some cases this is sufficient to view the target. If it is not then the field is acquired by means of a blind offset from a star that can be seen.

Once the light has passed through the slit it can be directed into FOS-2, or into the red and blue channels of ISIS. Dichroic mirrors allow simultaneous observation with the red and blue channels, or with FOS-2 and the blue channel.

The two ISIS channels have similar optical systems but are optimised for different wavelengths. Both include a filter slide, a collimator mirror, a grating and a camera. Four different gratings are provided for the blue channel and four for the red channel. Each channel also has a cross-dispersion element, but it is optional and can be removed from the light path. The gratings can be tilted in order to vary their wavelength coverage. The instrument as a whole has a spectral range of 3000 to 11000Å.

### 5.2.2 FOS-2

FOS-2 is optimised for high throughput, which it achieves by minimising the number of optical surfaces in its light path. There are four optical components between the slit and the detector: a shutter, a dispersion assembly (which includes a transmission grating, three cross-dispersion prisms, and an aspheric surface), a concave mirror, and a field-flattening lens. There is no collimator, but the resulting distortion is largely corrected by the aspheric surface. The dispersion assembly is bonded together to reduce the number of glass-air interfaces.

Unlike ISIS, the FOS-2 detector is integrated into the instrument. It is a CCD,

and is mounted in a vacuum chamber together with the field flattening lens, the mirror, and one side of the aspheric surface. This arrangement is a necessary consequence of the optical design and although the CCD can be upgraded it is not a trivial task to do so.

The cross-dispersion prisms separate the first- and second-order spectra, extending the spectral range of the instrument. The second order spectrum occupies an area of the CCD that would otherwise be occupied by the first-order sky background. A dekker mask is used to prevent inter-order contamination. When using FOS-2 with the multi-slit unit, the second-order spectrum is blocked using a filter. This is necessary because there is insufficient space on the CCD to accommodate both spectral orders for a reasonable number of targets.

### 5.2.3 The Multi-Slit Unit

To use FOS/ISIS as a multi-slit spectrograph, it is necessary to replace the ISIS long slit with an aperture mask. The long slit is mounted on a slide, so the multi-slit unit can be installed permanently without interfering with normal use of the spectrograph. The slide is motorised, allowing the observer to switch between the two slit assemblies during the course of a night.

The masks are rectangular, with dimensions of 40mm in the dispersion direction and 71mm in the spatial direction. They are made from 0.5mm engraving brass and cut using the CAMM-3 milling machine. The field of view and hence the number of slits that can be accommodated depends on the instrument that is used. In the case of FOS-2, the field of view is 2 arc-minutes in the dispersion direction and 3.5 arc-minutes in the spatial direction. This is normally sufficient for about 8 slits.

The slit-viewing optics require that the slit be inclined with respect to the focal plane. This is not possible with an aperture mask as some of the slits

would be out of focus. Neither ISIS nor FOS permit undispersed imaging, so the field acquisition procedures developed for LDSS-1 and LDSS-2 are inapplicable. An alternative field acquisition method is therefore required for the multi-slit unit.

The method chosen is to use two masks: one that lies in the focal plane, for the exposure, and one that is tilted, to acquire the field. No additional hardware is required as the dekker slide (part of the long slit assembly) can be used to hold the second mask. However, brass is less reflective than stainless steel, so the image reaching the slit viewing camera is reduced by about 1 magnitude.

The masks must be aligned with each other to a high level of accuracy, as an error will directly affect the field acquisition accuracy and thus the throughput. Using the formula in section 3.2.4, the error allowed for a  $300\mu\text{m}$  slit is  $54\mu\text{m}$ . Allowance must be made for other sources of error so an accuracy of about  $30\mu\text{m}$  is required.

### 5.3 Field selection

There are two important differences between the FOS/ISIS multi-slit unit and LDSS-1 that are relevant to the field selection procedure:

- The FOS-2 cross-dispersion prisms have non-linear dispersion functions, which result in the spectra being curved. This must be allowed for when determining whether two spectra overlap.
- The number of slits that can be accommodated by a FOS-2/ISIS mask is considerably lower than an LDSS-2 mask, so a greater level of manual intervention is needed to achieve an optimum mask layout.

LEXT is not designed to handle curved spectra and at this stage it could not generate a mask layout file in the format required by the CAMM-3 driver program. Therefore, rather than try to adapt LEXT, it was decided that it would be quicker to write a stand-alone program for FOS-2/ISIS mask

layout.

The program was written in FORTRAN. It reads the astrometric data from a file and allow the user to flag objects as targets or guide stars. The astrometric file contains the the equinox to which the coordinates refer (which is used to calculate the precession) followed by a table of objects. The table lists the right ascension and declination of each object, its type (target or guide star), and optionally a comment to help identify it.

The latitude and longitude of the telescope are hardwired into the program and the epoch of the observation is entered by the user each time the program is executed. The hour angle is initially assumed to be zero but can be changed if necessary. The commands implemented by the program are as follows:

- M Display menu
  - ? Display menu (synonym for 'M')
- AT Set object attributes (requests object number and object type: target, guide star, both or neither; where appropriate allows slit length to be specified to left and right of target)
- CP Clear plotting device
- DE Delete object from list of selected targets (requests object number)
- DF Display field on plotting device
- EX Exit
- HA Set hour angle (requests absolute value in hours)
  - LI List objects (optional range parameter)
  - LF List objects within field of view (optional range parameter)
- MA Move rotator angle relative to current position (requests offset in degrees)
- MC Move field centre relative to current position (requests offset in arc-seconds)
- RE Restore object to list of selected targets (requests object number)
- SA Set rotator angle (requests absolute position in degrees)

- SC Set field centre (requests absolute position in RA and Dec)
- SF Set display format (requests value: 0=targets shown as crosses, guides that are not targets shown as boxes; 1=as 0 but deleted objects shown as circles; 2=as 1 but also number all objects; 3=show predicted spectrum positions)
- SS Set display scale (requests magnification factor)
- WF Write mask layout data to output file

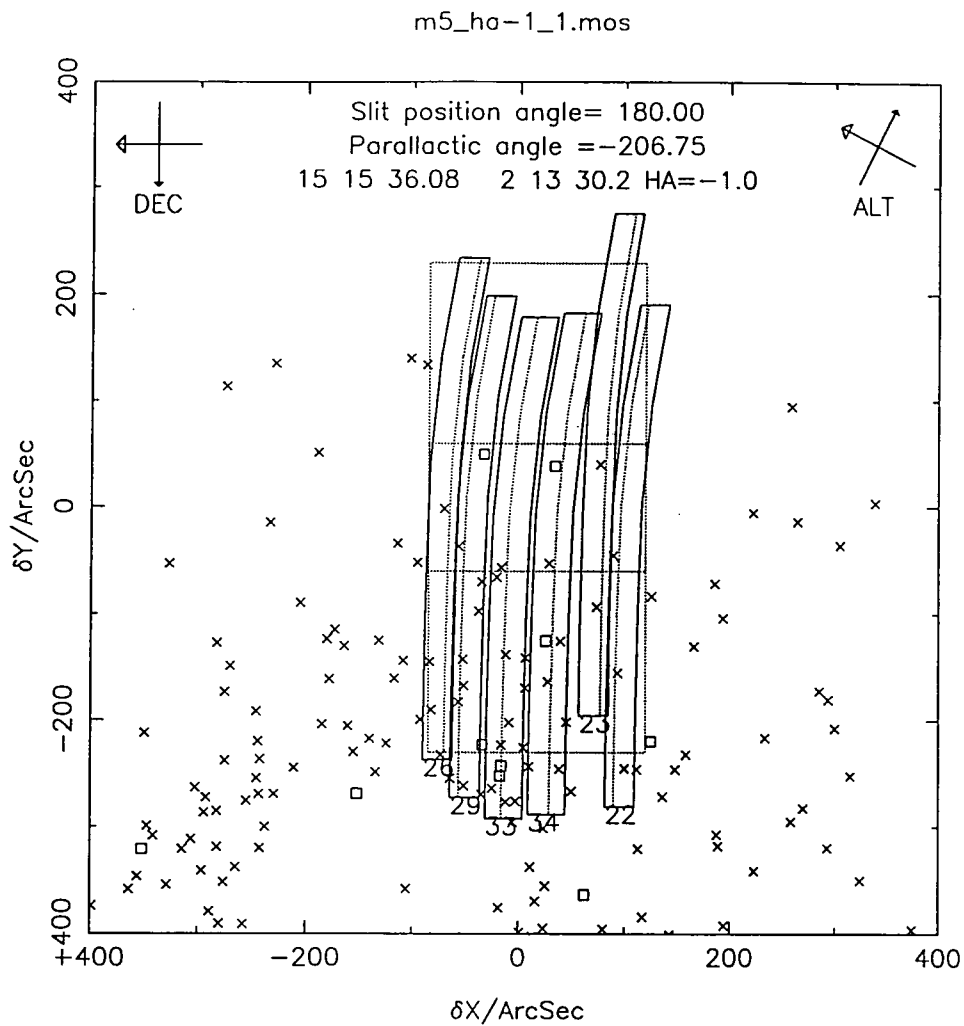
The altitude and azimuth axes are shown next to the field, so it is easy to see how far the rotator angle deviates from the parallactic angle. The right ascension and declination axes are also shown to aid the user. A typical display is shown in figure 5.1.

The output of the program is a file which describes the mask layout in a manner that is independent of any particular fabrication technology. The file is represented using a subset of the ASCII character set that is preserved by most common electronic mail gateways, so the file can be created at the observer's home institution and E-mailed to the observatory. A second program then translates the file into a command sequence that is understood by the CAMM-3 machine.

The dekker mask has the same layout as the main mask, but it must be stretched in the dispersion direction to allow for the fact that it is tilted. This is done by the CAMM-3 driver program, so there is no need to generate a second mask description file.

## 5.4 Results

During its commissioning run the multi-slit unit was tested with two fields in the globular cluster M5. This target was chosen because it is bright and because accurate astrometric data is available. Fainter objects are more difficult to observe, but this is mostly attributable to the preliminary astrometry and the data reduction. A relatively bright target was therefore



- Outer dotted box: field of view of detector
- Inner dotted box: usable area of aperture mask
- Small boxes: potential or actual targets
- Small crosses: potential or actual fiducial stars
- Curved strips: positions of sky background spectra
- Curved dotted lines: positions of target spectra

Figure 5.1: A display generated by the FOS/ISIS MSU field selection software

sufficient to test the field acquisition procedure and allowed the tests to take place while the moon was present.

Initial tests using the comparison lamps had identified a misalignment of  $0.35^\circ$  between the multi-slit masks and the dekker masks. This corresponds to 0.64 arc-seconds at the edge of the field (compared to a slit width of 1.34 arc-seconds), so the error would certainly cause a large drop in throughput and might prevent the field being acquired at all. There was insufficient time to remake the masks so the error was corrected by modifying the acquisition procedure.

In the event, the first field was acquired successfully and the second with partial success. The error in the latter case was characterised as a rotation of approximately  $0.2^\circ$ . It could have been caused either by the modified acquisition procedure (which is no longer necessary) or by movement of the dekker mask relative to its mount (which was known to be unsatisfactory and has since been improved.)

The slit quality was tested using the method described in section 3.2.3, except that a blank sky field was used instead of the tungsten lamp. From measurements of 6 slits, the worst-case variation in the width was found to be not more than 0.07% ( $0.2\mu\text{m}$ ). This is an upper limit, as faint background objects may be present in the sky field.

(Subsequent measurements using LDSS-2 were consistent with this result, but were less sensitive as the CCD was not flat-fielded. For comparison, irregularities of up to 3.1% can be permitted without significantly affecting the sky subtraction accuracy.)

## 5.5 Conclusion

The difficulties encountered with the second field clearly demonstrate the need for high mechanical accuracy and reliability if multi-slit techniques are

to work. However, the successful acquisition of the first field did prove the principle of the acquisition method and gave confidence that the methods proposed for LDSS-2 would also be viable.

Also apparent was the need for a direct imaging facility (which is provided by LDSS-1 and LDSS-2), and for a slide or carousel holding several aperture masks (provided by LDSS-2). In addition to increasing the flexibility of the instrument, direct imaging would simplify the field acquisition procedure and if necessary allow the instrument to function with fainter fiducial stars. A mask carousel would allow most if not all of the masks to be loaded into the instrument at the start of the night, greatly improving observing efficiency.

The slit quality was well within specification and acceptable for use with both FOS-2/ISIS and LDSS-2. In particular, the quality was considerably better than that achieved with the photochemically etched masks used with LDSS-1. For this reason, it was decided that CAMM-3 masks should be used for the LDSS-2 commissioning run and until such time as a better alternative was available.

# Chapter 6: LDSS-2 Optical and Mechanical Design

## 6.1 Introduction

This chapter looks at the optical and mechanical design decisions made prior to and during the construction of LDSS-2.

LDSS-2 is a low dispersion survey spectrograph, built as a collaboration between Durham University Physics Department and the Royal Greenwich Observatory and commissioned on the William Herschel Telescope in March 1992.

It builds upon experience gained by the department during the construction of LDSS-1, mentioned earlier. Both are multi-slit spectrographs with similar optical specifications. The main improvements are:

- The level of automation. LDSS-1 is operated manually using levers on the outside of the instrument case. This requires an operator to be present inside the dome, in the AAT Cassegrain cage. In contrast, LDSS-2 is automated to the extent that all relevant optical components can be controlled remotely using the telescope system computer.
- The ability to refocus the camera while on target. This could not be done with LDSS-1 as any focus change required the instrument to be partially dismantled.
- The optical system, which is expected to have a higher throughput than LDSS-1 and thus allow fainter objects to be observed. The optics have also been modified to account for the focal ratio of  $f/11$  at the WHT cassegrain focus (cf.  $f/8$  on the AAT).
- The number of filters and grisms that can be mounted simultaneously. The LDSS-1 can only hold two filters and two grisms, whereas LDSS-2

has space for seven filters and three gratings.

- The amount of space between the collimator and the camera. This has been increased to allow larger (ie. higher dispersion) gratings to be used. This gives LDSS-2 a maximum dispersion of  $100\text{\AA}/\text{mm}$  (cf.  $164\text{\AA}/\text{mm}$  with LDSS-1).

Of these the first is almost certainly the most important, partly because it allows more efficient use of telescope time, but mostly because it makes the instrument more accessible to the astronomical community by improving its ease of use.

(It is recognised that multi-slit instruments will inevitably need a substantial amount of support from the observatory staff for at least the foreseeable future. There is however an important distinction between instruments that can be made generally available on a 'common user' basis and those that can only be used by or in association with the group that built the instrument. LDSS-1 is not a common user instrument; LDSS-2 is.)

## 6.2 Optical Design

### 6.2.1 Introduction

The design of a generic multi-slit spectrograph was discussed in some detail in chapter 2, and will not be repeated here. However, while there is little that is unusual about LDSS-2, its optics are worthy of study for three reasons:

- They reflect the astronomical priorities that motivated the construction of the instrument.
- They define the requirements for the mechanical structure and the control system.
- They define the characteristics and performance expected of the instrument, against which it can be assessed during its commissioning

period.

A schematic diagram of LDSS-2 is shown in figure 6.1. It is designed to operate with wavelengths in the range 3700Å to 7500Å and the efficiency and image quality are optimised solely for that region (Allington-Smith *et al*, 1990a). This is justified because detector efficiencies are poor at shorter wavelengths and the night sky spectrum becomes very cluttered with sky emission lines at wavelengths longer than 7000Å. A typical night sky background spectrum is shown in figure 6.2.

The telescope has a focal ratio of  $f/10.94$ . It is focussed onto the currently selected aperture mask, which is mounted in the aperture wheel. The wheel has eight positions and can be operated by remote control. Position 0 is reserved for direct imaging so up to 7 masks can be mounted at any given time.

Immediately below the aperture wheel is the collimator. It too is focussed onto the aperture mask, and converts the diverging light rays into a collimated beam. It has a field of view of 153mm, corresponding to 11.5 arc-minutes on the sky, and a focal ratio of  $f/10.94$ , which matches the telescope. Pupil imaging is used to minimise the size of subsequent optical components.

There are two wheels below the collimator: the filter wheel and the grism wheel. Both can be operated by remote control. The filter wheel has eight positions, one of which is reserved as clear. The remaining seven can be used to hold filters, Hartmann shutters and (in theory) polarisers.

The grism wheel has six positions, but for mechanical reasons only three are adapted to hold grisms. Of the remainder, one is reserved as clear and two accept the same component cells as the filter wheel. The latter are normally used to hold Hartmann shutters.

After the light has been dispersed by the grism, it passes through the shutter.

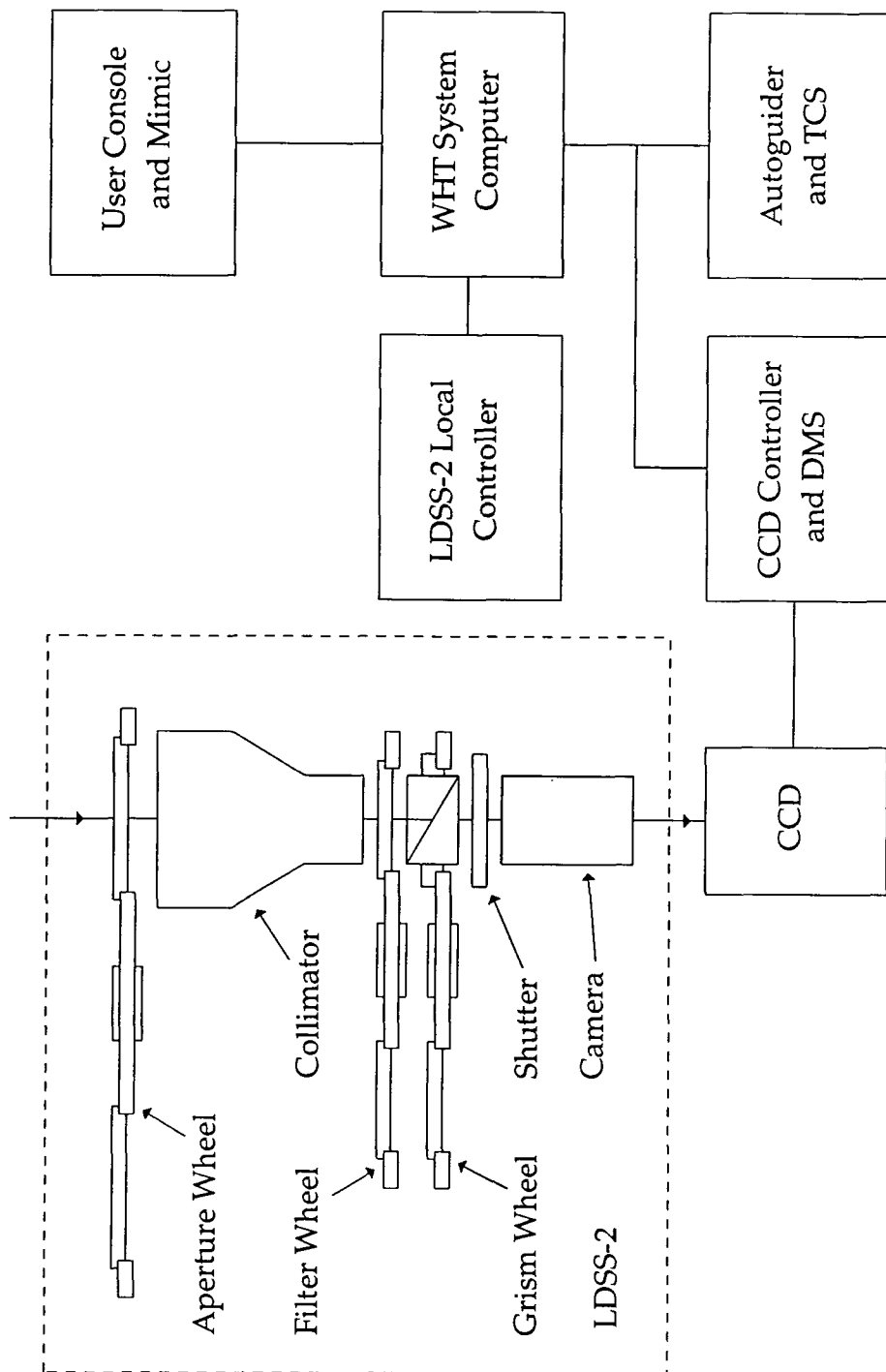


Figure 6.1: A schematic diagram of LDSS-2

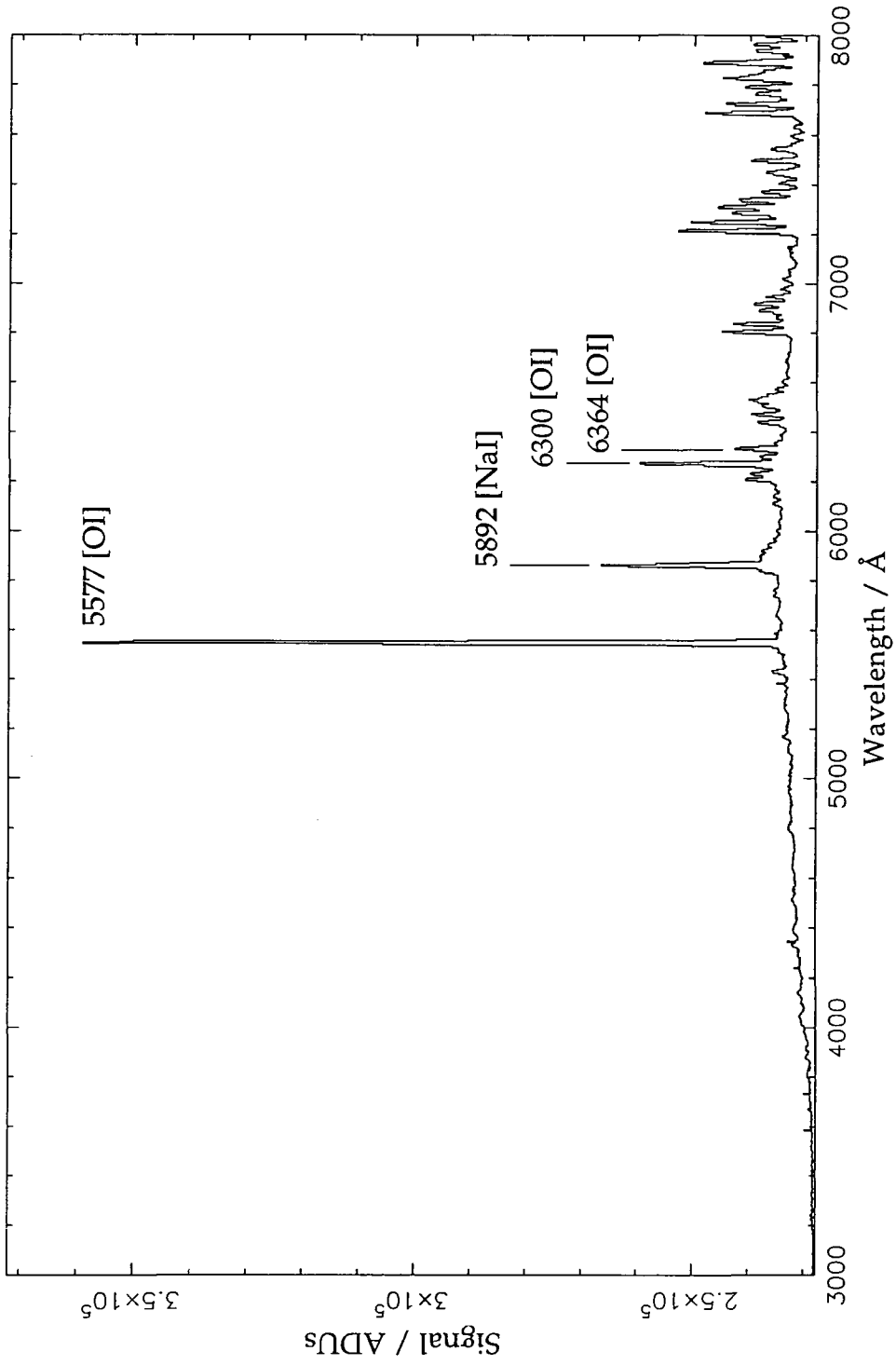


Figure 6.2: A typical night sky background spectrum

Below the shutter is the camera, which has a focal ratio of  $f/2$  and focuses the light onto the detector. The focus can be adjusted by remote control and is used to optimise the instrument performance for a specific wavelength.

The instrument was designed to operate with either a CCD (Charge-Coupled Device) or IPCS (Imaging Photon Counting System) detector. At the time, only an IPCS was able to exploit the wide field of view available, but modern large format CCDs have eliminated this advantage. It is now likely that the instrument will be used exclusively with CCD detectors as they are smaller and lighter, introduce less image distortion, and have higher quantum efficiencies. The detector used during the commissioning run was a 'Tektronix 1024' CCD.

Note that in this chapter the  $x$ ,  $y$  and  $z$  axes will normally be used to refer to the dispersion direction, the spatial direction and the optical axis respectively.

### 6.2.2 Aperture Masks

To date, two different methods have been used to produce LDSS-2 aperture masks: mechanical milling and photochemical etching. The first of these is preferred as it gives better results, is cheaper, and has a shorter lead time. The second was originally developed for use with LDSS-1 so is well tested, but should normally be used only as a backup process. Further information about mask production techniques can be found in chapter 3.

For a spectrum to be observed, the image and the mask must be aligned to a high level of accuracy. The maximum acceptable error was calculated in section 3.2.4 to be  $36\mu\text{m}$ , of which the final telescope pointing error should account for no more than about  $21\mu\text{m}$  (0.09 arc-seconds).

It is impossible to achieve this level of precision directly as it exceeds both the blind-pointing accuracy of the telescope and the accuracy with which the telescope and the instrument are attached to each other. It is therefore

necessary to acquire the field in several steps using undispersed images of the field to calculate the necessary offsets. The recommended procedure is as follows:

1. Between two and five 'fiducial stars' are selected. They must lie within the field of view of the instrument and have positions that are known accurately relative to the target objects. A circular hole, usually 10 arc-seconds in diameter, is cut in the aperture mask for each of these stars.
2. One of the stars in the field is used to locally calibrate the telescope pointing model. This typically improves the blind pointing accuracy of the telescope within that field to between 1 and 2 arc-seconds.
3. The telescope is moved to the centre of the field and an exposure taken with the mask in place but no grism. The alignment at this stage will normally be good enough to ensure that all of the fiducial stars can be seen through their mask holes, though they will not necessarily be centred.
4. The positions of both the fiducial stars and the mask holes are measured. The offset and rotation needed to align the field are then calculated and applied to the telescope.
5. A second exposure is taken to check the alignment. If there is any error then the sequence is repeated from step (4).

For the fiducial stars to be seen within the mask holes, the sum of the mask position error, the pointing error and the stellar image radius must be less than the radius of the mask hole (5 arc-seconds). This implies an absolute maximum pointing error of about 3 arc-seconds. Larger fiducial holes could be used, but doing so would reduce the mask area available for slits.

To avoid de-focussing, the mask must also be in the correct position relative to the z-axis. The telescope focus can be changed to compensate for displacements, but doing so will change the image scale. If the nominal focal length of the telescope is  $f$  and the focus is changed by  $\delta f$  then an object at

radius  $r$  from the centre of the aperture mask will be displaced by  $\delta f \cdot r / f$ . The focal length of the WHT is 45.738m (Unger *et al*, 1988, p30) and the diameter of an LDSS-2 mask is 153mm, so in order to limit the error to an acceptable level (about 5 $\mu$ m) the focus should not be changed by more than about 3mm.

Tilt in the  $x$ - $z$  and  $y$ - $z$  planes is more critical as it cannot be corrected by refocussing. The depth of focus was calculated in section 3.2.7 and found to be 3.2mm, of which the tilt should account for no more than 1.6mm (ie.  $\pm 0.8$ mm). The usable mask diameter is 153mm so this corresponds to a tilt of 0.6 $^\circ$ .

One advantage of the acquisition method given above is that it does not require the aperture mask to be moved once it is in place, so the demands on the accuracy of the mechanism are minimised. However, LDSS-2 is designed to accommodate several other methods and for this reason the aperture wheel specification includes two further tolerances. The first is that any two masks in the wheel be aligned relative to each other to within 25 $\mu$ m. The second is that if the wheel is moved, it can be sent back to a previous position with an accuracy of 25 $\mu$ m.

### 6.2.3 The Collimator

The collimator is the largest and most expensive optical component in the instrument and as such its design involves a number of compromises. It is necessary to achieve a balance between several parameters, the most important of which are the diameter of the field of view and the height of the collimated space. It is also necessary to consider the form of the point spread function and effects such as vignetting, radial distortion and chromatic aberration.

The design chosen includes a total of 8 lenses, and has a field diameter of 11.5 arc-minutes. Pupil imaging is used to place the stop 65mm from the last lens. There are 8 glass-air interfaces, so efficient anti-reflection coatings are

essential.

For optimum performance, the collimator must be focussed onto the aperture mask and its optical axis must coincide with that of the instrument. However, this alignment can be carried out during the assembly of the instrument and does not need to be changed in normal operation.

#### 6.2.4 Filters

LDSS-2 is supplied with six filters: PB, PV, PR, S1, S2 and S3. Their specifications are listed in table 6.1, where  $T_0$  is the peak throughput,  $\lambda_0$  is the wavelength of that peak, and  $\lambda_1$  and  $\lambda_2$  are the half-power points.

Filter	$\lambda_0$	$T_0$	$\lambda_1$	$\lambda_2$	Prescription
PB	4140	0.785	3660	4630	1×BG12, 2×BG39, 1×GG385
PV	5270	0.937	5010	5880	2×GG495, 2×BG39
PR	6030	0.712	5740	6830	2×OG570, 2×KG3
S1	—	1.000	3890	—	3×GG375
S2	—	0.980	4340	—	3×GG420
S3	4000	0.920	3410	4790	1×BG23, 1×BG39, 1×WG280
	/Å		/Å	/Å	/mm

Table 6.1: LDSS-2 filter specifications

PB, PV and PR are broadband filters. They are useful for producing images for target selection, as statistical surveys often have selection criteria based on colour. S1 and S2 are order blocking filters, used to limit the wavelength range of the instrument and thus prevent the first and second order spectra from overlapping. S1 is used with the Low and Med-B grisms and S2 with the Med-R grism. S3 is a band-pass filter, used to fit more slits onto each mask when only a small wavelength range is of interest. It passes the region around 4000Å, which includes the Calcium H and K lines. These features can be used to measure velocity distributions in galaxies and clusters.

Filters are insensitive to translations in  $x$  and  $y$  so long as they cover the pupil. They are also insensitive to translation in  $z$  and rotation in the  $x$ - $y$

plane. Tilts in the x-z or y-z planes should be avoided as they would cause reflections that would appear as ghost images. All of the filters have anti-reflection coatings to improve efficiency.

### 6.2.5 Hartmann Shutters

LDSS-2 is supplied with four Hartmann shutters, used to focus the instrument. They are inserted into the collimated space and divide the aperture into two halves. One half is clear, the other opaque. Two of the shutters are orientated to the left and right of the spatial axis and are normally placed in the grism wheel. The other two are orientated above and below the dispersion axis and are used with one of the grisms, so must be placed in the filter wheel.

### 6.2.6 Polarisers

Although spectropolarimetry is not one of the design objectives of LDSS-2, there is no reason in principle why polarisers could not be introduced into the collimated space. However, this option has not been tested and polarisers are not supplied with the instrument.

### 6.2.7 Grisms

LDSS-2 is supplied with four grisms: low dispersion, medium dispersion with blue blaze, medium dispersion with red blaze, and high dispersion. Their specifications are listed in table 6.2, where  $\lambda_{\text{blaze}}$  is the blaze wavelength and  $\lambda_{\text{undev}}$  is the wavelength for which the deviation is zero.

$\Delta\lambda/\Delta x$  is the mean dispersion, which in the right hand column assumes a pixel size of  $24\mu\text{m}$ . All of the grisms have anti-reflection coatings to improve efficiency. Further details can be found in Allington-Smith (1992a).

Grism	Rules	$\lambda_{\text{blaze}}$	$\lambda_{\text{undev}}$	$\Delta\lambda/\Delta x$	$\Delta\lambda/\Delta x$
Low	150	4980	5560	470	11.28
Medium-Blue	300	5020	5560	220	5.28
Medium-Red	300	6500	5560	220	5.28
High	600	4000	4190	100	2.40
	/mm <sup>-1</sup>	/Å	/Å	/Å mm <sup>-1</sup>	/Å pixel <sup>-1</sup>

Table 6.2: LDSS-2 grism specifications

Grisms are insensitive to translations in  $x$  and  $y$ , so long as they cover the pupil. They are also insensitive to translations in  $z$ . Tilts in the  $x$ - $z$  and  $y$ - $z$  plane will result in image shifts so should be minimised.

Rotation in the  $x$ - $y$  plane will cause the dispersion direction to be skewed relative to the slit axes. This results in the wavelength scales at different points along the slit being shifted relative to each other, hindering sky subtraction. There will also be a skew relative to the detector axes, so the spectrum will not be aligned with the pixel grid. This can be corrected by the data reduction software but causes an effective reduction in the detector resolution. For these effects to be negligible the rotation must cause a shift of at most 1 pixel across a 1024 pixel field. This corresponds to a maximum error of  $0.05^\circ$ .

### 6.2.8 The Shutter

The shutter has two functions, the first of which is to define the period of an exposure. In many applications the exact timing will be unimportant, but some types of observation, such as spectrophotometry, do require a degree of precision.

Any error will be a constant so will be relatively unimportant for long exposures. Conversely, it is unreasonable to expect high shutter precision

for very short exposures, so it is reasonable to consider 30s as the worst case for accurate spectrophotometry. Other sources of error usually limit the accuracy of such measurements to about 1%, so a shutter timing error of 100ms or 0.3% would be small by comparison. It is also desirable to ensure that the shutter opens and closes quickly.

The second function of the shutter is to protect the detector. CCD cameras are unaffected by daylight or normal room lighting, but IPCS detectors can be permanently damaged. LDSS-2 can be interfaced to an IPCS, so as a safety precaution the shutter is interlocked with the access doors. A 'panic button' is also provided, though in practice it is unlikely it could be pressed before the damage was done.

### **6.2.9 The Camera**

LDSS-2 uses a similar camera design to LDSS-1. It performs the inverse function to the collimator so many of its optical characteristics are very similar. Its optical axis must coincide with that of the instrument and it must be focussed onto the detector surface. The first of these can be performed as part of the instrument alignment procedure but the second may need to be adjusted while observing. This is because the instrument optics are not completely achromatic and different focus positions are used to optimise for different wavelengths.

The camera has 9 lenses with 10 glass-air surfaces, so as with the collimator anti-reflection coatings are essential. Pupil imaging is used to locate the camera stop 60mm in front of its first element. Together with the collimator this gives a collimated space that is a little over 110mm high, which is sufficient to accommodate the filter wheel, the grism wheel and the shutter.

## 6.3 Mechanical Design

### 6.3.1 Introduction

Although the optical elements are the 'active' components of the spectrograph, they must be supported by a mechanical structure if they are to function as intended. This structure must satisfy three criteria:

- it must be strong enough to support its own weight and that of the optics
- it must be rigid enough to prevent the optics from moving as the telescope is rotated about the sky
- it must be manufactured accurately enough to locate the optics in their required positions (if necessary after manual alignment)

The main load bearing component is the outer case, which was manufactured from 6mm mild steel by an external contractor. It has a flange at one end with which to bolt the instrument to the A&G box and an adaptor ring at the other to which a detector can be fitted. It can be split at two points along its length to give access to its internal components.

The internal components are mostly made of aluminium. They are supported either by the outer case or by one of two aluminium 'D-plates'. One of the D-plates is located between the upper and middle sections and supports the filter wheel. The other lies between the middle and lower sections and supports the grism wheel and the shutter.

### 6.3.2 The Aperture Wheel

The aperture wheel has 8 positions, allowing up to 7 aperture masks to be mounted at any one time. This figure is a compromise between observing efficiency and the amount of physical space available for the mechanism. A wheel was used rather than a slide in order to utilise the space as efficiently as possible. Nevertheless, it was necessary for the instrument case to be

extended on one side in order to accommodate the wheel.

The wheel is driven by a stepper motor and can be operated by remote control. The motor is linked to the wheel by a gearbox and a synchronous belt, which increase the resolution and the available torque, but reduce the speed and introduce backlash. It is possible to exercise some control over the backlash by adjusting the belt tension, but even under the best circumstances it corresponds to about 1mm at the wheel perimeter. This is well outside the required positional accuracy so an additional mechanism is needed to perform the final alignment.

The method chosen was to fix 8 'V-blocks', illustrated in figure 6.3, around the perimeter of the wheel, one at each positions where the wheel is to stop. A clamp is then lowered into the block to hold it in place. The clamp head is cylindrical and can rotate, so finds the centre of of the block with a high level of accuracy and repeatability.

Once the V-blocks were accurately positioned, dowels were inserted to prevent further movement. The clamp is held in place by a slide which allows it to move vertically but not horizontally. At first a ball slide was used, but it was unable to withstand the lateral forces caused by the wheel. The ball bearings were deformed and this increased the friction and reduced the accuracy of the slide. The ball slide was therefore replaced with a roller slide, which has a larger contact area so can hold the clamp with more force.

The clamp is spring-loaded and raised pneumatically by a piston. Some care is needed when adjusting the spring tension as it must be high enough to hold the wheel securely, but not so high that the air pressure cannot lift the clamp. The telescope air pressure is nominally 100psi but the instrument is specified to function down to 80psi. In view of this and allowing for wear and tear, the clamp should be set for a pressure of at most 70psi. A needle valve is used to control the release of air as the clamp is lowered, in order to reduce noise and vibration.

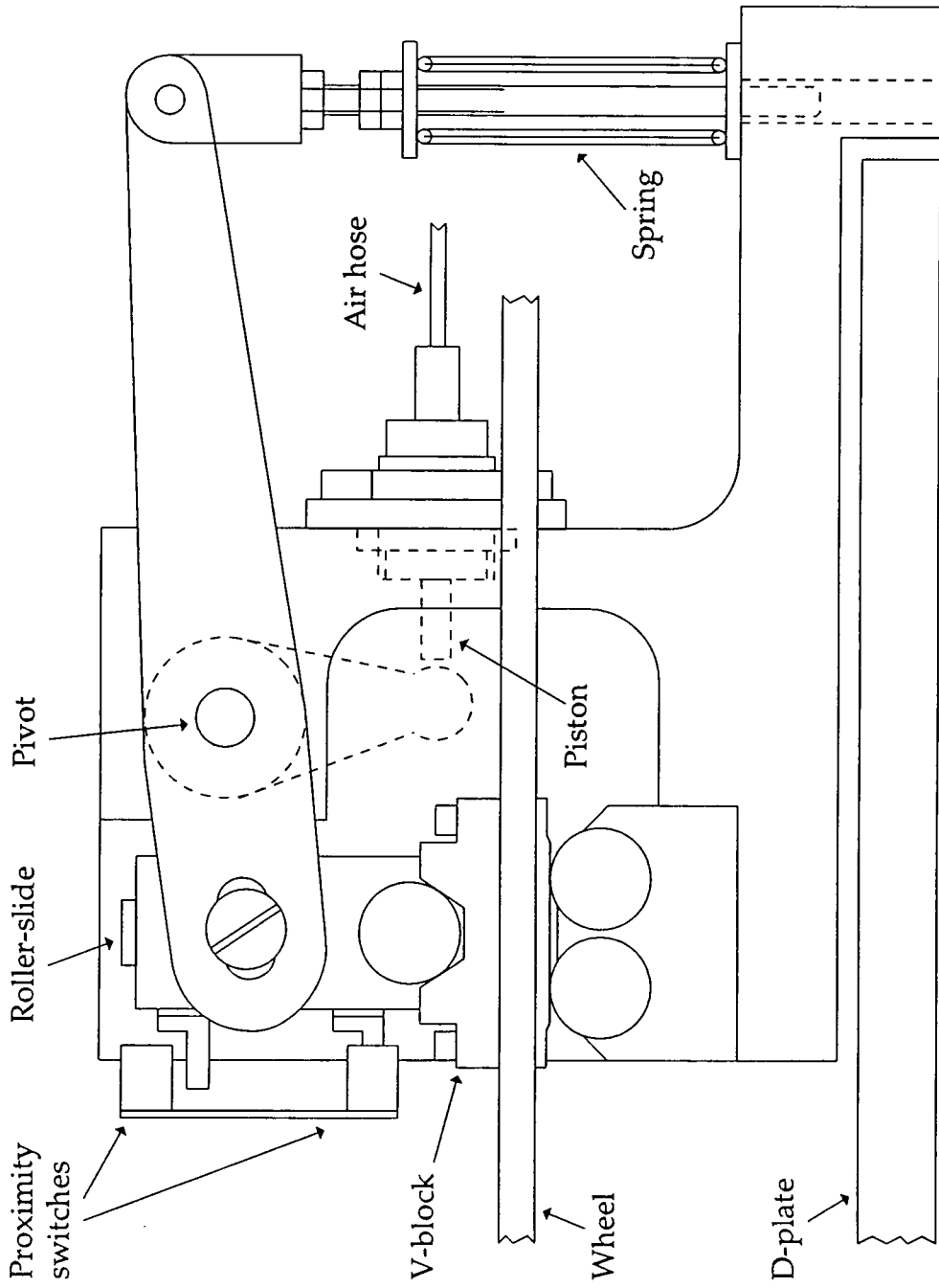


Figure 6.3: The LDSS-2 aperture wheel clamp (radial view)

Two proximity switches are used to sense the position of the clamp and a rotary encoder to read the position of the wheel. The encoder is linked directly to the wheel axle via a flexible coupler, in order to avoid backlash.

The wheel must allow the mask cells to be changed quickly but with a high level of accuracy. The arrangement used is illustrated in figure 6.4. A mask cell has three degrees of freedom in the horizontal plane (translation in  $x$  and  $y$  and rotation in the  $x$ - $y$  plane). Three notches are therefore cut in its perimeter and each notch has a corresponding adjustment screw on the wheel. Each screw tip touches a flat edge of one of the notches and the mask cell is in position when all three screws are touching. Four latches are then used to clamp the cell firmly against the wheel.

Within the cell, the mask position is defined by two dowels. One is inserted into a circular hole in the mask and defines two degrees of freedom. The other is held against one of the flat edges of a notch and defines the third. An annular ring is screwed down on top of the mask to hold it in place.

### **6.3.3 The Collimator Mount**

The collimator is not moved while observing, but it does need to be adjustable during the optical alignment procedure. It is supported from above, and five degrees of freedom must be accurately defined (translation in  $x$ ,  $y$  and  $z$ , and rotation in the  $x$ - $z$  and  $y$ - $z$  planes).

The position in the  $x$ - $y$  plane is the least critical and is adjusted by moving a plate which is bolted to the instrument structure. The collimator is held against the plate by three further bolts. Between the collimator and the plate are three kinematic seats which allow the collimator to be removed and replaced with good repeatability. The pins that make contact with the seats are threaded so their heights are adjustable. Between them they define the tilt and the  $z$ -translation. Each pin has a grub screw that can be tightened to hold it in place once its height has been set.

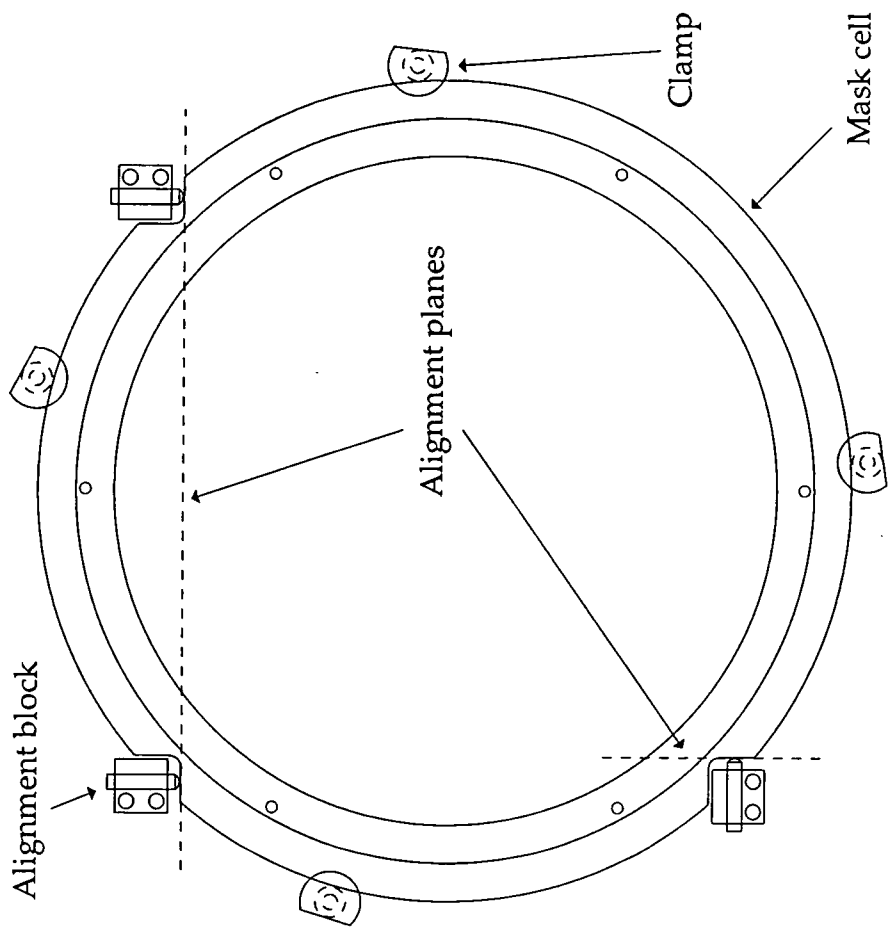


Figure 6.4: An LDSS-2 aperture mask cell

#### 6.3.4 The Filter Wheel

The filters do not need to be positioned to a high level of accuracy, but it is nevertheless desirable for them to use the same type of mechanism as the aperture masks. This is because sharing the design results in a considerable saving in development effort.

The main differences between the two are the wheel diameter and the type of mounting cell used. Filters are considerably smaller than aperture masks so the wheel is smaller too. This allows it to fit entirely within the main cylinder of the instrument body. The aperture mask mounting cells are designed for high accuracy and frequent mask changes and as a consequence are relatively elaborate. Neither of these requirements apply to the filters so it is sufficient to screw the cells directly to the wheel.

#### 6.3.5 The Grism Wheel

The grism wheel also uses the same type of mechanism as the aperture wheel, though in this case there are 6 V-blocks instead of 8. The wheel itself is the same size as the filter wheel and fits entirely within the instrument body.

Three of the wheel positions hold grism cells. The grisms are much heavier than the other wheel-mounted components (the largest has a mass of 718g). For this reason they are distributed symmetrically about the wheel and the cells containing the smaller grisms include counterweights. It is possible to move the wheel when it is out of balance, but this is not recommended as it places an unnecessary strain on the motor. For this reason the grism wheel should be operated with either three grisms in place or none at all.

The cells must hold the grisms lightly but firmly. Applying too much pressure would introduce stresses into the glass which would distort the dispersed image. Eight supports are used: four above the grism and four below. The upper supports are rigid, ensuring that the upper face of the

grism is perpendicular to the optical axis. The lower supports are held in place by springs, which are adjusted to apply enough force to support the weight of the grism plus a 50% safety margin. Displacement and rotation in the x-y plane are controlled by six nylon screws. Two hold the front and back faces of the grism and four the side faces.

### **6.3.6 The Camera Mount**

The camera is held in position by three kinematic seats. It is supported from below and secured using three bolts. Both the tilt and the focus can be changed during the alignment procedure by adjusting the kinematic seat pins, but the focus can also be changed while observing by moving the whole supporting assembly up and down.

The support is held in place by two ball slides which limit its motion to the z-axis only. A stepper motor drives a lead screw which raises the focus support via a lever. Countering the force of the lever are four springs which pull the support downwards.

Together, the lead screw and the lever give the mechanism a large mechanical advantage, so a relatively small motor can be used. They also improve the resolution to a little under  $1\mu\text{m}$ , though backlash reduces the accuracy to about  $25\mu\text{m}$ . To counter the backlash, a linear encoder measures the position of the support directly and is used to provide feedback to the control system.

### **6.3.7 The Access Ports**

LDSS-2 has two access doors and seven access hatches. The doors are located opposite each other in the upper section of the instrument and are used for changing aperture masks, filters and grisms. It must be possible to open them during the course of an observing run, but for safety reasons they are interlocked with both the shutter and the wheels (see chapter 7). It is not necessary to automate them completely, so manual latches are used but with

a remote-controlled locking system.

Each door has two latches, one of which is illustrated in figure 6.5. When shut, the edge of the door frame is held between the door and the latch bolt. The door is opened by pulling the latch handle, which retracts the bolt. It is locked by inserting a locking pin into a hole drilled through the bolt. When the pin is in place, the bolt cannot be moved. The pins are driven by a piston which is in turn controlled by a solenoid valve.

The locking pins are spring-loaded and default to the locked state, so an alternative method is provided for when either the air supply or the control system are unavailable. Each door has a small hole, mid-way between the latches, with a cover that can be unscrewed. Inserting a screwdriver (or similar tool) into the hole causes the pins to be retracted. This is only intended for use during assembly and maintenance.

The hatches are located in the middle and lower sections of the instrument, and are used only for assembly and maintenance. There is no requirement to open them while observing so they are secured with screws. Both the doors and the hatches incorporate gaskets in order to prevent light leakage.

### **6.3.8 The Handling Frame**

The main function of the handling frame is to assist in mounting the instrument onto the telescope. When fully assembled, LDSS-2 weighs approximately 750Kg. It must be lifted so that it meets the lower flange of the A&G box. The observing floor can be raised to supply most of the height, but this cannot be used for the last few centimetres as any overshoot would risk damaging both the instrument and the telescope. The handling frame therefore incorporates a hydraulic scissor jack which lifts the instrument from below. The jack is pumped manually so can be controlled very accurately.

Another use of the handling frame is to 'split' the instrument, either between

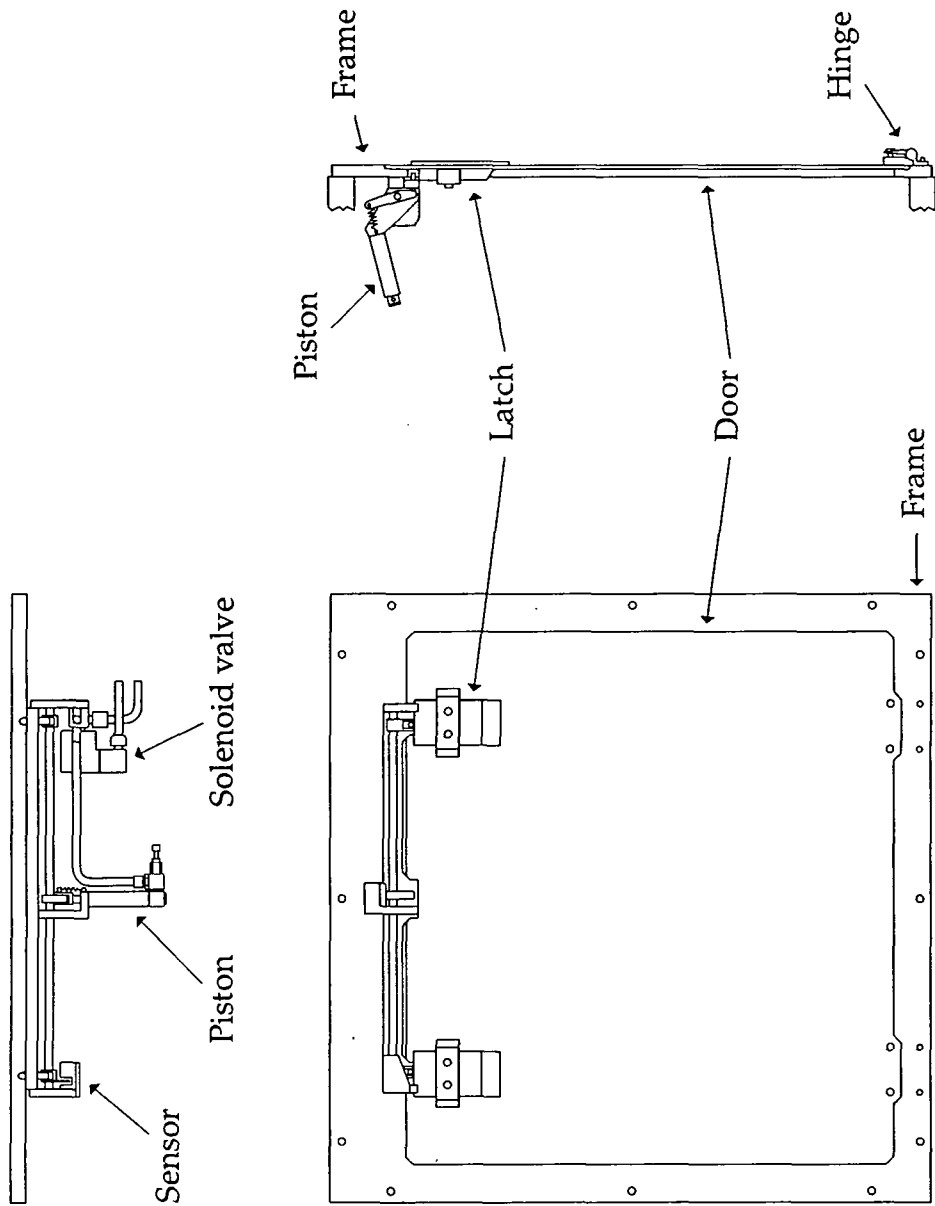


Figure 6.5: An LDSS-2 door latch mechanism

its upper and middle sections or its middle and lower sections. This is done by lifting the instrument with the jack, holding the top section in place, unbolting the appropriate flanges and lowering the jack. The reverse process is used to reassemble the instrument.

The frame has wheels and can be lifted using a crane. It is used to store the instrument and has sufficient ground clearance to support it with a CCD camera in place. This is useful for aligning and testing the instrument.

# Chapter 7: The LDSS-2 Control System

## 7.1 Introduction

The main reason for building a multi-object as opposed to a single-object spectrograph is to make more efficient use of telescope time. It is therefore logical to address other areas in which efficiency gains can be made. One such area is the provision of an effective control system.

## 7.2 Objectives

The control system is both a physical and a logical interface between the user and the instrument:

- a physical interface in that it must send and receive the correct electrical signal levels to drive the various actuators and sensors within the instrument
- a logical interface in that it must hide the low-level details of the instrument from the user by abstracting them into a higher-level model

The electrical functions are relatively straightforward to implement, though there are a number of issues that need careful attention if the instrument is to function reliably. These include:

- Electromagnetic compatibility, both within LDSS-2 and between LDSS-2 and its environment. The telescope dome is electrically very noisy, but while the instrument must be able to function there, it should avoid exacerbating the problem by adding excessive noise of its own.
- Heat dissipation. This should be minimised in order to avoid causing convection currents that would affect astronomical seeing. Particular care must be taken within the instrument housing, especially with components located near to the light path.

- Heat sinking and ventilation. The telescope is sited approximately 7000 feet above sea level where the reduced air pressure makes ventilation significantly less effective. Equipment must therefore be 'de-rated' relative to sea-level power specifications. We were advised by the RGO that a 25% de-rating was appropriate.
- Use of indicator lights. Although the instrument and detector are theoretically light-tight, in practice light levels in the dome should be kept to an absolute minimum (including the near infra-red). It would be inconvenient to dispense with indicators entirely, so it is normal practice to provide a switch that can enable or disable them as required.
- Use of optical or infra-red sensors. These can be used so long as they are fully enclosed to prevent light leakage. Alternatively it may be possible to arrange for them to be switched off during exposures. If not, a different type of sensor must be chosen.

The design of the user interface is a much more complex issue as the objectives are not at all well defined. It is however possible to identify a number of basic principles of good interface design:

- The user interface should be consistent. Although LDSS-2 itself is new, the telescope control system (taken as a whole) is not and LDSS-2 must be integrated into that system. In such situations it is usually better to conform to the existing standards even if they are imperfect (as all standards are).
- The user interface should function at the same level of abstraction as the user. Picking a level that is too low results in unnecessary extra work, while choosing too high a level reduces the flexibility of the instrument by making it difficult to perform tasks not anticipated by the designer.
- If necessary, different interfaces should be provided for different classes of user (for example, separate user and engineering modes).

- This is particularly relevant where some operations could endanger the safety of the instrument (or indeed, the safety of the operators).
- Common actions should be easy to perform, while dangerous actions should be very difficult to perform. The user interface should however avoid pre-judging what actions are allowed and what are not (as it is far better to keep users within an established user interface when doing something dangerous than to force them to go outside it).

## 7.3 System Overview

The WHT, like most modern telescopes, is operated from a control room that is adjacent to but separate from the dome. This is not just for the convenience of the astronomers: the smaller the number of heat-generating objects in the dome (including both computers and people) the better.

If heat were the only consideration then the ideal control system would itself be located entirely within the control room, but unfortunately there are several reasons why this would not be practical:

- The total cable length between the instrument and the control room is several tens of metres. The telescope is an electrically noisy environment and the longer the cable the greater the risk of interference. This is especially true of the SLVC transducer used to measure the focus, which is an analogue device and which the system must be able to read to a high level of accuracy.
- A long cable also makes it more difficult to drive the various actuators in the instrument and in particular the stepper motors. The greater the length, the greater the attenuation and degradation of the drive pulses. The cable would also act as an antenna, resulting in interference that could affect both the instrument and other devices on the telescope.
- LDSS-2 is a relatively simple instrument, yet it has well over 50 conductors that must be connected to the control unit. Routing this and all the other devices on the Cassegrain turntable through two



cable wraps would not be a trivial undertaking and could lead to serious problems with regard to reliability and maintenance.

A compromise is therefore made whereby the low-level functions are carried out by a 'local controller' located close to the instrument on the turntable, while the high-level functions are performed by a minicomputer located in the control room. The two are connected by the telescope 'utility network'.

The layout is illustrated in more detail in figure 7.1. The instrument contains a total of four stepper motors, six solenoids, three rotary encoders, one linear encoder and twelve slotted proximity switches. These are grouped together into six mechanisms:

- the aperture wheel
- the grism wheel
- the filter wheel
- the camera focus
- the shutter
- the access doors

The mechanisms are wired to a pair of connector panels, one for the upper half of the instrument and one for the lower half. These are linked to the local controller by a set of cables, together with an air line for the pneumatic system.

The local controller consists of a 4MS system (a 6809-based rack-mounted microcomputer), an SMDM (Stepper Motor Driver Module), and a power supply unit. It can be operated directly from a terminal in the control room, but it is more usually controlled by the system computer over the utility network. A small control handset allows the shutter and doors to be operated from within the dome.

The observer sits at a VaxStation, which acts as a graphics terminal to the system computer. From there it is possible to issue commands to LDSS-2,

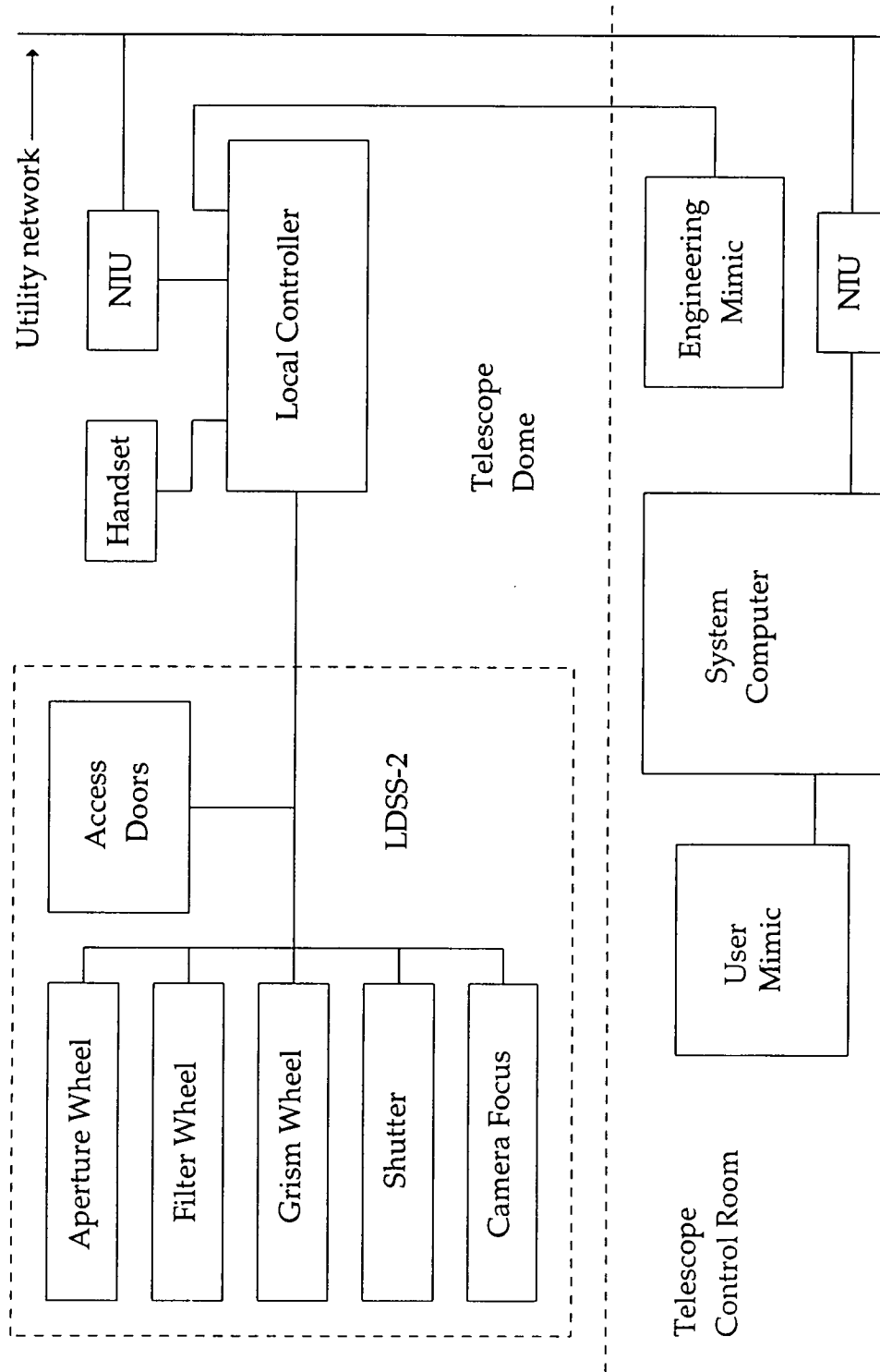


Figure 7.1: The LDSS-2 control system

together with most of the other telescope services. The status of each service can be monitored using a multi-page 'mimic' display which tracks the position of each mechanism in real time.

## **7.4 Mechanism Characteristics**

### **7.4.1 Introduction**

Before proceeding further, it is necessary to consider the characteristics of each mechanism from the perspective of the control system. This includes:

- the characteristics of the mechanism actuators and sensors
- the interactions between those components
- the behaviour required of the mechanism as a whole

### **7.4.2 The Aperture, Filter and Grism Wheels**

For the purposes of the control system, these three mechanisms are very nearly identical, the only difference being the number of valid positions in which each wheel can be clamped (eight for the aperture and filter wheels, six for the grism wheel).

Each wheel has two actuators and three sensors:

- a stepper motor
- a solenoid valve
- a rotary encoder
- two slotted proximity switches

The motor is driven by the Stepper Motor Driver Module (SMDM) in the local controller (see section 7.5). The SMDM allows both the maximum velocity and the acceleration of the wheel to be set, and can operate the motor in either full- or half-stepping mode. Half-steps were chosen because the higher resolution reduces the risk of the motor stalling.

The wheel resolution is 16000 steps per turn (including the effects of the

motor gearbox and the drive belt. Note that in this context, one “step” is actually a half-step). Experiments showed that under moderate load it could operate reliably at up to 1800 steps/s. However, for safety, a speed of 1200 steps/s was chosen, corresponding to approximately 14 seconds for one revolution of the wheel.

The acceleration parameter takes a value between 1 and 50, but is not calibrated in any specific units because the velocity profile is not a simple trapezoid. A setting of 50 results in the motor starting almost instantaneously, but if it is loaded it is likely to stall. Reducing the value to 5 gives acceptable performance, but a value of 1 was used for maximum reliability. (This increases the acceleration period to about a second, but that is still a small part of the total travel time.)

During development, it was found that the drive belt added a large amount of backlash to the system. This was corrected by adjusting the tension, but as a precaution it was decided that it would be prudent to rotate the wheel unidirectionally. (This effectively eliminates the effects of backlash so long as the wheel is balanced but will not work if it is badly out of balance.)

The rotary encoder provides feedback on the wheel position. It does not, however, form part of a closed-loop system, as the open-loop accuracy of the drive is good enough to bring the wheel within the capture range of the target v-block. The only time the wheel should fail to reach its destination is when there has been some form of catastrophic failure. It is therefore sufficient for the encoder to report any error in the position rather than try to correct it.

The encoder is an optical device, but there is no light leakage as it is fully enclosed. There are three outputs, A, B and M (Phase-A, Phase-B and Mark), all at TTL-compatible levels. The A and B outputs produce a quadrature pulse train as the wheel is rotated and with an appropriate decoder board it is possible to measure the magnitude and direction of any change in angular

position (see figure 7.2).

This type of encoder is known as an incremental encoder as it measures displacement rather than absolute position. It is not as convenient to use as an absolute encoder but it does have the advantages of lower cost, smaller size and lower heat dissipation. Furthermore, such an encoder can be used to measure absolute position so long as it starts from (or later passes) a known position. The M output is provided for this purpose and generates a pulse whenever the encoder passes its reference point. Once that happens, it is possible to track the absolute position until the next time the system is reset.

The encoder signals are processed by three special-purpose interface cards in the 4MS system, one for each wheel. Each card has a counter which increments or decrements for each transition of an A or B input according to the direction of rotation. The counter is automatically reset whenever an M pulse is detected, so the board can operate autonomously without processor intervention.

The encoder resolution is 2000 steps per turn. Tests with the aperture wheel showed that its repeatability and accuracy were both  $\pm 1$  step or better, well within the  $\pm 4$  step acceptance window allowed by the control software. (The clamp cannot be lowered unless it is either fully inside or fully outside a v-block, so a  $\pm 4$  step window is sufficient to determine whether the wheel is in a valid position.)

The solenoid valve operates at 24V and is driven by the SMDM. It has an integral LED indicator, but it does not cause any light leakage as the wheels are never moved during exposures. The valve opens and closes almost instantaneously but the clamp does not. The SMDM was therefore programmed to wait 100ms between opening the valve and starting the motor and between closing the valve and de-energising the motor.

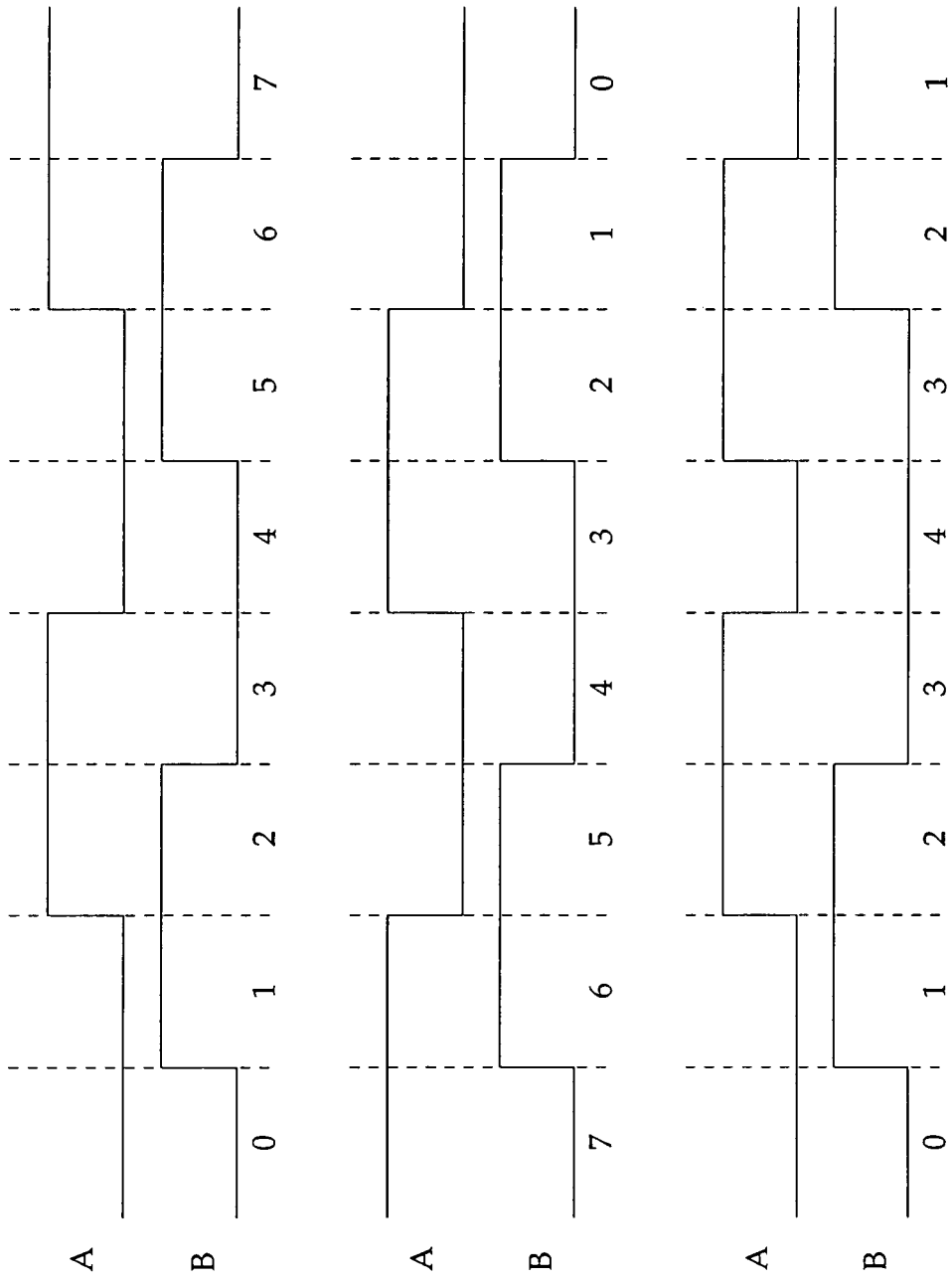


Figure 7.2: The output signals from the rotary incremental encoder

The position of the clamp is sensed by two inductive slotted proximity switches: one to detect when the clamp is up and one to detect when it is down. Inductive rather than optical devices were used to avoid light-leakage. The switches have active-low open-collector outputs which are connected directly to the SMDM.

To move the wheel, the following sequence of operations is followed:

1. Energise the stepper motor. This does not move the wheel, but does stop it free-wheeling under gravity if it is out of balance.
2. Energise the solenoid valve. Delay 100ms to allow the clamp to open.
3. At this stage the clamp proximity switches should be checked to ensure that the wheel has indeed been unclamped. Unfortunately, there is a problem with the design of the SMDM that prevents this test being performed (see below).
4. Rotate the motor through the appropriate number of steps. In the case of the grism wheel this must be calculated in such a way that no cumulative error arises from the non-integer number of steps per position.
5. De-energise the solenoid valve. Delay 100ms to allow the clamp to close.
6. De-energise the stepper motor.
7. Check the clamp proximity switches to ensure that the wheel has been properly clamped, and the rotary encoder to ensure that it is within one of the v-blocks.

The problem with the SMDM occurs when a stepper motor is energised but held stationary for more than about a second. It manifests itself in a number of ways, including SMDM processor crashes and corruption of its on-board non-volatile RAM. The symptoms appear intermittently but with sufficient regularity that they would make the instrument unusable.

A considerable amount of effort was expended both by us and by the RGO

to attempt to diagnose and if possible correct this failure mode. The most credible (though incomplete) explanation was that the motor, being an inductive load, would draw more current when energised by a DC voltage (when it was stationary) than by an AC voltage (when it was moving). If continued for any length of time then this might (somehow) cause more noise to be coupled from the driver circuits to the SMDM processor board, or alternatively make the processor more susceptible to existing noise by affecting its power supply.

Unfortunately there was insufficient time to test this theory and it is unlikely the RGO would have had sufficient resources to change the SMDM design (and upgrade its existing units) even if the fault were identified. It was therefore necessary to accept the problem and design around it.

The most likely situation in which the clamp would fail is if the air pressure were too low. An air pressure sensor was therefore added to the instrument to detect this condition. If the pressure is low then the wheels are interlocked and any command to move them will fail.

The only other precaution that can be taken is to ensure that as far as possible each wheel is balanced. This is desirable anyway as it reduces the load on the motor, but it also limits the extent to which the wheel will rotate under gravity should it be left unclamped between v-blocks. The grism wheel requires particular attention in this respect as the grisms are heavy and could easily be knocked out of alignment.

In addition to the air pressure, the wheels are interlocked with the access doors. This is a safety measure as the stepper motors would probably be powerful enough to cause serious injury if activated at the wrong moment. Both of these interlocks can be overridden should the need arise.

Two initialisation sequences are provided. The default command is quicker, but will only work if the wheel is already clamped in a v-block. It has just

one step:

1. Rotate the wheel through 360° using the normal movement sequence.  
This ensures that the encoder passes its reference point, initialising the relevant encoder board.

The full initialisation command works from any starting point but should only be used when the telescope is parked at the zenith. It adds the following two steps:

2. Read the encoder to determine the position of the wheel.
3. Rotate the wheel through the appropriate number of steps to bring it to the v-block at position zero, again using the normal movement sequence.

The reason for only using this command at the zenith is that between steps (1) and (3) the motor is de-energised. If the telescope were at an angle then an out of balance wheel might rotate under gravity, causing an error in the stepcount for stage (3). There is also the risk that an error in the encoder reading could leave the wheel in an unclamped position even if it were clamped to begin with. The full initialisation command is therefore only normally used when the wheel is known to be unclamped.

Finally, a command is provided to clamp or unclamp the wheel and leave it in that state. The unclamp instruction should only be used when the telescope is parked, but is useful when components are being mounted as it allows the wheel to be rotated by hand. The clamp instruction is provided for completeness but it is normally better to use the full initialisation command instead.

### **7.4.3 The Camera Focus**

The focus mechanism has one actuator and one sensor:

- a stepper motor
- a linear encoder

The stepper motor drives the focus via a lead screw. The range of travel is approximately  $850\mu\text{m}$ , but a safety margin is needed at both ends to allow for calibration errors and only the central  $768\mu\text{m}$  is used. No clamp is required, as friction is sufficient to prevent the mechanism moving when idle.

The motor is driven by the fourth channel of the SMDM but at a lower speed than the wheels (600 steps/s). It has a resolution of  $0.83\mu\text{m}$  per step, but its open-loop accuracy (and repeatability) are closer to  $\pm 25\mu\text{m}$ . This is outside the specification of  $\pm 8\mu\text{m}$  so closed-loop operation is necessary.

Feedback is provided by a Super Linear Variable Capacitor (SLVC), which is the capacitive equivalent of the better known LVDT. It is used with a signal conditioner unit, which generates the necessary drive waveforms for the sensor and converts the result into a simple DC signal in the range 0 to 10V. The range of travel is 5mm so the sensitivity is nominally 2V/mm.

The signal is fed into a 12-bit analogue to digital converter (ADC) in the 4MS rack. This has 4096 possible states and a range of 0 to 10V, so its resolution is nominally 2.5mV, or  $1.25\mu\text{m}$ . This was tested experimentally and the results are shown in figure 7.3.

As can be seen, the encoder is indeed highly linear. A least squares fit shows the resolution to be  $1.22\mu\text{m}$ , with an RMS deviation of  $5\mu\text{m}$  over a range of  $4900\mu\text{m}$ . Most of the deviation can be attributed to experimental error and electrical noise.

The SLVC noise level was a cause for concern because, unlike the linearity, it affected the repeatability of the mechanism as well as its accuracy. If the mechanism is to be positioned within  $\pm 4\mu\text{m}$  (see below) then the feedback needs to be accurate to (at worst) about  $\pm 2\mu\text{m}$  (4mV). All cables were screened and the encoder signals were kept separate from the high current stepper motor and solenoid signals. Nevertheless, the results were barely

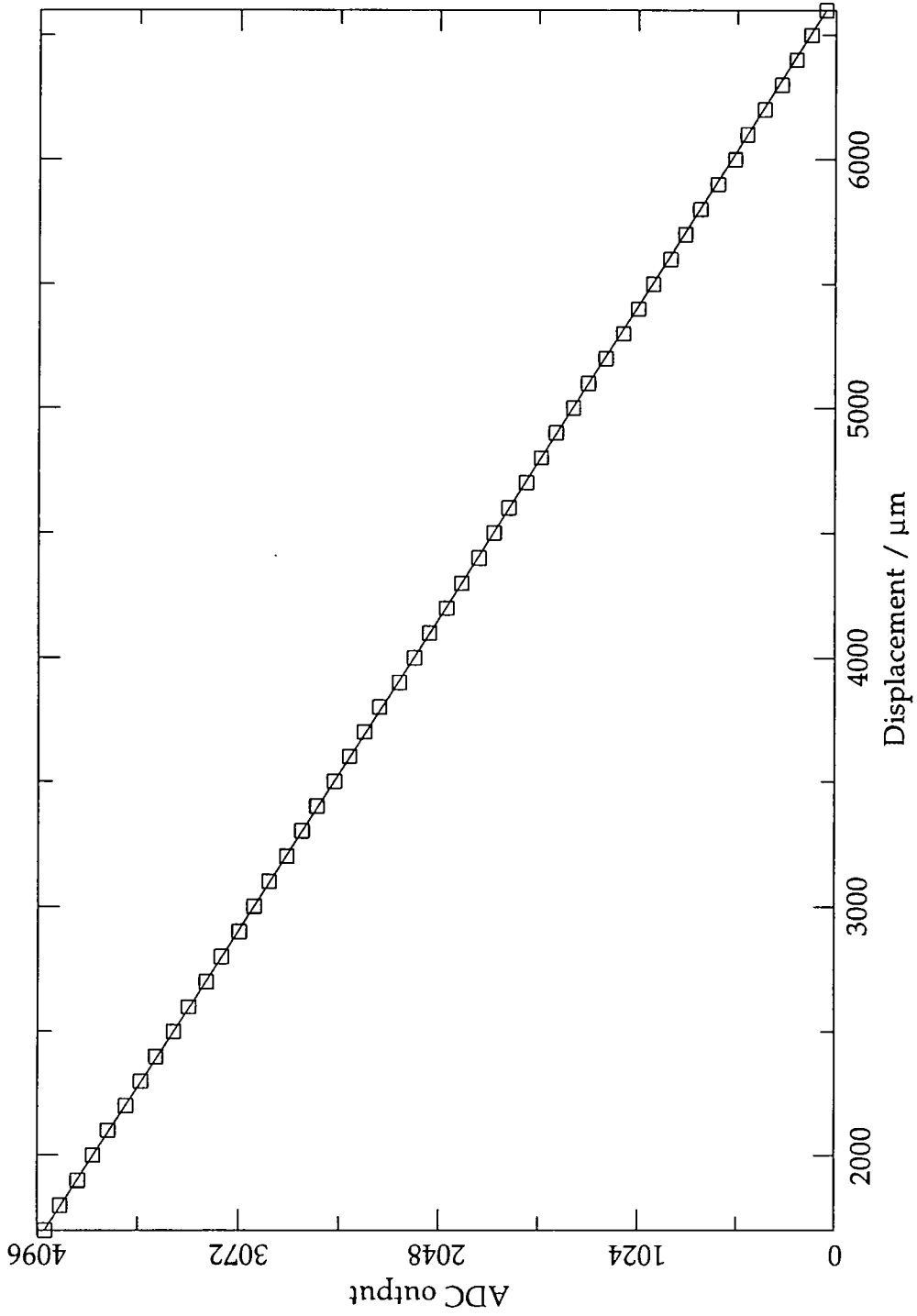


Figure 7.3: The SLVC/ADC signal transfer function

acceptable, so it was necessary to post-process the signal to improve its accuracy further.

The signal conditioner unit minimises noise by restricting the bandwidth of its amplifier stages. The local controller can do the same by applying a digital filter to the signal. A median filter was chosen, to give maximum immunity to impulse noise. A three-sample filter was found to be sufficient to reduce the noise to an acceptable level.

The sequence of operations to move the focus is relatively simple, as it is not necessary to apply feedback in real time. It consists of five steps:

1. Set the iteration count to zero.
2. Measure the current encoder position and compare it with the target position. If it is within  $\pm 4\mu\text{m}$  then stop.
3. Estimate the number of motor steps between the current position and the target position and move that number of steps.
4. Increment the iteration count. If it is less than 10, loop back to step (2).
5. Measure the current encoder position and compare it with the target position. If it is within  $\pm 8\mu\text{m}$  then the command succeeds, otherwise it fails.

As a precaution the software checks that the encoder reading is non-zero before entering the feedback loop. This is because a value of zero indicates that the encoder is not connected and would cause the focus to be driven into its end stop if the command were allowed to proceed.

The reason for using two different tolerances is that although an accuracy of  $\pm 8\mu\text{m}$  is acceptable, it makes sense to improve the result further if possible. The  $\pm 4\mu\text{m}$  window is typically achieved within three or four iterations.

#### 7.4.4 The Shutter

The shutter mechanism has one actuator and two sensors:

- a solenoid-operated shutter

- two slotted proximity switches

The solenoid operates at 24V and is driven by the Shutter Control Card (SCC) in the 4MS rack. The shutter is opened by energising the solenoid and closed by de-energising it.

Because the solenoid is very close to the light path, its heat dissipation must be minimised. Shutters are available that will stay open without power, but they do not fail safe in the way that a spring-loaded shutter does (an important consideration when the instrument was likely to have been used with an IPCS).

The solenoid draws about 1A at 24V, a total of 24W. It would be undesirable to reduce the voltage when opening the shutter for two reasons:

- It would increase the risk of the shutter jamming by reducing the amount of force available to open it. This has been a problem with previous instruments and can waste a lot of observing time.
- It would increase the amount of time taken by the shutter to open. This would reduce the accuracy of the exposure time setting.

However, whereas the full 24V is needed to open the shutter, it will stay open at just 12V. The SCC takes advantage of this by switching in a 22R heatsinked series resistor after 100ms, reducing the solenoid power dissipation to just 6W. (A further 6W is dissipated in the local controller but it does little harm there compared to inside the instrument.)

Inductive proximity switches are used to avoid light leakage. One switch detects whether the shutter is fully open, the other whether it is fully closed. They have active-low open-collector outputs and like the shutter solenoid are connected to the SCC.

Unlike the other mechanisms, commands to the shutter are not routed via the utility network or the 4MS system. This is because some types of observation (such as spectrophotometry) require accurate control of the

exposure time. The 4MS is too slow and too unpredictable, so a trigger cable is connected directly from the CCD or IPCS controller to the SCC. The cable also carries return signals from the proximity switches so that the controller knows the state of the shutter.

The shutter is interlocked with the access doors of both LDSS-2 and the A&G box and will not open unless they are all closed and locked. This feature was most important when the instrument was to have been used with an IPCS detector as excess light could permanently damage the image tube. CCDs cannot be damaged in this way but it is still important to close the doors to avoid contaminating the data.

These interlocks are implemented in hardware for speed and reliability. If necessary they can be partially overridden and the shutter opened manually using the control handset.

#### **7.4.5 The Access Doors**

There are two access doors, one on each side of the instrument. They are opened and closed manually but locked pneumatically. The control system treats them as a single mechanism with two actuators and four sensors:

- two solenoid valves
- four slotted proximity switches

There is one solenoid valve per door, but they are wired together in parallel so it is not possible to unlock the doors separately. The solenoids operate at 24V and are driven by the Shutter Control Card (SCC) in the 4MS rack. The doors are unlocked by energising the solenoids and locked by de-energising them.

Inductive proximity switches are used in order to avoid light leakage. Each door has two switches, one to detect whether it is closed and one to detect whether it is locked. (Note that the lock can engage even when the door is open, so both switches must be checked.) The switches have active-low

open-collector outputs.

The command to unlock the doors has two steps:

1. Energise the solenoid.
2. Wait for the switches to show that both doors are unlocked. The command fails if this does not occur within 8.4s.

The lock command is similar, and has three steps:

1. Check the switches. If either door is open then the command fails.
2. De-energise the solenoid.
3. Wait for the switches to show that both doors are closed and locked. The command fails if this does not occur within 8.4s.

(The choice of timeout period may appear somewhat arbitrary. This is because the software that implements it takes the programmer's estimate of the time required (200ms), doubles it (400ms), and adds eight seconds for safety (a total of 8.4s).)

As discussed above, the doors are interlocked with the shutter and cannot normally be opened unless the shutter is closed. If necessary this interlock can be overridden and the doors opened manually using the control handset.

## 7.5 Local Controller Hardware

To maintain compatibility with other telescope equipment (in terms of both software and spare parts), the RGO strongly recommended that we use a 6809-based microcomputer known as a '4MS' system. It consists of a backplane mounted in a 19-inch 3U DIN-41494 subrack into which up to twelve eurocard-sized circuit boards can be inserted.

A local controller 4MS would normally be built around five standard cards:

- a processor card, which includes a FORTH interpreter ROM and 8K of RAM

- a memory expansion card, which adds 32K of RAM
- a Bus Buffer Interface (BBI) card, which in our application adds reset and interrupt buttons and a watchdog timer to the system
- an ACM3 card, which provides three asynchronous serial interfaces, each of which can be configured as either an RS-232 or an RS-422 port
- a GPIB card which, provides an interface to the disc drive unit used for software development.

Once the software has been written and tested it is copied into a set of EPROM chips. They then replace up to four of the five RAM chips on the processor and memory expansion cards and allow the local controller to operate without a disc drive.

The remaining backplane slots are used to meet the specific requirements of individual instruments. The LDSS-2 controller contains the following:

- three incremental encoder cards
- an Analogue to Digital Converter (ADC) card
- a Parallel Interface Adaptor (PIA) card
- a (custom-designed) Shutter Control Card (SCC)

Also located in the rack is the Stepper Motor Driver Module (SMDM) which was designed and supplied by the RGO. It interfaces to the 4MS via an RS-422 port and is able to drive up to four stepper motors, eight solenoids and sixteen sensors. (Note however that the stepper motors are multiplexed, so only one can be energised at any given time.) Each SMDM has its own microprocessor and FORTH interpreter, though the unit is normally used as an embedded component.

The shutter control card and the SMDM both require a +24V supply, which is taken from a shared PSU on the Cassegrain turntable. All other voltages are derived from the 240V AC mains. The local controller includes a three-rail switch-mode PSU (supplying +5V at 8A, +12V and -12V to the 4MS) and a smaller two-rail linear PSU (supplying +15V and -15V to the SLVC signal

conditioner). These voltages are monitored by a set of LEDs on the front panel, which can be switched off when observing.

Two problems were encountered with the PSU. One was that, like many switch mode supplies, it does not operate correctly under very light loads. To give proper regulation, at least 25% of the rated current must be taken from both the +5V and the +12V lines (2A and 0.9A respectively). The first condition was met by the 4MS system but the second was not and the only practical solution at the time was to connect a heatsinked 10R resistor across the +12V and 0V lines (at the expense of generating 14W of heat).

The second problem was that the high current drawn by the 4MS system (typically about 4A) was causing a substantial voltage drop in the power supply cable (several hundred millivolts). The supply voltage tolerance for a TTL logic chip is  $\pm 0.25V$ , so the maximum permissible resistance is less than  $0.1\Omega$ .

To solve this, the 4MS rack was rewired using multiple connector pins and multiple cables in parallel to increase their current capacity. Joints that had previously been crimped were soldered, and together these measures reduced the voltage drop to about 100mV. As a final precaution the nominal supply voltage was increased to 5.10V to compensate (though it would have been better to use a PSU with a remote sense line if there had been time).

## 7.6 Network Protocol

The telescope utility network consists of a 'thick Ethernet' cable together with a number of Network Interface Units (NIUs). Its topology is illustrated in figure 7.4.

The purpose of an NIU is to allow up to four other devices to be connected to the network, using standard RS-232 interface ports. At the time the network was designed this was (and may still be) simpler and cheaper than

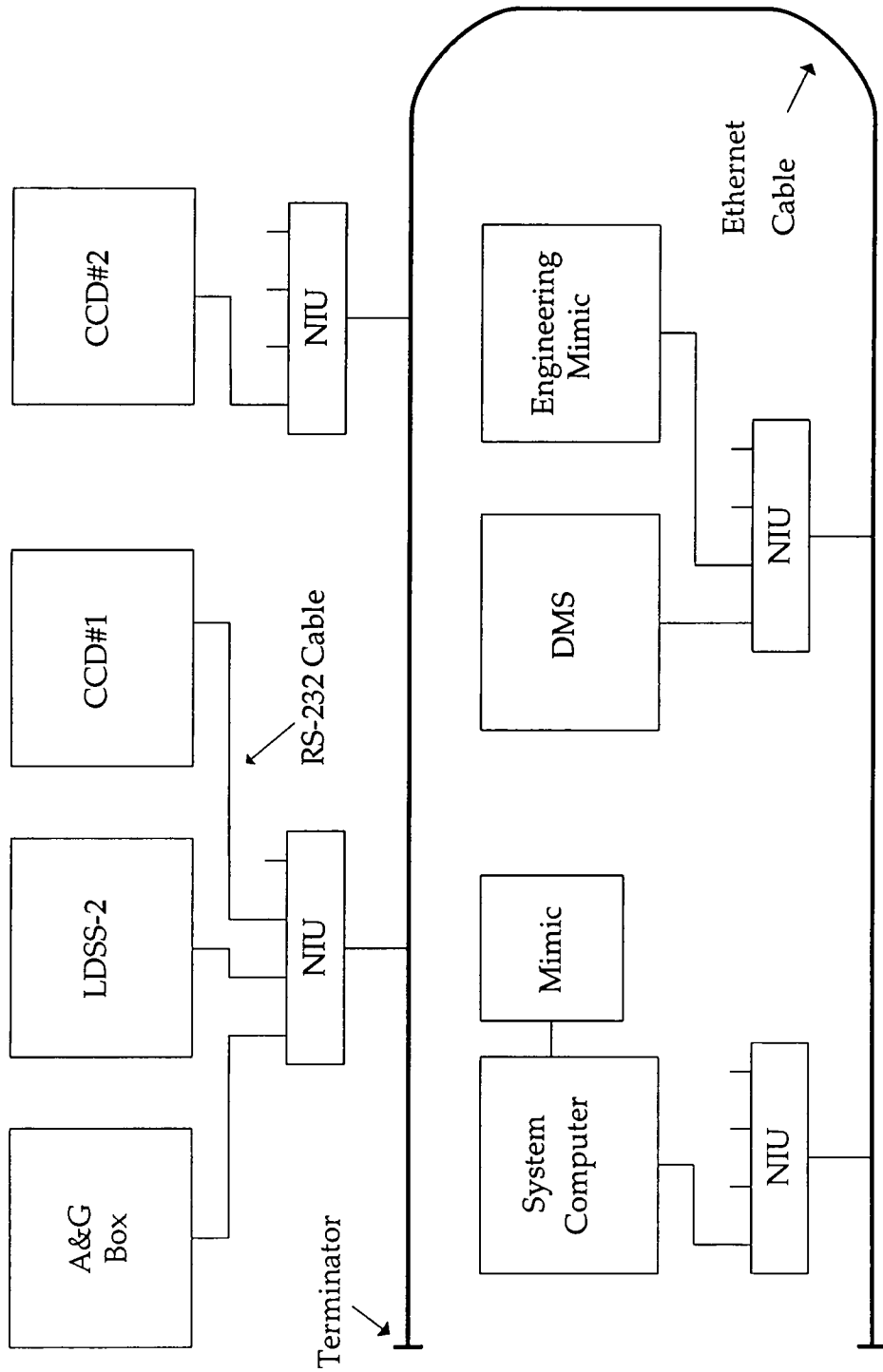


Figure 7.4: The WHT Utility Network

connecting devices directly to the cable. All network nodes use this method, including the system computer.

The NIU is responsible for packet routing and error checking, but it does not guarantee that any given packet will arrive at its destination: that function is carried out by software at each end of the link. When a data packet does arrive an acknowledgement packet is returned to the sender. If the sender does not receive an acknowledgement within a fixed timeout period then it will resend the data packet (several times if necessary). Each packet has a sequence number so that duplicates can be discarded.

The format of the packet body is standardised, but with scope for variation to suit individual instruments (Vlot and Johnson, 1986 and Johnson, 1987). Two types of data packet are allowed: command packets and status response packets. Each may contain one or more commands or status responses, but it is not possible to mix both in the same packet.

A command consists of a three letter mnemonic which specifies the mechanism to be used and a three digit code which specifies the operation to be performed. In some cases the code is followed by a parameter list enclosed within parentheses. For example, the command to move the aperture wheel to position 5 is 'APW101(5)'.

LDSS-2 supports a total of 12 mnemonics:

- INS Instrument status (status of watchdog timer and air pressure)
- MON Monitor mode (controls flow of real-time status packets)
- HMS Health monitor Status (SMDM serial link status)
- ALL All mechanisms (for full status report or for all stop)
- RES Reset (software reset of local controller)
- NET Network (Ethernet interface software)
- APW Aperture wheel
- FLW Filter wheel
- GRW Grism wheel

FOC Focus  
DOR Access doors  
SCC Shutter control card

The first six are common to most instruments using the network protocol and control general functions of the local controller. The remainder are specific to LDSS-2 and refer to individual mechanisms. Operation codes begin with a '1' for actions and a '2' for status requests. There are eight operation codes:

100 Stop  
101 Move to location  
102 Initialise (from clamped)  
181 Reprogram SMDM  
182 Initialise (from any position)  
183 Clamp or unclamp wheel  
200 Request immediate status  
201 Request delayed status

Of these, codes 100, 101, 102, 200 and 201 are common to all instruments and 181 is recognised by most controllers that incorporate SMDMs. The remainder are specific to LDSS-2.

Not all mnemonic/code combinations are valid. For example, INS, HMS and SCC exist only to return status information, so do not respond to 101 commands. Full instructions, including the use of parameters and the semantics of each command type, are given in the instrument documentation.

The format of a status response is identical to that of a command except that the operation code begins with an '8':

800 Response to immediate status request (200 command)  
801 Response to delayed status request (201 command)  
802 Monitor mode report of unexpected movement

803 Monitor mode report at start of scheduled movement

804 Monitor mode report during scheduled movement

The parameter list details the state of the mechanism actuators and sensors and flags any error that may have occurred as a result of a previous command. Full details of how to interpret the status values are given in the instrument documentation.

## 7.7 Local Controller Software

The software for the LDSS-2 local controller is divided into five modules:

- the kernel tasks
- the status maintain tasks
- the mechanism job tasks
- the SMDM support routines
- the Ethernet support routines

All are adapted to a greater or lesser extent from existing software used by the A&G box local controller. The status maintain and mechanism job tasks are mostly new code, whereas the changes to the kernel and the SMDM support routines are largely superficial. The Ethernet routines are completely unmodified and are common to any 4MS-based local controller that uses the utility network.

As their names suggest, the SMDM and Ethernet support modules are implemented as subroutines, whereas the kernel, status maintain and mechanism job tasks are autonomous processes. The use of separate tasks ensures that the kernel can respond to a status request even if there is another operation in progress. (In instruments with more than one SMDM it also improves performance by allowing commands to execute in parallel.)

Cooperative multitasking is used, meaning that task switches only occur at points explicitly allowed by the programmer. All tasks have the same

priority and are executed in strict round-robin order, but the amount of CPU time used depends on how often each task returns control to the scheduler. Some care is therefore needed to ensure that the time available is shared equitably. The advantage of this approach is that the tasks are very tightly synchronised to each other, greatly simplifying inter-task communication.

The interactions between the modules are summarised in figure 7.5. When a packet is sent to the instrument over the network it is first processed by the Ethernet module, which verifies its integrity, acknowledges it and passes it to the command interpreter.

The command interpreter is part of the kernel. It checks each command for syntax errors and identifies the mnemonic and the operation code. Status requests and stop commands are executed immediately. Other commands are stored in the 'present-status table' for later execution by a 'job task'.

The present-status table is a global data structure that is used to pass information between the kernel, status maintain and job tasks. It has one record for each mechanism mnemonic (except ALL, RES and NET) and holds:

- the current command being (or waiting to be) executed
- the result (error status) of the previous command
- the state of any actuators and sensors

Each job task polls the present-status table until it encounters a command for one of the mechanisms it controls. LDSS-2 has two job tasks: one for the wheels and the focus (which share the SMDM so cannot operate concurrently) and one for the access doors. The SCC mnemonic does not need a job task as it only returns status.

In order to make the central loop as simple as possible, most of the mechanism-specific routines are vectored through the 'command-table'. This also has one entry per mechanism and contains:

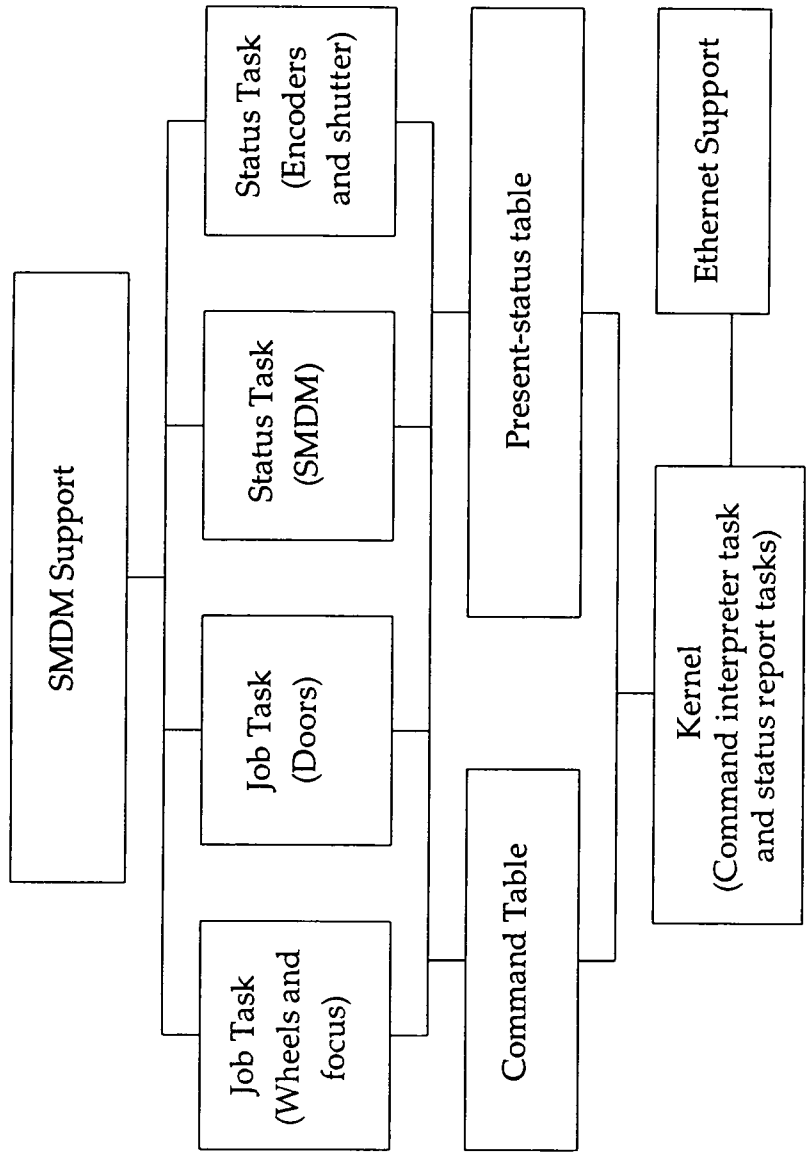


Figure 7.5: The LDSS-2 local controller software

- the mnemonic used to refer to that mechanism
- the operation codes that are valid for that mechanism
- the upper and lower bounds of the mechanism position
- the number of SMDM steps per position and the zero offset
- the addresses of the mechanism move and position-check routines

By parameterising these characteristics it is possible to (for example) use a single piece of code for all three wheels, even though two of them have eight slots and the other has six.

Both the kernel and the job tasks rely on the mechanism status information stored in the present-status table so it is important that it is kept up to date. LDSS-2 has two status maintain tasks for this purpose. One monitors the SMDM and the devices attached to it, the other the encoders and the shutter control card. A full update is performed every time the status tasks gain control of the processor, normally about five times per second.

The kernel is responsible for sending status information back over the network. A node can obtain status information in two ways:

- By sending an explicit status request
- By registering for 'monitor-mode' status messages

Sending a MON101(1) command registers a node for type-1 monitor-mode messages. These are sent at the start and end of each operation and in response to any unexpected movement (eg. lifting a clamp manually). A MON101(2) command additionally requests type-2 messages, which give real-time information about operations in progress. This facility is used by the mimic display in order to accurately track the state of the instrument.

In addition to the network status messages, a number of diagnostic routines are provided that can be executed using a terminal connected directly to the local controller. This is more reliable for troubleshooting as it completely bypasses the kernel and the network software. The commands provided

include facilities to examine internal status tables and to simulate incoming network packets.

## 7.8 System Computer Software

There are two components to the system computer software:

- the command interpreter
- the mimic display

Both are used to control other instruments in addition to LDSS-2, so are extensions of existing software. The code was written by Philip Taylor at the Royal Greenwich Observatory.

The commands that can be sent over the network are both simple and terse. This is intentional: it is not easy to modify the local controller software once it has been burned into EPROM, so it is important that the network protocol be as general as possible. However, better telescope efficiency can be achieved if the interface seen by the user operates at a higher level than the network.

The main features of the user-level software are:

- the automatic processing of status information and its translation into human-readable form
- the ability to specify wheel positions by name rather than by number. This is done using a look-up table that records, for example, that position 2 of the filter wheel contains a PV filter. The table must be updated manually whenever the wheel contents are changed
- the ability to move the focus automatically whenever the filter is changed. This is necessary because the optimum focus position depends on the wavelength range being observed. A look-up table stores an offset for each filter. The zero point is entered at the start of each observing run
- the ability to define macros that perform composite functions. An

example of this is the pre-defined command LDSS\_INIT, which initialises the three wheels and the focus in one operation

The mimic display allows the observer to view the status of any instrument attached to the utility network. It is not possible to display everything on one screen, so the information is divided into a number of 'pages'. The LDSS-2 mimic occupies one page and includes:

- a stylised cross-section of the instrument, showing the light path passing through the wheels and the shutter and entering the camera
- a set of tables showing the wheel contents
- the focus position in microns
- the status of the doors (open/closed and locked/unlocked)

In each case, a colour code is used to convey additional information. The mechanisms and their annotations are normally drawn in green, but turn blue when in motion and red when there is an error. (White is used when the software starts up to indicate that the status is not yet known.)

## 7.9 Testing

### 7.9.1 Introduction

It is difficult to perform proper tests on an astronomical instrument before it is shipped to the telescope, but there are a number of important reasons for doing so:

- telescope time is expensive and cannot be wasted on unnecessary commissioning runs
- although there is a considerable amount of expertise available at the telescope site, the actual facilities are very limited and it is much easier to fix faults before the instrument is shipped
- testing is the only way to determine whether the various elements of the control system will work with each other as well as individually

Two sets of pre-commissioning tests were therefore performed, one in Durham (where the instrument was constructed) and one in Cambridge (using the telescope simulator at the Royal Greenwich Observatory). The latter were combined with the flexure tests described in the next chapter.

The principle objectives of the tests were:

- to ensure that all utility network commands function correctly
- to ensure that all error conditions result in the correct response and the correct error message
- to ensure that all mechanisms function reliably
- to ensure that all mechanisms function correctly at any telescope attitude (Cambridge tests only)

### 7.9.2 Command Functionality Tests

There are two types of test that can be performed to check the functionality of a piece of software:

- directed tests, which look for the special cases and boundary conditions at which the software is most likely to fail
- random tests, which are usually less effective but are unaffected by preconceptions on the part of the tester

Examples of directed tests included moving and initialising the wheels at their first and last positions, with particular attention to any rounding errors that might occur with the grism wheel (due to the non-integer number of steps per position). The focus was also tested at its limits and a check made that it would function correctly even if it were manually moved to beyond those limits. The only problem found was that the focus could jam if it was driven too far into one of its limits, either manually or using the stepper motor, but this should not occur in practice.

It was not necessary to perform separate random tests, as their requirements are identical to the reliability tests below. Indeed, the only reason for

drawing a distinction between the two is that one tests the reliability of the hardware, the other the software. A large number of consecutive commands were used in order to detect conditions such as stack overflow and process synchronisation errors.

In addition to testing mechanisms individually, an attempt was made to test them in combination to look for any unwanted interactions between them. This could occur if, for example, moving one mechanism corrupted a data structure associated with a different mechanism. No such problems were found.

### **7.9.3 Error Condition Tests**

The list of error conditions that can occur is extensive. Causes include hardware failures, communications errors, interlocks and invalid commands. To be reported correctly an error must be detected by the local controller, transmitted over the network to the system computer, and conveyed to the user in a human-readable form.

An attempt was made to simulate as many errors as possible, either by tampering with the hardware or entering commands with erroneous parameters. A small minority were impossible to simulate as they could only arise through internal inconsistencies in the software, but the remainder were successfully shown to function in accordance with the specification.

### **7.9.4 Reliability Tests**

During the course of a 10 hour observing run LDSS-2 will typically be required to execute perhaps 50 commands that result in a mechanism being moved. Any errors will result in a loss of telescope time so it is important that the mechanisms operate reliably.

It is useful to draw a distinction between 'soft' errors (which can be fixed by repeating the command or reinitialising the system) and 'hard' errors (which

require an actual repair). Appropriate limits would be a soft error rate of 1% (per operation) and a hard error rate of 0.01%. These would correspond to one soft error every two days and one hard error every six months.

In practice, if the test sequence is to complete in a reasonable amount of time then it must be limited to at most a few hundred operations per mechanism.

The program used was as follows:

1. Move aperture wheel to positions 0, 2, 1, 3, 2, 4, 3, 5, 4, 6, 5 and 7, repeating 10 times
2. Move filter wheel to positions 0, 2, 1, 3, 2, 4, 3, 5, 4, 6, 5 and 7, repeating 10 times
3. Move grism wheel to positions 0, 2, 1, 3, 2, 4, 3 and 5, repeating 10 times
4. Move camera focus to positions 0, 400, 200, 600, 400, 750 and 600, repeating 20 times

There are a total of 520 operations in the sequence. It executes in about an hour, but corresponds to about 10 days on the telescope. If the test program completes without any errors then, assuming a poisson distribution, there is a 99.5% probability that the soft error rate is less than 1%.

In fact, the test program was run several times at Durham and Cambridge and on La Palma, and while some errors were seen, the rate was clearly well below one per test sequence. No attempt was made to compile any statistics as the conditions were not properly controlled, but a reasonable estimate of the soft error rate would be 0.1% or less, corresponding to one error every three weeks.

It must be emphasised that this result is based on measurements made in a very different environment to the telescope dome and it is likely that the reliability will be degraded by factors such as electrical noise and extremes of temperature. However, so far as it went the result was encouraging, and it was thought unlikely that any insurmountable problems would be

encountered at the telescope.

### **7.9.5 Instrument Attitude Tests**

As the telescope is moved about the sky, the forces on the instrument mechanisms will change and in theory could cause them to fail. No problems were anticipated with the focus or the shutter, but the wheels are sensitive to out of balance loads and they will fail if the torque on the stepper motors becomes too great.

The instrument was therefore tested on the telescope simulator with the aperture and filter wheels arranged to be as far out of balance as possible. This was not done with the grism wheel, as it is not supposed to be used without three grisms and testing it would have risked causing misalignment or even damage.

Failure is most likely when the zenith distance is set to  $90^\circ$  and the instrument rotated in position angle, but to be safe other less severe zenith distances were also tested. Also of interest was the instrument reliability when actually in motion, as this introduces additional forces. The simulator tests this well as its angular velocity and acceleration are significantly greater than those of the telescope.

When the tests were carried out the instrument did perform as expected and no failures were observed. Nevertheless, as a precaution it is recommended that the wheels be operated in balance where possible, as this does reduce the strain on the stepper motors.

### **7.9.6 Conclusion**

Although the pre-commissioning tests had limitations, they were very valuable and undoubtedly saved time when on the telescope. Of particular importance were the skills practised as the tests were carried out, such as bolting the instrument to the telescope and loading the aperture masks.

As can be seen from the results above, no serious difficulties were encountered during the tests, as most potential problems had been identified and corrected during the construction of the instrument. The next step was therefore to proceed with the commissioning and the system characterisation.

# Chapter 8: LDSS-2 Instrument Characterisation

## 8.1 Introduction

This chapter describes some of the methods used to measure the optical characteristics of LDSS-2 using both the telescope simulator at the Royal Greenwich Observatory in Cambridge and the William Herschel Telescope itself on La Palma. The results of these measurements are used to assess whether the instrument has achieved its design objectives.

## 8.2 Flexure Tests

### 8.2.1 Introduction

The aim of this section is to determine to what extent mechanical flexure of the instrument affects the position of an image on the detector as the telescope attitude is varied.

A Cassegrain focus instrument package must be able to function correctly at any angle from  $0^\circ$  to nearly  $90^\circ$  to the vertical. In particular, it is important that the optical system remain rigid as the telescope tracks across the sky. If that is not the case then long exposures will be blurred and there may even be a loss of field acquisition.

In the case of LDSS-2 the total flexure is specified to be at most  $10\mu\text{m}/\text{hour}$  in the dispersion direction and  $15\mu\text{m}/\text{hour}$  in the spatial direction (Allington-Smith *et al*, 1990a). The two main potential sources of non-rigidity are flexure of the instrument structure and movement of wheels within their clamps.

The outer case of LDSS-2 (the main load-bearing structure) is made from 6mm thick mild steel. It was originally designed to support an IPCS

(Imaging Photon Counting System) as the detector. Now that large-format CCD cameras are available it is unlikely that LDSS-2 will ever be used in that configuration. CCD detectors are smaller and lighter so the instrument structure should achieve its flexure specification by a comfortable margin.

Flexure due to the wheel clamp mechanisms is difficult to predict, as it depends on a number of factors including the adjustment of the clamp spring, the performance of the roller slide used in the clamp, and the extent to which the relevant wheel is in or out of balance. The clamp design had been tested as a prototype and when properly adjusted allows very little movement of the wheel, but improper adjustment can result in very poor performance.

To measure the instrument flexure experimentally, two separate sets of tests were performed:

- the first prior to commissioning, using the telescope simulator at the Royal Greenwich Observatory in Cambridge
- the second during the commissioning period, using the telescope itself

### **8.2.2 Simulator Tests, Experimental Method**

The telescope simulator is an adapted welding rig to which instruments can be attached and moved around the 'sky' in both elevation and rotator angle. It is not necessary to vary the azimuth as it should have no significant effect on the performance of the instrument.

A special mask was fabricated with three small holes, equally spaced in a line perpendicular to the dispersion direction. The mask was placed in the instrument and illuminated with an arc lamp. A grism was then placed in the light path and a CCD detector attached.

The resulting image consisted of an array of points, with each point corresponding to an emission line from one of the three holes in the mask. Three of the emission lines were selected for the measurements, giving a

total of nine points arranged in a 3×3 matrix. The CCD controller was set up to measure the centroid of each point and the resulting coordinates were recorded.

Further sets of measurements were made as the instrument attitude was varied. There are several ways in which this could be done; the method chosen was to pick a rotator angle then take readings for zenith distances of 0°, 30°, 60°, 30°, 0°, -30°, -60°, -30° and 0° in that order. This allows both the maximum excursion and the hysteresis to be determined. The test was repeated for further rotator angles in 30° increments over a range of 180°. It is not necessary to rotate through 360°, because of the symmetry of the experiment.

Any flexure of the instrument will cause the matrix of points to move. Four parameters were defined to characterise this motion:

$x_t = \Delta x_{22}$  (displacement of the central point in the dispersion direction)

$y_t = \Delta y_{22}$  (displacement of the central point in the spatial direction)

$x_r = \Delta(x_{23}-x_{21})$  (rotation measured using a 200-pixel baseline in the spatial direction)

$y_r = \Delta(y_{32}-y_{12})$  (rotation measured using a 620-pixel baseline in the dispersion direction)

where  $x_{ij}$  is the coordinate in the dispersion direction,  $y_{ij}$  is the coordinate in the spatial direction,  $i$  labels the points in the dispersion direction, and  $j$  labels the points in the spatial direction.

### 8.2.3 Simulator Tests, Results

The results from the simulator run are too long to reproduce in full, but it is worth looking at an example for one of the rotator angles. Figures 8.1 and 8.2 show how the translational and rotational displacement vary with the zenith distance, while figure 8.3 illustrates the variation of the x-translation as a hysteresis curve.

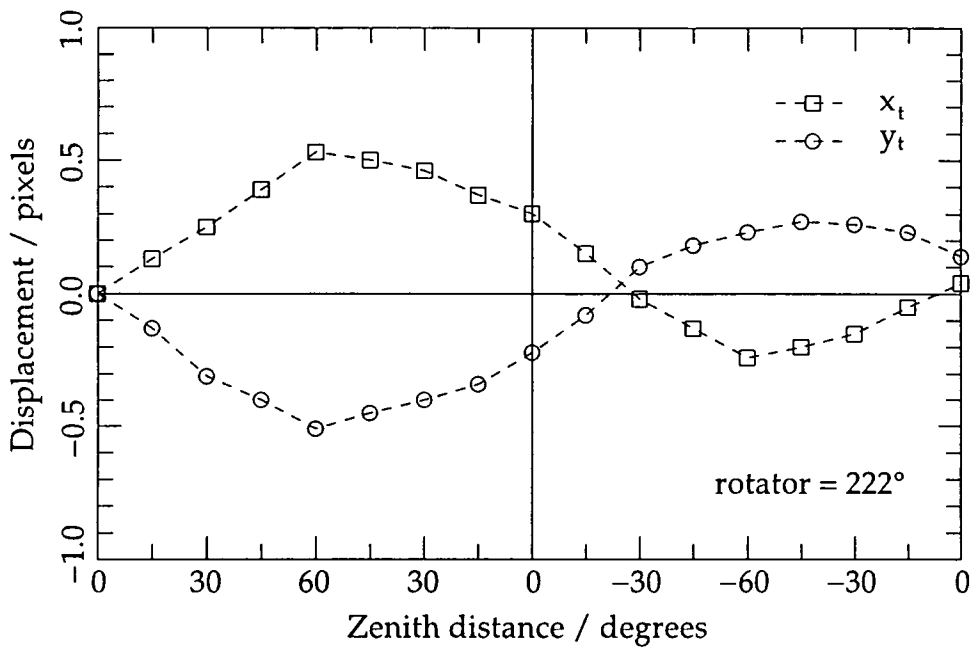


Figure 8.1: Variation of LDSS-2 translational flexure with zenith distance

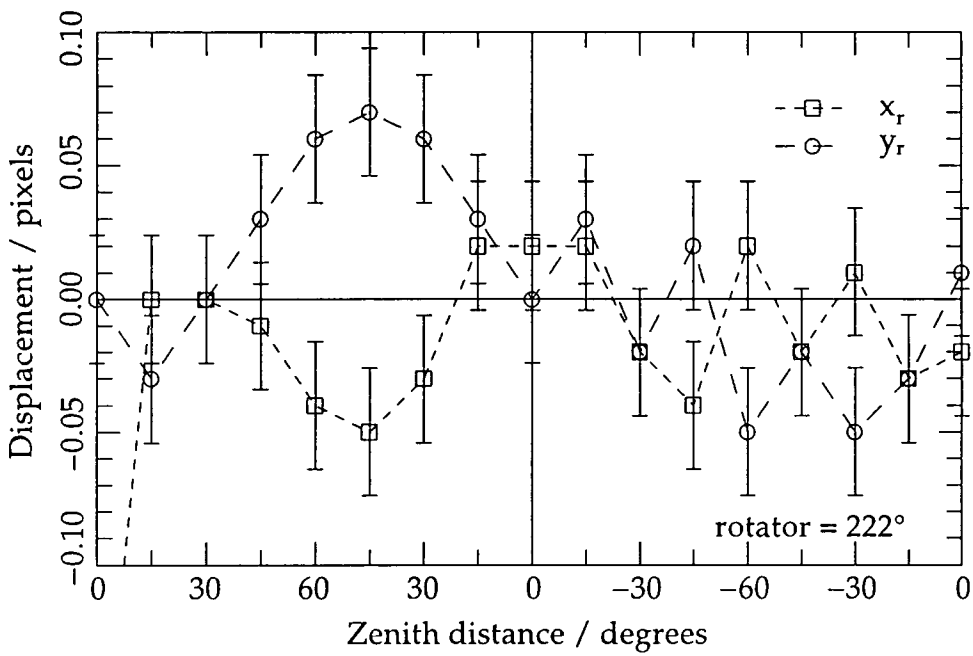


Figure 8.2: Variation of LDSS-2 rotational flexure with zenith distance

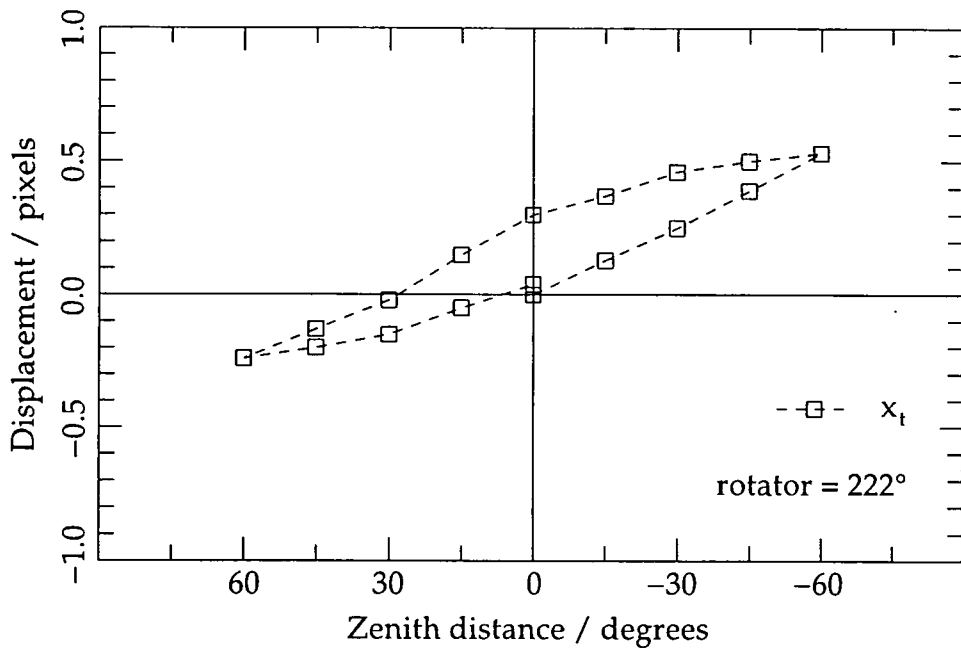


Figure 8.3: LDSS-2 translational flexure hysteresis curve

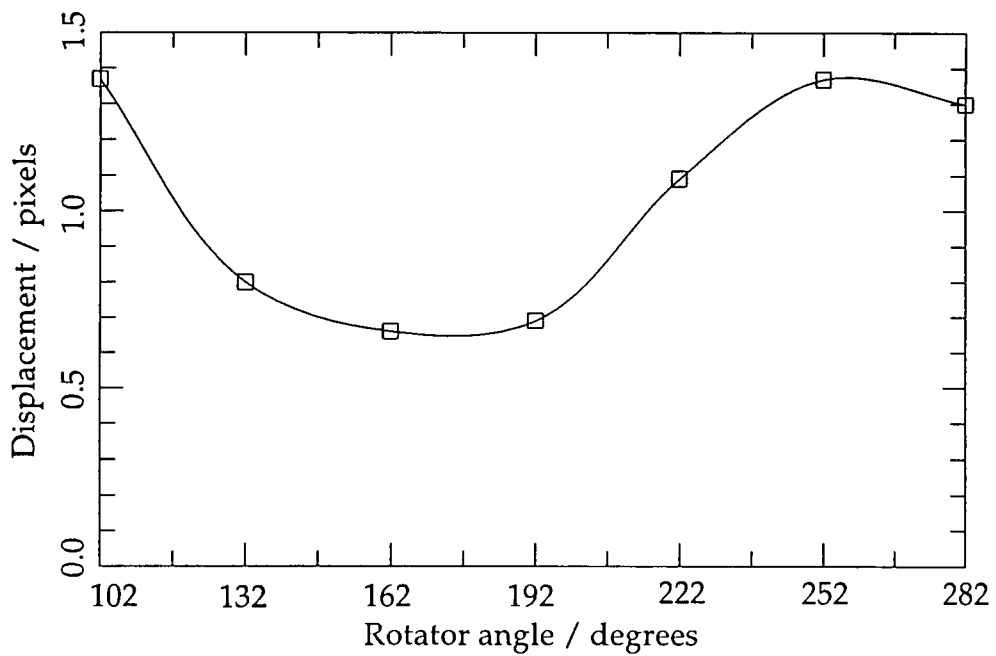


Figure 8.4: Variation of LDSS-2 flexure with rotator angle

The error bars were estimated by observing that there is little if any correlation between  $x_r$  and the zenith distance in figure 8.2. The standard deviation is 0.024 pixels and defines the error bars for  $x_r$  and  $y_r$ . The translation is measured using fewer independent variables so the corresponding error bars for  $x_t$  and  $y_t$  are 0.017 pixels.

Between  $-60^\circ$  and  $60^\circ$ ,  $\Delta x_t$  is  $0.77 \pm 0.024$  pixels and  $\Delta y_t$  is  $0.74 \pm 0.024$  pixels. The total displacement ( $s_t$ , where  $s_t^2 = x_t^2 + y_t^2$ ) over a  $120^\circ$  arc through the zenith is therefore  $1.1 \pm 0.024$  pixels ( $24 \pm 0.54 \mu\text{m}$  at  $22.5 \mu\text{m}/\text{pixel}$ ).

Between the first and second measurements at  $0^\circ$ ,  $\Delta x_t$  is  $0.30 \pm 0.024$  pixels and  $\Delta y_t$  is  $0.22 \pm 0.024$  pixels. The total hysteresis over the arc is therefore  $0.37 \pm 0.024$  pixels ( $8.4 \pm 0.54 \mu\text{m}$ ).

As discussed above, the correlation between  $x_r$  and the zenith distance is at best very weak. In view of this, the strongest statement that can be made is that  $\Delta x_r$  is less than 0.07 pixels over the range  $-60^\circ$  to  $60^\circ$ . With a 200 pixel baseline, this corresponds to a field rotation of  $<0.2^\circ$  and extrapolates to  $<0.36$  pixels over a 1024 pixel baseline.

$y_r$  shows a stronger correlation with the angle,  $\Delta y_r$  being  $0.12 \pm 0.034$  pixels over the range  $-60^\circ$  to  $60^\circ$ . This is not surprising as the baseline is 620 pixels as opposed to 200 pixels. The field rotation is  $0.011 \pm 0.003^\circ$  and extrapolates to  $0.20 \pm 0.06$  pixels over a 1024 pixel baseline.

An analysis of the results for the other rotator angles shows a clear systematic variation in  $\Delta s_t$ . This is to be expected, because although the outer case of LDSS-2 is partially symmetric, its internal components are not. The variation is by a factor of 2:1 and is illustrated in figure 8.4.

It is not possible to make a direct comparison between these results and the specification, because when tracking an astronomical target the altitude and the rotator angle change simultaneously. However, an estimate of the flexure rate at the zenith can be made by assuming that  $\Delta s_t$  varies

sinusoidally with the zenith distance. If  $\Delta s_t$  is equal to  $A \cdot \sin(\alpha)$ , where  $\alpha$  is the zenith distance, then the flexure between  $-60^\circ$  and  $60^\circ$  will be  $1.73A$ . The flexure rate per radian at  $\alpha=0$  will be  $A$ , so the flexure rate per hour will be  $0.26A$ .

The graph shows that between  $\alpha=-60^\circ$  and  $\alpha=60^\circ$  the maximum value of  $\Delta s_t$  is 1.4 pixels, so  $A$  is equal to 0.81 pixels per radian. This corresponds to 0.21 pixels per hour ( $4.7\mu\text{m}$  per hour), which is within the specification for both the spatial and dispersion directions.

#### 8.2.4 Astronomical Test, Experimental Method

Simulator tests of the above type are the best way to investigate the worst case behaviour of the instrument, but it was thought desirable to cross-check them with measurements made under more normal observing conditions.

To detect any significant flexure, a series of exposures were needed over a period of several hours. The experiment clearly did not justify that amount of telescope time so data from a previous observing run was used. The only special requirement was that the aperture mask not be moved between exposures.

Rather than attempt to reduce the spectra of the targets themselves, it was thought better to track the positions of the night-sky emission lines. (This was partly because the objects were very faint and partly to ensure that the results did not depend on the performance of the autoguider.) The data reduction was therefore performed without any sky subtraction.

The spectrum from one of the slits was extracted for each of five separate exposures. A gaussian fitting routine was then used to measure the positions of the centroids of a selection of sky emission lines. The resulting displacements were averaged and tabulated against the time of the exposure.

### 8.2.5 Astronomical Test, Results

The average displacements that were measured were as shown in table 8.1. The result for exposure 43643 has been corrected to account for a one pixel shift introduced by the CCD controller. This was an intermittent but clearly identifiable fault that affected several exposures during the commissioning run.

Exposure	43642	43643	43645	43646	43648
Time/hours	0	0.7	1.6	2.5	3.4
Altitude/degrees	58	61	61	55	46
Azimuth/degrees	153	166	195	218	235
Rotation/degrees	-24	-12	13	32	46
Displacement/pixels	0	0.14	0.30	0.44	0.72

Table 8.1: LDSS-2 flexure measured using astronomical target

Figure 8.5 shows the same results plotted graphically. A least squares fit indicates a flexure rate of 0.20 pixels/hour in the dispersion direction ( $\Delta x_t = 4.8 \mu\text{m}$  at  $24 \mu\text{m}/\text{pixel}$ ), which is within the relevant specification. If the flexure in the spatial direction were the same then the combined flexure would be 0.28 pixels/hour.

### 8.2.6 Conclusion

The flexure measured by the astronomical test is higher than would be expected from the simulator tests, but there are several factors that could explain the discrepancy. The simulator test measured the flexure by varying the zenith distance, whereas the flexure in the astronomical test was mostly attributable to variation of the rotator angle. It is known that different CCDs were used for the two experiments and it is possible that adjustments were made to the clamp spring and/or the detector mounting ring.

Despite this, both sets of results do lie comfortably within the design limits of  $10 \mu\text{m}/\text{hour}$  in the dispersion direction and  $15 \mu\text{m}/\text{hour}$  in the spatial

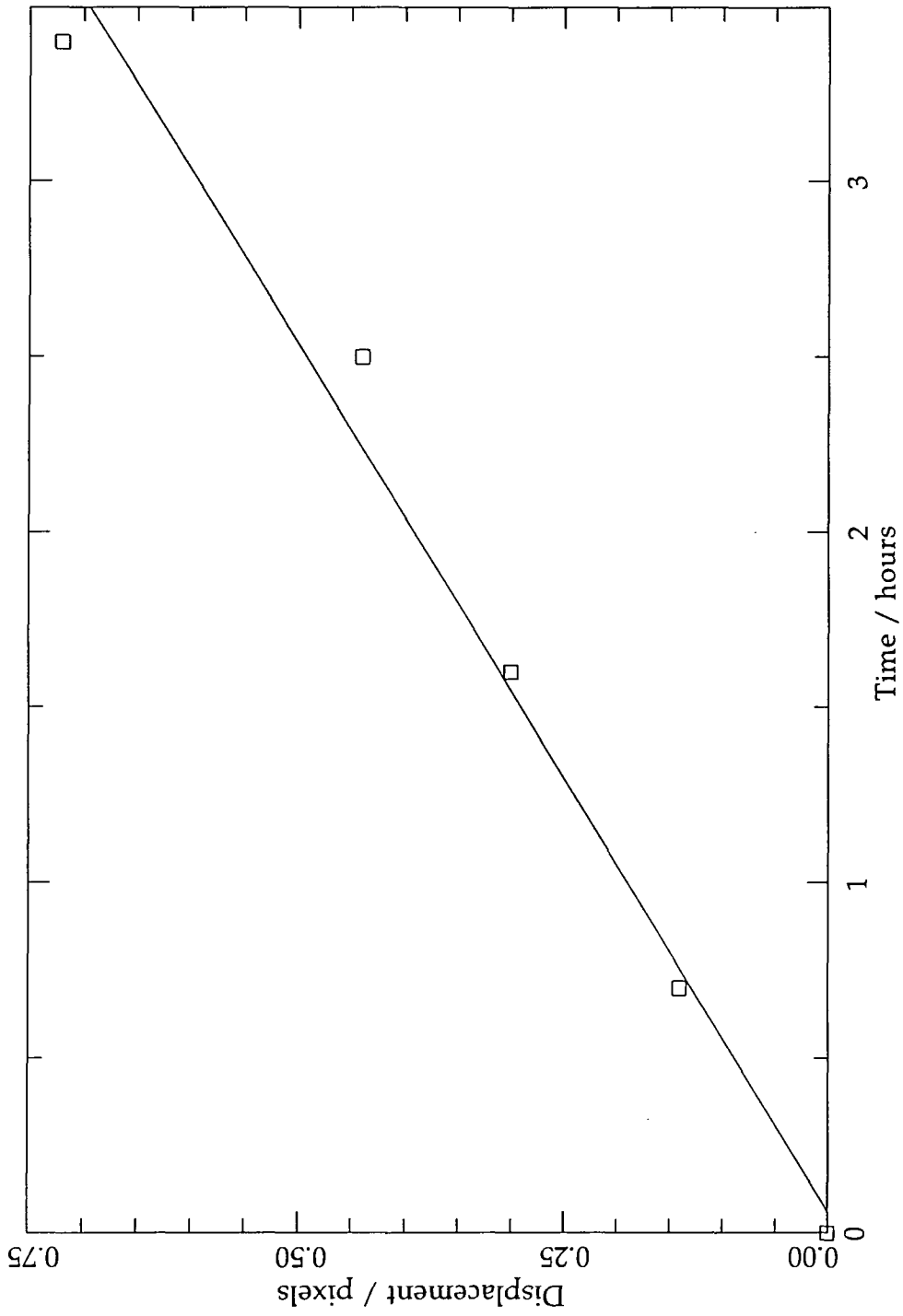


Figure 8.5: Variation of LDSS-2 flexure in dispersion direction versus time

direction. There should not therefore be any need to reacquire a target field during an exposure sequence, through regular confirmation of the field alignment is still recommended.

## 8.3 Image Distortion

### 8.3.1 Introduction

The aim of this section is to measure the chromatic and non-chromatic image distortion caused by the LDSS-2 collimator and camera.

Distortion is measured by defining two cartesian coordinate systems: one on the surface of the mask,  $C$ , and one on the CCD,  $C'$ . They are scaled and aligned so that, near the optical axis, if the coordinates of a point on the mask (measured in  $C$ ) are  $(x,y)$  and the coordinates of the image of that point (measured in  $C'$ ) are  $(x',y')$  then  $x=x'$  and  $y=y'$ .

If there is non-chromatic distortion then, away from the optical axis,  $(x,y)$  and  $(x',y')$  will no longer be equal. The distortion is defined by a vector field  $(\Delta x, \Delta y)$ , where  $x'=x+\Delta x$  and  $y'=y+\Delta y$ . If the instrument is correctly aligned then the field will be radial (ie.  $\Delta x/x=\Delta y/y$ ). If it is not then a small non-radial component will be present.

The distortion is expected to be about 2% (7 arc-seconds) at the edge of the field. This is too high to perform accurate astrometry: a mask cut directly from an LDSS-2 image would be impossible to align. For this reason, it is necessary to map the distortion using a matrix mask and use the result to remove the distortion from subsequent images (see section 4.3.3). Dispersed images are not processed in this way because the disadvantage of having to resample the image outweighs any advantages.

If there is chromatic distortion then  $(\Delta x, \Delta y)$  will also depend on the wavelength. As above, the effect will be radial if the instrument is correctly aligned. The effect is expected to be small but even a small shift can

seriously distort the shape of a stellar image. For this reason direct imaging is usually performed using a broadband filter. Chromatic distortion is present in dispersed images, but at most causes a small deviation in the dispersion curve and/or a small amount of cross-dispersion. Both these effects will be negligible compared to non-chromatic distortion.

### 8.3.2 Experimental Method

A mask was prepared with an orthogonal array of circular holes, spaced 10 arc-seconds apart and nominally aligned with the detector axes. Three undispersed exposures were taken of the mask using the tungsten lamp with the PB, PV and PR filters respectively.

### 8.3.3 Data Reduction

The LEXT procedure 'Analyse\_Matrix' was used to generate a list of centroid coordinates for each exposure. The list was sorted and arranged into a matrix of position vectors  $(x,y)_{ij}$ .

Preliminary tests indicated that the field was indeed radial and that the field centre was located in the vicinity of  $(x,y)_{77}$ . The distortion in this region was found to be negligible, so it was possible to estimate the grid alignment offset by averaging the coordinates of a set of points near to  $(x,y)_{77}$ . A similar method was used to estimate the grid spacing.

Using these estimates, the radial component of the distortion field was plotted for each grid point against the radial component of the position vector. A strong correlation was observed and was modelled using an interpolation function of the form:

$$P(r)=a_0+a_1\cdot r+a_2\cdot r^2\ .\ .\ .$$

where  $(r,\theta)_{ij}$  is the position vector in polar coordinates. Two constraints were used to reduce the number of degrees of freedom. First, continuity of the distortion field requires that  $P(0)$  be equal to zero and therefore that  $a_0=0$ .

Second, if the distortion field is radial then  $P$  must be an even function of  $r$ , requiring that  $a_{2n+1}=0$  for integer  $n$ . In practice  $a_2$  was also found to be small and the best results were achieved when the distortion was modelled by the quartic  $P(r)=a_4 \cdot r^4$ .

If any of the parameters used to derive the distortion field are inaccurate then the accuracy of the model will be reduced. It was therefore possible to use the model to improve the accuracy of the parameters by minimising the root mean square moduli of the residuals. Once this was done  $a_4$  was recalculated and the corresponding distortions at radii of 2, 4 and 5.75 arc-minutes were tabulated (5.75 arc-minutes is the nominal field radius).

The non-radial component of the distortion was measured by calculating the root mean square of the radial and transverse components of the residual distortion field. These components were also plotted against the direction of the position vector and an attempt made to correlate them with a function of the form  $a \cdot \sin(\theta + \delta)$  where  $\delta$  is an offset.

The chromatic distortion was measured by comparing the values of  $a_4$  measured for the three exposures. So long as the filter does not introduce any additional distortion, any difference in this coefficient will be a chromatic effect.

#### 8.3.4 Results

Satisfactory interpolation functions were obtained for all three exposures and are listed in table 8.2. The corresponding distortions at radii of 2, 4 and 5.75 arc-minutes are listed in table 8.3.

A weak correlation was observed between the residual distortion vectors and the direction of the position vectors, but the effect was small compared to the noise. The RMS residuals are listed in table 8.4, where  $\sigma_r$  is the RMS radial component,  $\sigma_t$  is the RMS transverse component and  $\sigma_m$  is the RMS modulus.

Exposure	Filter	$\lambda_{\text{mean}}$	$a_4$
43028	PB	4805	$5.23 \pm 0.69$
43027	PV	5715	$4.48 \pm 0.27$
43030	PR	6680	$4.20 \pm 0.20$
		$/\text{\AA}$	$/10^{-11} \text{ pixel}^{-3}$

Table 8.2: Interpolation functions for LDSS-2 image distortion

$\lambda_{\text{mean}}$	$r=2'$	$r=4'$	$r=5.75'$	$r=2'$	$r=4'$	$r=5.75'$
4805	0.089	1.43	6.1	0.044	0.35	1.04
5715	0.076	1.22	5.2	0.038	0.30	0.89
6680	0.072	1.15	4.9	0.035	0.28	0.84
$/\text{\AA}$	$/\text{pixels}$	$/\text{pixels}$	$/\text{pixels}$	$\%$	$\%$	$\%$

Table 8.3: LDSS-2 image distortion at selected radii

Exposure	$\sigma_r$	$\sigma_t$	$\sigma_m$
43028	0.223	0.328	0.397
43027	0.104	0.216	0.185
43030	0.077	0.185	0.201
	$/\text{pixels}$	$/\text{pixels}$	$/\text{pixels}$

Table 8.4: RMS residuals for LDSS-2 distortion functions

### 8.3.5 Conclusion

The radial distortion at the field edge lies well within the expected value of 2% for the three pass-bands that were tested and it appears likely that this would also be true over the remainder of the instrument pass-band. The distortion field is sufficient to affect astrometric measurements even at relatively small radii, but it is mathematically well behaved and LEXT should be able to correct it to a high level of accuracy.

The correlation between the residual distortion vectors and the direction of the position vectors does not necessarily imply that the distortion field has a non-radial component as the same effect could be caused by an error in the

field centre or the grid alignment offset. However, the measured RMS residuals do place an upper limit on the magnitude of such a component and confirm that it is small compared to the radial distortion.

The distortion level does appear to fall as the wavelength increases but the effect is small. Between the PB and PR filters (which lie 1875Å apart) the distortion vector at the nominal edge of the field changes by  $1.20 \pm 0.84$  pixels ( $\pm 1.43\sigma$ ). This is of marginal statistical significance (a two-tail normal error function gives an 85% confidence that the distortion is non-zero) so it is not possible to make a reliable estimate of the chromatic distortion using this method.

## 8.4 Wavelength Calibration

### 8.4.1 Introduction

The aims of this section are:

- to measure the average dispersion, undeviated wavelength and linearity of the instrument when used with each of its gratings
- to generate a set of arc-lamp line identification charts for use when calibrating dispersed exposures.

LDSS-2 is supplied with four gratings: low dispersion, medium dispersion with blue blaze, medium dispersion with red blaze, and high dispersion. Their specifications are listed in table 6.2. The dispersion is specified as an average as it is expected to vary with both wavelength and position.

Wavelength calibration of a dispersed image is usually carried out using an emission line spectrum generated by an arc lamp. A selection of lines are identified and their positions plotted against wavelength. The results are interpolated using a suitable function (in this instance a polynomial was used).

Line identification is carried out with the aid of an emission line 'atlas'. Such

atlases are readily available, but lines can be hard to identify unless the instrument and the atlas have similar spectral resolutions. It is therefore useful to generate a set of line identification charts using the instrument itself, ensuring that the resolution is appropriate.

#### 8.4.2 Experimental method

The WHT Acquisition and Guidance (A+G) Box provides a number of lamps for generating emission line spectra, including the following:

- CuAr (Copper-argon)
- CuNe (Copper-neon)
- FeAr (Iron-argon)
- ThAr (Thorium-argon)
- AlMgCa (Aluminium-magnesium-calcium-neon)

Of these, the first two feed directly into an integrating sphere, while the remainder are linked via fibre-optic couplers. As a result the CuAr and CuNe lamps are over ten times brighter than the others so give better signal to noise ratios for a given exposure time.

All of the lamp spectra are dominated by either neon or argon. The argon spectrum is particularly well suited for calibration as its lines are generally distinct and well spaced with relatively few blends. Unfortunately, these lines exist only in the red part of the spectrum, cutting off sharply at about 6900Å. Neon is a little better, extending down to 5800Å, but not to the instrumental limit of 3700Å.

The choice of lamp was therefore determined by the number and quality of lines at the blue end of the spectrum. Preliminary tests showed that the CuAr, FeAr and ThAr lamps have a small but acceptable number of lines in this region, whereas the CuNe and AlMgCa lamps are less suitable. The CuAr lamp was chosen because it is brighter than the other Argon lamps and suitable line identification charts are more widely available.

A 300 $\mu\text{m}$ -wide long slit was used for the experiment. The width was chosen to maximise the chromatic resolution (300 $\mu\text{m}$  was the narrowest slit that could be reliably manufactured using the CAMM-3 machine). The length was arbitrary as only the central part of the slit was used. One exposure was taken with each grism with the exposure time set to give a strong but unsaturated first-order spectrum (saturation of the zero-order was unavoidable). An additional undispersed exposure was used to determine the position of the slit.

### 8.4.3 Data Reduction

The Figaro program 'ARC' was used to fit a gaussian to each line and to interactively match lines to wavelengths. Accurate wavelength tables and line identification charts were obtained from Zuiderwijk and Knapen (1989).

Well over 60 emission lines can be identified with a copper-argon arc lamp and a medium dispersion grism, but it is neither practical nor desirable to use all of them when calibrating the wavelength scale. Many lines are blends of two or more wavelengths and should not be used unless either the distance between the components is small compared to the pixel scale or the intensity of one of the components is large compared to the others. Unsuitable lines should be removed and the remainder balanced to give an even coverage of the wavelength range.

During the selection process ARC displays the deviation of each line from the current interpolating polynomial. There is a strong temptation to simply remove the lines with the greatest deviations, but this should be resisted (Taylor, pp141-146, 1982). The resulting polynomial will fit the remaining data points very accurately but this does not make it a more accurate calibration function. In fact it is likely to be less accurate because there are fewer measurements to filter the noise.

ARC determines the polynomial coefficients automatically, but the

polynomial order is set by the user. For the best result the polynomial must be flexible enough to follow the underlying trends in the data but not so flexible that it also tracks the noise. Low order polynomials are therefore preferred where possible.

The method used to select the polynomial order was to look at how it affects the RMS deviation between the polynomial and the data. For example, the deviation for the low dispersion grism are as shown in table 8.5.

Order	1	2	3	4	5
RMS Deviation	26.5	7.26	2.23	0.74	0.56
Order	6	7	8	9	10
RMS Deviation	0.56	0.55	0.53	0.53	0.52

Table 8.5: Variation of wavelength calibration residual with polynomial order

The 2nd, 3rd and 4th order components clearly have a significant effect on the accuracy of the fit and there is little doubt that they are mapping a genuine trend. The 5th order component results in some further improvement, but beyond this there is little significant reduction in the error. This does not mean that the wavelength scale has no component in those dimensions but it does suggest that the effects are below the noise level. The wavelength scale for this grism was therefore interpolated using a 5th order polynomial.

#### 8.4.4 Results

Satisfactory polynomial fits were obtained for all four grisms and are listed in table 8.6, where the dispersion and non-linearity are averaged over the range 3700Å to 7500Å for the low, medium-red and medium blue grisms, but over 3700Å to 5500Å for the high dispersion grism. Full details, including line lists and line identification charts, can be found in Appendix A.

Grism	Order	RMS error	$\lambda_{\text{undev}}$	Dispersion	Non-Linearity
Low	5	0.563	5720	10.59	0.43
Med-B	4	0.576	5750	5.05	0.50
Med-R	4	0.669	5750	5.06	0.49
High	3	0.390	4380	2.36	0.33
		/Å	/Å	/Å pixel <sup>-1</sup>	/%

Table 8.6: LDSS-2 wavelength calibration results

#### 8.4.5 Conclusion

The measured dispersion is closest to the expected value for the high dispersion grism where the difference is 1.7%. This increases to 4.3% for the medium dispersion grisms and 6.1% for the low dispersion grism. If these errors were caused by distortion in the camera then it would affect each image to approximately the same extent and the percentage errors would be expected to be constant. The fact that they are not suggests that the errors are instead caused by the grisms themselves.

The undeviated wavelengths show errors of between 160 and 190Å compared to the specified values. The camera can have little if any effect on the undeviated wavelength, indicating that these errors are also attributable to the grisms.

Although the errors measured in this section are larger than expected, they have no direct effect on the performance of the instrument. The grism specifications are to some extent arbitrary, as they were intended to cover a wide range of observing requirements, and errors under 10% can be considered negligible. The grism characteristics measured in this section are therefore satisfactory for the purposes of the instrument.

## **8.5 Variation of Dispersion with Slit Position**

### **8.5.1 Introduction**

The aim of this section is to determine, for one of the grisms, to what extent the wavelength calibration scale varies across the field of view.

The wavelength calibration measurements in section 8.4 are based on a single long slit at the centre of the field of view. In practice many of the slits in a multi-object mask will be a considerable distance off-axis, so it is useful to know to what extent the calibration scale varies with position.

### **8.5.2 Experimental Method**

An existing mask was used with a good selection of slits distributed across its surface. Two exposures were taken: one with no grism to measure the slit positions, and one with the medium-blue grism and a copper-argon arc lamp to obtain a calibration spectrum. The mask was not moved between the exposures.

### **8.5.3 Data Reduction**

Two sets of slits were selected: one varying mostly in  $x$  (the dispersion direction) and one mostly in  $y$  (the spatial direction). Some variation in the other coordinate was inevitable but it was limited to 300 and 200 pixels respectively.

The undispersed exposure was used to measure the position of each slit. (The  $y$ -coordinate of a slit was defined to be at its midpoint.) The arc lamp spectrum was then extracted for each slit and five well spaced lines chosen. The  $x$ -coordinates of those lines were measured and the results tabulated.

### **8.5.4 Results**

The results for the slits distributed in the dispersion and spatial directions

are given in tables 8.7 and 8.8 respectively. The coordinates of the arc lines have been shifted so that in each case the slit is at  $x=500$ . Any residual variation down a column is therefore entirely due to changes in the dispersion curve.

x/pixels	y/pixels	$\lambda=8264$	$\lambda=7383$	$\lambda=6416$	$\lambda=5495$	$\lambda=4199$
382.6	482	—	191.0	372.6	549.0	811.0
484.1	295	—	189.7	372.1	549.7	813.1
567.1	227	24.5	188.8	372.1	550.1	815.4
665.2	330	21.9	186.9	371.1	550.4	816.9
736.1	595	20.2	185.8	370.8	550.8	818.6
853.8	437	17.6	184.2	370.5	551.4	—

Table 8.7: Variation of dispersion with x-coordinate of slit

x/pixels	y/pixels	$\lambda=8264$	$\lambda=7383$	$\lambda=6416$	$\lambda=5495$	$\lambda=4199$
567.1	227	24.5	188.8	372.1	550.1	815.4
686.1	397	21.3	186.5	371.0	550.5	817.2
617.8	515	22.8	187.3	371.1	549.5	815.4
558.5	680	24.2	188.3	371.5	549.6	814.2
741.2	792	20.6	186.2	371.2	551.5	819.8
538.1	932	25.5	189.8	373.0	551.0	815.8

Table 8.8: Variation of dispersion with y-coordinate of slit

In the first table the line positions are strongly correlated with the slit x-coordinate. At  $\lambda=8264$  the correlation is  $-0.024$  pixels/pixel and at  $\lambda=4199$  it is  $+0.021$  pixels/pixel. This is a total of  $0.045$  pixels/pixel for a wavelength difference of  $4065\text{\AA}$  (approximately 794 pixels). By linear extrapolation (which from the data would appear to be reasonable) this corresponds to 6% across a 1024 pixel field.

The second table shows little if any correlation between the line positions and the slit y-coordinate and the differences that are present can in be attributed to the (unintended) changes in the x-coordinate. Compensating for the difference in  $x$ , the full  $4065\text{\AA}$  range corresponds to 790.9 pixels at  $y=227$  and 791.6 pixels at  $y=932$ . This is a 0.09% variation across 705 pixels, or 0.13% over a 1024 pixel field. The effect may be partly or wholly caused

by noise and is clearly negligible compared to the correlation with the x-coordinate.

### **8.5.5 Conclusion**

The results above cannot be compared directly with the image distortion measurements in section 8.3 because the optical configurations are different. The dispersion can be affected by both the grism and the camera, but is independent of the collimator.

The dispersion curve of a grism is nominally symmetric with respect to translations in  $y$ , whereas the camera is rotationally symmetric. The fact that the line positions correlate only with the  $x$ -coordinate and that the correlation is monotonic and nearly linear strongly suggests that most of the distortion is caused by the grism.

A distortion level of 6% is acceptable because it can be removed by the wavelength calibration procedure. However, it clearly justifies the practice of using a separate wavelength calibration spectrum for each slit.

## **8.6 Filter Throughput**

### **8.6.1 Introduction**

The aim of this section is to measure the transmission function of each of the LDSS-2 filters.

The transmission function is equal to the ratio of transmitted flux to incident flux as a function of wavelength, and is the main parameter defining the optical behaviour of a filter. It is useful to measure the transmission, partly as a check against the manufacturing specifications, and partly to assess how the insertion of a filter would affect the exposure time required for a given observation.

### 8.6.2 Experimental method

LDSS-2 is supplied with six filters, labelled PB, PV, PR, S1, S2 and S3. Their specifications are listed in table 6.1.

A 300 $\mu$ m-wide long slit was used for the experiment, but most of the length of the slit was blocked using opaque adhesive tape. This was done to reduce the level of scattered light present in the image and to facilitate the subtraction of what remained.

Two dispersed images were taken for each filter: one with the filter and a grism and one with just the grism. The exposure time was set to 10 seconds to ensure that any shutter timing error would be negligible. Neutral density filters were used to avoid saturation. One further exposure was taken with a CuAr arc lamp to calibrate the wavelength scale.

A tungsten lamp was used as the light source in order to avoid sharp gradients in the light source spectrum. This reduces the sensitivity of the experiment to errors in the alignment of the two images. It was necessary to ensure that the lamp intensity remained constant during the experiment and initially there was some concern that this might not be the case. However, preliminary tests indicated that the lamp stability was acceptable, and this was confirmed by comparing the undispersed exposures taken throughout the experiment. The RMS variance was calculated and found to be less than 0.1%.

### 8.6.3 Data reduction

The tungsten lamp intensity peaks at approximately 6500 $\text{\AA}$  with a FWHM of approximately 1000 $\text{\AA}$ . This gives good coverage of the instrument pass-band at the red end of the spectrum but results in very low signal levels (less than 1% of the peak) below 5000 $\text{\AA}$ . Accurate subtraction of the background signal is therefore essential if meaningful results are to be obtained at the instrumental limit of 3700 $\text{\AA}$ .

The background signal is composed of the CCD bias level, together with a low level of scattered light that varies across the field. The Figaro program 'POLYSKY' was used to measure the background level outside the slit and thus estimate its value within the slit. This technique is most effective when the interpolation distance is small, hence the use of adhesive tape to shorten the length of the slit.

The background was subtracted from both the filtered and the unfiltered images and the Figaro program 'EXTRACT' used to sum the pixel rows that lay within the slit. To calculate the throughput, the first spectrum was divided by the second and a wavelength calibration scale applied. The result was then smoothed using a gaussian filter to improve the signal to noise ratio at short wavelengths.

#### 8.6.4 Results

Transmission functions for all six filters were measured and are shown in figures B.1 to B.4. The results are tabulated in detail in appendix B, with expected values based on the filter prescriptions. Also listed are measurements made by the NOAO using their 'Lambda 9' spectrophotometer of a set of broadband filters manufactured to the same prescriptions as the LDSS-2 PB, PV and PR filters.

The result for the PB filter shows two secondary peaks: one at  $5600\text{\AA}$  and one at  $9400\text{\AA}$ . The first of these is part of the expected filter response, but the second is not. It is, however, located at close to twice the wavelength of the primary peak, so there is good reason to believe that it represents the second order spectrum. The PV filter shows a similar effect, though in that case the peak lies outside the wavelength range that was investigated.

#### 8.6.5 Conclusion

The results for the PR, S1 and S2 filters generally agree well with the predictions. The differences can be attributed to a combination of:

1. Scattering due to dust on the surface of the filter
2. Reflection losses at internal glass-cement-glass interfaces (PB, PV, PR and S3 filters)
3. Wavelength calibration errors (especially where the gradient of the transmission function is large)
4. Differences between the nominal and actual thicknesses of the glass layers

The throughput of the PV filter is lower than expected (its peak being at 88% instead of 94%), but the difference is not excessive and the LDSS-2 measurements do agree well with the NOAO measurements.

The PB and S3 filters show much larger deviations (64% instead of 80% and 74% instead of 86% respectively). The error increases as the wavelength shortens, causing the peaks to be shifted to the red. (The secondary peaks are unaffected, indicating that the wavelength calibration is probably correct.)

A systematic error cannot be discounted as both of the affected filters have pass-bands at the far blue end of the spectrum. The tungsten lamp spectrum is very weak in this region, so the results are highly sensitive to errors in the background level subtraction. However, the nature of the deviation clearly varies from filter to filter, so could not be caused by an error that depended only on the wavelength.

Alternatively, the PB, PV and S1 filter throughputs may indeed be lower than predicted. This possibility is supported by the fact that the NOAO PB filter measurement is also lower (74% instead of 80%), and that a filter with the same prescription that is used on La Palma was measured by the RGO to have a peak throughput of about 50%. This suggests that the manufacturing tolerances (for some prescriptions at least) are considerably wider than had been anticipated and may therefore account for the anomalous LDSS-2 measurements.

## 8.7 Grism Throughput

### 8.7.1 Introduction

The aim of this section is to measure the throughput of each of the four gratings in three separate pass-bands (generated by the PB, PV and PR filters).

The transmission function of a grating cannot be measured in the same way as that of a filter, because the grating cannot be removed from the light path if it is needed to disperse the image. However, it is possible to use the broadband filters to define a set of wavelength bands and to measure the average efficiency of a grating in each of those bands.

These results are not as useful as the full transmission function, but they do allow the performance of the grating to be assessed. By calculating the transmission profile of each pass-band (which depends on the tungsten lamp, the filter and the detector) it is possible to compare the results with transmission functions measured by the RGO. The RGO results are shown in figure 8.6 and were obtained after the gratings were coated but before they were shipped.

### 8.7.2 Experimental Method

A wide slit was used for the experiment to ensure that the measured intensity of the undispersed slit image was not affected by its position relative to the pixel grid. Two exposures were taken for each filter/grating combination: one with the filter and the grating and one with just the filter. It was not possible to test the low dispersion grating as it was not mounted in the instrument at the time.

The exposure time was set at 10 seconds to ensure that any shutter timing error would be negligible. Neutral density filters were used to avoid saturation. A tungsten lamp was used as the light source to ensure that the pass-band profiles were smooth.

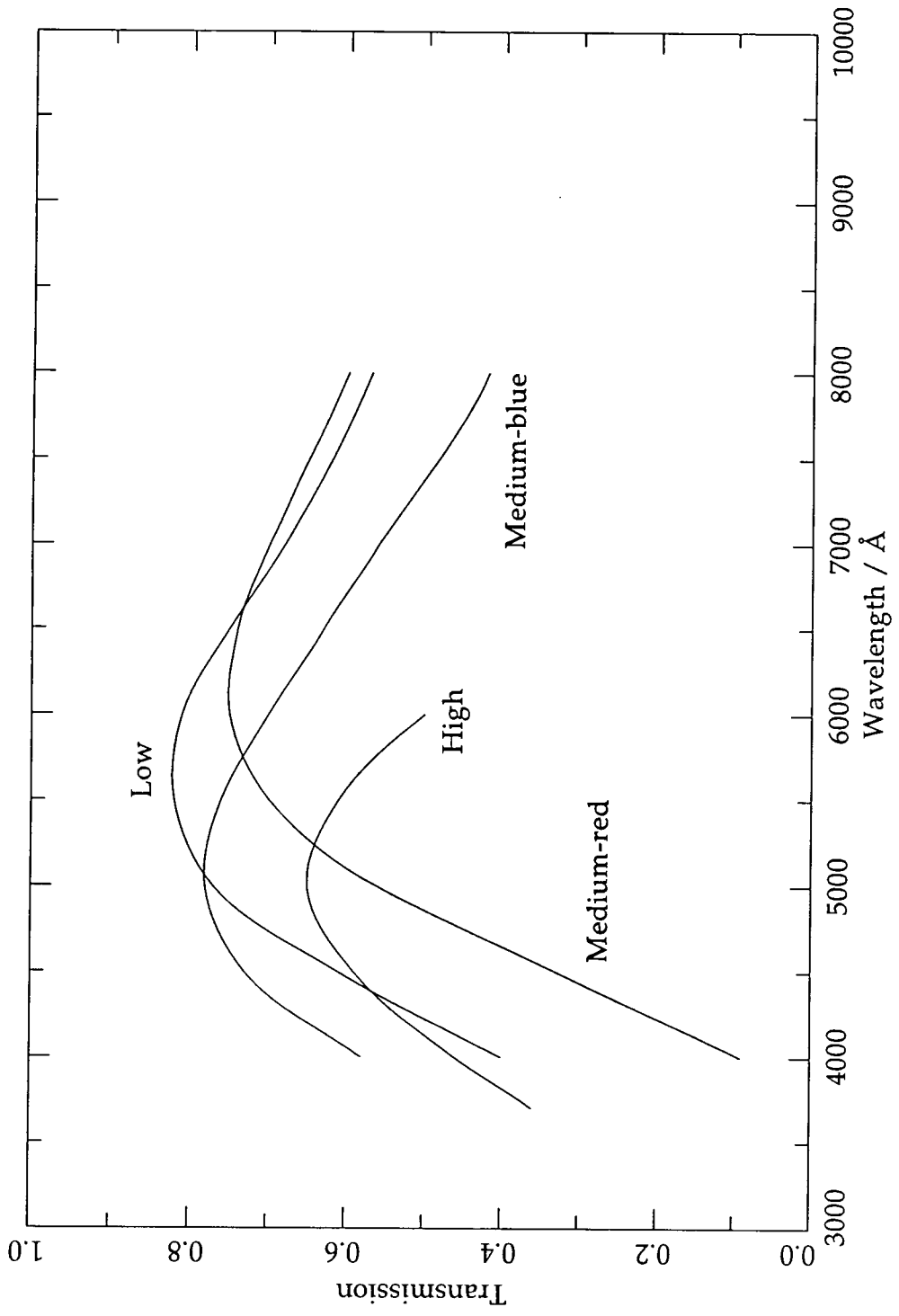


Figure 8.6: LDSS-2 grism efficiencies measured by RGO

For the throughput to be measured accurately it is important that the whole of the spectrum be captured by the CCD. If this is not the case then some of the light will be lost and the efficiency will appear lower than it actually is. This effect made the high dispersion grism measurements unusable and resulted in a small but correctable error in the throughput of the two medium dispersion grisms with the red filter.

### 8.7.3 Data Reduction

For each grism/filter combination, four rectangular regions of the CCD were defined:

1. A region with its x-coordinates set to cover the whole of the first-order spectrum in the dispersed image (but not including any part of the zero-order or second order) and its y-coordinates set to cover a 50 pixel band near the middle of the slit
2. A region with the same x-coordinates of the first but its y-coordinates shifted to cover a nominally unexposed area of the chip
3. A region with the same y-coordinates of the first but its x-coordinates set to cover the undispersed image of the slit (plus a margin of about 50% of the slit width on either side)
4. A region with the same y-coordinates as the second and the same x-coordinates as the third

The total number of counts in the dispersed image was measured for regions one and two and the number of counts in the undispersed image for regions three and four. The second total was then subtracted from the first (to give the total signal with the grism after removing the background and the bias level). Similarly, the fourth total was subtracted from the third (to give the signal without the grism). The throughput was calculated by dividing the first difference by the second.

#### 8.7.4 Predictions

The results obtained from this experiment represent weighted averages over pass-bands up to 2000Å wide. These pass-bands are not the same as those of the filters because they are also influenced by the tungsten lamp spectrum and the spectral response of the CCD. It was therefore necessary to determine what the pass-bands were in order to use them to make predictions based on the laboratory measurements.

Exposures from a previous experiment were used to obtain a low dispersion spectrum of the comparison lamp through each of the three filters. Each spectrum was then divided by the expected throughput of the low dispersion grism and normalised to sum to one. The result is a weighting function for each pass-band that reflects the relative significance of each wavelength channel.

The mean wavelength of each pass-band was found by averaging the product of the weighting function and its wavelength scale. Similarly, the predicted throughput of each combination of filter and grism was found by averaging the product of the weighting function and the expected grism transmission function.

#### 8.7.5 Results

The throughputs measured for the medium-blue and medium-red grisms are given in table 8.9. The images obtained using the PR filter fell partly outside the field of view of the CCD chip, but only a small tail at the red end of the spectrum was missing. The error was estimated as 2%, and the results (marked with a \*) have been corrected to allow for this. The predictions for the two grisms are given in table 8.10. Note that the filter transmission functions are not symmetric, so the peak wavelength of the pass-band may differ significantly from the mean wavelength.

	PB	PV	PR
Medium-Blue	0.74	0.74	0.59*
Medium-Red	0.42	0.72	0.70*

Table 8.9: LDSS-2 grism throughput measurements

	PB	PV	PR
$\lambda_{\text{mean}}/\text{\AA}$	4805	5715	6680
Medium-Blue	0.74	0.73	0.60
Medium-Red	0.43	0.71	0.70

Table 8.10: LDSS-2 grism throughput predictions

### 8.7.6 Conclusion

The results clearly agree well with the predictions and confirm the throughput measurements made by the RGO.

## 8.8 Flat-field Profile

### 8.8.1 Introduction

The aim of this section is to measure how the relative efficiency of the WHT/LDSS-2 optical system varies across its field of view.

When light passes through a complex optical system, such as that within LDSS-2, it is inevitable that some light paths will transmit a greater proportion of the light than others. Two important reasons for this are:

- Vignetting. In theory, it would be possible to construct a collimator/camera system where no light path within the field of view was obstructed. In practice, the optics required to achieve this would be both large and expensive, so it is necessary to accept some loss of efficiency for off-axis light rays.
- Reflection. Different parts of a lens will lie at different angles to the optical axis. Reflection at the lens surface tends to be greatest for large

angles of incidence, again reducing the efficiency of the system for off-axis rays.

Both effects are expected to be small (less than 1%) across much of the field, but to increase rapidly near to the edge. If the instrument is correctly aligned then they will be approximately symmetric about the optical axis.

### 8.8.2 Experimental Method

A blank night-sky field was used in preference to a calibration lamp because it is less likely to have a significant large-scale intensity gradient. A secondary advantage is that the result will correspond to the combined effect of both LDSS-2 and the WHT, which is of more interest to observers than LDSS-2 alone. The sky was not completely dark at the time of the exposure, but the field was located away from the horizon.

One exposure was taken, with a PV filter but with no mask or grism. (The presence of the filter was incidental as the exposure was also being used for other purposes.) The exposure time was set at 100s to ensure that the shutter transition time would be negligible.

### 8.8.3 Results

A cross-section through the centre of the image (after subtracting the CCD bias level) is illustrated in figure 8.7. It shows some variation in intensity between the centre and the edge of the field, but the effect is small (6% between  $x=625$  and  $x=50$ ) and is masked by readout and shot noise (which have a combined RMS amplitude of about 120 counts).

An attempt was made to reduce the noise level by smoothing the image but the results were not entirely satisfactory. The noise amplitude is significant even at low spatial frequencies but if a powerful filter is used then it is not possible to make measurements near to the edge of the field. A suitable compromise was found to be a 5 pixel top-hat filter. A cross-section through

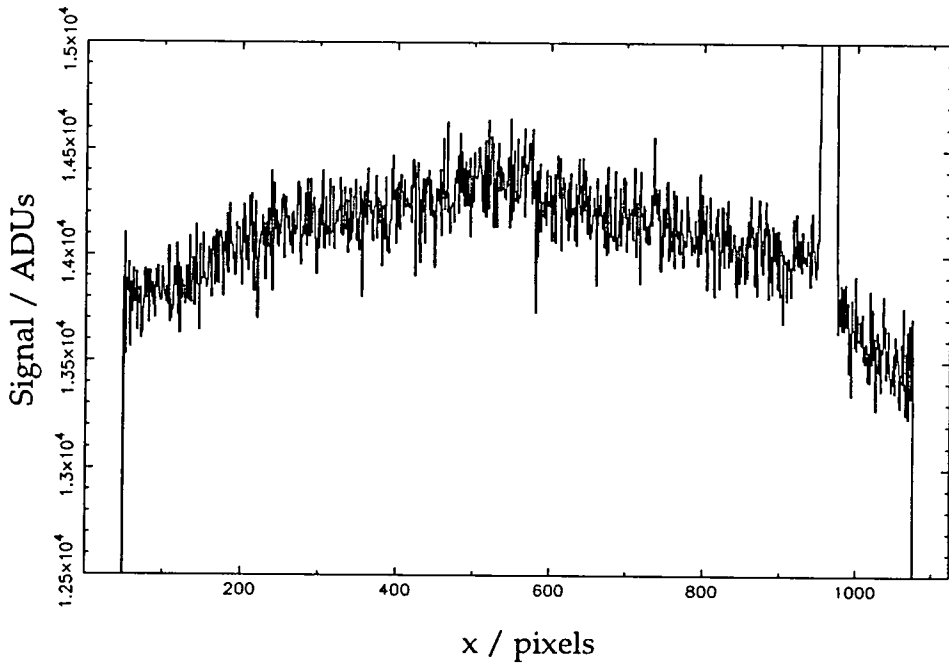


Figure 8.7: Unfiltered cross-section through LDSS-2 flat field

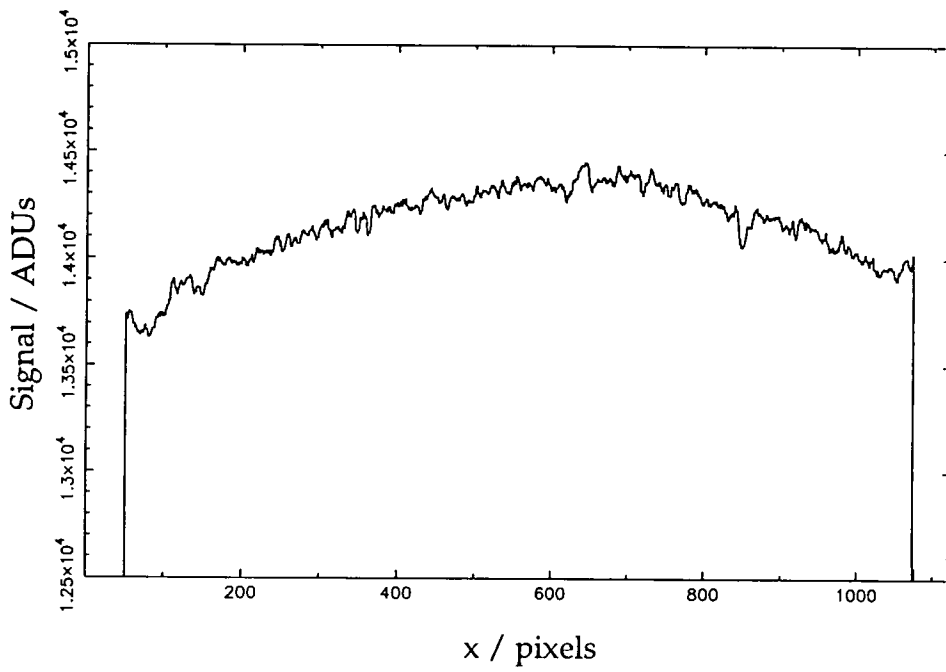


Figure 8.8: Filtered cross-section through LDSS-2 flat field

the result is shown in figure 8.8.

In addition to the noise, the image displayed a number of local imperfections, one of which was seen in the unsmoothed cross-section. Most of the large imperfections are compact and circular and can be attributed to either faint stars or galaxies (in the case of enhancements) or particles of dust (in the case of depletions). Smaller imperfections may be caused by variations in the sensitivity of the CCD.

The peak intensity at the centre of the image is  $1.435 \times 10^4$  counts. It remains above 99% of this level out to a radius of 250 pixels (2.5 arc-minutes), after which it quickly drops to 98% at 350 pixels (3.4 arc-minutes) and 87% at 584 pixels (5.75 arc-minutes, the nominal field radius). It should be noted, however, that the effect is not perfectly radial and these are approximate values only.

#### 8.8.4 Conclusion

A reduction in the off-axis throughput of the instrument has two effects on its performance:

- It causes the absolute flux calibration to vary across the field of view.
- It increases the limiting magnitude of the instrument for off-axis targets.

The first effect is relevant to multi-slit spectrophotometry, which has not yet been attempted with LDSS-2. It is negligible near to the centre of the field, but if high accuracy were required it would be necessary to correct it outside a radius of 2 to 3 arc-minutes.

The second effect is relevant to any type of observation, but it is of marginal significance. A 2% drop in throughput corresponds to 0.02 magnitudes, while a 13% drop corresponds to 0.15 magnitudes. This is small compared with other parameters that affect the limiting magnitude, though it is prudent to avoid using the edge of the field where possible.

## 8.9 Ghosting

### 8.9.1 Introduction

The aim of this section is to measure the intensity, as a fraction of the incident light, of any ghost images or diffuse background illumination that may be generated within the spectroscope, and where possible to determine which optical elements they are associated with.

When light is normally incident on an air-glass boundary, 96% of will be transmitted, but 4% will be lost to reflection. Anti-reflection coatings improve the throughput dramatically but they are not effective at all wavelengths. Stray light can also be generated by vignetting in the optical system, reflections from the surface of the detector and dust on the surface of optical components. The effect of such interference will depend on whether the reflections are specular or diffuse:

- Specular reflection will cause distinct 'ghost' images and have the potential to cause serious confusion when identifying faint emission lines.
- Diffuse reflection will cause a more general increase in the background light level, though it will not necessarily be spread evenly over the detector.

Unfortunately, it is very difficult to predict in advance how severe these problems will be, so experimental measurements are necessary. If the amount of reflected light were found to be excessive then action could then be taken to reduce it.

### 8.9.2 Experimental Method

A 300 $\mu$ m by 90mm long slit was used for the experiment together with a Copper-Argon arc lamp. An arc lamp was used in preference to a tungsten lamp because it is easier to identify ghost images in a dispersed exposure if

the light source has a line spectrum. Three exposures were taken:

- a 1 second exposure, with no filter or grism
- a 1 second exposure, with the low dispersion grism but no filter
- a 10 second exposure, with the low dispersion grism and the PB filter

### 8.9.3 Data Reduction

The diffuse background in an exposure was measured by subtracting the bias level, then summing over first the area containing the foreground image and second over the remainder of the chip. The second sum divided by the first gives the background level relative to the foreground. This method will only work correctly when the area occupied by the foreground image is relatively small.

The relative intensities of the ghost emission lines, relative to their counterparts in the main spectrum, were measured by subtracting the local background levels, summing across the ghost line and across the main line in the dispersion direction, then dividing the first sum by the second. If different numbers of pixel rows had been used to extract the two spectra then it would have been necessary to correct the result accordingly.

### 8.9.4 Results

The first exposure was inspected for ghost images but none were found. However, there was clear evidence of a diffuse background, of which about 45% was concentrated near to the slit and the remainder spread evenly throughout the image. Its intensity was measured to be 23.2% relative to the foreground image, but it extends to the edge of the CCD so this is almost certainly an underestimate. The background is not present in the CCD bias strip so it is unlikely to be an electrical effect.

The second exposure showed four distinct ghost spectra, spanning pixel rows 125..185 and illustrated in figure 8.9. The main spectrum, which covers pixel rows 186..864, is shown in figure 8.10 for comparison. By measuring

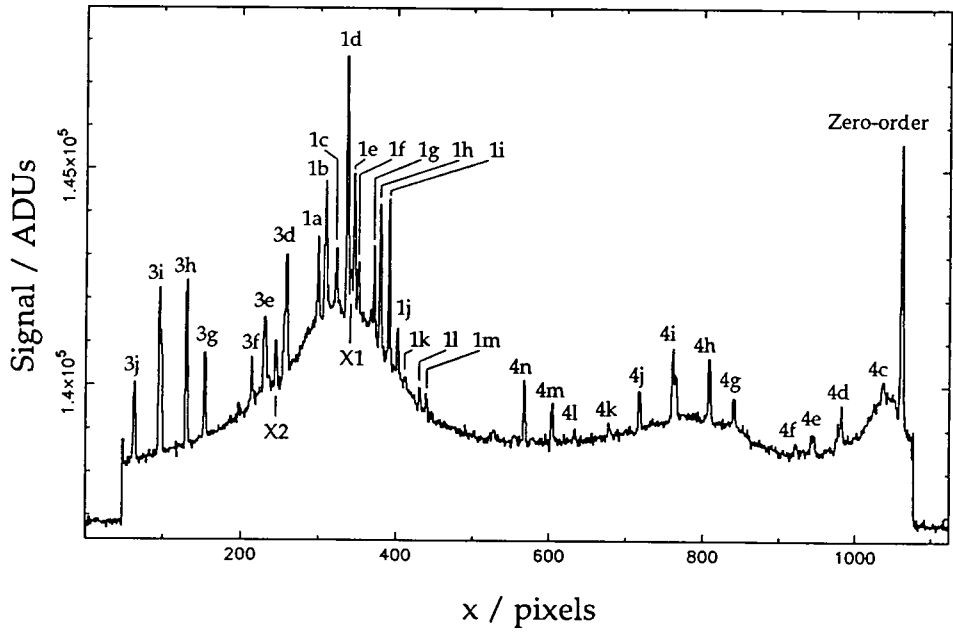


Figure 8.9: Ghost spectra observed in an LDSS-2 calibration exposure

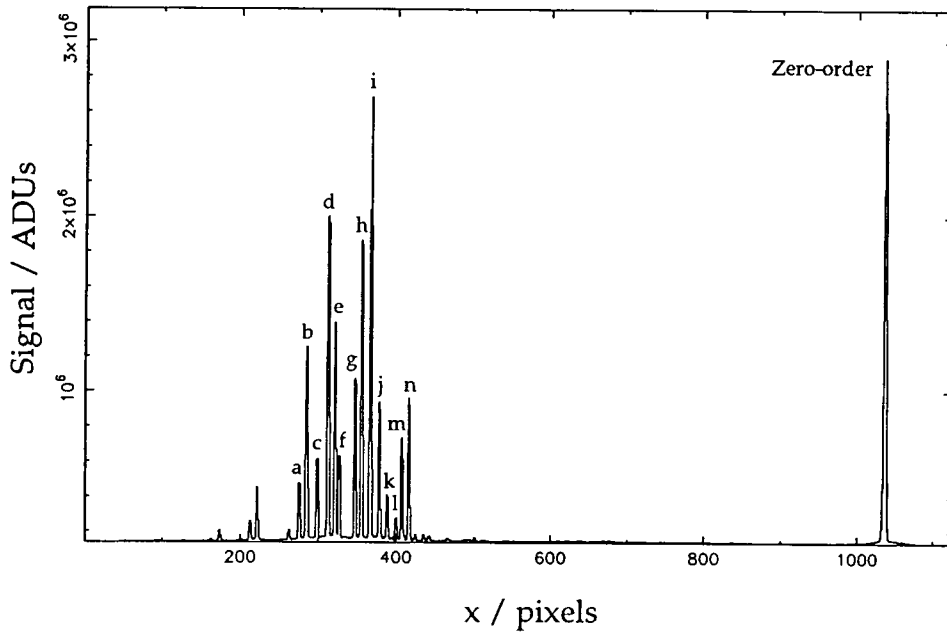


Figure 8.10: Main spectrum for comparison with figure 8.9

the spacing between the lines and the line widths, most of the ghosts were matched with lines in the main spectrum with a reasonable level of confidence. Three ghost spectra were identified:

1. A first order spectrum, of which 13 lines are visible between rows 290 and 450. It is displaced by  $\delta x = -25$  pixels from the main spectrum.
2. A reversed third order spectrum, of which 7 lines are visible between columns 60 and 260.
3. A reversed fourth order spectrum, of which 12 lines are visible between columns 560 and 1040.

Two further lines (marked X1 and X2) were isolated but could not be identified. The strongest ghost line is labelled 1d and has an intensity of 0.28% relative to its counterpart in the main spectrum. The strongest line relative to the main spectrum is labelled 1a and has a relative intensity of 0.43%.

Figure 8.9 does show a diffuse background and its peak (near to column 320) correlates well with the main concentration of lines in figure 8.10. It cannot be meaningfully quantified, as the main spectrum covers too great a fraction of the image, but a comparison with an exposure taken using a different slit indicated that both the local and extended background levels scale with the slit area.

Cross-sections through the third exposure were examined, but there was no evidence of a diffuse background or of any ghost emission lines.

### 8.9.5 Conclusion

The fact that the diffuse background scales with the slit area indicates that it is mainly composed of light that has passed through the aperture mask and that most of the scattering occurs in the collimator and the camera. It should therefore be possible to reconcile the level of the background with the optical efficiency of those two components.

The throughput of the collimator and the camera were measured by the RGO prior to their installation in LDSS-2. Between 7000 and 8000Å (where most of the CuAr emission lines are concentrated) the combined throughput averages to 48%, so 52% of the incident light is lost. This includes the effects of scattering, reflection and absorption.

A background level of 23% corresponds to 19% of the incident light, or 36% of the light that is lost. These measurements are therefore consistent with the efficiency, though it was not expected that such a large proportion of the scattered/reflected light would reach the detector. Possible explanations would include reflections off the surface of the CCD (which are not included in the efficiency calculation above) and an increase in the level of dust and other contamination on the lens surfaces.

The background should have little effect on most astronomical exposures because the light in an astronomical image is usually highly localised. The peak count rate may therefore be high but the average over the field as a whole will be much lower. A problem is more likely to occur when taking calibration exposures using a comparison lamp and this was encountered when measuring the filter transmission functions. The solution adopted in that case was to reduce the length of the slit and thus reduce the amount of light available to be scattered.

The third and fourth order ghost spectra may result from internal reflections in the grism or from reflection off another spectrograph component. The first order ghost spectrum may be caused in the same way but it could also result from reflections elsewhere in the spectrograph. A relative intensity of less than 0.5% should not significantly affect an astronomical exposure, but it is (evidently) sufficient to affect a calibration exposure. Care is therefore necessary when reducing such images.

## 8.10 System Throughput

### 8.10.1 Introduction

The aim of this section is to measure the end-to-end quantum efficiency, as a function of wavelength, that can be achieved when observing with LDSS-2.

There are several ways in which the quantum efficiency of an astronomical system can be defined. The definition that will be used in this section is as follows:

$$E_q = N_{\text{out}}/N_{\text{in}}$$

where, for a given exposure time and wavelength range,  $N_{\text{in}}$  is the number of photons from a given astronomical target that would strike the primary mirror if the air mass were zero, and  $N_{\text{out}}$  is the number of photons from the target that would be detected by the CCD chip if the air mass were one.

This definition of  $E_q$  includes the following sources of inefficiency:

- the absorption caused by the atmosphere, normalised for a target at the zenith
- the absorption and scattering caused by the primary and secondary telescope mirrors
- the absorption, reflection and scattering caused by the LDSS collimator, grism and camera
- any vignetting that occurs after the light has been reflected by the primary mirror
- the quantum inefficiency of the CCD detector

A photon is defined to have been detected by the CCD if it increases the number of electrons measured by the charge amplifier, as it is that value which determines the level of shot noise in the final signal.

### 8.10.2 Theory

The absolute flux  $F$  from a star is measured in Janskys, where 1Jy is equal to  $10^{-26} \text{W m}^{-2} \text{Hz}^{-1}$ . Multiplying this by the collecting area of the mirror,  $A$  (in  $\text{m}^2$ ), the bandwidth,  $\Delta f$  (in Hz), and the exposure time,  $t$  (in s), gives the total amount of energy collected during an exposure.

A photon of frequency  $f$  has energy  $h \cdot c / \lambda$ , where  $h$  is Planck's constant and  $c$  is the speed of light, so the number of photons collected,  $N_{\text{in}}$ , is given by:

$$N_{\text{in}} = F \cdot A \cdot \Delta f \cdot t \cdot \lambda / h \cdot c$$

In the limit,  $\Delta f$  is equal to  $c \cdot \Delta \lambda / \lambda^2$  for small  $\Delta f$ , giving:

$$N_{\text{in}} = F \cdot A \cdot \Delta \lambda \cdot t / h \cdot \lambda$$

Extracting the spectrum from the image gives the number of counts per pixel column,  $C_x$ . (In RGO literature, a count is often described as an 'ADU' or 'Analogue to Digital converter Unit'.)  $N_{\text{out}}$  is related to  $C_x$  by the equation:

$$N_{\text{out}} = C_x \cdot \Delta \lambda / d \cdot g$$

where  $g$  is the gain of the CCD (the number of counts per electron) and  $d$  is the dispersion (the wavelength increment per pixel). Dividing  $N_{\text{out}}$  by  $N_{\text{in}}$  gives the quantum efficiency:

$$E_q = C_x \cdot h \cdot \lambda / F \cdot A \cdot d \cdot g \cdot t$$

The following items of information are therefore required in order to calculate the efficiency:

- an absolute flux spectrum of the calibration star
- a dispersed image of the calibration star, with a known exposure time and zenith distance
- a wavelength calibration function for the dispersed image (which can also be used to calculate the dispersion)

- the collecting area of the primary telescope mirror
- the gain of the CCD detector

The CCD gain can be determined by measuring how the noise level in a frame varies with the signal level. The signal from a CCD is subject to three types of noise, which sum in quadrature:

$$\sigma_T^2 = \sigma_{RN}^2 + \sigma_S^2 + \sigma_{FF}^2$$

where  $\sigma_T$  is the total noise,  $\sigma_{RN}$  is the readout noise,  $\sigma_S$  is the shot noise and  $\sigma_{FF}$  is the flat-field noise.

The readout noise varies randomly from pixel to pixel and from frame to frame. Its RMS amplitude depends on the specific CCD chip and amplifier being used, and on the temperature, but is otherwise constant. A typical value would be between 2 and 20 electrons for an astronomical CCD system.

The shot noise also varies randomly between pixels and between frames, but unlike the readout noise its amplitude varies with the signal level. It obeys poisson statistics, so the RMS amplitude is equal to the square root of the signal (both measured in electrons).

The flat-field noise varies randomly between pixels, but for any given pixel and signal level it is constant between frames (as it is fixed when the CCD is manufactured). It is directly proportional to the signal level.

For any given frame, a plot of noise squared versus signal level would thus follow a quadratic equation of the form:

$$\sigma_T^2 = \sigma_{RN}^2 + g \cdot C + (f \cdot C)^2$$

where  $C$  is the signal level,  $g$  is the gain of the CCD (in counts per electron), and  $f$  is a constant representing the flat-field noise. Note that both  $\sigma$  and  $C$  are measured in counts (not electrons).

Using this equation it would be possible to determine  $g$  from a single frame by means of a quadratic least-squares fit, but a more accurate result is possible if two test frames are available. For a given image, the flat-field noise does not vary from frame to frame, so if two frames of an identical image are subtracted then the flat-field noise cancels out. The readout and shot noise are random, so they do not cancel and are in fact increased by a factor of 2. The noise is thus given by:

$$\sigma_D^2 = 2\sigma_{RN}^2 + 2g \cdot C$$

The gradient can now be calculated using a linear least-squares fit and is equal to  $2g$ .

### 8.10.3 Experimental Method

Four criteria were used to select a suitable calibration star:

- the availability of an absolute flux spectrum for the star, preferably in electronic form
- the zenith distance at which the star can be observed (which should be as small as possible, to minimise the scope for error when the result is scaled to one air mass)
- the luminous intensity of the star (which must give a satisfactory count rate at all relevant wavelengths)
- the extent to which the spectrum is smooth (large gradients are undesirable, as they increase the sensitivity of the experiment to errors in the wavelength calibration)

The final selection cannot be made until the time of the observation is known, as the time determines the zenith distance. In the event two sets of exposures were taken on two different nights, as detailed in table 8.11.

Date	Time	Object	Air Mass
22/08/92	01:40-02:00UT	BD +28 4211	1.01-1.03
22/08/92	21:31-21:56UT	BD +25 3941	1.02-1.05

Table 8.11: LDSS-2 system throughput calibration exposures

A very wide slit was used (12.4 arc-seconds across) in order to minimise the amount of light lost from the edge of the seeing disk. This does result in a substantially higher night-sky background level and makes the wavelength calibration more difficult, but it has little effect on the spectral resolution of the observations themselves because most of the light from the star is still concentrated in the centre of the seeing disk.

Exposures were taken with each of the three installed grisms. The exposure times were chosen to give strong but unsaturated spectra and varied between 20s and 60s. On both nights, two additional dispersed exposures were taken with a tungsten lamp with identical exposure times in order to calculate the gain of the CCD.

#### 8.10.4 Data Reduction

The image of the spectrum was sky-subtracted using the FIGARO program 'POLYSKY' and reduced to a 1D spectrum (equal to  $C_x$ ) using the program 'EXTRACT'. Wavelength calibration was performed by shifting the polynomials in appendix A by an appropriate offset. This is not a completely satisfactory method, but the large width of the slit prevents the use of normal wavelength calibration procedures. The spectrum was rebinned onto a linear wavelength scale using the program 'SCRUNCH'. The program was instructed to conserve the total flux so the result was equal to  $C_x \cdot \Delta\lambda / d$ .

The absolute flux spectrum is supplied with FIGARO in the form of a table, which was converted into a 'spiketrum' (a spectrum defined only at a

specified set of wavelengths) using the program 'GSPIKE'. The spiketrum was divided by the measured spectrum using the program 'CSPIKE', which also multiplies by the exposure time and divides by the size of a wavelength bin. The result was therefore equal to  $F \cdot d \cdot t / C_x$ .

The efficiency is equal to  $C_x \cdot h \cdot \lambda / F \cdot A \cdot d \cdot g \cdot t$  and was calculated by dividing the result of CSPIKE into  $\lambda \cdot h / 10^{-29} \cdot g \cdot A$ . The measurements below 3000Å and above 8600Å were excluded because of their signal to noise ratio. The remainder were interpolated and smoothed, and the result scaled to one airmass using data from King (1985).

The CCD gain was calculated using the method described in section 8.10.2. The results are listed in table 8.12.

Exposure	g
50985/86	0.403
49487/88	0.425
	/counts electron <sup>-1</sup>

Figure 8.12: LDSS-2 CCD gain measurements for system throughput calibration

The collecting area of the telescope was calculated using information obtained from Unger *et al* (1988, p30). The working diameter of the mirror is 4180mm, but 9.083% of its surface is obstructed, so the collecting area is 12.48m<sup>2</sup>.

### 8.10.5 Results

Results were obtained on both nights for all three grisms. With the medium-blue grism the throughput was found to peak at 16.7% on the first night and 20.4% on the second. This difference is not unusual, as the transparency of the atmosphere varies from night to night. The definition of the system efficiency assumes that the sky is clear, so it is the higher value (the result from the second night) that should be used.

The measured efficiency functions are plotted graphically in figure 8.11 and summarised in table 8.13.  $T_0$  is the peak throughput,  $\lambda_0$  is the wavelength of that peak, and  $\lambda_1$  and  $\lambda_2$  are the half-power points. The results for the medium-blue grism are also listed in table 8.14 at 500Å intervals, together with predictions based on laboratory measurements of the optical components performed by the RGO.  $T_{\text{atm}}$  is the throughput of the atmosphere (taken from King (1985)),  $T_{\text{tel}}$  the telescope (assuming a canonical 85% reflectance at each mirror surface),  $T_{\text{opt}}$  the collimator and camera,  $T_{\text{grs}}$  the grism and  $T_{\text{CCD}}$  the CCD detector.  $T_{\text{pred}}$  is the throughput predicted by multiplying the preceding values and  $T_{\text{meas}}$  is the throughput measured.

Grism	$\lambda_0$	$T_0$	$\lambda_1$	$\lambda_2$
Medium-blue	5915	20.4	4135	7225
Medium-red	6100	21.1	4870	7445
High	5175	15.4	4070	5520
	/Å	/%	/Å	/Å

Figure 8.13: Summary of measured LDSS-2 system throughput

$\lambda$	$T_{\text{atm}}$	$T_{\text{tel}}$	$T_{\text{opt}}$	$T_{\text{grs}}$	$T_{\text{CCD}}$	$T_{\text{pred}}$	$T_{\text{meas}}$
4000	76	72	53	58	60	10	7.3
4500	85	72	67	73	63	19	14.3
5000	89	72	71	78	63	22	17.8
5500	91	72	78	76	67	26	19.6
6000	92	72	84	69	69	26	20.4
6500	95	72	81	63	70	24	17.5
7000	97	72	68	57	69	19	12.7
7500	98	72	51	48	64	11	7.6
/Å	/%	/%	/%	/%	/%	/%	/%

Figure 8.14: Comparison of measured and expected LDSS-2 system throughput

### 8.10.6 Conclusion

It can be seen that the throughput is approximately 20% lower than expected at 4000Å, falling to 35% lower at 7000Å. Although at first sight this is a very

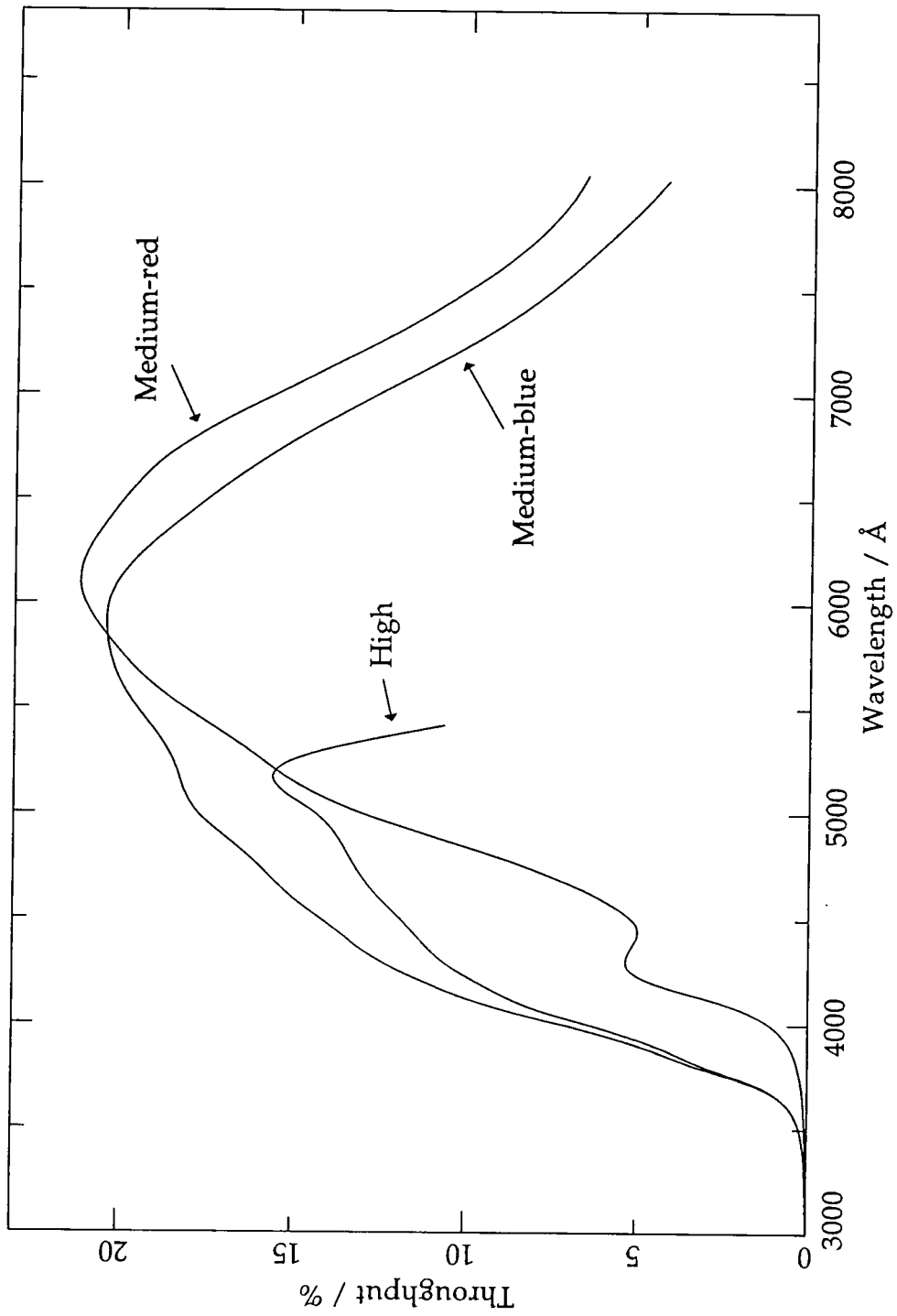


Figure 8.11: LDSS-2 system throughput

large discrepancy, it is within the range experienced when developing previous instruments of this type. Possible explanations include higher than expected atmospheric extinction, lower mirror reflectance, contamination of exposed lens surfaces, and lower CCD quantum efficiency.

## Chapter 9: Conclusion

My main achievements during my period of study have been my role in the construction and installation of LDSS-2 and my study of mask manufacturing techniques.

LDSS-2, shown in figure 9.1, is now a fully operational, common-user instrument. It was used by four groups of astronomers following its commissioning run in August 1992:

- Ellis and Glazebrook (Durham), who used it to conduct a redshift survey of faint field galaxies
- Shanks *et al* (Durham), who also used it to conduct a survey of faint galaxies, as a backup program for a MARTINI observing run
- Butcher *et al* (Kapteyn, Roden), who used it to investigate faint blue galaxies in a rich, high-redshift cluster
- Mason *et al* (MSSL), who used it for identification and follow-up observations of ROSAT sources

Figures 9.2, 9.3, 9.4 and 9.5 show examples of spectra obtained by Allington-Smith, Oemler, Ellis and Zirbel during the commissioning period. The targets are members of a group of galaxies associated with the radio galaxy 5C12.121.D. The exposure time was  $10^4$  seconds. In each case several emission and absorption lines can be seen. This allows the redshifts to be measured and confirms that the targets are indeed group members. Spectra for a further 10 targets were obtained from the same exposure but were determined to be either foreground or background objects. Figure 9.6 shows a typical dispersed multi-slit exposure.

The LDSS-1 project described in chapter 4 demonstrated the extent to which

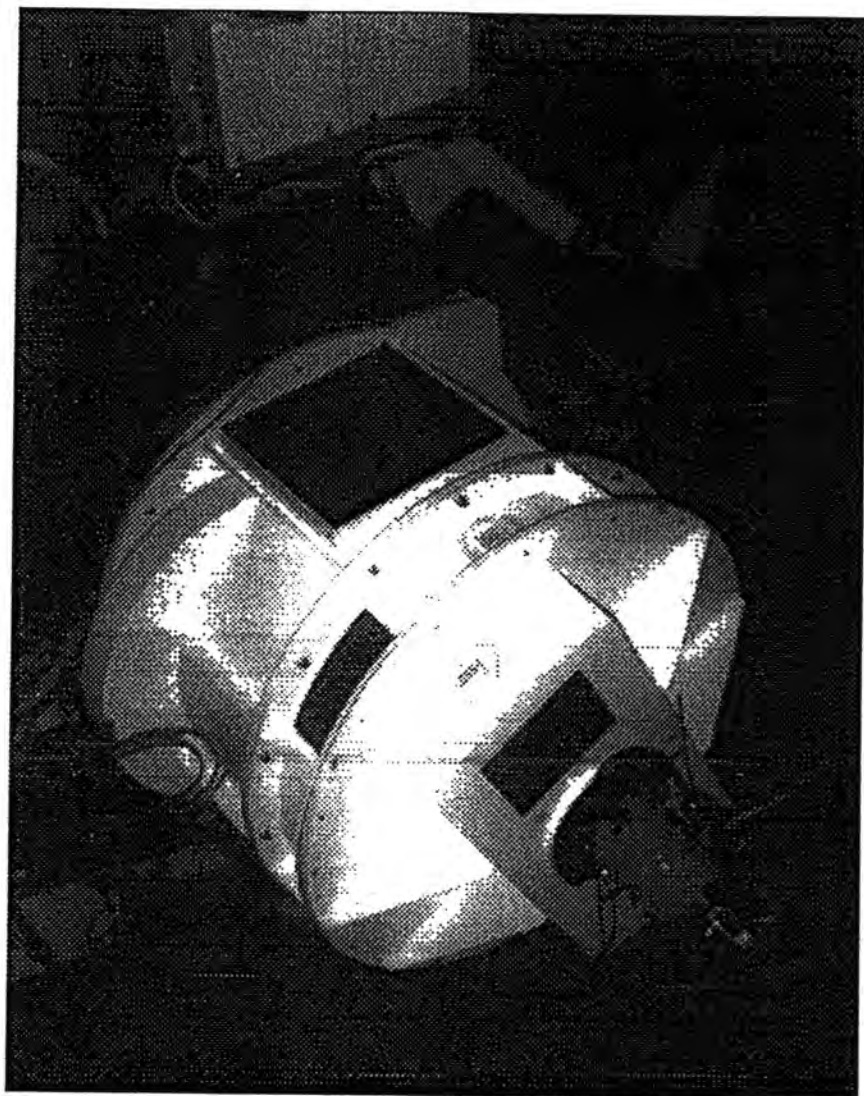


Figure 9.1: LDSS-2, installed at the Cassegrain focus of the WHT

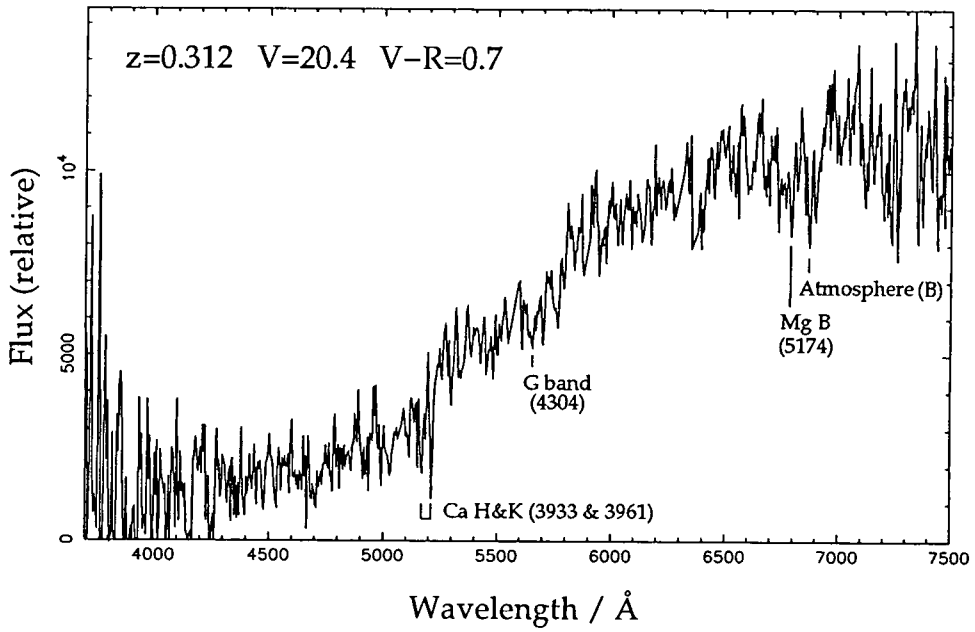


Figure 9.2: The spectrum of 5C12-group galaxy number 121

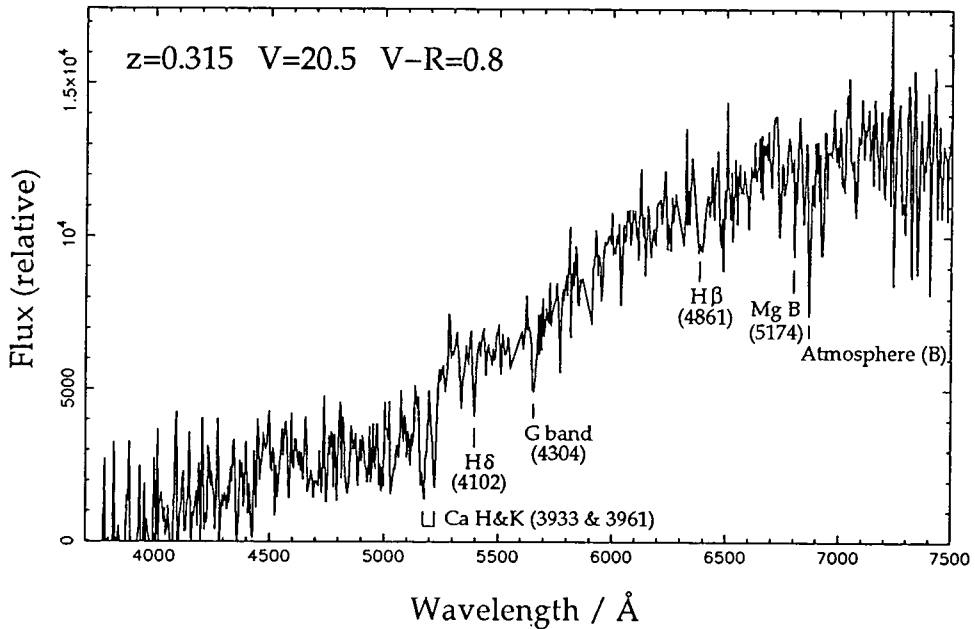


Figure 9.3: The spectrum of 5C12-group galaxy number 131

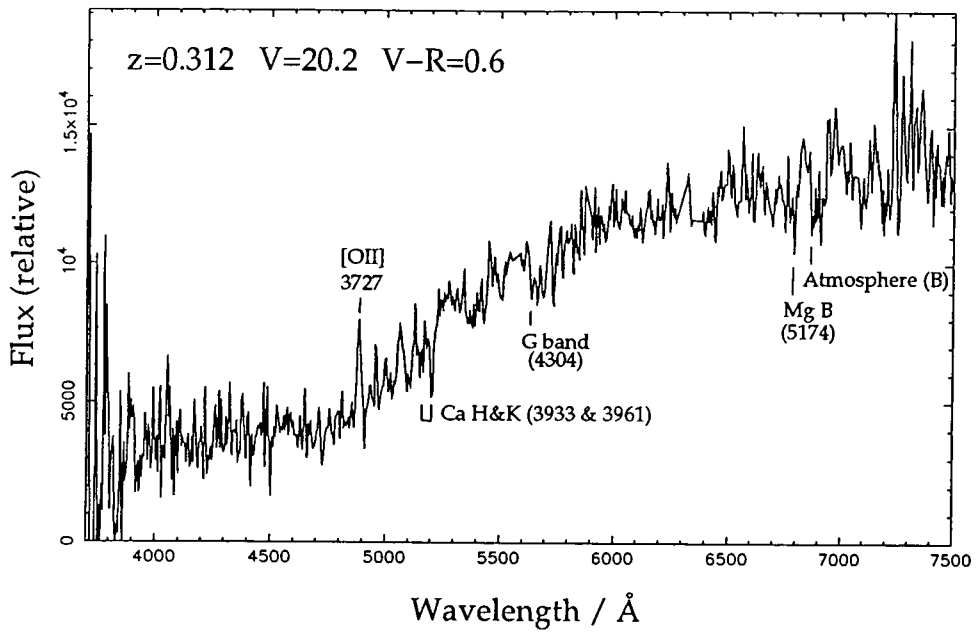


Figure 9.4: The spectrum of 5C12-group galaxy number 180

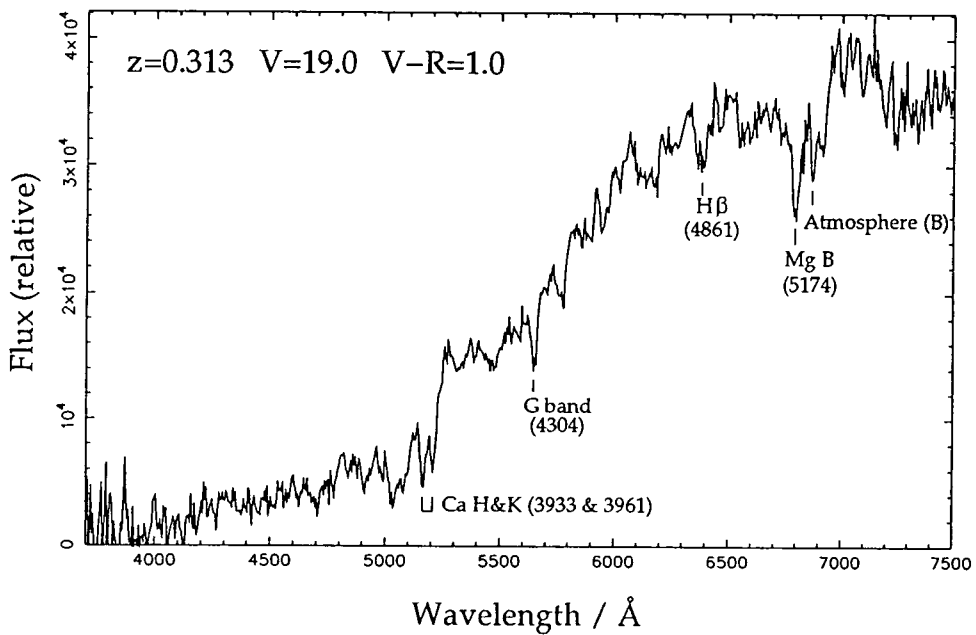


Figure 9.5: The spectrum of 5C12-group galaxy number 217

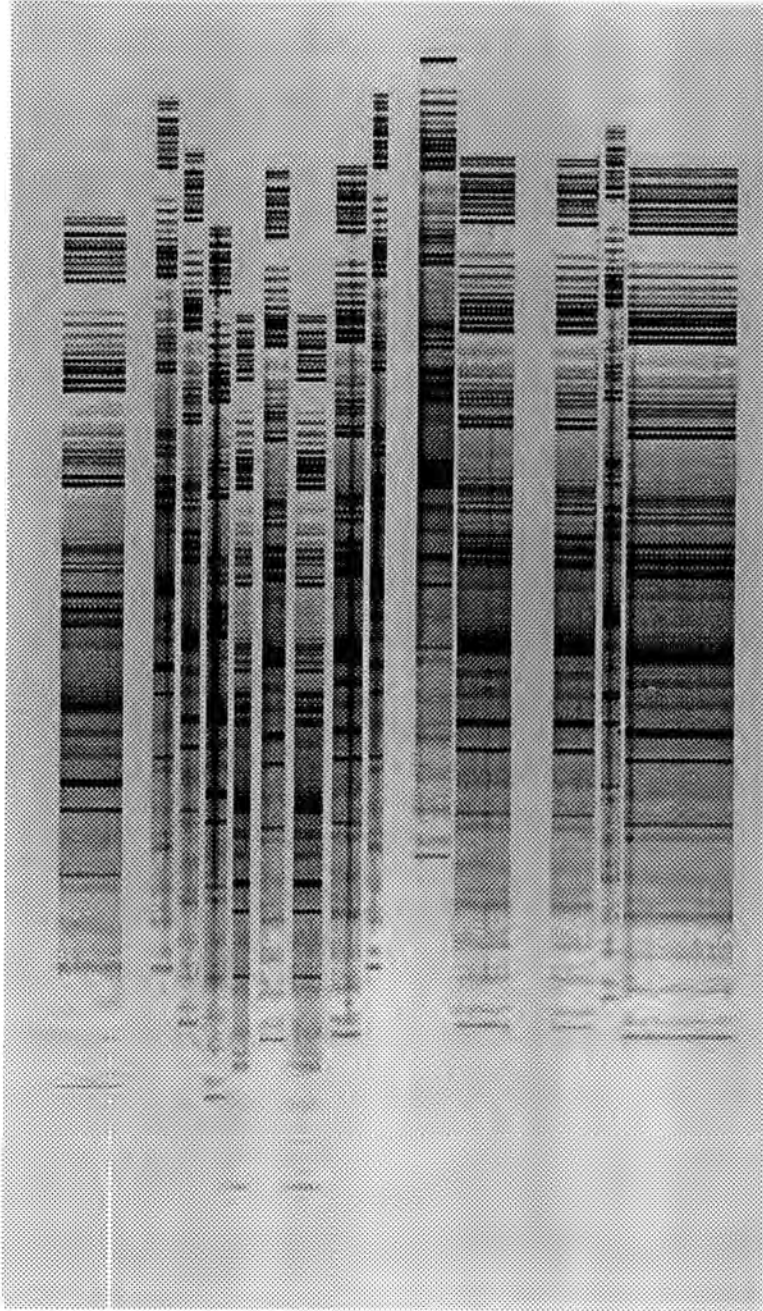


Figure 9.6: A typical dispersed LDSS-2 exposure

multi-slit spectroscopy can reduce the telescope time needed to conduct a large survey. The majority of the targets were identified, despite their proximity to the limiting magnitude of the instrument. The project resulted in a paper (Colless *et al*, 1991) concerning the count-magnitude and colour-magnitude relationships for faint QSOs and faint galactic stars.

The FOS-2/ISIS multi-slit unit, though limited in its capability, has also produced useful scientific data. For example, it was used to identify two further members of the galaxy cluster described above. For most purposes the unit has now been superseded by LDSS-2, but its development was justified by its use during the interim period and by the information it provided about mask manufacture, field acquisition and data reduction methods (Allington-Smith *et al*, 1990b).

A considerable amount of experience was gained during the construction of LDSS-2 and it is hoped that this will benefit future instrumentation projects undertaken at Durham. Instruments are becoming more complicated, so greater emphasis will have to be placed on specification, testing and documentation. However, it would be a mistake to treat instrument development purely as an engineering task, as that would make it much more difficult to research new techniques.

The tests performed prior to and during the commissioning run demonstrated that LDSS-2 performs largely as it was intended and that it is capable of good astronomical performance. The results of the tests were as follows:

- The control system passed the reliability tests performed at Durham and Cambridge, and while some problems were encountered at the telescope, its performance is now satisfactory.
- The flexure tests performed in Cambridge and at the telescope confirmed that the flexure of the instrument is within its specification

and that it should not have any significant effect on the performance of the instrument in normal use.

- The non-chromatic image distortion was found to be approximately radial in nature, reaching 1% at the edge of the field of view. The distortion tests were not sensitive enough to detect any chromatic distortion.
- The grism dispersions were found to differ from their predicted values, but it was decided that the difference was acceptable. The dispersion varies significantly across the field of view, so a separate wavelength calibration spectrum is required for each slit.
- The transmission functions of three of the filters (PR, S1 and S2) were found to agree well with their predictions, but the other three (PB, PV and S3) had throughputs that were significantly lower than expected. The reason for this is not known and further tests would be needed to determine whether it is a measurement error or a real effect.
- The measured throughputs of the medium dispersion grisms were in good agreement with their predictions. It was not possible to test the throughput of the low and high dispersion grisms.
- The throughput of the instrument was found to vary across its field of view. The effect is approximately radial: at 2.5 arc-minutes from the field centre the relative throughput is 99%, at 3.4 arc-minutes it is 98%, and at 5.75 arc-minutes it is 87%. This is acceptable, but it is prudent to avoid using the edge of the field where possible.
- The scattered light level at the detector was found to be substantial, equal to 23% of the light passing through the aperture mask. Dispersed exposures were additionally found to contain a number of ghost images. The effect on astronomical exposures will be small, but may be significant for some types of calibration exposure.

- The throughput of the observing system as a whole (including the CCD, instrument, telescope and 1 airmass) was found to peak at 20.4% (5915Å) with the medium-blue grism, 21.1% (6100Å) with the medium-red grism, and 15.4% (5175Å) with the high dispersion grism. These figures are lower than would be expected by calculation, but in line with experience with previous instruments.

An 8-position aperture wheel was found to be sufficient for most purposes and is a good balance between capacity, physical size and access time. Loading aperture masks does require some skill as care is needed to ensure correct alignment, but the task is not unduly difficult or time-consuming. The filters and grisms are more difficult to change, but this is acceptable because frequent access is not required.

A comparison between the field acquisition procedure used with LDSS-2 and that used with the FOS-2 multi-slit unit demonstrates the importance of a direct imaging capability. Imaging may also be used in the future to allow astrometry and target selection to be carried out during the observing run, though the practicality and efficiency of this method have not yet been assessed.

My study of mask manufacturing technologies had the objectives of identifying a fabrication method suitable for use with FOS-2/ISIS and LDSS-2 in the short term and investigating technologies that could be developed to meet the needs of LDSS-2 and other instruments in the longer term. My findings were as follows:

- Photochemically etched masks have acceptable slit quality but are poor compared to CAMM-3 masks. The fabrication lead time is substantial, reducing the flexibility with which the astronomer can operate. Etching is a relatively mature technology so there is limited scope for future development.

- Mechanically punched masks suffer from a number of disadvantages, including poor slit quality and inflexible slit dimensions. The punching head wears quickly, so the quality is likely to be variable and the maintenance requirements high. Some of these characteristics could be improved with development, but on balance punching is unlikely to become competitive with other fabrication methods.
- Mechanically milled masks produced using CAMM-3 have been used successfully with both FOS-2/ISIS and LDSS-2. The slit quality is excellent and the cutting speed acceptable, but naturally an increased speed would be advantageous. CAMM-3 has in general operated reliably but it was not designed to cut metal and Interact-4 is expected to be considerably more robust.
- Laser cut masks have the potential to offer shorter lead times and improved equipment reliability compared to mechanical milling, while maintaining a similar level of quality. However, these goals have not yet been achieved. Lemaître *et al* have shown that using a Nd-YAG laser to cut metal masks is practical, but a laser powerful enough to operate at high speeds would (at present) be prohibitively expensive. The work at Durham to use a CO<sub>2</sub> laser to cut plastic masks is at an early stage of development and carries a significant technical risk.
- Movable slit masks are in most respects ideal for multi-slit spectroscopy: they are reusable, they can be configured while the telescope is on target, and they can have a slit quality comparable to a long-slit spectrograph. Their limitation is that they cannot generate an arbitrary slit layout, which greatly reduces their multiplex gain. They are therefore best suited to instruments such as FORS, where remote operation is a particular advantage.
- Liquid crystal masks are currently at a very early stage of

development. They would combine the re-usability and remote configuration of a movable slit mask with the arbitrary layout of a milled or laser-cut mask. However, there are potential disadvantages, and a system intended for astronomical use would have to offer high resolution, a large contrast ratio, and high throughput when transparent. It is too early to say whether these objectives can be achieved, but in view of the potential benefits further research is justified.

In the short term it is intended that LDSS-2 mask production be transferred from CAMM-3 to Interact-4 once the latter device has been commissioned. In the longer term laser cut masks and liquid crystal masks appear to have the most potential for development, but they would have to demonstrate clear technical advantages over mechanical milling if they were to be adopted.

Future developments in multi-slit spectroscopy will be strongly motivated by the requirements of the coming generation of 8-metre class telescopes. The challenge is to maintain the same field of view and spectral resolution without allowing the dimensions of the instrument to scale with the telescope aperture. Several 8-metre class spectrographs have been proposed or are under development, including FORS for the VLT (Appenzeller and Rupprecht, 1992), LRIS for the Keck Telescope, and IFOS for the Gemini telescopes (Allington-Smith *et al*, 1992b).

# Appendix A: LDSS-2 Wavelength Calibration

## A.1 Introduction

This appendix details a set of wavelength calibration lines suitable for use with LDSS-2, together with best fit polynomials derived from those lines.

Separate line lists are given for each of the four grisms. In all cases, they were obtained using a copper-argon arc lamp. The lists were selected to give reasonable coverage of the relevant wavelength range, and screened to exclude lines likely to degrade the result. Full details of the methods used can be found in section 8.4.

Note that the polynomial coefficients and the line channel numbers are only valid for a slit in the exact position specified. A first order correction can be obtained by replacing  $x$  with  $x+\Delta x$ , but for slits a long way from the field centre (as would occur on a multiobject mask) it is recommended that the entire line list be re-measured.

In tables A.2 to A.5, the channel is the  $x$ -coordinate of the line centre when the slit is at the position specified in table A.1.  $\sigma$  is the assumed line width used by the gaussian fitting routine.  $\lambda_{\text{std}}$  is the true wavelength of the line, taken from Zuiderwijk and Knapen (1989). Note that values for blended lines are only accurate to 2 decimal places.  $\lambda_{\text{calc}}$  is the calculated wavelength when polynomial is applied to  $x$ -position of line centre. Error is the difference between measured and calculated wavelengths.

## A.2 Polynomial Coefficients

The coefficients for the best-fit wavelength calibration polynomials are given in table A.1. The slit channel is the x-coordinate of the centre of the slit that was used to perform the calibration. The error is the RMS deviation between the measured and interpolated wavelengths over the relevant wavelength range.

Grism	Slit Channel	Order	Coefficients/Å	Error/Å
Low	531.303	5	$a_0 = +1.15789E+04$ $a_1 = -1.07968E+01$ $a_2 = -2.73575E-03$ $a_3 = +9.07911E-06$ $a_4 = -1.33976E-08$ $a_5 = +8.30623E-12$	0.563
Med-B	531.303	4	$a_0 = +8.56803E+03$ $a_1 = -5.44331E+00$ $a_2 = +2.84236E-04$ $a_3 = -2.02654E-07$ $a_4 = +2.91973E-10$	0.576
Med-R	532.176	4	$a_0 = +8.57513E+03$ $a_1 = -5.43117E+00$ $a_2 = +2.12007E-04$ $a_3 = -7.83746E-08$ $a_4 = +2.18868E-10$	0.669
High	531.303	3	$a_0 = +5.66500E+03$ $a_1 = -2.48389E+00$ $a_2 = +1.04542E-04$ $a_3 = +9.60242E-08$	0.390

Table A.1: Wavelength calibration polynomial coefficients

### A.3 Low Dispersion Grism

Table A.2 lists the recommended wavelength calibration lines for the low dispersion grism. Line identification charts are shown in figures A.1 and A.2.

Line	Channel	$\sigma/\text{\AA}$	$\lambda_{\text{std}}/\text{\AA}$	$\lambda_{\text{calc}}/\text{\AA}$	Error/ $\text{\AA}$
1	162.327	1.0	9784.503	9784.703	0.200
2	173.710	1.0	9657.786	9657.572	-0.214
3	212.512	1.0	9224.499	9224.343	-0.156
4	221.591	1.0	9122.967	9123.047	0.080
5	262.415	1.0	8667.944	8668.161	0.217
6	275.613	1.0	8521.422	8521.360	-0.062
7	298.741	1.0	8264.523	8264.442	-0.081
8	327.269	1.0	7948.176	7948.189	0.013
9	347.534	1.0	7723.980	7724.011	0.031
10	355.579	1.0	7635.106	7635.132	0.026
11	378.379	1.0	7383.981	7383.597	-0.384
12	388.426	1.0	7272.936	7272.949	0.013
13	399.881	1.0	7147.042	7146.928	-0.114
14	407.134	1.0	7067.218	7067.220	0.002
15	416.408	1.0	6965.430	6965.396	-0.034
16	424.888	1.0	6871.289	6872.401	1.112
17	435.704	1.0	6752.834	6753.915	1.081
18	442.803	1.0	6677.282	6676.249	-1.034
19	466.687	0.8	6416.307	6415.537	-0.770
20	513.152	1.0	5912.085	5911.510	-0.575
21	551.805	1.0	5495.874	5496.447	0.573
22	597.093	1.0	5017.163	5017.063	-0.101
23	602.012	1.0	4965.080	4965.564	0.484
24	631.665	0.8	4657.901	4658.003	0.102
25	669.305	1.0	4277.528	4276.259	-1.269
26	676.894	1.0	4199.630	4200.689	1.060
27	690.009	1.0	4072.110	4071.375	-0.735
28	702.683	1.0	3947.530	3948.064	0.534

Table A.2: Recommended wavelength calibration lines for low dispersion grism

## A.4 Medium Dispersion Blue Grism

Table A.3 lists the recommended wavelength calibration lines for the medium-blue grism. Line identification charts are shown in figures A.3 and A.4.

Line	Channel	Sigma/Å	$\lambda_{\text{std}}/\text{Å}$	$\lambda_{\text{calc}}/\text{Å}$	Error/Å
1	55.871	1.5	8264.523	8264.767	0.243
2	114.535	1.5	7948.176	7948.061	-0.115
3	156.254	1.5	7723.980	7723.836	-0.144
4	172.835	1.5	7635.106	7634.946	-0.160
5	219.831	1.5	7383.981	7383.688	-0.292
6	240.622	1.5	7272.936	7272.867	-0.069
7	264.259	1.5	7147.042	7147.122	0.080
8	279.298	1.5	7067.218	7067.261	0.043
9	298.512	1.5	6965.430	6965.398	-0.032
10	316.225	1.5	6871.289	6871.655	0.366
11	338.597	1.5	6752.834	6753.502	0.668
12	353.144	1.5	6677.282	6676.824	-0.458
13	366.835	1.0	6604.853	6604.770	-0.083
14	402.739	1.5	6416.307	6416.344	0.037
15	408.784	1.0	6384.717	6384.701	-0.016
16	435.768	1.0	6243.120	6243.746	0.626
17	449.693	1.0	6172.030	6171.208	-0.821
18	499.591	1.0	5912.085	5912.468	0.383
19	533.088	1.0	5739.520	5739.927	0.407
20	559.162	1.0	5606.733	5606.327	-0.406
21	580.690	1.0	5495.874	5496.521	0.647
22	642.028	1.0	5187.746	5186.416	-1.330
23	667.034	1.0	5062.037	5061.287	-0.750
24	686.210	1.0	4965.080	4965.879	0.799
25	718.674	1.0	4806.021	4805.542	-0.479
26	726.946	1.0	4764.865	4764.935	0.069
27	772.101	1.0	4545.052	4545.179	0.127
28	779.060	1.0	4510.733	4511.616	0.883
29	844.773	1.5	4199.630	4199.041	-0.589
30	865.032	1.0	4103.912	4104.394	0.482
31	899.055	1.0	3947.530	3947.439	-0.091
32	930.564	1.0	3803.172	3804.460	1.288
33	939.588	1.0	3765.270	3763.956	-1.314

Table A.3: Recommended wavelength calibration lines for medium-blue grism

## A.5 Medium Dispersion Red Grism

Table A.4 lists the recommended wavelength calibration lines for the medium-red grism. Line identification charts are shown in figures A.5 and A.6.

Line	Channel	Sigma/Å	$\lambda_{\text{std}}/\text{Å}$	$\lambda_{\text{calc}}/\text{Å}$	Error/Å
1	57.315	1.5	8264.523	8264.529	0.006
2	115.956	1.5	7948.176	7948.128	-0.048
3	157.653	1.5	7723.980	7723.994	0.014
4	174.224	1.5	7635.106	7635.117	0.011
5	221.202	1.5	7383.981	7383.796	-0.185
6	241.976	1.5	7272.936	7272.974	0.038
7	265.604	1.5	7147.042	7147.172	0.130
8	280.635	1.5	7067.218	7067.279	0.061
9	299.840	1.5	6965.430	6965.369	-0.062
10	317.539	1.5	6871.289	6871.618	0.329
11	339.866	1.5	6752.834	6753.599	0.765
12	354.421	1.5	6677.282	6676.810	-0.472
13	368.109	1.0	6604.853	6604.708	-0.145
14	404.071	1.5	6416.307	6415.836	-0.471
15	410.063	1.0	6384.717	6384.447	-0.270
16	437.034	1.0	6243.120	6243.463	0.343
17	450.914	1.0	6172.030	6171.116	-0.914
18	500.767	1.0	5912.085	5912.469	0.384
19	534.032	1.0	5739.520	5741.042	1.522
20	560.504	1.0	5606.733	5605.349	-1.384
21	581.829	1.0	5495.874	5496.540	0.666
22	643.041	1.0	5187.746	5186.918	-0.828
23	668.046	1.0	5062.037	5061.706	-0.332
24	687.166	1.0	4965.080	4966.502	1.422
25	719.696	1.0	4806.021	4805.659	-0.362
26	728.065	1.0	4764.865	4764.526	-0.339
27	773.086	1.0	4545.052	4545.049	-0.002
28	780.077	1.0	4510.733	4511.261	0.528
29	845.692	1.5	4199.630	4198.214	-1.416
30	865.575	1.0	4103.912	4104.922	1.010

Table A.4: Recommended wavelength calibration lines for medium-red grism

## A.6 High Dispersion Grism

Table A.5 lists the recommended wavelength calibration lines for the medium-blue grism. Line identification charts are shown in figures A.7 and A.8.

Line	Channel	Sigma/Å	$\lambda_{\text{std}}/\text{Å}$	$\lambda_{\text{calc}}/\text{Å}$	Error/Å
1	68.512	2.0	5495.874	5495.344	-0.530
2	86.019	2.0	5451.652	5452.171	0.520
3	151.016	2.0	5292.517	5292.606	0.089
4	194.057	2.0	5187.746	5187.623	-0.124
5	234.031	1.2	5090.495	5090.647	0.152
6	286.079	2.0	4965.080	4965.214	0.134
7	335.071	2.0	4847.810	4848.068	0.258
8	352.734	2.0	4806.021	4806.068	0.047
9	370.171	2.0	4764.865	4764.729	-0.136
10	415.707	2.0	4657.901	4657.393	-0.508
11	436.210	2.0	4609.567	4609.363	-0.204
12	464.006	2.0	4545.052	4544.560	-0.492
13	478.626	2.0	4510.733	4510.621	-0.112
14	526.081	2.0	4400.760	4401.185	0.425
15	549.255	2.0	4348.064	4348.159	0.095
16	555.511	2.0	4333.561	4333.893	0.332
17	633.055	2.0	4158.591	4158.817	0.227
18	645.095	2.0	4131.724	4131.937	0.212
19	657.605	2.0	4103.912	4104.095	0.183
20	707.017	2.0	3994.792	3995.039	0.247
21	729.012	2.5	3947.530	3946.976	-0.554
22	774.003	1.5	3850.581	3849.613	-0.968
23	813.016	2.0	3765.550	3766.259	0.709

Table A.5: Recommended wavelength calibration lines for high dispersion grism

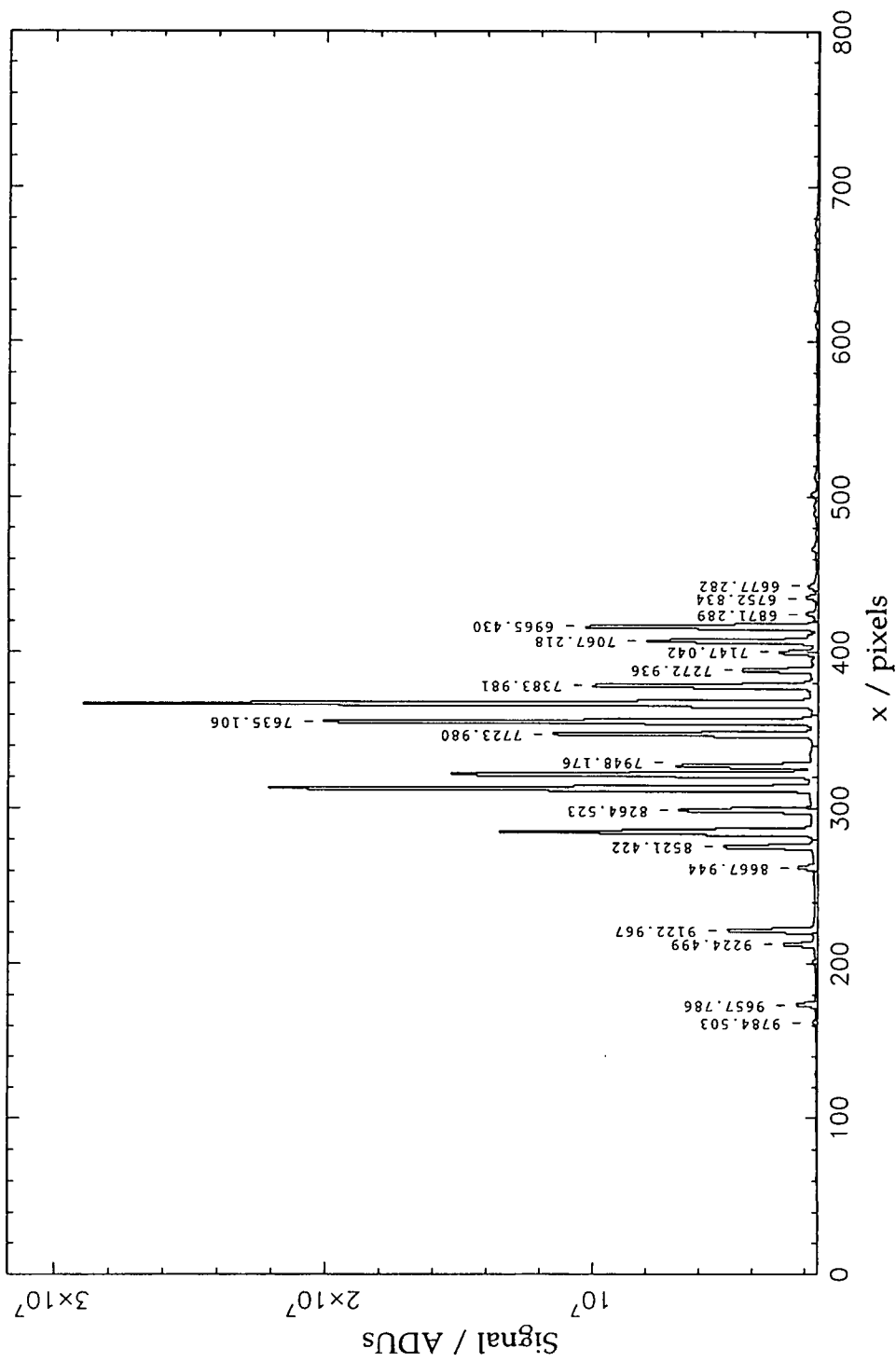


Figure A.1: CuAr line identification chart for low dispersion grism (1)

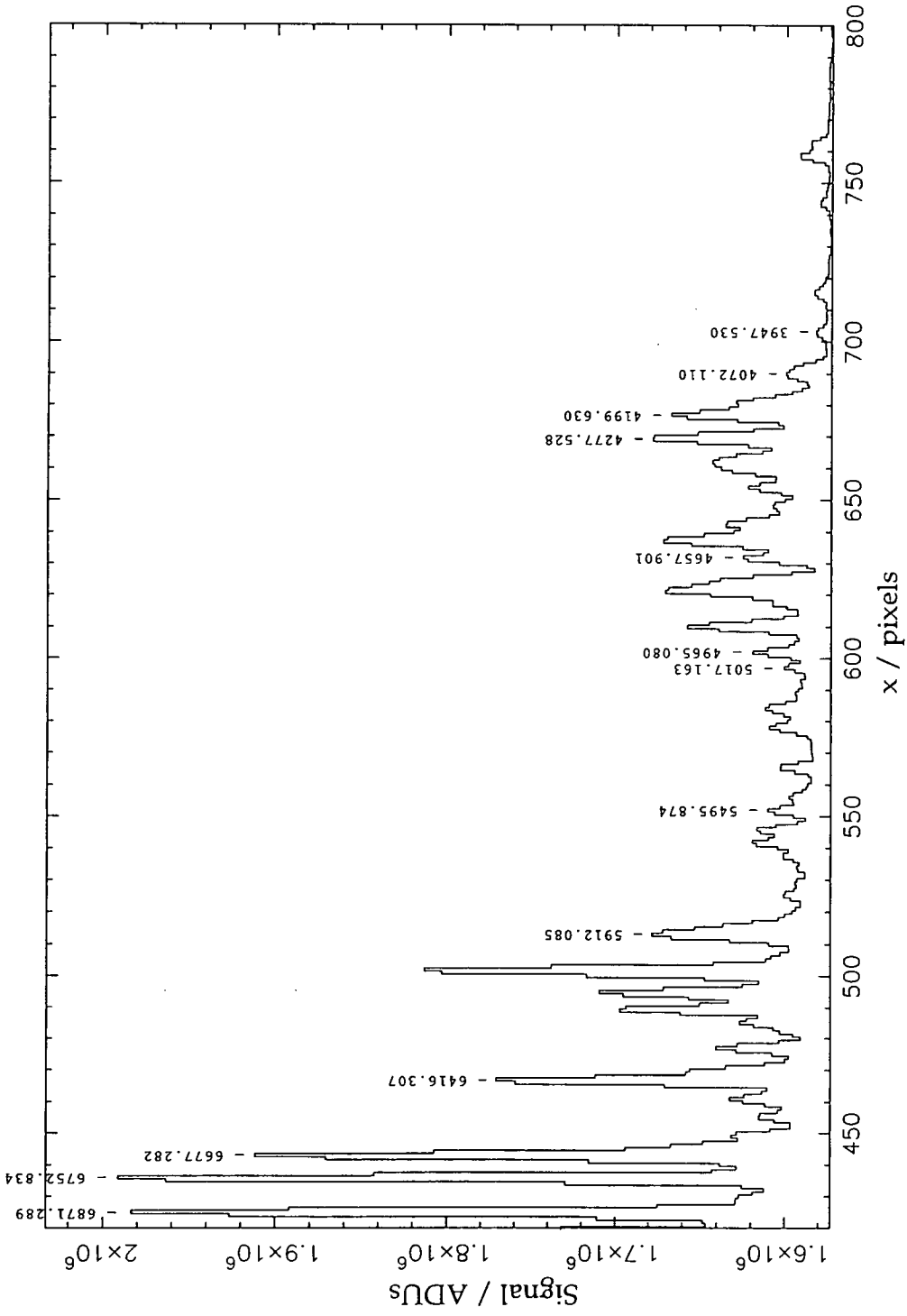


Figure A.2: CuAr line identification chart for low dispersion grism (2)

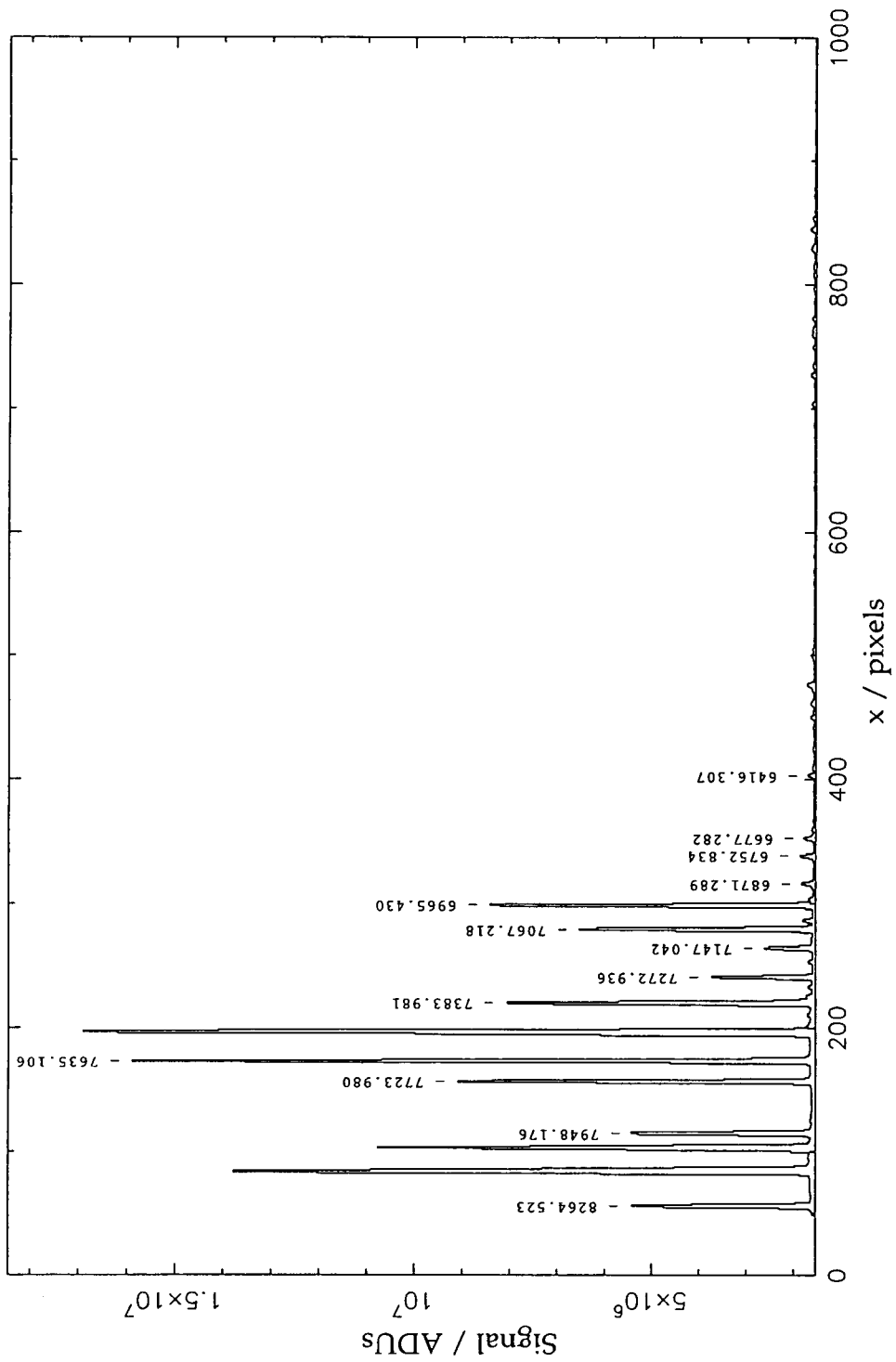


Figure A.3: CuAr line identification chart for medium-blue grism (1)

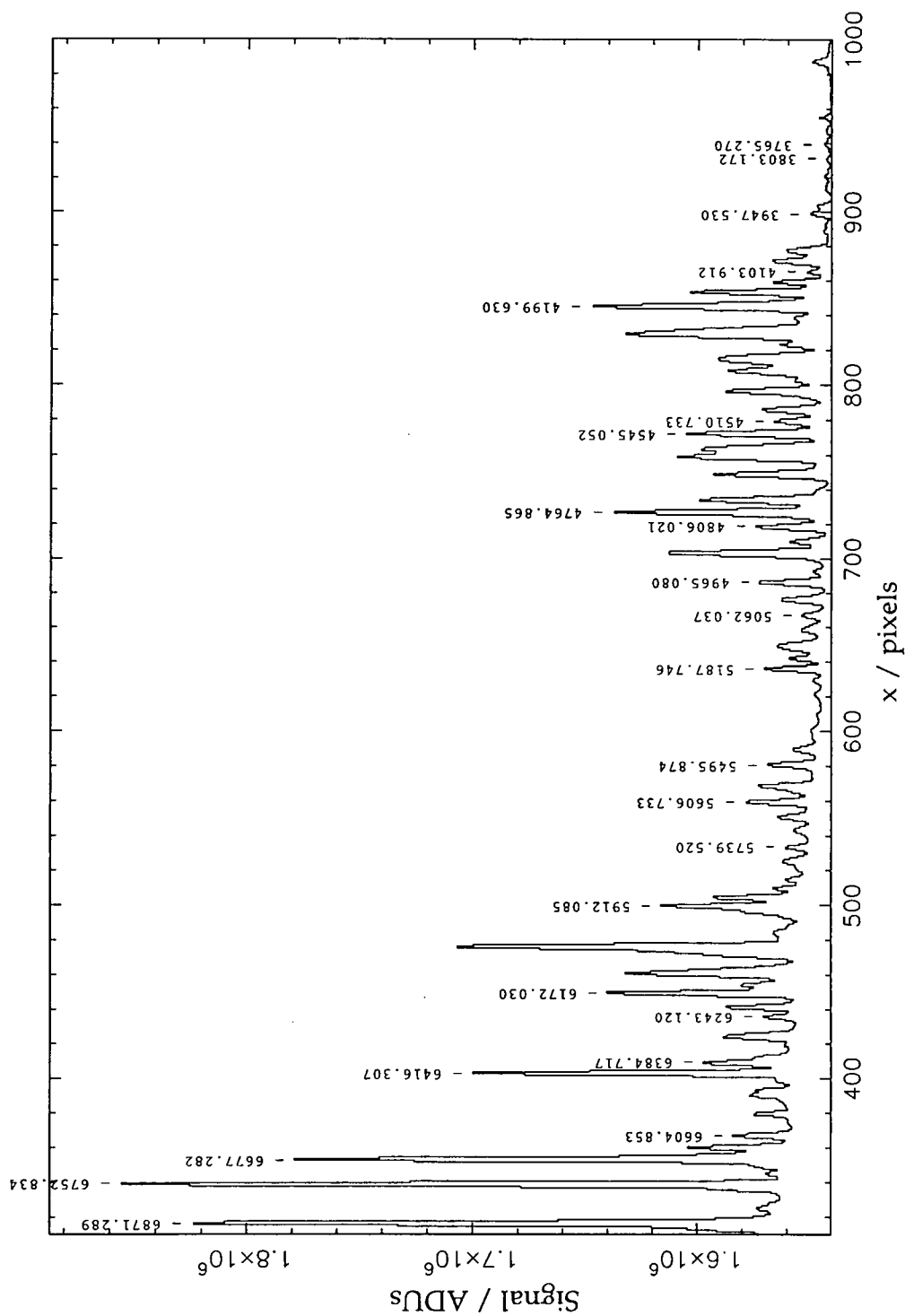


Figure A.4: CuAr line identification chart for medium-blue grism (2)

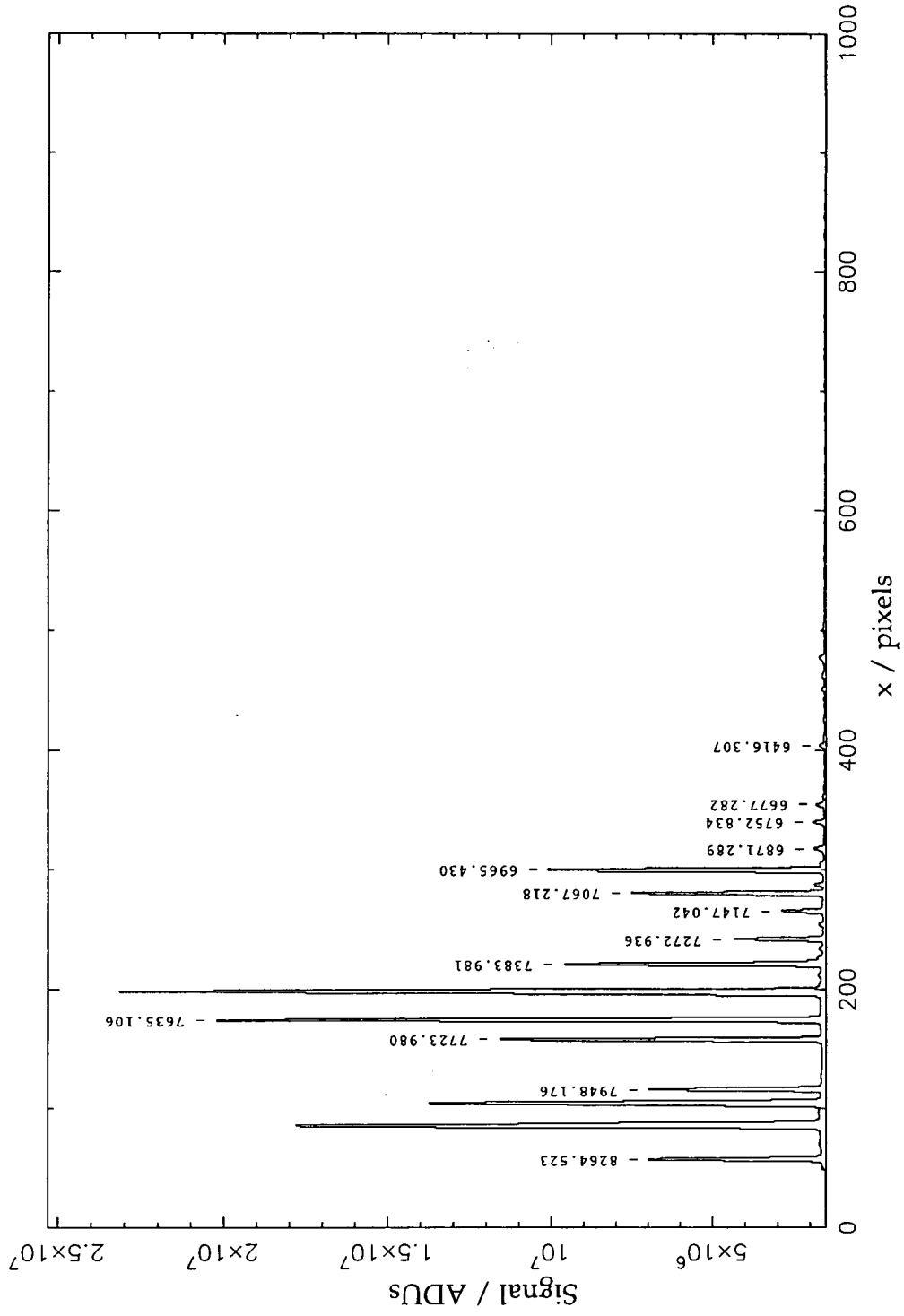


Figure A.5: CuAr line identification chart for medium-red grism (1)

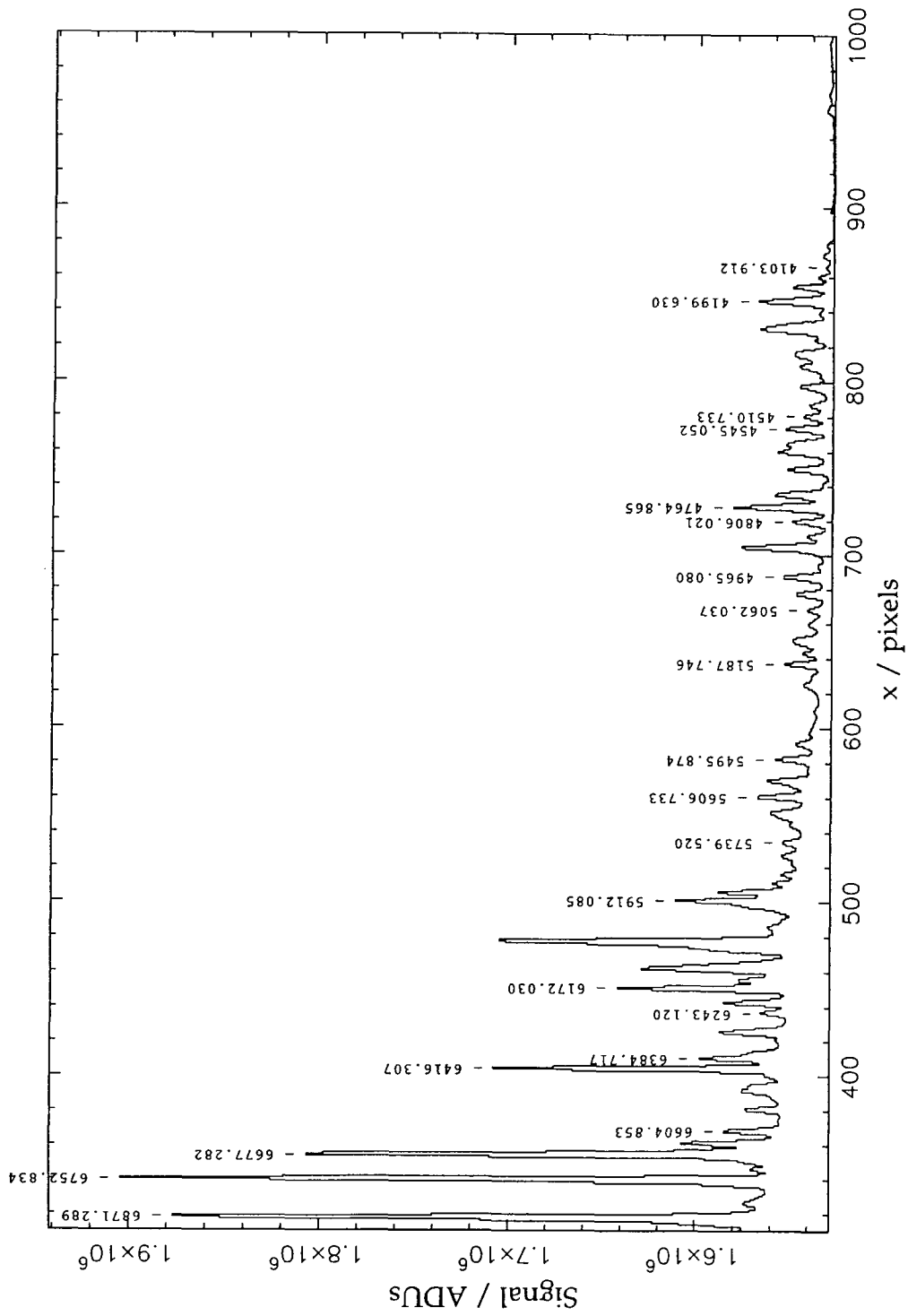


Figure A.6: CuAr line identification chart for medium-red grism (2)

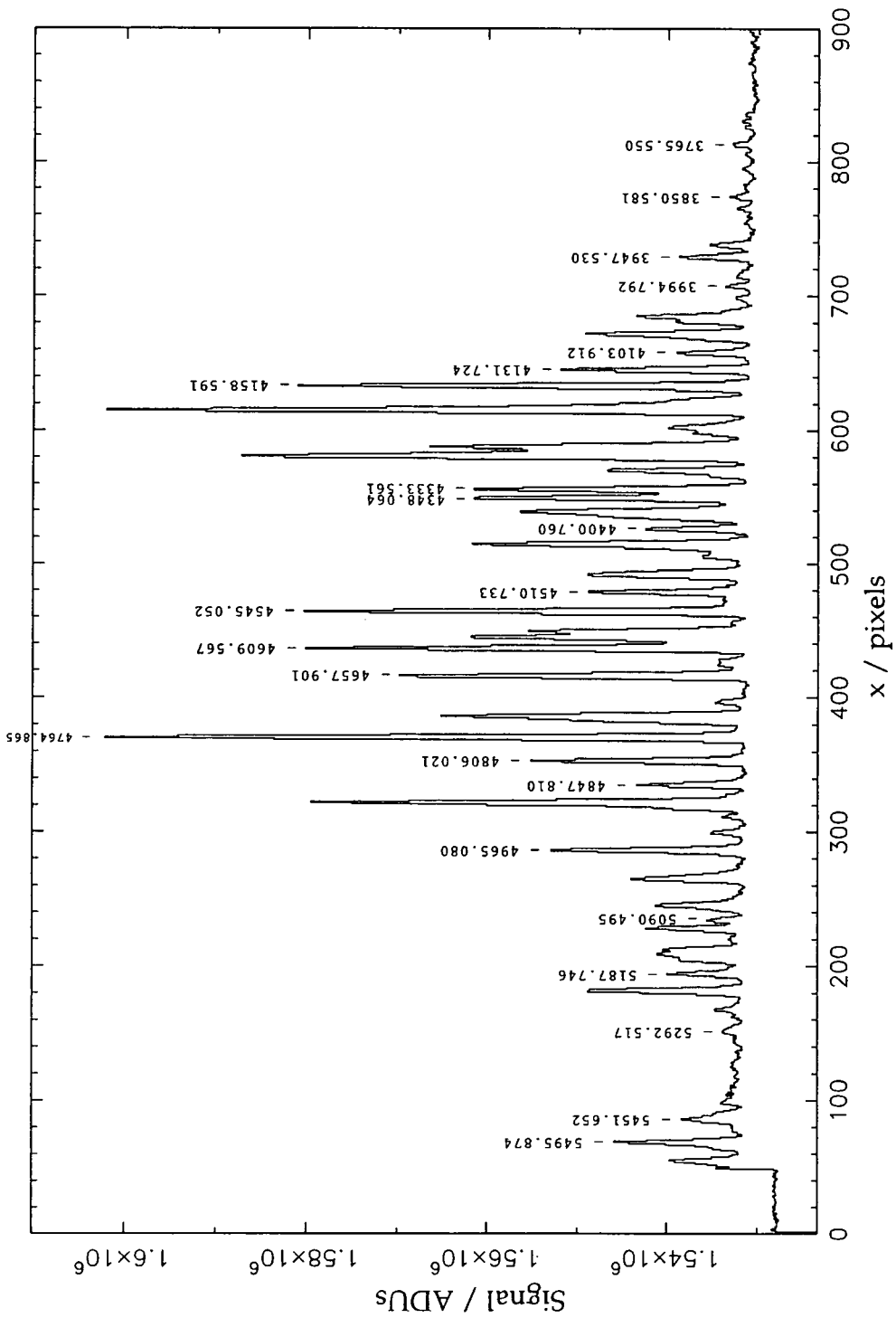


Figure A.7: CuAr line identification chart for high dispersion grism (1)

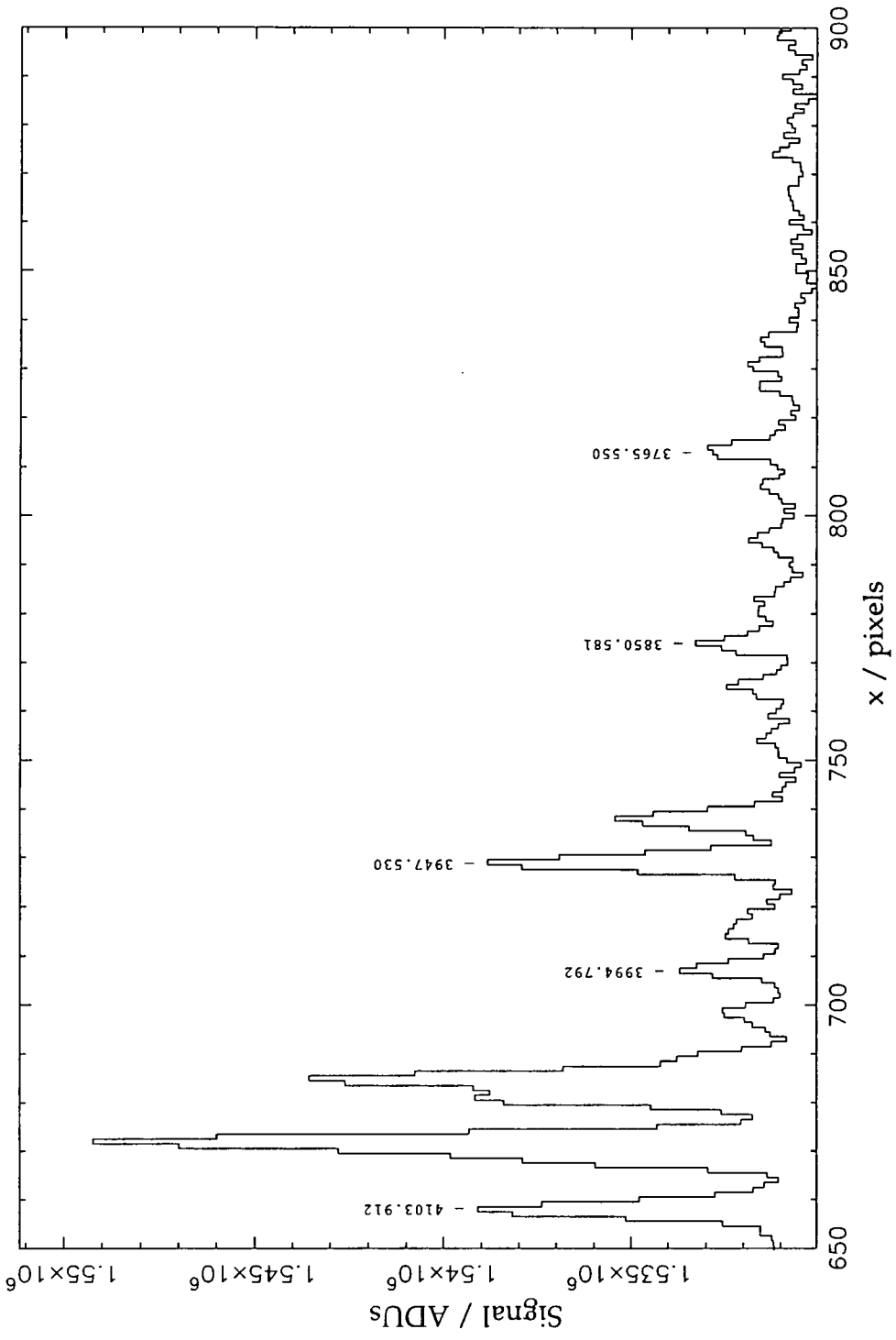


Figure A.8: CuAr line identification chart for high dispersion grism (2)

# Appendix B: LDSS-2 Filter Transmission Functions

## B.1 Introduction

This appendix contains detailed throughput measurements for the LDSS-2 filters. Three sets of measurements are listed:

- the theoretical transmission functions, calculated from the filter prescriptions
- the actual transmission functions of a similar set of filters, measured using a spectrophotometer
- the actual transmission functions of the LDSS-2 filters, measured using the instrument

The theoretical transmission function was calculated by multiplying the transmissions of the component glasses (scaled to account for the glass thicknesses) together with the transmission of the anti-reflection coating that was applied by the RGO.

The spectrophotometer measurements were performed by the NOAO using their 'Lambda 9' spectrophotometer. The filters were made to the same prescriptions as the LDSS-2 PB, PV and PR filters, though the anti-reflection coatings may not have been the same. Differences can also be expected due to the manufacturing tolerances for the glass thickness.

The LDSS-2 measurements are detailed in section 8.6. They were carried out using a tungsten lamp, which peaks at about 6500Å. The signal to noise ratio deteriorates rapidly below 4600Å and above 8000Å. The affected results are marked with a \*.

In tables B.1 to B.3,  $\lambda$  is the wavelength.  $t_c$  is the transmission calculated from prescription,  $t_t$  is the transmission measured using the telescope and  $t_s$  is the transmission measured using the spectrophotometer.

## B.2 PB and PV Filters

Table B.1 lists the results for the PB and PV filters. The results are shown graphically in figure B.1.

$\lambda/\text{\AA}$	PB: $t_c$	PB: $t_s$	PB: $t_t$	PV: $t_c$	PV: $t_s$	PV: $t_t$
3000	0.000	0.000	—*	0.000	0.000	—*
3200	0.000	0.000	—*	0.000	0.000	—*
3400	0.000	0.000	—*	0.000	0.000	—*
3600	0.007	0.052	—*	0.000	0.000	—*
3800	0.551	0.425	—*	0.000	0.000	—*
4000	0.745	0.650	0.437*	0.000	0.000	0.003*
4200	0.804	0.731	0.584*	0.000	0.000	0.006*
4400	0.789	0.735	0.639*	0.000	0.000	0.002*
4600	0.686	0.668	0.607	0.000	0.000	0.003
4800	0.430	0.431	0.397	0.044	0.151	0.006
5000	0.176	0.186	0.167	0.756	0.832	0.706
5200	0.038	0.046	0.040	0.941	0.887	0.876
5400	0.008	0.011	0.009	0.895	0.841	0.854
5600	0.015	0.020	0.016	0.771	0.714	0.759
5800	0.002	0.003	0.002	0.560	0.507	0.588
6000	0.000	0.000	0.001	0.335	0.278	0.370
6200	0.000	0.000	0.000	0.144	0.108	0.176
6400	0.000	0.000	0.000	0.044	0.028	0.060
6600	0.000	0.000	0.000	0.010	0.005	0.014
6800	0.000	0.000	0.000	0.002	0.000	0.002
7000	0.000	0.000	0.000	0.000	0.000	0.000
7200	0.000	0.000	0.000	0.000	0.000	0.000
7400	0.000	0.000	0.000	0.000	0.000	0.000
7600	0.000	0.000	0.000	0.000	0.000	0.000
7800	0.000	0.000	0.000	0.000	0.000	0.000
8000	0.000	0.000	0.000	0.000	0.000	0.000
8200	0.000	0.000	0.001*	0.000	0.000	0.000*
8400	0.000	0.000	—*	0.000	0.000	—*
8600	0.000	0.000	—*	0.000	0.000	—*
8800	0.000	0.000	—*	0.000	0.000	—*
9000	0.000	0.000	—*	0.000	0.000	—*
9200	0.000	0.000	—*	0.000	0.000	—*
9400	0.000	0.000	—*	0.000	0.000	—*
9600	0.000	0.000	—*	0.000	0.000	—*
9800	0.000	0.000	—*	0.000	0.000	—*

Table B.1: PB and PV filter transmission functions

### B.3 PR and S1 Filters

Table B.2 lists the results for the PR and S1 filters. The results are shown graphically in figures B.1 and B2 respectively.

$\lambda/\text{\AA}$	PR: $t_c$	PR: $t_s$	PR: $t_t$	S1: $t_c$	S1: $t_t$
3000	0.000	0.000	—*	0.000	—*
3200	0.000	0.000	—*	0.000	—*
3400	0.000	0.000	—*	0.000	—*
3600	0.000	0.000	—*	0.057	—*
3800	0.000	0.000	—*	0.603	—*
4000	0.000	0.000	0.064*	0.884	0.909*
4200	0.000	0.000	0.029*	0.941	0.937*
4400	0.000	0.000	0.016*	0.962	0.931*
4600	0.000	0.000	0.007	0.962	0.945
4800	0.000	0.000	0.005	0.962	0.947
5000	0.000	0.000	0.002	0.962	0.955
5200	0.000	0.000	0.002	0.962	0.956
5400	0.005	0.001	0.002	0.960	0.956
5600	0.572	0.202	0.405	0.960	0.957
5800	0.854	0.795	0.838	0.958	0.957
6000	0.853	0.820	0.839	0.958	0.955
6200	0.817	0.777	0.795	0.958	0.954
6400	0.757	0.712	0.734	0.956	0.953
6600	0.687	0.637	0.662	0.956	0.951
6800	0.608	0.553	0.582	0.955	0.951
7000	0.509	0.459	0.490	0.955	0.949
7200	0.419	0.368	0.398	0.953	0.949
7400	0.329	0.284	0.312	0.953	0.947
7600	0.250	0.210	0.235	0.951	0.947
7800	0.179	0.149	0.169	0.949	0.944
8000	0.129	0.102	0.117	—	0.944
8200	0.089	0.067	0.078*	—	0.943*
8400	0.059	0.043	—*	—	—*
8600	0.039	0.027	—*	—	—*
8800	0.030	0.017	—*	—	—*
9000	0.019	0.009	—*	—	—*
9200	0.010	0.006	—*	—	—*
9400	0.005	0.004	—*	—	—*
9600	0.004	0.002	—*	—	—*
9800	0.003	0.001	—*	—	—*

Table B.2: PR and S1 filter transmission functions

## B.4 S2 and S3 Filters

Table B.3 lists the results for the S2 and S3 filters. The results are shown graphically in figures B.3 and B4 respectively.

$\lambda/\text{\AA}$	S2: $t_c$	S2: $t_t$	S3: $t_c$	S3: $t_t$
3000	0.000	—*	0.000	—*
3200	0.000	—*	0.002	—*
3400	0.000	—*	0.285	—*
3600	0.000	—*	0.660	—*
3800	0.000	—*	0.816	—*
4000	0.000	0.220*	0.854	0.605*
4200	0.478	0.529*	0.852	0.724*
4400	0.855	0.771*	0.810	0.732*
4600	0.922	0.830	0.703	0.652
4800	0.933	0.874	0.439	0.406
5000	0.943	0.909	0.177	0.117
5200	0.943	0.921	0.039	0.039
5400	0.943	0.924	0.009	0.009
5600	0.933	0.932	0.018	0.019
5800	0.922	0.925	0.002	0.003
6000	0.922	0.914	0.000	0.000
6200	0.920	0.914	0.000	0.000
6400	0.930	0.909	0.000	0.000
6600	0.939	0.910	0.000	0.000
6800	0.947	0.924	0.000	0.002
7000	0.947	0.937	0.001	0.004
7200	0.955	0.941	0.000	0.002
7400	0.955	0.940	0.000	0.001
7600	0.953	0.940	0.000	0.001
7800	0.953	0.940	0.000	0.001
8000	—	0.938	0.000	0.001
8200	—	0.938*	0.000	0.001*
8400	—	—*	0.000	—*
8600	—	—*	0.000	—*
8800	—	—*	0.000	—*
9000	—	—*	0.000	—*
9200	—	—*	0.000	—*
9400	—	—*	0.000	—*
9600	—	—*	0.000	—*
9800	—	—*	0.000	—*

Table B.3: S2 and S3 filter transmission functions

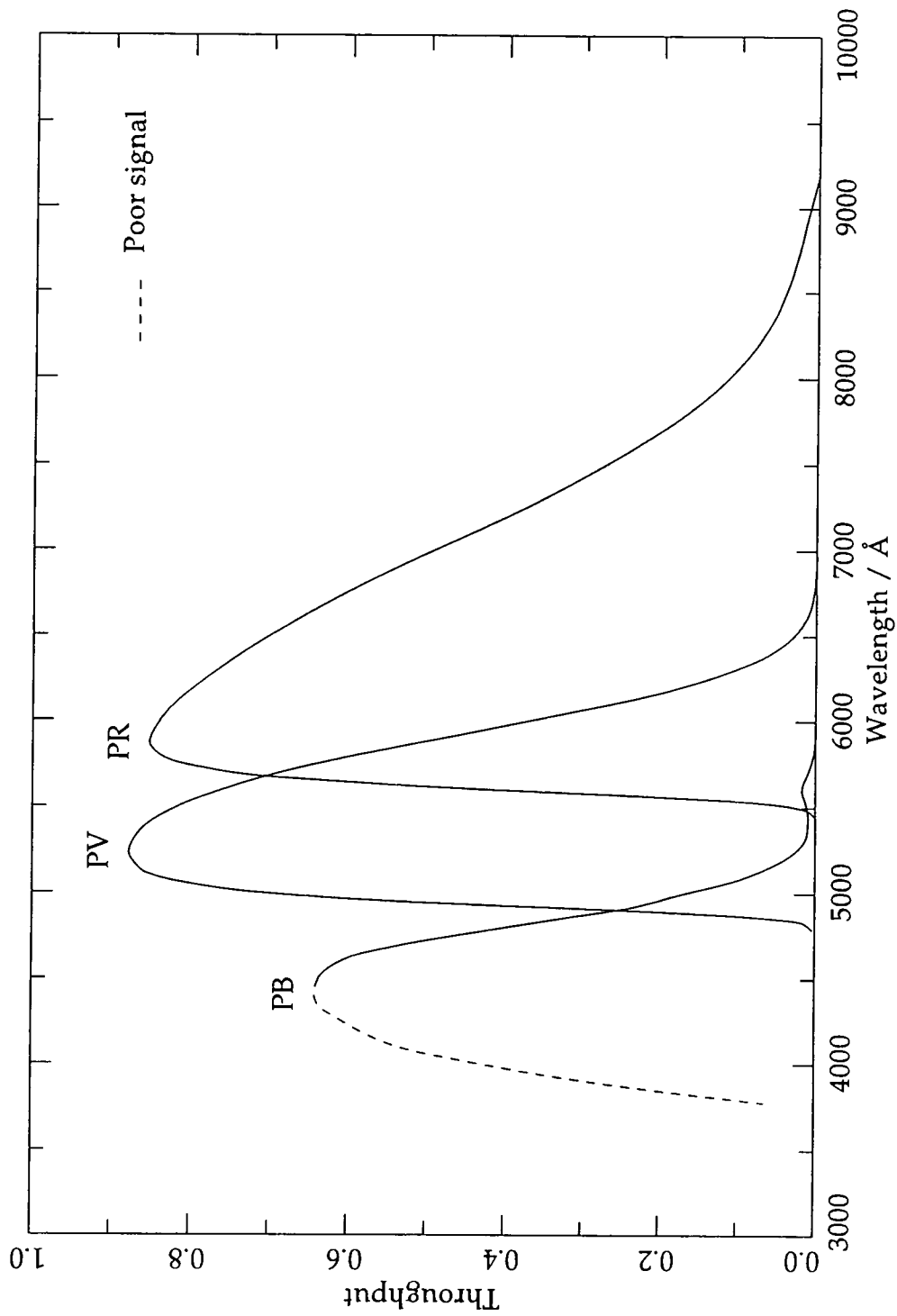


Figure B.1: PB, PV and PR filter transmission functions

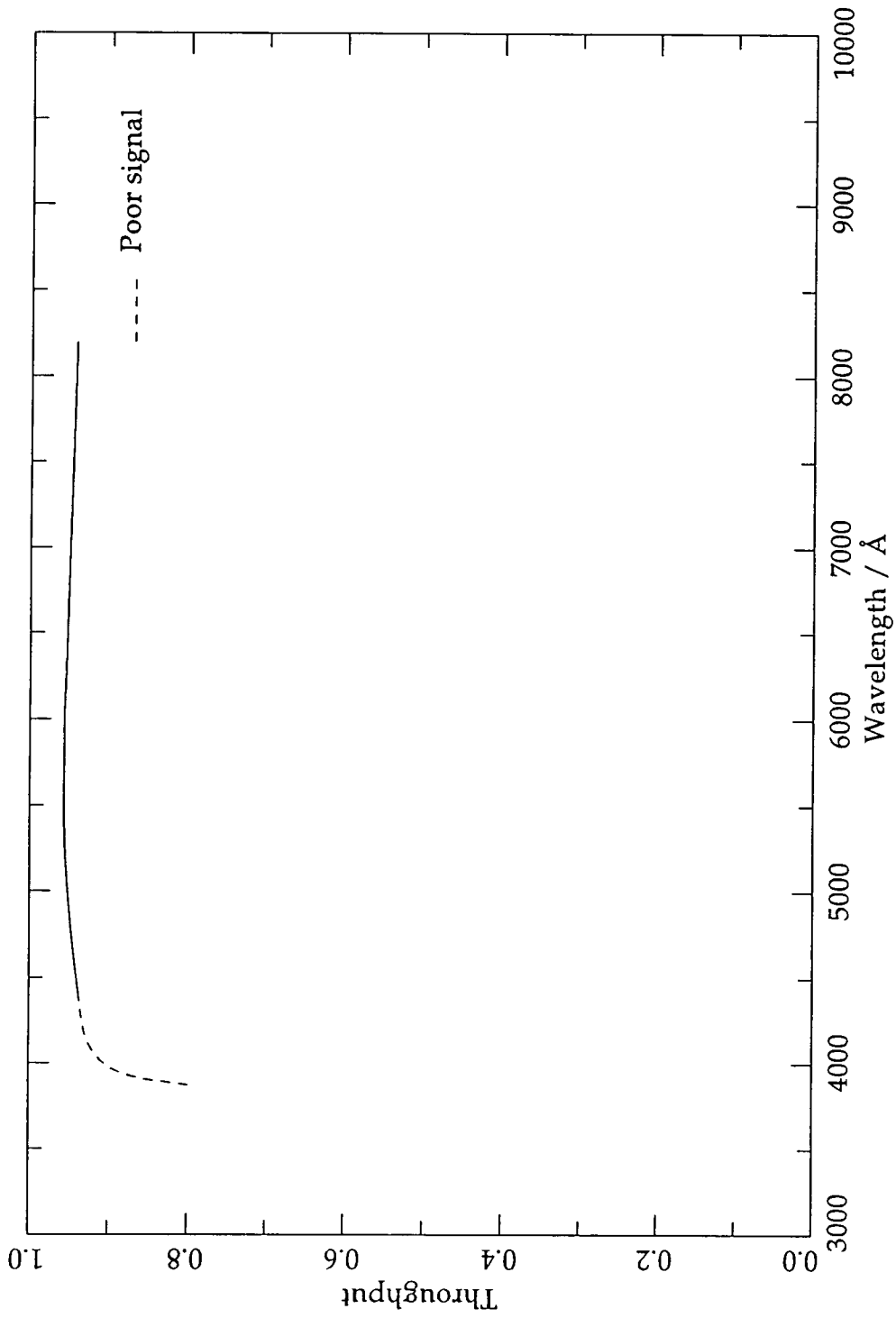


Figure B.2: S1 filter transmission function

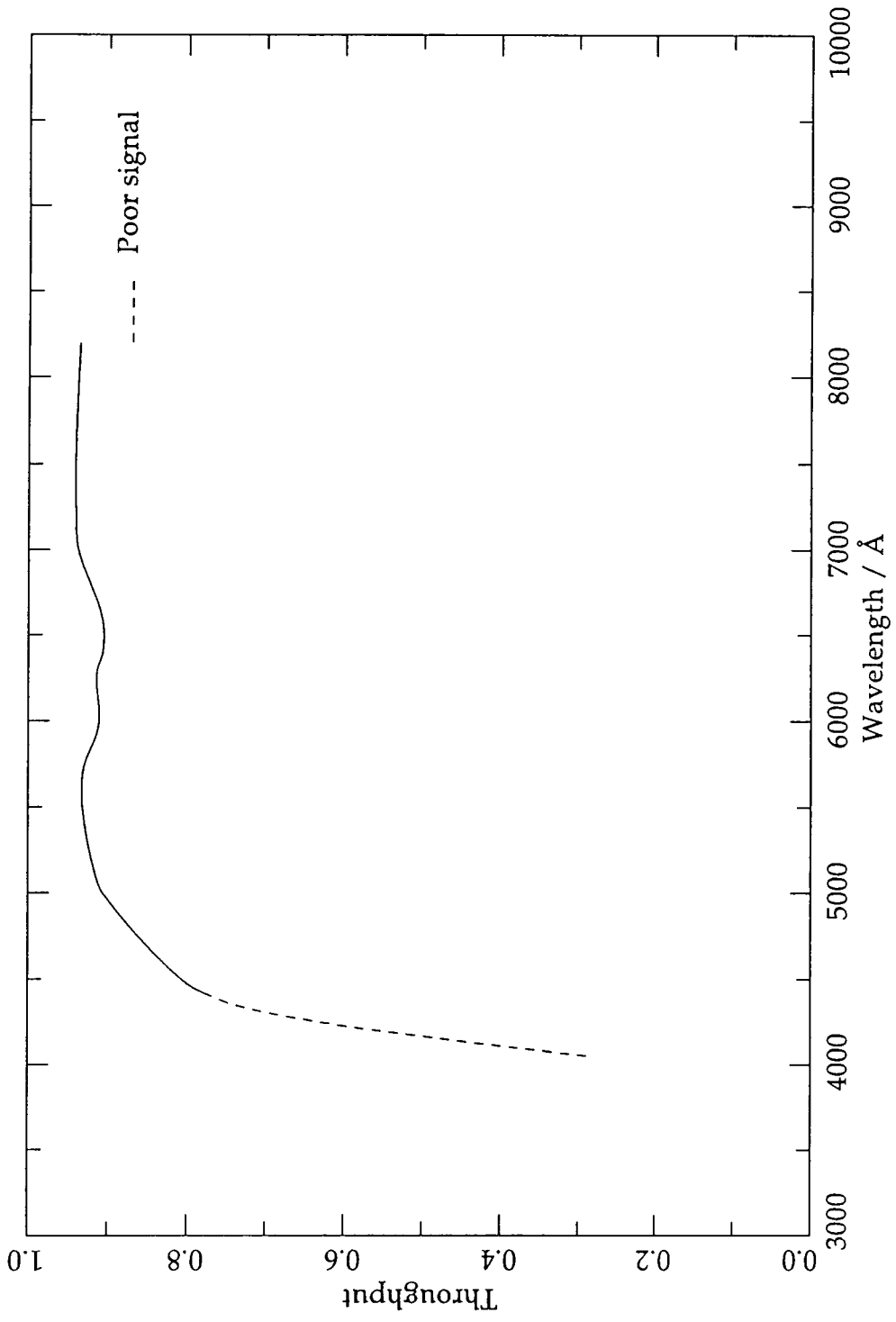


Figure B.3: S2 filter transmission function

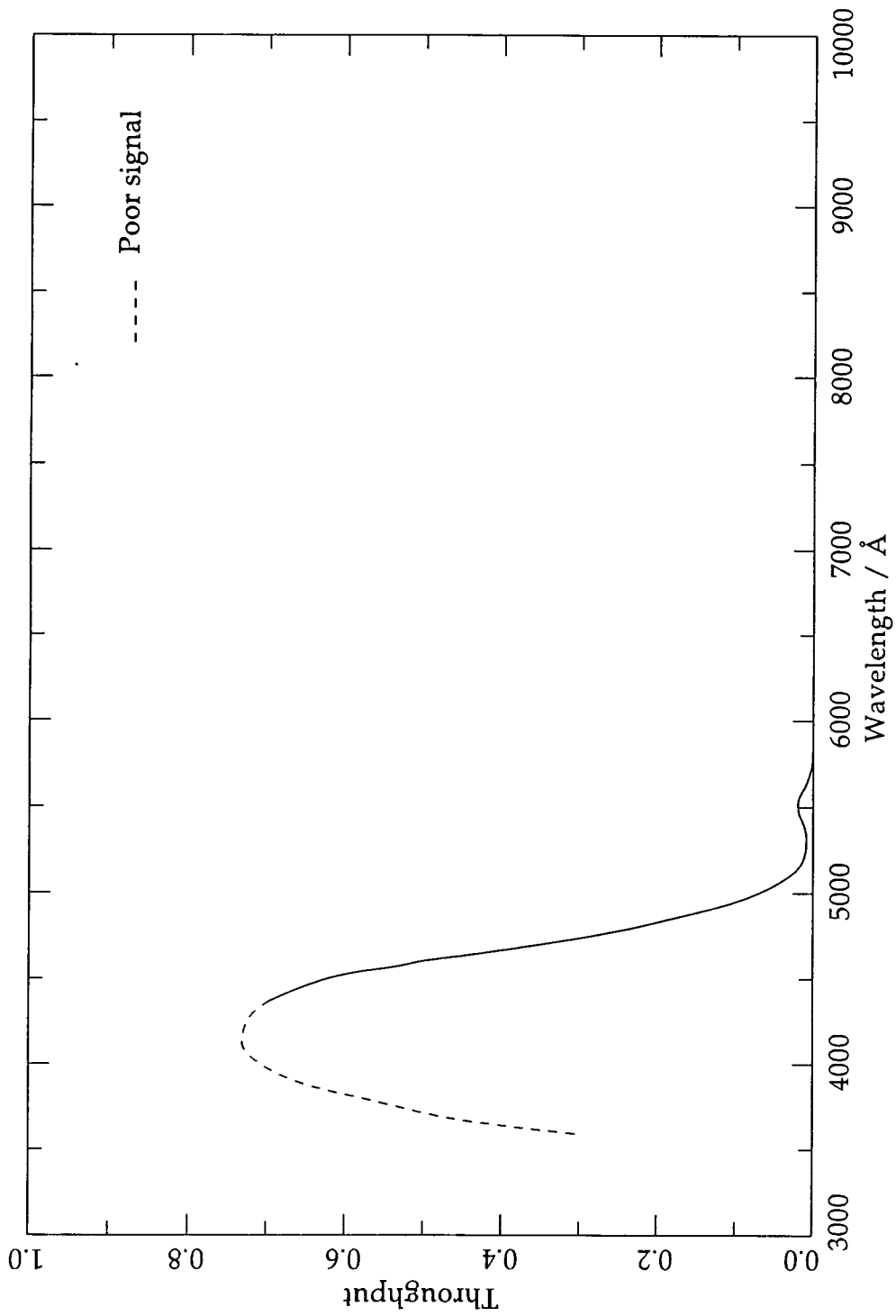


Figure B.4: S3 filter transmission function

# Glossary

- 4MS 4 Metre Telescope Microcomputer System
- AAT Anglo Australian Telescope
- ADC Analogue to Digital Converter
- ASCII American Standard Code for Information Interchange
- BBI Bus Buffer Interface card
- CCD Charge Coupled Device
- CFHT Canada-France-Hawaii Telescope
- EFOSC ESO Faint Object Spectrograph and Camera
- EMMI ESO Multi-Mode Instrument
- EPROM Erasable Programmable Read Only Memory
- ESO European Southern Observatory
- FORS Focal Reducer / Low Dispersion Spectrograph
- FOS Faint Object Spectrograph
- FOS-2 Faint Object Spectrograph 2
- FWHM Full Width Half Maximum
- GPIB General Purpose Instrument Bus
- IPCS Imaging Photon Counting System
- LAMA LAsEr MACHine
- LDSS-1 Low Dispersion Survey Spectrograph 1
- LDSS-2 Low Dispersion Survey Spectrograph 2
- LED Light Emitting Diode
- LPO La Palma Observatory
- LRIS Low Resolution Imaging Spectrograph
- LVDT Linear Variable Displacement Transducer
- MOS/SIS Multi-Object Spectrograph / Sub-arcsecond Imaging Spectrograph
- NIU Network Interface Unit
- NTT New Technology Telescope
- PATT Panel for the Allocation of Telescope Time

PIA Parallel Interface Adaptor  
PSU Power Supply Unit  
PUMA PUnching MACHine  
QSO Quasi-Stellar Object  
RAM Random Access Memory  
RGO Royal Greenwich Observatory  
RMS Root Mean Square  
ROM Read Only Memory  
SCC Shutter Control Card  
SLVC Super Linear Variable Capacitor  
SMDM Stepper Motor Driver Module  
VLT Very Large Telescope  
WHT William Herschel Telescope

## References and Bibliography

1. Allington-Smith J R, Breare J M, Ellis R S, Parry I R, Shaw G D, Webster J, Gellatly D W and Worswick S P, "A Low Dispersion Survey Spectrograph for the William Herschel Telescope" (SPIE 1990 Symposium on Astronomical Telescopes for the 21st Century, 1990a)
2. Allington-Smith J R, Benham D, Breare J M, Ellis R S, Gellatly D W and Shaw G D, "A Multislit System for FOS-2, ISIS and LDSS-2" (Durham University technical note, 1990b)
3. Allington-Smith J R (Ed), "Low Dispersion Survey Spectrograph LDSS-2 Observer Manual" (Durham University, 1992a)
4. Allington-Smith J R, Worswick S P and Gellatly D W, "An Imaging Faint Object Spectrograph (IFOS) – A Design Study for the Gemini 8-m Telescopes" (ESO Conference on Progress in Telescope and Instrumentation Technologies, 1992b)
5. Allington-Smith J R, Breare J M, Ellis R S, Gellatly D W, Glazebrook K, Jordan P, MacLean J F, Oates A P, Shaw G D, Tanvir N R, Taylor K, Taylor P B, Webster J and Worswick S P, "A Low Dispersion Survey Spectrograph (LDSS-2) for the William Herschel Telescope" (ESO Conference on Progress in Telescope and Instrumentation Technologies, 1992c)
6. American Society for Metals, "Metals Handbook" (Vol 2, 9th Ed, American Society for Metals, Ohio, 1979)
7. Appenzeller I and Rupprecht G, "FORS – The Focal Reducer for the VLT" (ESO Messenger, No 67, March 1992a)

8. Appenzeller I, Duensing K H, Fricke K, Gong S, Hess H -J, Kiesewetter S, Kudritzki R -P, Möhler S, Muschielok B, Nicklas H, Östreicher R, Roth M, Rupprecht G, Siefert W and Stahl O, "FORS: A Multi-purpose Instrument for the ESO VLT" (ESO Conference on Progress in Telescope and Instrumentation Technologies, 1992b)
9. Bracewell Ron, "The Fourier Transform and its Applications" (McGraw Hill, New York, 1965)
10. Breda I G and Parker N M, "FORTH and microprocessor applications at the Royal Greenwich Observatory" (Microprocessors and Microsystems, Vol 7 No 5, 203–211, 1983)
11. Brodie Leo, "Starting FORTH" (FORTH Inc, 1981)
12. Brown Earle B, "Modern Optics" (Reinhold Publishing Corporation, New York (USA), 1965)
13. Burden Richard L and Faires Douglas J, "Numerical Analysis" (4th Ed, PWS-KENT Publishing Company, USA, 1989)
14. Buzzoni B, Delabre B, Dekker H, D'Odorico S, Enard D, Focardi P, Gustafsson B, Nees W, Paureau J and Reiss R, "The ESO Faint Object Spectrograph and Camera (EFOOSC)" (ESO Messenger, No 38, 1984)
15. Colless M, Ellis R S, Taylor K and Hook R N, "The LDSS deep redshift survey" (Mon.Not.R.astr.Soc, 244, 408–423, 1990)
16. Colless M, Ellis R S, Taylor K and Shaw G D, "A spectroscopic survey of faint compact objects" (Mon.Not.R.Astr.Soc, 253, 686–702, 1991)

17. Crampton D, Grundmann W A, Leckie B, Morbey C L, Lemonnier J P, Felenbok P, Marteaud M, Vola P, Georgelin Y, Le Fèvre O, Grundseth B, Monnet G and Salmon D, "Multi-Aperture and Subarcsecond Imaging Spectrograph for CFHT" (ESO Conference on Progress in Telescope and Instrumentation Technologies, 1992)
18. Dekker H and D'Odorico S, "Multiple Object Spectroscopy (MOS) with EFOSC" (ESO Operating Manual No 5, April 1986)
19. Dekker H and D'Odorico S, "EMMI Through the Last Tests Before Entering Regular Use" (ESO Messenger, No 62, December 1990)
20. Dekker H, D'Odorico S, Kotzlowski H, Lizon J -L, Longinotti A, Nees W and De Lapparent-Gurriet V, "Multi Object Spectroscopy with the ESO Multi Mode Instrument at the NTT" (ESO Messenger, No 63, March 1991)
21. Di Biagio B, Le Coarer E and Lemaître G, "2D Mask Generation by YAG laser for multi-object spectroscopy at CFHT: LAMA" (SPIE Instrumentation in Astronomy VII, Vol 1235, 1990)
22. D'Odorico S and Dekker H, "The Five Observing Modes of EFOSC, the ESO Faint Object Spectrograph and Camera Designed Around a CCD Detector (ESO Proceedings, The Optimisation of CCD Detectors in Astronomy, 1986)
23. D'Odorico S, "EMMI, the ESO Multi-Mode Instrument, Successfully Installed at NTT" (ESO Messenger, No 61, September 1990)
24. Duensing K -H, Harke R, Nicklas H, Renziehausen H, Bönhardt H, Hess H -J, Kiesewetter S and Mitsch W, "Prototype of the FORS Multiple-Object Spectroscopy Unit Under Test" (ESO Messenger, No 71, March 1993)

25. Duley W W, "Laser Processing and Analysis of Materials" (Plenum Press, 1983)
26. Fried D L, "The Nature of Atmospheric Turbulence Effects on Imaging and Pseudo-Imaging Systems, and its Quantification" (IAU Colloquium No 50, 1978)
27. Flügge W, "Handbook of Engineering Mathematics" (McGraw Hill, USA, 1962)
28. Hecht Jeff, "The Laser Guidebook" (McGraw Hill, New York, 1986)
29. Johnson M R, "4.2 Metre William Herschel Telescope Utility Network Instrument Control Recommendations" (Royal Greenwich Observatory, ER415 Rev 3, 1987)
30. Kaye G W C and Laby T H, "Tables of Physical and Chemical Constants" (15th Ed, Longman, Harlow, 1986)
31. King D L, "ING La Palma Technical Note 31" (La Palma Observatory, 1985)
32. Koebner Hans (Ed), "Industrial Applications of Lasers" (John Wiley & Sons, Chichester, 1984)
33. Lefaux René, "Practical Toxicology of Plastics" (Iliffe Books, London, 1968)
34. Le Fèvre O, Crampton D, Felenbok P and Monnet G, "CFHT MOS/SIS Spectrograph Performance" (Preprint, 1993)
35. Lemaître G and Vigroux L, "All-Reflective Aspherized Grating Spectrographs at the Prime Focus of the CFHT" (Instrumentation for Ground-Based Optical Astronomy, Ninth Santa Cruz Summer Workshop, Robinson L B (Ed), Springer-Verlag, 275–295, 1987)

36. Mathsoft, "Mathcad 3.1 User's Guide, Windows Version" (Mathsoft Inc, Cambridge (Mass, USA), 1991)
37. Ready John F, "Industrial Applications of Lasers" (Academic Press, New York, 1978)
38. Taylor John R, "An Introduction to Error Analysis" (University Science Books, California (USA), 1982)
39. Trade & Technical Press, "Handbook of Industrial Materials" (1st Ed., Trade & Technical Press Ltd., Surrey)
40. Unger S W, Brinks E, Laing R A, Tritton K P and Gray P M, "ING La Palma Observer's Guide" (V2.0, Royal Greenwich Observatory, 1988)
41. Vlot M C and Johnson M R, "4MS Network Layer Software for Ethernet Applications" (Royal Greenwich Observatory, ER410, 1986)
42. Weast Robert C (Ed), "Handbook of Chemistry and Physics" (58th Ed, CRC Press Inc, Cleveland (USA), 1977)
43. Wurtz R and Stocke J T, "Tests of Liquid Crystal Screens for Use in Multi-Object Slit Spectroscopy" (PASP, 104, 931-938, 1992)
44. Wynne C G and Worswick S P, "A Low Dispersion Survey Spectrograph" (The Observatory, 108, 161, 1988)
45. Zuiderwijk E J and Knapen J, "ING La Palma Technical Note 70" (La Palma Observatory, 1989)

# Acknowledgements

My thanks to:

Jeremy Allington-Smith, Mike Breare, Matthew Colless,  
Richard Ellis, Dave Gellatly, Karl Glazebrook, Mick Johnson,  
Alan Lotts, John Maclean, John Major, Paddy Oates,  
James Scobbie, Ann Shaw, Duncan Shaw, Nial Tanvir,  
Keith Taylor, Philip Taylor, Helen Topping, John Webster,  
Sue Worswick, and the observatory staff on La Palma.

